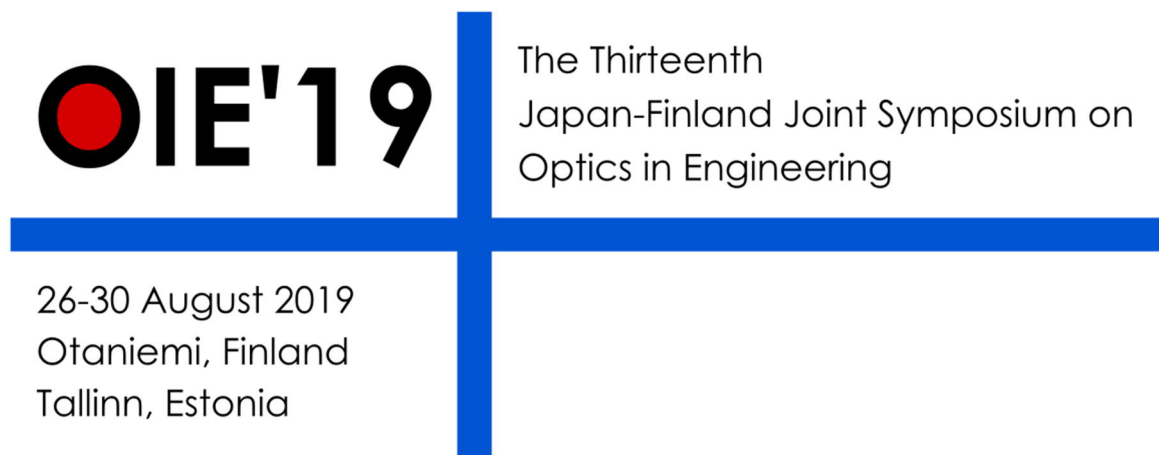


OIE 2019

The 13th Japan-Finland Joint Symposium on Optics in Engineering

26-30 August 2019, in Espoo and Tallinn



Proceedings of OIE 2019

Edited by: Petri Kärhä, Erkki Ikonen, Yoshio Hayasaki, and Kai Peiponen

Abstracts of the 13th Japan-Finland Joint Symposium on Optics in Engineering

Table of Contents

Preface	vi
Committee	vii
International Organizing Committee	vii
Local Organizing Committee	viii
Chairmen of the sessions	viii
Author Index (end of document)	ix

Session 1: Holography & Nanostructures

Ville A. Kaikkonen, Eero O. Molkoselkä and Anssi J. Mäkynen, "ICEMET – a sensor for in-cloud icing condition monitoring"	... 1
Yasuo Tomita, Toshi Aoi, Shuma Hasegawa, Kento Kaseda, Juro Oshima and Keisuke Odoi, "Hyperbranched polymer nanocomposite gratings for volume holographic optical elements"	... 3
Filipp Temerov and Jarkko J. Saarinen, "Enhanced photocatalytic activity of TiO ₂ inverse opal structures with gold-silver nanoparticles"	... 5
Masayuki Yokota, Tatsuya Ishikawa and Yoshinobu Aoki, "Polarization state of the object wave analyzed by using FMCW-digital holography"	... 7

Session 2: Imaging science & Optical computing

Yoshio Hayasaki, Ryo Sato and Yujiro Ito, "Single-pixel imaging with hole-array coding masks"	... 9
Nathan Hagen, "High throughput spectral imaging with snapshot sensing"	... 11
Jun Tanida, Suguru Shimomura, Takahiro Nishimura, Yuki Miyata, Naoya Tate and Yusuke Ogura, "A quantum dot reservoir based on Förster resonance energy transfer for optical reservoir computing"	... 13
Shuji Taue, "Visualizing AC magnetic fields by using atomic magnetometer and micro-mirror device"	... 15
Yukitoshi Otani, Shuhei Shibata, Masayuki Suzuki and Nathan Hagen, "Video-rate imaging for Stokes parameters by polarization cameras"	... 17

Session 3: Posters

Mikko J. Huttunen, Radu Hristu, Adrian Dumitru, Mariana Costache and Stefan C. Stanciu, "Deep learning enhanced multiphoton microscopy for investigating the dermoepidermal junction in human skin"	... 18
Katri Kukkola, Anssi Mäkynen, Ville Kaikkonen, Gleb Bulygin, Eero Molkoselkä, Niklas Pikkarainen, Nanni Nielikäinen, Alekski Rantanen, Antti Kämppi, Tarja Tanner and Vuokko Anttonen, "Full arch dental imaging using an extraoral camera system"	... 20

Elnaz Fazeli, Takahiro Deguchi, Sami Koho, Juha Peltonen, Tuomas Näreoja and Pekka Hänninen, "Live cell imaging with integrated STED-AFM"	...	22
Kaustav Das, Yuta Kobori, Tomonori Yuasa, Hideki Funamizu and Yoshihisa Aizu, "Monte Carlo based investigation of spectral reflectance and point spread function in skin tissue model"	...	24
Benjamin O. Asamoah, James Amoani, Matthieu Roussey and Kai-E. Peiponen, "On optical sensing of microplastics in water"	...	26
A. Pokatilov, G. Porrovecchio and T. Kübarsepp, "Development of self-adjusting photodiode arrangement for accurate laser optical power measurements"	...	28
Ilpo Niskanen, Hiroshi Hasegawa, Jukka Rätty, Hariyadi Soetedjo, Kenichi Hibino, Hiroshi Oohashi, Rauno Heikkilä, Kiyofumi Matsuda and Yukitoshi Otani, "Polarimeter analysis of the birefringence of thermally modified Scots pine wood"	...	29
Kenji Harada, Sho Sakurai and Yutaro Shibata, "How to control polarization color and its applications"	...	31
Prince Bawuah, Mohammed Al-Sharabi, Cathy Ridgway, Anssi-Pekka Karttunen, Ossi Korhonen, Patrick Gane, Jarkko Ketolainen, Kai-Erik Peiponen, J. Axel Zeitler and Daniel Markl, "Predicting the refractive index of porous powder samples during compaction using terahertz time-domain spectroscopy"	...	33
Jeremias Seppä and Tuomas Helojärvi, "Ambient air spectroscopy and thermometry for accurate distance measurement"	...	35
Natsuki Suzuki and Katsuhiko Ishii, "Label-free and vibration-free imaging using low-coherent quantitative phase microscope"	...	37
Oskari Pekkala, Tomi Pulli, Alexander Kokka and Erkki Ikonen, "Setup for characterising the spectral responsivity of Fabry-Perot-interferometer-based hyperspectral cameras"	...	39
Harri J. Juttula, Matti Törmänen and Anssi J. Mäkynen, "Comparison of experimental and the Mie scattering coefficients of bulk suspensions of ideal and deformed cylindrical particles"	...	41
Virpi Korpelainen, Johan Nysten, Jeremias Seppä and Antti Lassila, "Development of metrological atomic force microscope"	...	43
Eero O. Molkoselkä, Gleb A. Bulygin, Justus F. Kleine and Anssi J. Mäkynen, "3D printed lens project for bachelor's education"	...	44
Yasuhiro Matsuda, Hiroshi Kigami, Noriyuki Unno, Jun Taniguchi and Shin-ichi Satake, "Three-dimensional flow measurements around micro-pillars in water by micro-digital holographic particle tracking velocimetry"	...	46
Janne Lauri, Antti Koponen, Sanna Haavisto and Tapio Fabritius, "Evaluation of yield stress from velocity fluctuations of microfibrillated cellulose suspension flow by optical coherence tomography"	...	48
Petri Kärhä, Hans Baumgartner, Kasper Kylmänen, Benjamin Oksanen and Erkki Ikonen, "Measurement setup for differential spectral responsivity of solar cells"	...	50

Päivi Heimala, Mikko Harjanne, Ari Hokkanen, Matteo Cherchi, Tapani Vehmas, Srivathsa Bhat and Timo Aalto, "VTT's versatile 3 μ m silicon photonics platform"	...	52
M. Baah, T. Kaplas and Y. Svirko, "Effect of nanometrically thin nickel catalyst on the properties of CVD synthesized graphitic films"	...	54
Sampson S. Andoh, Kenneth Nyave, Boniphace Kanyathare, Benjamin Asamoah, Tarmo Nuutinen, Cheetham Mingle, Kai-E. Peiponen and Matthieu Roussey, "Qualitative analysis for presence of Sudan IV in edible palm oil"	...	56
Andris Slavinskis, Antti Nasila, Mihkel Pajusalu, Jaan Praks, Anu Reinart, Iaroslav Iakubivskiy, Tomas Kohout, Colin Snodgrass and Geraint Jones, "OPTical Imager for Comets (OPIC) for ESA's F-class mission Comet Interceptor"	...	58
Markku Pekkarinen, Petri Karvinen and Jyrki Saarinen, "Direct 3D-printing of optical components at the University of Eastern Finland"	...	60

Session 4: Biomedical optics & nonlinear optics

Yusuke Ogura, Daiki Shinkawa, Takahiro Nishimura, Yosuke Tamada and Jun Tanida, "Super-resolution imaging by scanning subdiffraction-limit optical pattern"	...	61
Matti Huotari, Kari Määttä and Juha Röning, "The beneficial effects of the sauna exposures measured by PPG"	...	63
Léo Turquet, Xiaorun Zang, Joona-Pekko Kakko, Harri Lipsanen, Godofredo Bautista and Martti Kauranen, "Creation and observation of a longitudinally-polarized optical needle"	...	64
Jussi Hiltunen, Sanna Uusitalo, Sanna Aikio, Marianne Hiltunen, Olli-Heikki Huttunen, Johanna Hiitola-Keinänen, Christina Liedert and Pentti Karioja, "Opto-fluidic biosensors by roll-to-roll fabrication"	...	66
Yelena Kan, Sapun Parekh, Erik M. Vartiainen and Lasse Lensu, "Quantitative CARS spectral imaging in studying protein droplets"	...	68

Session 5: Interferometry 1

Kenichi Hibino, Toshiki Kumagai and Yasunari Nagaike, "Synthetic aperture phase-shifting measurement for high numerical-aperture spherical surfaces"	...	70
Ville Heikkinen, Johan Nysten, Ville Byman, Björn Hemming and Antti Lassila, "3D measurements of freeform samples using multi sensor optical profilometer"	...	72
Takamasa Suzuki, Bin Liu, Samuel Choi and Osami Sasaki, "Thickness distribution measurement with a full-field pulsed SD-OCT"	...	73
Katsuhiro Ishii, Masaharu Hoshikawa, Takeshi Makino, Takahiro Hashimoto, Hideaki Furukawa and Naoya Wada, "Low-coherence interferometer with 10MHz repetition rate"	...	75

Session 6: Interferometry 2

Jun Uozumi, "Plenary talk: Analyzing and applying light with randomness; from speckles to fractals and to spectra"	...	77
--	-----	----

Yukihiro Ishii, Shunpei Yukita, Kosuke Kiyohara, Jun Chen and Eiji Tokunaga, "Wavelength-tunable common-path interferometer with a diode source"	...	79
Ryohei Hanayama and Katsuhiko Ishii, "Speckle shearing interferometric vibrometer for heartbeat monitoring"	...	81
M. Roussey, R. Rao and S. Pélisset, "Multimode interferometers on strip-loaded waveguide for sensing"	...	83
Juha Toivonen, "Finnish flagship program on photonics research and innovation"	...	85

Session 7: Detectors, lasers, and integrated & printed optics

Takashi Okamoto and Keigo Imamura, "Designing random structures for random laser media"	...	87
Jussi Rossi, Juho Uotila, Toni Laurila, Erkki Ikonen and Markku Vainio, "Broadband electromagnetic radiation detector based on photoacoustic effect"	...	89
Meelis-Mait Sildoja, Charles W. Stark, Jüri Pahapill, Matt Rammo, Katrin Petritsenko and Aleksander Rebane, "Measurement facility for high accuracy multiphoton absorption spectra"	...	91
Marja Vilkmann, Kaisa-Leena Väisänen, Marja Välimäki, Mari Ylikunnari and Thomas Kraft, "Printed electronics in pilot scale processing and production of organic photovoltaics, CIGS solar cells and OLEDs"	...	93
Timo Dönsberg, Santeri Porrasmaa, Farshid Manoocheri and Erkki Ikonen, "Predictable quantum efficient detector (PQED) based on n-type silicon induced junction photodiodes"	...	95

Session 8: Optical spectroscopy, spectral imaging and lidars

Kim Patokoski, Joona Rissanen, Teppo Noronen, Regina Gumenyuk, Yuri Chamrovskii and Valery Filippov and Juha Toivonen, "Tapered fiber amplifier for coherent lidar"	...	97
Tommi Mikkonen, Caroline Amiot, Antti Aalto, Kim Patokoski, Goëry Genty and Juha Toivonen, "Fourier transform photoacoustic spectroscopy with supercontinuum light source"	...	99
Heikki Saari, Harri Ojanen and Ingmar Stuns, "Novel hyperspectral imager based on angle-tuned multi pass band filter, Leds and RGB image sensor"	...	101
Antti Näsilä, Heikki Saari, Kai Viherkanto, Christer Holmlund, Rami Mannila, Roberts Trops, Endija Briede, Akseli Miranto, Altti Akujärvi, Harri Ojanen, Ismo Näkki, Ingmar Stuns, Hans Toivanen, Tahvo Havia, Martti Blomberg, Sari Elomaa and Tapani Antila, "Miniaturized spectral imaging technologies at VTT"	...	103

Preface

The 13th Japan-Finland Joint Symposium on Optics in Engineering (OIE) will take place on 26-30 August 2019 in two locations: The Otaniemi campus of Aalto University in Finland and the historical city of Tallinn in Estonia. The first two days of the symposium will be held on the campus of Aalto University in Finland. The campus is designed by the renowned Finnish architect Alvar Aalto. The latter half of the symposium will be held in Tallinn, Estonia. The old town of Tallinn is listed as UNESCO World Heritage Site.

We will have a tightly packed scientific program which is designed to allow many possibilities for detailed discussions between the participants. This international symposium gathers together the best scientists working in the field of optics in Japan, Finland and Estonia.

On behalf of the OIE Committee I welcome all of you to the Symposium!

Erkki Ikonen

Aalto University

General Chair of the OIE 2019

OIE 2019 sponsored by Aalto University, City of Espoo, and Optical Society of Japan



Committee

General Chair

Erkki Ikonen (Aalto University)

Co-Chairs

Yoshio Hayasaki (Utsunomiya University)

Pekka Hänninen (University of Turku)

International Organizing Committee (Program Committee)

Chair

Kai-Erik Peiponen (University of Eastern Finland)

Members

Takamasa Suzuki (Niigata University)

Katsuhiro Ishii (The Graduate School for the Creation of New Photonics Industries)

Yukitoshi Otani (Utsunomiya University)

Yusuke Ogura (Osaka University)

Shuji Taue (Kochi University of Technology)

Yoshihisa Aizu (Muroran Institute of Technology)

Kenji Harada (Kitami Institute of Technology)

Yasuo Tomita (The University of Electro-Communications)

Jun Uozumi (Hokkai-Gakuen University)

Ken-ich Hibino (National Institute of Advanced Industrial Science and Technology)

Toshiaki Iwai (Tokyo University of Agriculture and Technology)

Nathan Hagen (Utsunomiya University)

Masayuki Yokota (Shimane University)

Tapio Fabritius (University of Oulu)

Jukka Hast (VTT Technical Research Centre of Finland)

Seppo Honkanen (Microsoft)

Jarkko Saarinen (University of Eastern Finland)

Zhipei Sun (Aalto University)

Juha Toivonen (Tampere University of Technology)

Erik Vartiainen (Lappeenranta University of Technology)

Local Organizing Committee

Petri Kärhä (Aalto University)

Toni Laurila (Aalto University)

Tomi Pulli (Aalto University)

Aigar Vaigu (VTT Technical Research Centre of Finland)

Chairmen of the sessions

Session 1: Holography & Nanostructures

Prof. Yoshio Hayasaki (Utsunomiya University)

Session 2: Imaging science & Optical computing

Prof. Jukka Hast (VTT Technical Research Centre of Finland)

Session 3: Posters

Doc. Petri Kärhä (Aalto University)

Session 4: Biomedical optics & nonlinear optics

Prof. Jun Tanida (Osaka University)

Session 5: Interferometry 1

Prof. Yukihiro Ishii (Tokyo University of Science)

Session 6: Interferometry 2

Prof. Yasuo Tomita (University of Electro-Communications)

Session 7: Detectors, lasers, and integrated & printed optics

Prof. Tapio Fabritius (University of Oulu)

Session 8: Optical spectroscopy, spectral imaging and lidars

Prof. Erik Vartiainen (Lappeenranta University of Technology)

ICEMET – a sensor for in-cloud icing condition monitoring

Ville A. Kaikkonen¹, Eero O. Molkoselkä² and Anssi J. Mäkynen²

¹ Unit of Measurement Technology, University of Oulu, Kajaani

² Optoelectronics and Measurement Techniques, University of Oulu, Oulu

Corresponding author: ville.kaikkonen@oulu.fi

Keywords: digital holography, clouds, imaging systems, optical instruments

Monitoring of icing conditions in cold regions has gained more interest in recent years, mainly due to the rapid increase in wind power [1]. To model atmospheric icing, one would need to know liquid water content (LWC), droplet concentration and the droplet size distributions (DSD), but now there is no standard way of measuring these parameters for the low-level clouds [2]. In this paper, we present a novel instrument for measuring droplet size distributions (DSD) and liquid water content (LWC) of icing clouds [3]. The measurement principle of the instrument is lensless point source digital holographic imaging. In this paper, we present the ICEMET-sensor and show results from field measurements.

The ICEMET-sensor is based on capturing the digital in-line holograms of cloud droplets and ice crystals. The in-line configuration is the simplest of holographic imaging geometries to implement. It produces diffracted shadow images from the objects located between the coherent light source and the detector screen. A holographic in-line imaging system can be implemented as a lensless imaging system, making the design simple and very robust, the latter an important factor when designing optical instruments for harsh environmental conditions. By using a visible wavelength laser diode as a coherent and divergent point source of light, the geometrically magnified holograms of the droplets can be recorded using a conventional and cost effective digital camera detector. The magnification of this type of hologram recording geometry at different distances from the laser can be simply calculated using the parameters in equation 1. The basic imaging geometry including the protective windows and droplets inside the imaging volume is shown in Fig. 1.

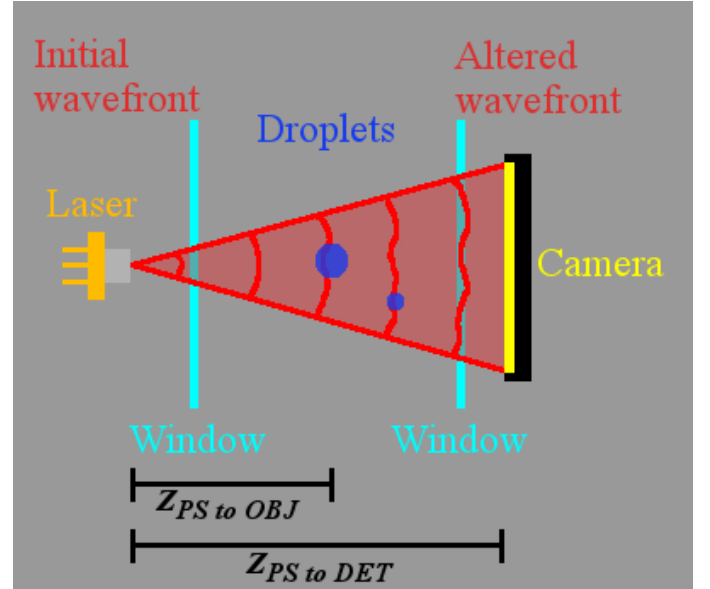


Fig. 1. A lensless in-line holographic imaging geometry.

$$M = \frac{Z_{PS\ to\ DET}}{Z_{PS\ to\ OBJ}} \quad (1)$$

The measurement volume, where the droplets are measured by the sensor, is located in the upper part of the sensor, see Fig. 2. The ICEMET-sensor was designed as a freely rotating construction. By the wing on the backside, it aligns itself against the wind so that the cloud droplets would always pass the sensor in optimally – orthogonally in the direction of the laser light. The sensor is mounted on a support arm from the bottom, the height of the sensor is 53 cm without the support arm. The weight of the sensor is 8 kg. The sensor is kept free from ice with heating elements with the total power of 500 W. Heating of the sensor is controlled by an adjustable digital thermostat controller and additional overheating protection thermostats are installed. Two symmetrical heads with knife-edge rims house the laser and the image sensor. The measurement volume is defined between the two protective windows in the middle of the two housing. The volume imaged in a single hologram is 0.5 cm³. The maximum frame rate of the sensor is 6 fps, resulting in a maximum sampling of approx. 3 cm³/s. The diameters of cloud droplets that can be measured with the sensor are 5 to 200 microns.

The sizes of the droplets are measured by first numerically reconstructing image slices at different positions between the laser and the image detector, then segmenting droplets and finding the best focus of each droplet in the segmented sub-windows. Then the reconstructed shadow images of the droplets are binarized and the diameters and other shape parameters are calculated from the binary images. After processing a statistically valid amount of particles, typically a period of one minute, the LWC is calculated. From the acquired DSD, the median volume diameter (MVD) typically used in icing modelling is calculated. MVD is a non-real droplet diameter, which defines the middle point of the water content of the whole measured DSD. The result from an icing event measurement on a wind turbine nacelle in Kivivaara-Peuravaara Wind Park, located in Suomussalmi, Finland, is shown in Fig. 3. The interval between the measurement points is 3 minutes. The rising of the LWC and MVD can be clearly seen from the plot as the icing cloud passes by the wind turbine.

The ICEMET-sensor is an instrument designed for evaluating present icing conditions in real time. In future, we aim to deploy more sensors in the field to gather enough data to help making weather forecasts, especially icing forecasts, more accurate. In industrial applications, the aim is to use the data provided by the sensor to improve the production of wind turbines in icing conditions. Monitoring present icing conditions near structures prone to icing, such as power line networks, would also benefit from the early warnings of hazardous icing conditions.



Fig. 2. An unmounted ICEMET-sensor

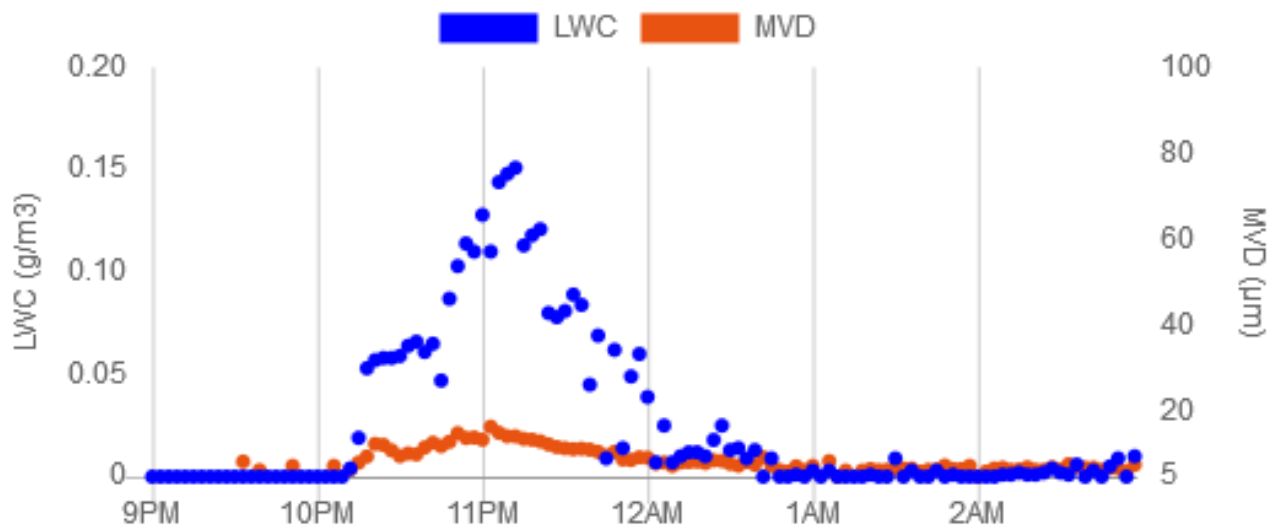


Fig. 3. LWC and MVD measured from Kivivaara-Peuravaara wind park on 20th and 21th of March 2017

References

1. Parent, Olivier, and Adrian Ilinca. "Anti-icing and de-icing techniques for wind turbines: Critical review." *Cold regions science and technology* 65.1 (2011): 88-96.
2. Krenn, A., et al. "Available technologies for wind energy in cold climates." *International Energy Agency Wind Task 19* (2016).
3. Kaikkonen, V., Mäkynen, A., Arstila T., Kananen, T. 2018, *Freezing of structures caused by cloud droplets*, WO2018220268, viewed 29 April 2019, retrieved from Espacenet

Hyperbranched polymer nanocomposite gratings for volume holographic optical elements

Yasuo Tomita,¹ Toshi Aoi,¹ Shuma Hasegawa,¹ Kento Kaseda,² Juro Oshima,² and Keisuke Odoi²

¹ Department of Engineering Science, University of Electro-Communications
1-5-1 Chofugaoka, Chofu, Tokyo 182-8585, Japan

² Materials Research Laboratories, Nissan Chemical Corporation, 722-1, Tsuboi, Funabashi. Chiba 274-8507, Japan

Corresponding author: ytomita@uec.ac.jp

Keywords: nanocomposite materials, photopolymer, volume gratings, holography

Holographic photopolymers have been investigated extensively for their use in photonics and information display such as holographic data storage, holographic optical elements, narrowband optical filters, GRIN lens, sensors, electrically switchable Bragg gratings, and three-dimensional and headup/headmount displays. These applications generally require a large saturated refractive index modulation amplitude (Δn_{sat}) to achieve high diffraction efficiencies (η) near 100%, high recording sensitivity and high dimensional stability (*i.e.*, mitigated polymerization shrinkage and low thermal changes in film thickness and refractive index). Other conditions such as wide acceptable angles (*i.e.*, wide Bragg apertures) are also demanded for some display and diffractive device applications. Since 2002 we have developed a new type of nanocomposite material system, the so-called photopolymerizable nanoparticle-polymer composite (NPC), in which either inorganic or organic nanoparticles having a large refractive-index difference between nanoparticles and the formed polymer are dispersed in photopolymer [1]. In this summary we report on the development of a new photopolymerizable NPC material that consists of ultrahigh refractive index hyperbranched polymer (HBP) acting as organic nanoparticles, together with an electron-donor/acceptor photo-initiator system, dispersed in a monomer blend including an alkyl substituted acrylate. We also investigate the volume holographic recording properties of photopolymerizable HBP-dispersed NPC films at a recording wavelength of 532 nm.

Our newly synthesized HBP containing triazine and aromatic ring units was prepared by the polycondensation of a diamine monomer with 2, 4, 6-trichloro-1, 3, 5-triazine in N, N-dimethylacetamide, followed by the end-capping reaction with aniline [2]. The average size of the HBP was estimated to be approximately 12 nm by a small angle X-ray scattering method. The heterogeneity index was 4.4 that was estimated by the gel permeation chromatography. The glass transition and decomposition temperatures were 200°C and 430°C, respectively. The refractive index (n) of the HBP was found to be 1.82 at a wavelength of 532 nm. The ultrahigh value of 1.82 is attributed to the incorporation of triazine and aromatic ring units to the HBP structure and is much higher than those of our previously reported poly(ethyl methacrylate) HBP ($n=1.51$) and polystyrene HBP ($n=1.61$) [3]. Its molecular structure is shown in Fig. 1. We employed a monomer blend consist-

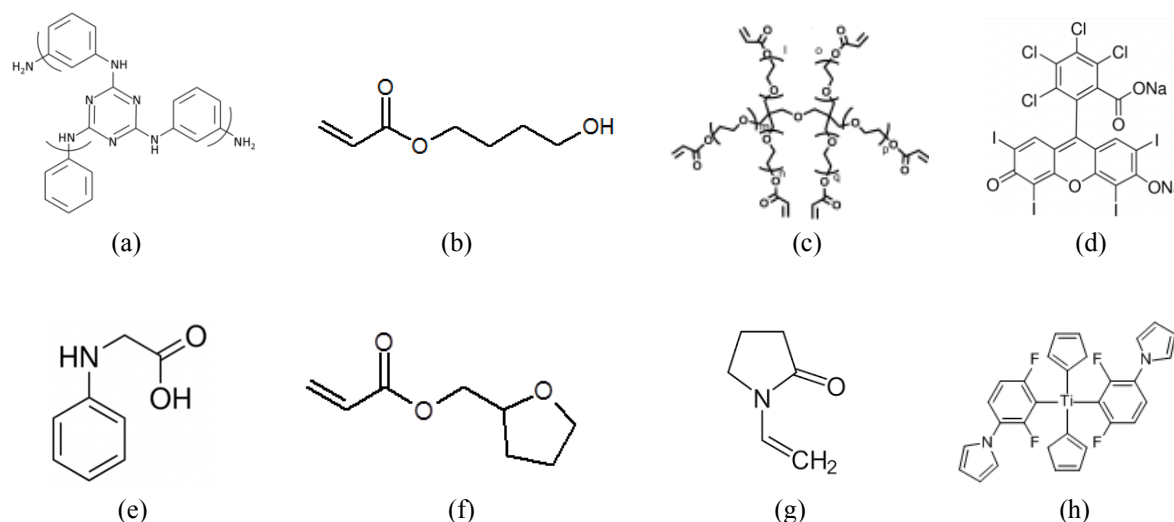


Fig. 1. (a) The synthesized HBP, (b) 4HBA, (c) A-DPH, (d) RB, (e) NPG, (f) THF-A, (g) NVP and (h) Irgacure784.

ing of a single functional alkyl substituted acrylate as host monomer (4HBA) and a multifunctional dipentaerythritol polyacrylate (A-DPH) as crosslinking monomer. We also added an electron-donor/acceptor photoinitiator system consisting of Rose Bengal (RB) and N-phenyl glycine (NPG) at their appropriate ratio to the monomer blend. These chemical structures are also shown in Fig. 1. It is known that a photoexcited RB acting as an electron acceptor forms an encounter complex with NPG acting as an electron donor. Such a complex in the excited state finally dissociates into one ionic radical pair, an anionic RB radical ($\text{RB}^{\bullet-}$) and a cationic NPG radical ($\text{NPG}^{\bullet+}$). The former acts as an inhibition radical, while the latter is continuously decomposed into the phenyl-amino-alkyl radical ($\text{PhNHCH}_2^{\bullet}$) as well as a proton and a carbon dioxide by decarboxylation [4-6]. This phenyl-amino-alkyl radical acts as an initiation radical for chain-growth polymerization under green light illumination. The mixed syrup was cast on a glass substrate loaded with a 5- μm spacer and was covered with another glass substrate to prepare NPC film samples. It is referred to as Sample #1. A similar NPC film sample was also prepared, consisting of the same HBP and a monomer blend consisting of N-vinylpyrrolidone (NVP), a tetrahydrofurfuryl acrylate (THF-A) and A-DPH with titanocen photoinitiator (Irgacure784) [2], as referred to as Sample #2, to compare their holographic recording performance with that of Sample #1.

We employed a two-beam interference setup to write an unslanted and plane-wave transmission volume grating at grating spacing of 1 μm with two mutually coherent s-polarized beams of equal intensities from a diode-pumped frequency-doubled Nd:YVO₄ laser operating at a wavelength of 532 nm. A low-intensity s-polarized He-Ne laser beam operating at a wavelength of 633 nm was employed as a photoinsensitive readout beam to monitor the buildup dynamics of an NPC grating being recorded. We defined η as the ratio of the 1st-order diffracted signal power to the sum of the transmitted 0th- and the 1st-order diffracted beam powers. The effective thickness of an NPC film sample was estimated by curve fitting of a Bragg-angle detuning dependence of the saturated η to Kogelnik's formula, by which the buildup dynamics of Δn was determined. Figure 2 shows a photograph of a recorded NPC grating of Sample #1 at HBP concentration of 23 vol.%. Figure 3 shows the buildup dynamics of Δn for Samples #1 (HBP 23 vol.%) and #2 (HBP 27 vol.%) at 532 nm. It can be seen that Sample #1 possesses the largest value for Δn_{sat} as high as 0.045 and the lowest optimum recording intensity of 5 mW/cm^2 . It is approximately a two-fold increase in Δn_{sat} and a fifteen-fold reduction in recording intensity as compared with those of Sample #2. Our obtained result is promising for an application to wearable glasses and head-mounted display for augmented and mixed reality [7].

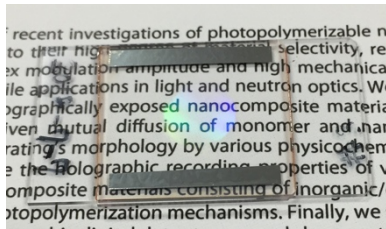


Fig. 2. Photograph of a recorded plane-wave transmission grating.

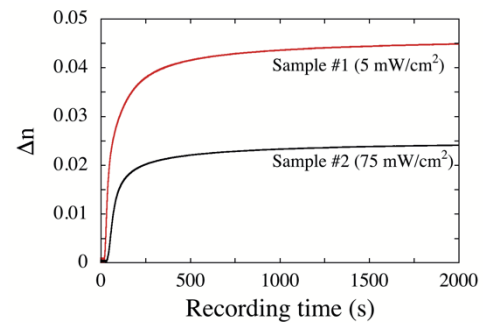


Fig. 3. Buildup dynamics of Δn , where optimum recording intensities are shown in the parenthesis.

References

1. Y. Tomita, E. Hata, K. Momose, S. Takayama, X. Liu, K. Chikama, J. Klepp, C. Pruner, and M. Faly, *J. Mod. Opt.* **63**, S1 (2016).
2. Y. Tomita, H. Urano, T. Fukamizu, Y. Kametani, N. Nishimura, and K. Odoi, *Opt. Lett.* **41**, 1281(2016).
3. Y. Tomita, K. Furushima, K. Ochi, K. Ishizu, A. Tanaka, M. Ozawa, M. Hidaka, and K. Chikama, *Appl. Phys. Lett.* **88**, 071103 (2006).
4. S. Ikeda and S. Murata, *J. Photochem. Photobiol. A: Chem.* **149**, 121 (2002).
5. J.-P. Fouassier, F. Morlet-Savary, J. Lalevée, X. Allonas, and C. Ley, *Materials* **2010**, 5130 (2010).
6. G. Chen, M. Ni, H. Peng, F. Huang, Y. Liao, M. Wang, J. Zhu, V. A. Roy, and X. Xie, *ACS Appl. Mater. Interfaces* **9**, 1810 (2017).
7. M.-L. Piao and N. Kim, *Appl. Opt.* **53**, 2180 (2014).

Enhanced photocatalytic activity of TiO₂ inverse opal structures with gold-silver nanoparticles

Filipp Temerov and Jarkko J. Saarinen

Department of Chemistry, University of Eastern Finland, Joensuu

Corresponding author: filipp.temerov@uef.fi

Keywords: TiO₂, inverse opal structure, metal nanoparticles, photocatalytic activity

Titanium dioxide (TiO₂) is a well-known semiconductor material with photocatalytic activity. Fujishima and Honda [1] demonstrated water splitting into hydrogen and oxygen in a seminal work in 1972 by irradiating TiO₂ electrode with an ultraviolet A (UVA) light that initiated a vast research of photocatalysis. TiO₂ is non-toxic and has a good stability but the anatase crystalline form has a rather large bandgap of 3.2 eV (~387 nm) in the UVA range. Moreover, TiO₂ has a high refractive index and limited light absorption due to reflection with a fast charge carrier recombination [2]. Therefore, a trend in recent research has been to shift the light absorption into the visible range. Enhanced photocatalytic activity in visible range can be used for solar-driven artificial photosynthesis and solar cells with a higher efficiency that may provide solutions for substitution from the current fossil fuel based economy into a more sustainable solar economy.

There are different approaches for solving this problem. For example, TiO₂ doping with noble metal nanoparticles (Au, Ag, Pt) or preparation of TiO₂ based nanostructures (nanotubes, nanorods, nanobelts) have been suggested. Recently, TiO₂ inverse opal (TiO₂ IO) photonic crystal structures have attracted attention due to its excellent properties such as photonic band gap, slow light photons, and localized photons [3]. TiO₂ IO has a three-dimensional ordered porous structure with a large specific surface area and optical properties associated with photonic crystals. Furthermore, TiO₂ IO photocatalytic activity can be enhanced by doping with noble metals such as silver or gold together with long interaction times due to slow light in photonic crystal.

In this study, TiO₂ IO structures were prepared and loaded with different nanoparticles for enhanced photocatalytic activity. TiO₂ IO was prepared using three well-known steps: first, self-assembly of polystyrene (PS) microspheres followed by infiltration of TiO₂ precursor. Finally, by calcination the PS particles were removed that also converted TiO₂ into the anatase crystalline form [4]. Three types of nanoparticles were prepared by hydrothermal method; gold, silver and gold-silver core-shell nanoparticles (AuNPs, AgNPs and Au-AgNPs) [5]. Nanoparticles were deposited into TiO₂ IO on glass substrate by casting on three solutions containing the same amount of above-mentioned nanoparticles. By slow evaporation in the oven and capillary forces, nanoparticles were successfully deposited into TiO₂ IO structure.

Historically photocatalytic activity has been characterized using an indirect method based on a color transformation of an optical dye such as methylene blue (MB) [6]. However, this method should not be used for photocatalytic activity measurements (especially at a visible range), as the incident light itself can bleach the used dye and therefore, induce an erroneous result [7]. Therefore, in this work the photocatalytic activity is measured using an in-house built detector for gas-phase oxidation of organic compounds such as acetylene (C₂H₂). The mineralization of carbon compounds into CO₂ can be directly and simply measured by monitoring the rate of CO₂ increase in the reaction chamber. Additionally, the gas-phase detection removes all mechanical stresses induced by liquid phase methods.

TiO₂ IO has a relatively uniform structure as shown in Fig. 1(A). However, the sample surface had some defects and cracks, which may affect the photocatalytic activity. The observed pore size was around 350 nm. The used PS spheres had a diameter of 400 nm, which indicates a shrinkage of approximately 12 – 13% during the calcination process. The crack formation mainly originates from shrinking and infiltration process. It should be noted that overlayers were not observed from the top view of the structures. The loading of noble metal nanoparticles was performed successfully, and the size distribution of loaded NPs is rather narrow. Figure 1 A inset shows the SEM image of TiO₂ IO structure with Au-AgNPs. It can be clearly seen that the rims of hexagonal structure are covered with small Au-Ag NPs with diameter of 30 – 50 nm. Agglomerated nanoparticles were found inside the honeycomb structure with diameter of 70 – 90 nm. Similar nanoparticles coverage was also observed for TiO₂ IO loaded with Au and Ag NPs.

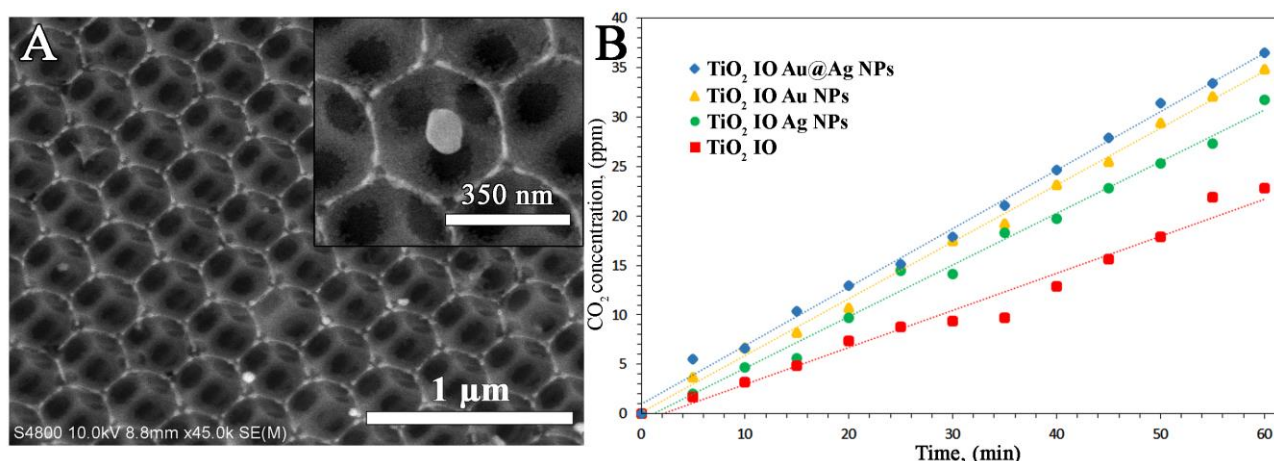


Fig. 1. (A) SEM image of TiO₂ IO structure with Au-Ag nanoparticles, (B) oxidation of C₂H₂ into TiO₂ IO structures with various noble metal nanoparticles loading.

The nanoparticle formation was confirmed by energy-dispersive X-ray spectroscopy (EDS) and ultraviolet-visible (UV-vis) spectroscopy. EDS mapping technique as well as characteristic absorption band confirmed the nanoparticle formation.

The photocatalytic activity was measured using an in-house built photocatalytic reactor. TiO₂ IO with nanoparticles were exposed to the UVA light ($\lambda_{\text{ex}}=365\text{nm}$, 100W lamp intensity) in reactor. Acetylene undergoes a photocatalytic oxidation on TiO₂ IO surface, and CO₂ produces. The photocatalytic activity can be characterized from the observed CO₂ increase. Figure 1(B) displays the measured photocatalytic activity of TiO₂ IO loaded with different metal nanoparticles. The lowest activity (22 ppm) was observed with pure TiO₂ IO without nanoparticle loading while TiO₂ IO with nanoparticles have an increased activity. The highest activity (36 ppm) was observed with TiO₂ IO loaded with Au-AgNPs with an increase of 60% in the activity. This is probably due to a higher capability of Au-AgNPs on TiO₂ IO for generating electrons and holes.

As a summary, in this work an infiltration approach was used for preparation of TiO₂ IO. However, a disadvantage of the method is the difficulty of forming large-area crack free films as during the infiltration step the probability for crack formation is very high. Our future research work will focus on crack-free method for inverse opal formation on large (100 $\mu\text{m} \times 100 \mu\text{m}$) area including heterostructures such as TiO₂/ZrO₂ IO structures. Furthermore, visible light activated photocatalysis will also be studied in the presence of plasmonic metal nanoparticles.

FT wishes to thank the Finnish Cultural Foundation for a research grant. JJS acknowledges the UEF Faculty of Science and Forestry 184 (Grant No. 579/2017) for the financial support.

References

1. A. Fujishima and K. Honda, Electrochemical photolysis of water at a semiconductor electrode, *Nature* **238**, 37–38 (1972).
2. F. Sordello, V. Maurino, and C. Minero, Improved photochemistry of TiO₂ inverse opals and some examples, *Molecular Photochemistry - Various Aspects*, InTech (2012).
3. J. Yu, J. Lei, L. Wang, J. Zhang, and Y. Liu, TiO₂ inverse opal photonic crystals: Synthesis, modification, and applications, *J. Alloy. Compd.* **769**, 740–757 (2018).
4. L. Liu, S. K. Karuturi, L. T. Su, and A. I. Y. Tok, TiO₂ inverse-opal electrode fabricated by atomic layer deposition for dye-sensitized solar cell applications. *Energ. Environ. Sci.* **4**, 209–215 (2011).
5. Q. Han, C. Zhang, W. Gao, Z. Han, T. Liu, C. Li, Z. Wang, E. He, and H. Zheng, Ag-Au alloy nanoparticles: Synthesis and in situ monitoring SERS of plasmonic catalysis, *Sensor. Actuat. B: Chem.* **231**, 609–614 (2016).
6. C. Xu, G.P. Rangaiah, and X.S. Zhao, Photocatalytic degradation of methylene blue by titanium dioxide: Experimental and modeling study, *Ind. Eng. Chem. Res.* **53**, 14641–14649 (2014).
7. X. Yan, T. Ohno, K. Nishijima, R. Abe, and B. Ohtani, Is methylene blue an appropriate substrate for a photocatalytic activity test? A study with visible-light responsive titania, *Chem. Phys. Lett.* **429**, 606–610 (2006).

Polarization state of the object wave analyzed by using FMCW-digital holography

Masayuki Yokota¹, Tatsuya Ishikawa¹ and Yoshinobu Aoki¹

¹ Graduate School of Natural Science and Technology, Shimane University

Corresponding author: yokota@ecs.shimane-u.ac.jp

Keywords: digital holography, FMCW, polarization state

Frequency-Modulated Continuous-Wave (FMCW) technique has been introduced into digital holography (DH) using an injection-current-induced frequency modulation of a commercial laser diode (LD). Since the frequency of beat signals observed in the hologram intensity variation recorded by a high speed camera depends on the optical path length difference between the reference and the object light waves, a polarization state of object wave transmitting through a transparent sample was investigated using two orthogonally linearly polarized reference waves having the different optical path lengths.

Recently, the FMCW technique has been introduced into digital holography (DH)[1,2]. In the method, a series of digital holograms are recorded during the frequency modulation period of a LD and the temporal Fourier analysis is applied to extract the object wave from the series of the recorded holograms. The image of a coin having a diffusely reflecting surface can be obtained based on the FMCW technique [1]. The position resolution of digital holography based on the FMCW technique depends on the frequency modulation bandwidth in the light source. The digital holographic microscope with a swept light source having the modulation bandwidth of more than 70 nm has been successfully demonstrated to image a swine sperm cell [2]. In this paper, to record and analyze the polarization state of the object wave transmitting through a transparent object, a Jones vector of a polarized object wave is determined by using two orthogonal linearly polarized reference waves having different optical path lengths.

Figure 1 shows the optical configuration for the polarization analysis. A LD with a wavelength of 782.4 nm whose optical frequency was modulated with a sawtooth function was used. The frequency modulation bandwidth of $\Delta f = 19.6$ GHz was achieved by changing the injection current of 7.0 mA. A period of the modulation signal was set at 1.0 s. Temperature of the LD was held to be constant at 25.0°C by using a temperature controller. By using a polarization beam splitter (PBS), the frequency-modulated laser beam was split into two orthogonally linearly polarized beams traveling different optical paths: 368 mm for the horizontally and 445 mm for the vertically polarized beams. The difference in their optical path length generates the different beat frequencies in their holograms. Holograms between the object and the two reference beams were recorded for 1.0 s by using a high speed CMOS camera with 1024×1024 pixels at 500 fps. The pixel size of the CMOS camera was $13.68 \times 13.68 \mu\text{m}^2$. A series of holograms were subjected to the further signal processing for the reconstruction. To observe the variation in the polarization state of object beam, the transparent PMMA ring having the outer (inner) diameters of 14.0 (3.0) mm and the thickness of 5.0 mm was set after QWP3 in the object optical path. The distance between the object and the CMOS camera was 215 mm.

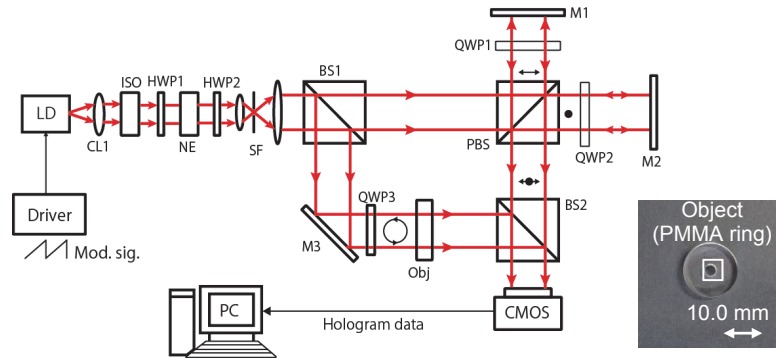


Fig. 1 Optical configuration for the polarization analysis: ISO, optical isolator; NE, laser power controller; H(Q)WP, half (quarter) wave plate; SF, spatial filter; BS, beam splitter; Obj, object (PMMA ring); Pol, polarizer; CMOS, high speed CMOS camera.

Figure 2 shows the reconstructed intensity and the phase images of the object wave recorded with the horizontally polarized reference wave before and after tightening a vice. By tightening the vice and compressed the PMMA ring, the patterns of the phase distributions are different between before and after tightening the vice. This is due to the induced birefringence of PMMA by applying stress to the sample. To see the variation in the polarization states before and after tightening the vice, the polarization state of the object wave was obtained and the polarization states of the typical points are shown in Fig. 3. As seen in Fig. 3, the polarization states of the object wave changes after tightening the vice. By compressing the PMMA ring with the vice, the polarization states were varied due to the stress induced birefringence in the PMMA. The results show the stress-induced variation of polarization states in the object wave by using the proposed FMCW-DH method.

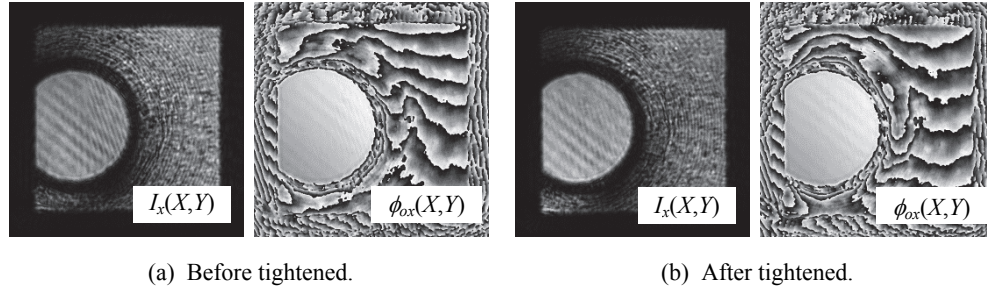


Fig.2 Reconstructed intensity and phase images of the object recorded for the horizontally polarized reference wave: (a) before and (b) after tightened with a vice.

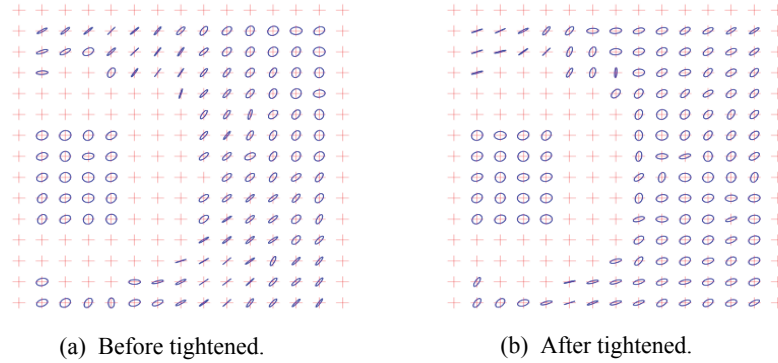


Fig. 3 Polarization states of the object wave before and after tightened by the vice.

Two orthogonally linearly polarized reference waves having the different optical paths have been introduced into the FMCW-DH system. By using the Jones matrix imaging [3-5], the polarization state of the object wave has been obtained. The technique was also applied to investigate the photoelastic effect in the stressed PMMA sample. It has been shown that the proposed technique can be used to investigate the polarization state of the object wave and to analyze the photoelastic analysis

References

1. A. Wada, Y. Miyamaoto, 14th Workshop on Information Optics Th-P9 (2015).
2. S. Chen, J. Ryu and Y. Zhu, Opt. Lett., 41(4), 665-668 (2016).
3. T. Colomb, P. Dhlgre, D. Beghuim, E. Cuche, P. Marquet, and C. Depeursinge, Appl. Opt., 41(1), 27-37 (2002).
4. M. Yokota, Y. Terui and I. Yamaguchi, Opt. Eng., 46(5), 0558011-0558017 (2007).
5. M. Yokota, Appl. Opt., 47(34), 6325-6333 (2008).

Single-pixel imaging with hole-array coding masks

Yoshio Hayasaki, Ryo Sato, and Yujiro Ito

Center for Optical Research and Education, Utsunomiya University

*Corresponding author: hayasaki@cc.utsunomiya-u.ac.jp

Keywords: Single-pixel camera, spatial light modulators, spectroscopy, computational imaging

1. Introduction

The single-pixel imaging architecture [1-2] is composed of optical coding masks, a photodetector, and a decoding calculation. The biggest feature is simple optics and simple electronics because it can perform an imaging without an image sensor. The implementation with a simple photodetector for the light detection gives wide opportunity for developing a new imaging system. Especially, it is very effective when an image sensor with a sufficient performance cannot be available for a given budget or in a frequency region that an image sensor is not existed at present. Recently it was extended to a complex amplitude to get a complex amplitude imaging [3]. The spectral imaging [4, 5] can be performed without a special technique only by replacing from the photodetector to a spectrometer. The coding masks are mostly implemented by a liquid crystal spatial light modulator (LCSLM) and a digital micromirror device (DMD). The spectral property of these devices gives a limit in the spectral imaging. The key idea of this study is that the coding mask is made of hole arrays drilled in a plate. It has no wavelength dependence except for an optical absorption of air. The hole arrays are placed on a disk that is rotated to change the coding mask. It is also possible to operate the rotation with a hand.

The coding masks are made of holes arrays drilled in a plate, which is the key idea in this research. The most important feature of the light modulation using holes is no wavelength dependence except for an optical absorption of air. In addition, it has an easy and low-cost fabrication. The hole arrays are placed on the circumference of a disk that is rotated to change the coding masks.

2. Experimental setup

Figure 1 shows an experimental setup for the single-pixel spectral imaging. The experimental setup was composed of an illumination light source, coding masks on a rotational disk, a spectrometer, a set of relay lenses, a laser, and a computer. A transmissive object was illuminated with white light generated by a halogen lamp (MHAB-150W-100V, Moritex). The light passing through the object was imaged on a coding mask and spatially encoded by the coding mask. The disk was rotated with a motorized rotation stage to evaluate the system performance. The arrangements of the holes were the pseudo-Hadamard matrix that the value of -1 was changed to the value of 0. Therefore, the first pixel had a lot of noises. The disk had another hole at the symmetric position of each mask for indicating the position of the light detection (a position indicator) illuminated by a He-Ne laser. The encoded image was detected by a fiber-based spectroscopy (C7473, Hamamatsu) through the relay lenses. The spectral range was from 200 nm to 950 nm with the resolution of < 2 nm. The spectrum was continuously detected at the minimum sampling period of 19 ms while the disk was rotating, and the intensity for each mask was extracted by referring the position indicator signal. Finally, the inverse matrix calculations were performed at each wavelength.

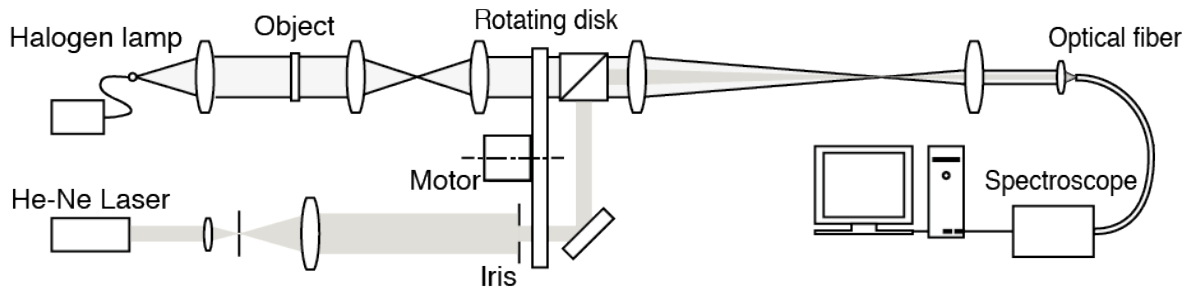


Fig. 1 Experimental setup.

Figure 2 shows an object and the reconstructed spectral images. The object shown in Fig. 4(a) was made of plastic color films with different spectral transparencies, which were put on the frame. The spectral images at 500, 600, and 700 nm are shown in Fig. 4(b). Figure 5 shows the spectrum of the red film from 300 nm to 750 nm. The red curve was obtained by an ordinary spectroscopy. The dots were obtained by the single pixel spectral camera. They were well agreed. The measurement RMS errors were 2.82% on the red film, 5.12% on the blue film, and 2.28% on the blue film.

We developed a new implementation method of a single-pixel camera for spectral imaging. The optical coding masks were composed of holes on a substrate, and arranged on the circumference of a disk enables us to switch with a rotation of the disk. The main features are small wavelength dependence other than air for wideband spectral imaging, and the simple structure. The spectral imaging for a sample composed of three color films was demonstrated, and the measurement accuracy of the present system was less than 3% at red channels. The spectral range from 300 to 750nm depended on the performance of the spectrometer we used. The next subjects of our single-pixel spectral camera will be to improve the detections speed and the spatial resolution.

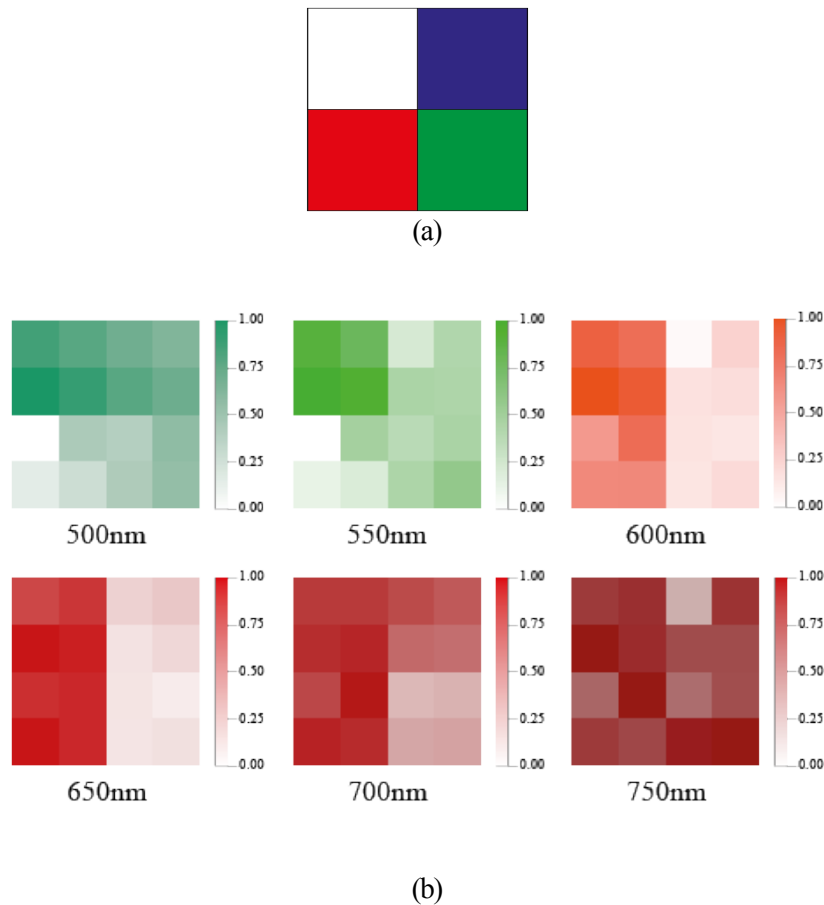


Figure 2 (a) Object made of plastic color films with different spectral transparencies. (b) The spectral images at 500, 600, and 700 nm.

References

1. M. F. Duarte, M. A. Davenport, D. Takhar, J. N. Laska, T. Sun, K. F. Kelly, and R. G. Baraniuk, "Single-pixel imaging via compressive sampling," *IEEE Signal Process. Mag.* **25**, 83–91 (2008).
2. D. L. Donoho, "Compressed sensing," *IEEE Trans. Inf. Theory* **52**, 1289–1306 (2006).
3. K. Ota and Y. Hayasaki, "Complex-amplitude single-pixel imaging," *Opt. Lett.* **43**, 3682–3685 (2018).
4. Y. Garini, I. T. Young, and G. McNamara, "Spectral imaging: principles and applications," *Cytometry Part A* **69A**, 735–747 (2006).
5. Q. Li, X. He, Y. Wang, H. Liu, D. Xu, and F. Guo, "Review of spectral imaging technology in biomedical engineering: achievements and challenges," *J. Biomed. Opt.* **18**, 100901 (2013).
6. W. L. Chan, K. Charan, D. Takhar, K. F. Kelly, R. G. Baraniuk, and D. M. Mittleman, "A single-pixel terahertz imaging system based on compressed sensing," *Appl. Phys. Lett.* **93**, 121105 (2008).

High throughput spectral imaging with snapshot sensing

Nathan Hagen

Utsunomiya University, Utsunomiya, Japan

email contact: nh.hagenlab.org

Keywords: spectral imaging, throughput, snapshot, remote sensing

The classic literature on spectral imaging talks about the “efficiency” of different architectures, such that the Fourier transform and Fabry-Perot spectrometers are mentioned as having the *Jacquinot* (throughput) advantage (or freedom from an exit slit), and the Fourier transform and Hadamard transform spectrometers as having the *Fellgett* (multiplex) advantage. However, it is not widely realized that modern detector technology has obsoleted both of these advantages, at least in their classic form. Using large arrays of detector elements instead of single detector elements has eliminated the Jacquinot advantage, while working with detectors that are limited by shot noise rather than detector noise has eliminated the Fellgett advantage. However, if we consider the geometry of light collection among the different spectral imaging architectures (Fig. 1), we can see that an important advantage remains. We can call this the *snapshot* advantage.[1]

Scanning imaging spectrometers collect a subregion of the datacube at a time, meanwhile using a slit or a filter to reject any light from the object from outside this subregion. By scanning this subregion across the object (or across the spectrum), the entire datacube is assembled by collecting together all of the scans. In contrast, snapshot imaging spectrometers collect the entire 3D datacube in a single integration period without scanning. While the existing literature cites advantages for snapshot instruments such as the lack of scanning artifacts and the increased robustness or compactness due to the lack of moving components, these qualities are actually secondary to *snapshot advantage* in light collection efficiency.

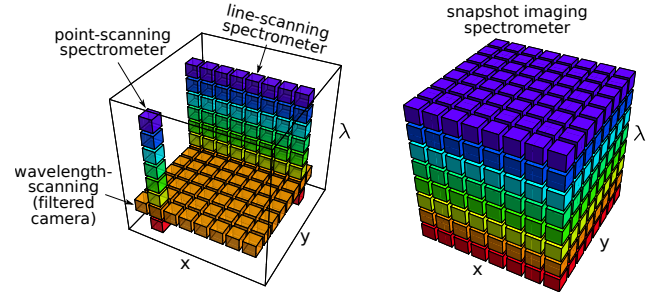


Figure 1: Scanning and snapshot data collection.

The snapshot advantage can be dramatic for larger datacubes. For a datacube of dimensions $(N_x, N_y, N_w) = (500, 500, 500)$, for example, it requires 500 scans in order to complete the dataset. As a result, any individual scan must reject light from 499/500ths of the cube at any given time, so that its light collection efficiency can never exceed 0.2% even under ideal conditions. A datacube $(500, 500, 25)$ in size is best scanned along the wavelength dimension, so that it only rejects 24/25ths of the light, for a maximum efficiency of 4%. For these two examples, the snapshot advantage will be a factor of 500 and 25, respectively.

In order for snapshot spectral imagers methods to work, systems need to be designed with much larger pixel counts than are typically used in scanning systems. In order to collect a datacube of dimensions $(N_x, N_y, N_w) = (500, 500, 500)$, a 125 MPix detector array is needed, assuming that none of the pixels are wasted. Some waste of detector real-estate, however, is inevitable. Thus, while the geometry of the datacube (Fig. 1) illustrates how scanning architectures are inefficient at light collection, another important consideration is how efficiently each architecture uses its pixels.

Figure 2 shows an idealized view of how the various 2D “slices” of the datacube are viewed on the detector array, for different snapshot architectures. What we can see is that, due to the need to provide some minimum spacing between slices, filtered cameras architectures are efficient when $N_x N_y \gg N_w$ (i.e. fluorescence microscopy); image slicers are efficient when $N_y N_w \gg N_x$, and fiber-based and lenslet-based methods are inefficient for every datacube aspect. Figure 3 shows the optical layout for an image slicing architecture, illustrating how the 3D volume of the datacube can be sliced into 2D subvolumes so that they can be simultaneously measured on a 2D detector array.

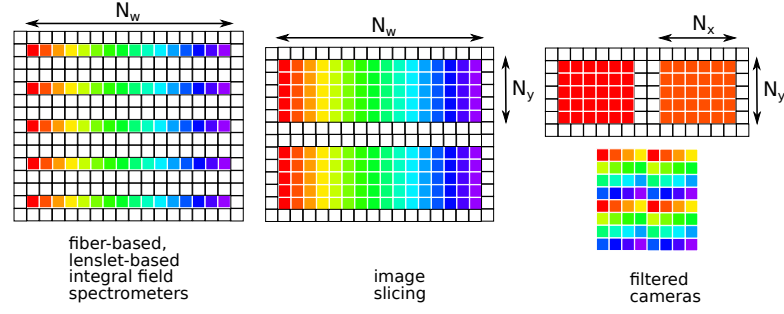


Figure 2: How each snapshot architecture utilizes detector array real estate, assuming $(N_x, N_y, N_w) = (5, 5, 16)$, and 1 pixel spacing. [2]

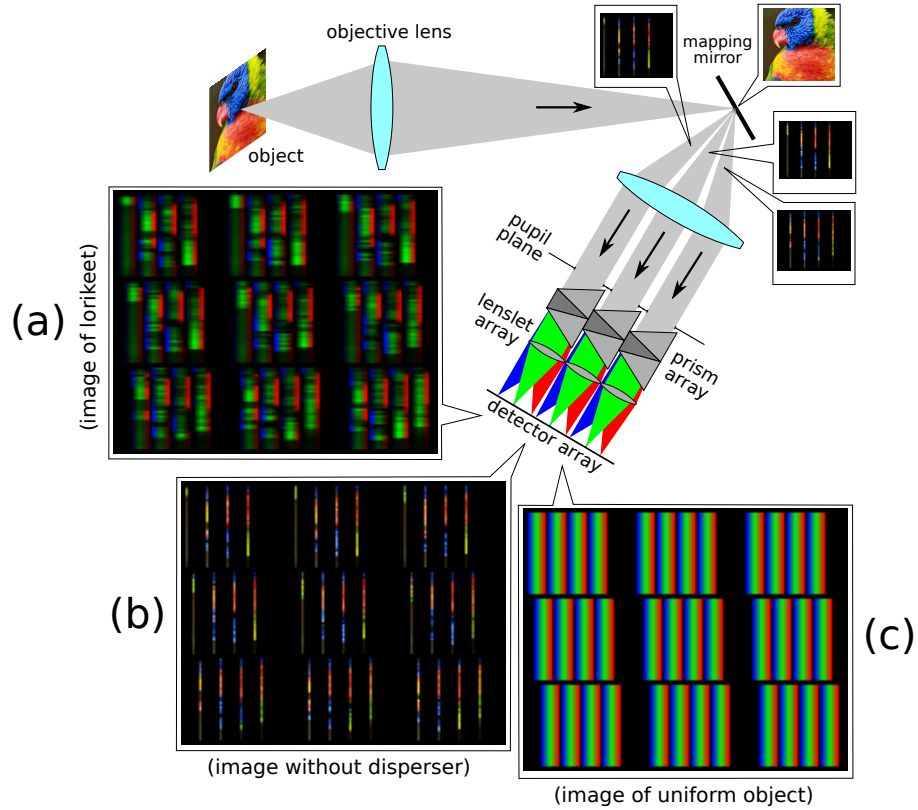


Figure 3: Optical layout for image slicing spectrometry. [2]

While the advantages of snapshot systems are many, they have serious drawbacks as well. They are generally difficult and expensive to build, requiring high-precision custom optics and mechanics, and high pixel-count detector arrays. They also require an extremely high rate of data flow in order to take full advantage of their speed and light collection. Thus it is only recently that detector arrays have achieved the combined speed and size to meet these challenges.

References

- [1] N. Hagen, R. T. Kester, L. Gao, and T. S. Tkaczyk, "Snapshot advantage: a review of the light collection improvement for parallel high-dimensional measurement systems," *Opt. Eng.* **51**, 111702 (2012).
- [2] N. Hagen and M. W. Kudenov, "Review of snapshot spectral imaging technologies," *Opt. Eng.* **52**, 090901 (2013).

A Quantum Dot Reservoir Based on Förster Resonance Energy Transfer for Optical Reservoir Computing

Jun Tanida¹, Suguru Shimomura¹, Takahiro Nishimura², Yuki Miyata³, Naoya Tate³, and Yusuke Ogura¹

¹ Graduate School of Information Science and Technology, Osaka University, Suita

² Graduate School of Engineering, Osaka University, Suita

³ Faculty of Information Science and Electrical Engineering, Kyushu University, Fukuoka

Corresponding author: tanida@ist.osaka-u.ac.jp

Keywords: optical neural systems, fluorescence, energy transfer, neural network

Reservoir computing is a kind of computational architecture categorized in a recurrent neural network[1]. The recurrent neural network has an internal feedback structure, so that applications on temporal information such as speech recognition and dynamic prediction are expected to be processed. Owing to simplicity and flexibility in construction, reservoir computing is a promising architecture for optical neural computing system. To date, several reservoir computing systems were proposed based on an optical fiber[2] and memristor[3]. As a fundamental drawback of these implementations, internal optical/electric signals are guided, so that their hardware is difficult to be reduced. In this research, an optical reservoir computing system using Förster resonance energy transfer (FRET) between quantum dots is investigated. Some preliminary experimental results are presented to show diverse response generated by ensemble of quantum dots.

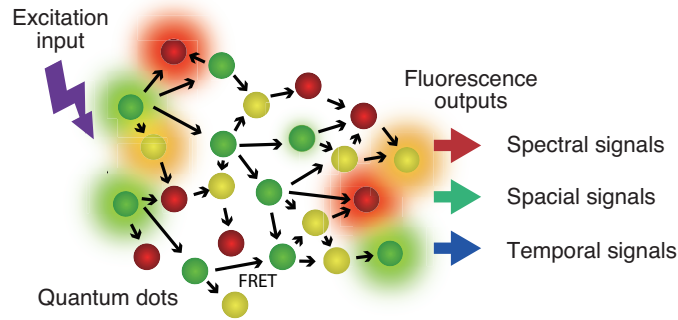


Figure 1: Schematic diagram of a quantum dot reservoir for optical reservoir computing.

Figure 1 shows a schematic diagram of an optical reservoir implemented by a quantum dot network. Several kinds of quantum dots are dispersed in a small space and an exciting light is induced to them. The excited quantum dots either emits a light or transfers the energy to adjacent quantum dots. This energy transfer is FRET and quite sensitive to the distance between the donor and the acceptor. With an adequate density of quantum dots, an energy transfer network can be constructed in the dispersed space. When the excitation light is induced to some part of the quantum dots, energy transfer through the network occurs and fluorescence lights are emitted from the bunch of the quantum dots. The output response reflects the distribution of the individual quantum dots and the position of the excitation light. Sort and composition of the quantum dots has a large amount of freedom and the excitation light can be modulated in the spatial and/or temporal domains. The observation position and the wavelength of the fluorescence light provides diversity of the output signals. Considering the flexibility and diversity of the configuration, the quantum dot network is expected to be an effective reservoir for optical reservoir computing.

The features of the quantum dot reservoir are compactness, low power consumption, and potential easy implementation. Because quantum dots distributed in a small space are the core component, tremendous hardware compaction is expected even if peripheral components are necessary for the operation. Ideally, a quantum dot is excited by a single photon and energy dissipation in each component during their operations is necessarily small. Even the output interface requires larger energy consumption, total consumption of the quantum dot-based device can be theoretically estimated as 100 eV order, which 10^{-2} - 10^{-3} smaller than the typical

electronic device. As a result, very low-power computation is expected. In terms of fabrication, it is enough that arbitrary composition of quantum dots are dispersed without precise arrangement. In the reservoir computing, weighted-sum of the output signals from the reservoir provides the processing result. Only the connecting weights of the output signals are variable and configured by the training for desired response. This process is performed after capturing the output signals by a computer, which is easy to implement.

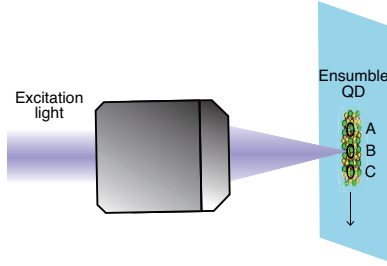


Figure 2: Experimental setup for exciting the quantum dot ensemble. Excitation position was changed by translation of the slide glass.

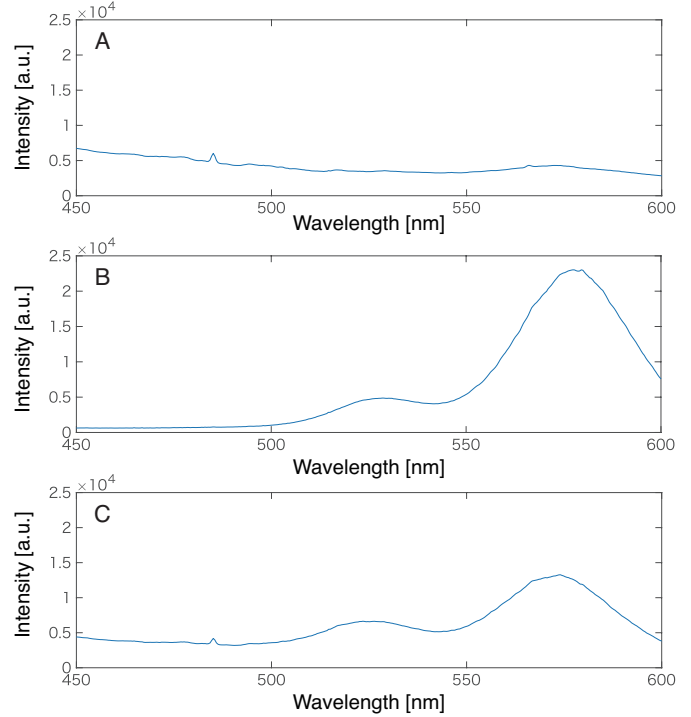


Figure 3: Spectra of the output signals observed at three different positions on the quantum dot ensemble.

To investigate the characteristics of the quantum dot reservoir, the response of quantum-dot aggregates containing three kinds of quantum dots, Q490, Q525, and Q575 was measured. The center peaks of their fluorescence wavelengths are 490nm, 525nm, and 575nm, respectively. To prepare the ensemble of the quantum dots, their solutions were dropped on a slide glass, and then dried at a room temperature. Figure 2 shows the experimental setup for the measurement. An excitation light of 405nm is focused on the prepared sample and the output light signal was measured by a spectroscope (Hamamatsu, C10083CAH). The spot size and the light power density at the focused point were $225\mu\text{m}$ and $34\text{mW}/\text{cm}^2$, respectively. Figure 3 shows the spectra observed at three different positions on the sample with 100ms of the measurement time. As seen from the signals, spatial variation of the quantum dot ensemble was observed. But further verification is required to confirm the evidence of energy transfer between the quantum dot network.

In this study, a quantum dot reservoir for optical reservoir computing was presented and an experimental evaluation of quantum dot samples was performed. The result indicates promising characteristics of the quantum dot reservoir. We will perform detailed evaluation on temporal characteristics and ensemble composition. This work was supported by JST CREST Grant Number JPMJCR18K2, Japan.

References

1. H. Jaeger, *et al.*, “Harnessing nonlinearity: predicting chaotic systems and saving energy in wireless communication,” *Science* **304**, 78–80 (2004).
2. Y. Paquot, *et al.*, “Optoelectronic Reservoir Computing,” *Sci. Rep.* **2**, 287 (2012).
3. C. Du, *et al.* “Reservoir computing using dynamic memristors for temporal information processing.” *Nat. Commun.* **8**, 2204 (2017).

Visualizing AC magnetic fields by using atomic magnetometer and micro-mirror device

Shuji Taue

School of system engineering, Kochi University of Technology, Kochi, Japan

Corresponding author: shuji.taue@kochi-tech.ac.jp

Keywords: Magneto-optic systems, Image detection systems, Zeeman effect

A spatial evaluation of an electromagnetic field is valuable to estimate positions of signal or noise sources. We propose an optical measurement system to detect spatial distributions of the AC magnetic field. The alkali-metal atoms and a micro-mirror device enable us to obtain field intensity distributions with a sub-mm spatial-resolution. Obtained field images from a fine metal-wire clearly indicated the wire position. This imaging technique has the potential for spatial evaluations of the AC field from electrical and electronic devices.

Electromagnetic waves have been already utilized in measurements, information-communications, identification, and electric power transmissions. In the meanwhile, electromagnetic interference (EMI) problems are often caused by integrated circuits in electronic devices. To visualize electromagnetic fields allows us to evaluate spatial distributions as signal or noise components with a pattern recognition manner. The well-known conventional methods to obtain AC field distributions are scanning a coil as a sensing probe or collocating a number of small probes. However, a spatial resolution is limited by the probe size. And the probes and signal wires attenuate and distort the magnetic field.

An atomic magnetometer is an optical detection method utilizing interactions between magnetic fields and electron's spins of vaporized alkali-metal atoms [1]. However well-controlled environmental DC-field is required to operate the magnetometer with high sensitivity, the optical detection of the AC field has advantages of accurate and low-invasive sensing because of sensing probe and signal wire containing less metal. We have already developed the atomic magnetometer with using cesium-133 to detect 70 kHz AC magnetic field [2]. An imaging technique for AC magnetic field distribution was performed by using a micro-mirror device [3]. As a demonstration, intensity distributions of an AC field generated from a thin metal-wire were obtained.

Figure 1 shows the schematic of experimental setups to obtain the AC field distributions. The sensor head is a glass cell with a 10 mm light path length and including cesium and buffer gases. The wavelength of the laser is turned to the cesium D2 line (852 nm), and the light transmits through the cell. The cell is placed at the center of a 300 mm diameter 3D Helmholtz coils which generate a DC field to control the environmental DC field. The signal source of the AC field is a fine metal-wire connected to the function generator (FG) applying a 70 kHz AC current. The wire is attached to the side of the glass cell as shown in Fig. 2. The transmitted light forms the image in the cell onto a digital micro-mirror device (DMD) by using lenses L2 and L3. The mirrors of the DMD are divided into 50×50 image-elements, and the light reflected from each element is detected by a photodetector (PD). The detected light signals are grabbed by a PC and the images are reconstructed.

Figure 3 shows a contour-plot image of the output signal intensity. At the left side in the figure, a white dotted circle indicates the position of the metal wire. Two dashed lines in x -direction indicate inner edges of

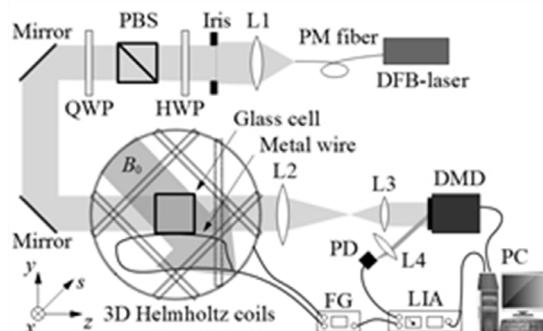


Fig. 1. Experimental setups for AC field imaging

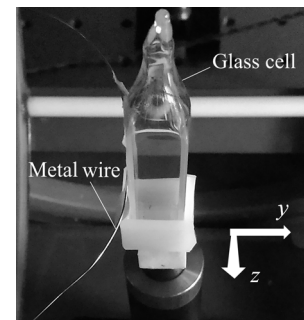


Fig. 2. Photo of the metal wire attached to the glass cell

the 10 mm-width glass cell. From the result, about 30 image-elements resolves the 10 mm cell region in y -direction. The circle-shaped intensity profile observed inside of the cell region represented the light transmitted area where was working as the magnetometer. In addition, the wire position in x -direction was easily recognized from the output intensity distribution. The intensity profile matches well with the theoretical field intensity profile. The signal source position in y -direction was estimated by using experimental and theoretical results. The estimated depth position (1.41 mm) was very close to the real position (1.25 mm).

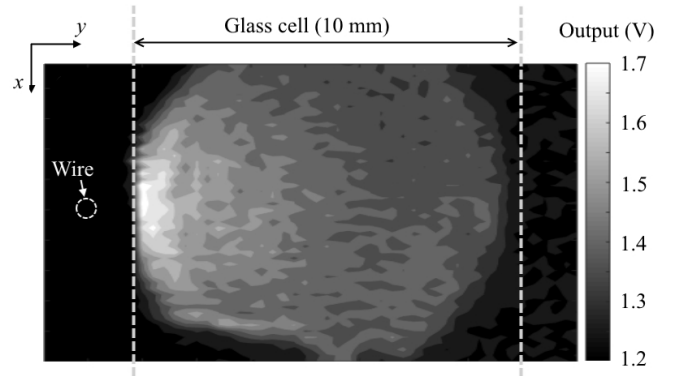


Fig. 3. Contour map of the output signal intensity

We constructed the AC field distribution imaging system. The atomic magnetometer and the DMD realized to visualize the field distribution with a sub-mm resolution. The position estimation of the signal source was performed by using field distributions, and the result is very close to the real position. The obtained field image has good potential for circuit evaluations and signal-source estimations.

References

1. E.B. Alexandrov and A.K. Vershovskiy, “ M_x and M_z magnetometer,” in *Optical Magnetometry*, D. Budker and D.F.J. Kimball, Eds. 60-84, (Cambridge University Press, New York, 2013).
2. S. Taue, M. Shinohara, Y. Toyota et al. *IEICE Trans. Commun.* (Japanese Edition), J100-B(3), pp. 158-165 (2017).
3. S. Taue and Y. Toyota, *Progress In Electromagnetics Research Symposium (PIERS2018)*, 2P15b-1 (2018).

Video-rate imaging for Stokes parameters by polarization cameras

Yukitoshi Otani, Shuhei Shibata, Masayuki Suzuki and Nathan Hagen
 Department of Optical Engineering / Center for Optical Research and Education (CORE)
 Utsunomiya University, Japan
 Corresponding author: otani@cc.utsunomiya-u.ac.jp

Keywords: polarization imaging, Stokes parameters, polarization camera

Polarization technology has become an important area in the field of optical science and engineering, especially in display technology, optical data storage, semiconductor technology, nano-material research, bio-technology and interferometry. We have proposed some new technologies for measuring states of polarizations by a polarization camera whose adjacent 4 pixels are attached on an image sensor and aligned to 0, 45, 90 and 135° of azimuthal direction of linear micro-polarizer arrays [1]. A polarized camera is often used for video-rate measuring partial Stokes parameters but it is not so easy to measure full Stokes parameters. We have already proposed a full-Stokes polarimeter [2] but it required for mechanical mechanism.

We propose a video-rate imager for Stokes parameters by polarization cameras. Figure 1 shows its optical arrangement. An object with Stokes parameters is imaged on to polarization cameras by a camera lens. The incident light is divided into two optical paths by a non polarizing beam splitter (NPBS). Both transmitted and reflected light pass through retarders. The Stokes parameters is analyzed 8 intensities with different azimuthal angles of two polarization cameras as shown in Fig.1. In addition, we compensate error of retardance and out of alignment of pixelated polarizers in advance. The measurement accuracy is affected by birefringence phase difference error of the non polarizing beam splitter so that we also need to calibrate it. Figure 2 shows a picture of video-rate full-Stokes imager.

We demonstrate to measure a circular dichroism (circular diattenuation) of a beetle. Albert Michelson first viewed scarab beetles through circular polarizers in 1911. Figure 3 shows one of the measured results of circular diattenuation image calculated by S_3 parameter. We succeeded to identify the beetle tracking by polarization parameters.

We proposed a video-rate imaging for full-Stokes parameters by polarization cameras. It is succeeded to reconstruct a full Stokes imaging in the video-rate.

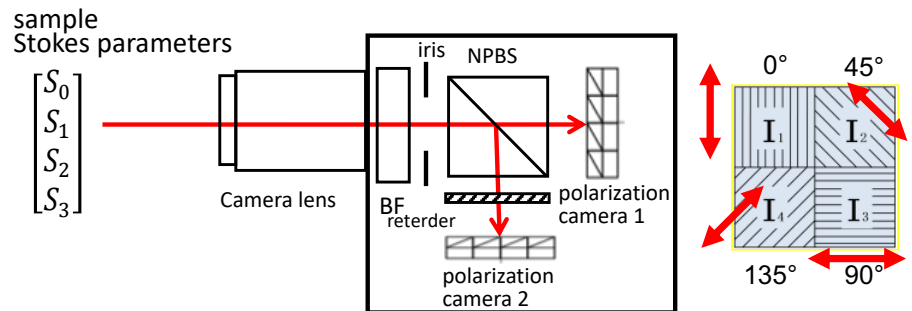


Fig. 1 A schematic diagram of video-rate Stokes imager



Fig.2 Picture of video-rate full-Stokes imager



Fig.3 Circular diattenuation image

References

1. Nathan Hagen, Shuhei Shibata, Yukitoshi Otani: Calibration and performance assessment of microgrid polarization cameras Optical Engineering, **58**,8, 082408 (2019).
2. Shuhei Shibata, Nathan Hagen, Yukitoshi Otani : Robust full Stokes imaging polarimeter with dynamic calibration, Optics Letters, **44**, 4, 891-894 (2019).

Deep Learning Enhanced Multiphoton Microscopy for Investigating the Dermoepidermal Junction in Human Skin

Mikko J. Huttunen¹, Radu Hristu², Adrian Dumitru³, Mariana Costache³ and Stefan C. Stanciu²

¹ Photonics Laboratory, Physics Unit, Tampere University, Tampere, Finland

² Center for Microscopy-Microanalysis and Information Processing, University Politehnica of Bucharest, Bucharest, Romania

³ Department of Pathology, Carol Davila University of Medicine and Pharmacy, Bucharest, Romania

Corresponding author: mikko.huttunen@tuni.fi

Keywords: Label-free, nonlinear microscopy, machine learning, deep learning, tissue characterization

Histopathological image analysis of stained tissue slides is routinely used to diagnose many pathologies, such as cancer [1]. A highly trained pathologist performs the analysis, which is labour-intensive, time consuming and even contains a risk for bias or human error. Therefore, a need exists for faster, more accurate and less invasive approaches. Ideally, the approaches should also be *in-vivo* compatible that could remove the time-consuming bottleneck of performing tissue biopsy.

Multiphoton microscopy (MPM) and emergence of convolutional neural networks (CNNs) have recently attracted interest for medical diagnosis [2,3]. First, MPM allows label-free and minimally invasive imaging of tissues. For example, texture analysis of second-harmonic generation (SHG) images from unstained ovarian tissues has been used to quantify remodeling of tissues surrounding cancer and to classify ovarian cancer types [4]. Furthermore, MPM is compatible with *in-vivo* tissue investigations showing potential to dramatically speed-up the diagnosis [5]. Second, CNNs have led to a revolution in computer vision, where many challenging image-processing tasks are now routinely and automatically performed promising to dramatically reduce the need for human intervention in diagnosis [3]. Despite rapid progress, so far only a few demonstrations exists where deep learning enhanced MPM has been utilized for medical diagnosis [6,7].

Here, we demonstrate how by fine-training pre-trained CNNs we can perform automated classification of MPM images of the dermoepidermal junction (DEJ) in human skin. We wanted to study the potential of the approach for skin cancer screening and early diagnosis, because successful diagnosis facilitates timely intervention ultimately reducing the morbidity rates. As a proof of principle, we investigated fixed but unstained transversal tissue sections, which were prepared and imaged using intrinsic and nonlinear two-photon fluorescence (TPEF) and SHG modalities. In total 358 MPM images were recorded, and a binary CNN-based classifier was trained using a training/validation scheme [3]. Due to the relatively small size of our data set (250 training images), we systematically studied how data augmentation by using image reflections, rotations, contrast enhancement and filtering affects the training results. We found out that the fine-trained CNN (GoogLeNet) can achieve an outstanding 93.5 % classification accuracy alongside with ~94 % and ~92 % specificity and sensitivity, respectively.

We performed combined SHG and TPEF microscopy of unstained samples by using a modified confocal laser-scanning microscope (Leica TCS-SP). Representative MPM images from healthy and dysplastic tissues are shown in Fig. 1. Ti:Sapphire femtosecond laser (Chameleon Ultra II, Coherent) outputting ~140 fs pulses at the incident wavelength of 860 nm was used for excitation through an objective lens (40× 0.75 NA). We recorded backward-generated MPM signals and kept the average powers reaching the samples below 15 mW in order to avoid possible sample damage.

Three spectral channels were simultaneously detected, where the first channel (425–435 nm) corresponded to SHG emission. The second channel collected TPEF signals emitting at 440–490 nm (TPEF1), which corresponded to autofluorescence of reduced nicotinamide adenine dinucleotide phosphate (NAD(P)H). The third channel collected TPEF signals emitting at 510–600 nm (TPEF2) corresponding to autofluorescence mainly due to flavin adenine dinucleotides (FAD). These

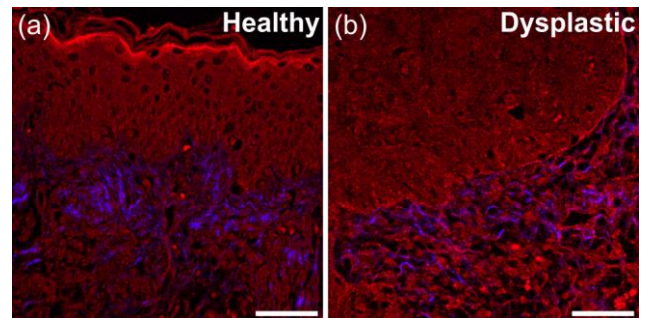


Fig. 1. Representative MPM images from (a) healthy and (b) dysplastic tissues near the DEJ of human skin. TPEF signals (red) originate from the epidermis, while SHG emission (blue) is due to fibrous collagen and elastin fibers present in the dermis. The DEJ is the area joining the dermis and the epidermis of the skin. Scale bars are 50 μm .

TPEF1 and TPEF2 signals were then used to calculate the so-called redox ratio often written as $FAD/(NAD(P)H + FAD)$, which has been associated with changes in the cellular level metabolic activity [8]. In addition, combined TPEF images were formed by averaging the TPEF1 and TPEF2 images. The final MPM images were transformed into composite RGB images, where each color channel corresponded to either of the MPM signals (SHG, TPEF1, TPEF2 or redox ratio).

Processed MPM images were then randomly divided into validation and training sets using a ratio of 30/70, respectively. Supervised learning scheme was used for training where the ground truth was provided by a pathologist inspecting adjacent H&E stained tissue sections. In total, $N = 14$ healthy and $N = 14$ dysplastic tissue sections were imaged. Because the MPM data set size was relatively small, the amount of training data was increased by performing data augmentation [9]. Here we used horizontal and vertical reflections alongside with 4-level Gaussian blur pyramid in order to augment the data set resulting in a 20-fold increase in the training set size (5000 training images). We repeated the training process 25 times due to the random nature of the set selection, and report here the mean sensitivities, specificities and accuracies along with their standard deviations. In order to investigate the role of each collected MPM signal (SHG, TPEF1, TPEF2 and redox ratio) for overall image classification performance, the network training was repeated for three different data set permutations (see Fig. 2).

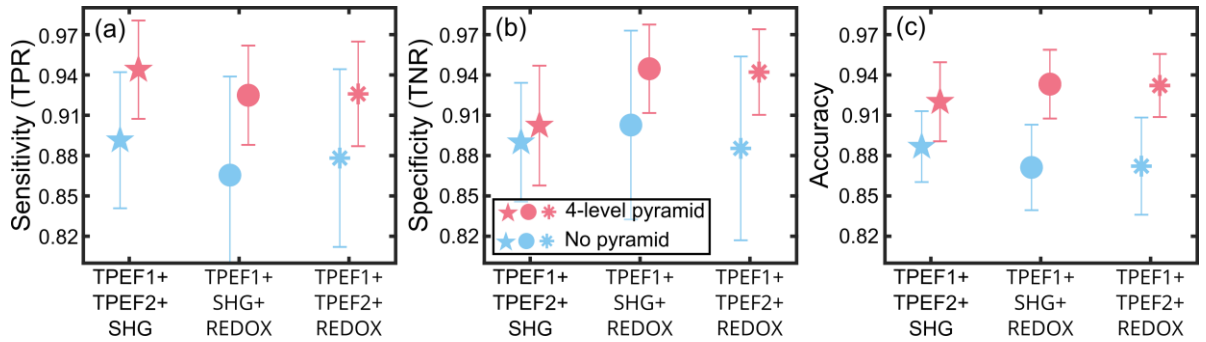


Fig. 2. Calculated classification sensitivity (a), specificity (b) and accuracy (c). (a)-(c) Performance improvement is seen when data augmentation includes also a 4-level Gaussian blur pyramid (red markers), compared to data augmentation not utilizing the pyramid (blue markers). (c) Highest classification accuracy (93.5 %) is achieved by including the redox ratio into the data set.

In the future, it would be interesting to study whether polarization-sensitive or super-resolution MPM could be used to provide data sets resulting in even better performance [10,11]. In addition, we intend to investigate whether coupling traditional computer vision tools, such as invariant feature descriptors, to CNNs could further improve the performance and robustness of the approach for varying acquisition conditions [12].

To conclude, we have performed automated classification of combined second-harmonic generation and two-photon excitation fluorescence multiphoton microscopy images collected from the dermoepidermal junction of human skin. Our approach is based on convolutional neural networks (GoogLeNet) and provides real-time image classification sensitivity, specificity and accuracy all exceeding 92 %. The demonstrated methodology is label-free and compatible for *in-vivo* investigations. Our results show great promise for speeding up and improving the current methodologies used in skin cancer screening and diagnosis.

References

1. M. N. Gurcan *et al.*, *IEEE Rev. Biomed. Eng.*, **2**, 147–171 (2009).
2. W. R. Zipfel, R. M. Williams, and W. W. Webb, *Nat. Biotechnol.*, **21**, 1369–1377 (2003).
3. C. Szegedy *et al.*, in *Proc. of IEEE Conf. on Computer Vision and Pattern Recognition*, 1–9 (2015).
4. B. L. Wen *et al.*, *Sci. Rep.*, **6**, 35734 (2016).
5. R. B. Saager *et al.*, *J. Biomed. Opt.*, **20**, 066005 (2015).
6. S. Weng, X. Xu and S. T. C. Wong, *J. Biomed. Opt.*, **22**, 106017 (2017).
7. M. J. Huttunen *et al.*, *J. Biomed. Opt.*, **23**, 066002 (2018).
8. M. C. Skala *et al.*, *Proc. Natl. Acad. Sci. U.S.A.*, **104**, 19494–19499 (2007).
9. L. Perez and J. Wang, *arXiv preprint:1712.04621* (2017).
10. M. J. Huttunen *et al.*, *J. Opt.*, **19**, 085504 (2017).
11. H. Lee *et al.*, *Biomed. Opt. Express*, **4**, 909–916 (2013).
12. D. Ünay and S. G. Stanciu, *IEEE Access*, **6**, 40154–40164 (2018).

Full arch dental imaging using an extraoral camera system

Katri Kukkola¹, Anssi Mäkynen¹, Ville Kaikkonen¹, Gleb Bulygin¹, Eero Molkoselkä¹, Niklas Pikkarainen¹,
Nanni Nielikäinen¹, Aleksi Rantanen¹, Antti Kämppi^{2,3}, Tarja Tanner², Vuokko Anttonen²

¹*Optoelectronics and Measurement Techniques Unit, Faculty of Information Technology and Electrical Engineering,
University of Oulu, Oulu*

²*Oral Health Sciences Unit, Faculty of Medicine, University of Oulu, Oulu*

³*Department of oral and Maxillofacial Diseases, Faculty of medicine, University of Helsinki, Helsinki*

Corresponding author: katri.kukkola@oulu.fi

Keywords: intraoral, extraoral, dental, imaging, caries screening, oral health

Caries is a common oral disease, which affects quality of life by causing pain and discomfort. [1]. Caries can be arrested if it is detected early and restoring can be conducted using Minimally Invasive techniques (MI) [2]. Usually caries is detected on visual inspection conducted by dentists, but optical imaging is also successfully used for caries screening [3]. Caries is a lifestyle and behavior related disease, so the patient has a key role in caries prevention [4]. Easy caries screening and information of the personal situation could help motivate the maintaining of oral health, in which visualization and images are effective ways to convey information. Thus, we started to examine optical imaging tools for dentition photographing that could be used in easy access oral health services. The target was to find an imaging system which would enable both caries screening and informing and motivating patients to adopt and maintain habits that support oral health.

There are several intraoral cameras commercially available whose performance against visual inspection has been reported by several authors [5,6,7,8]. However, the equipment is mainly targeted for imaging a single tooth as in Fig1 which shows pictures of a tooth with different intraoral cameras (DIAGNOcam, SoproCare and VistaCam iX). There are issues when applied for imaging whole dentition: the usability of handpieces and controls was challenging in some positions, which also affected image quality. The included image softwares were either unstable or the storing and naming of images was slow. The most remarkable hinderance to the use any of these intraoral cameras was the time spent on imaging: taking images of all teeth took between 11 to 15 minutes, which is uncomfortably long for the patient and unacceptable for easy access type of services.



Fig. 1. Images of same tooth with different intraoral cameras a) DIAGNOcam, b) SoproCare and c)VistaCam iX.

In addition to intraoral cameras other cameras and smartphones have been used for dental photographing and teledentistry [9,10,11]. In order to get an image of the full dental arch, typically mirrors are placed into the mouth for the duration of photographing. Our target was to make an imaging solution which is pleasant for the patient, meaning no mirrors. Additionally our target was to make the photographing fast and minimize needed procedures for infection prevention.

The main challenge of extraoral full arch imaging is to optimize camera and flash position so that the image area unobscured and covers the full dental arch, and that the arch is properly illuminated. There is variation on how patients can open their mouths and the individual adjustment of imaging angle. Our solution uses multiple cameras and optics with large depth of focus. Their set up and positioning is based on assessments of camera angles and mouth positions that are feasible for various patient sizes and mouth opening angles. The camera system consists of board level cameras (Basler daA2500-14uc) with 6 mm optics (C 6 mm F1.8/ 1/2"). It is possible to use different kinds of filters on the cameras and flashlights that also enable fluorescent imaging. Anti-reflection coated plastic plates protect the cameras and filters, while also enabling easy cleaning after each photographing. Miniature fans blow away the mist that forms on the plates from the patients breathing. The frames of the plates have mechanical guides that guide patient positioning for photographing and live video that shows to the patient how their teeth are visible for assisting the cameras in final adjustments to the

image. Fig. 2 shows the fully constructed camera system and fig 3. shows dental arch images taken with it. To have fascial tooth surfaces visible a cheek retractor is needed, we have used the Optragate [12], which is soft and flexible and retracts cheeks and lips evenly around the mouth.

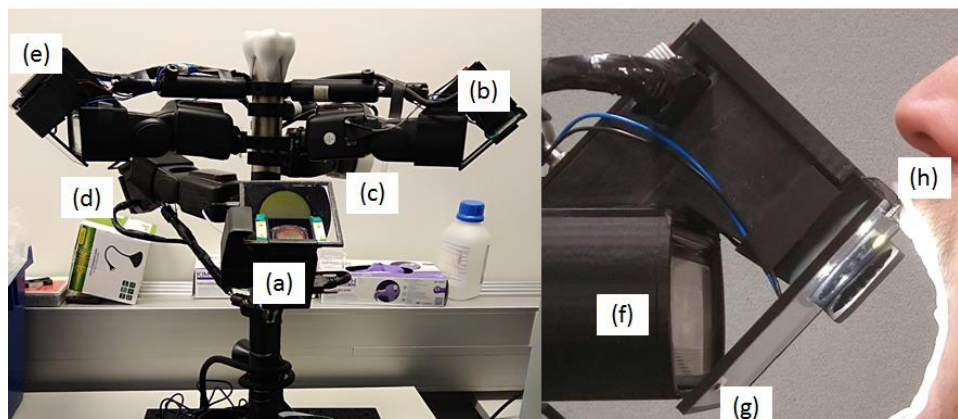


Fig. 2. Our camera system consists of five separate cameras a) upper arch camera, b) lower arch camera, c) frontal teeth camera, d) fluorescent upper arch camera, e) fluorescent lower arch camera, figure on the right shows parts f) flash, g) protective plate and h) mechanical positioning guide and the fan on its right side.



Fig. 3. System produces five images a) upper arch, b) lower arch, c) frontal teeth,, d) fluorescent upper arch, e) fluorescent lower arch.

In the initial evaluation dentists have been able to identify and distinguish different caries levels: dentin caries, active enamel caries and inactive enamel caries. The images enable detection of plaque and dental calculus. Furthermore, dentists have made some other observations such as abrasions and attrition. However further analysis and validation is required.

References

1. P.E. Petersen, and H. Qgawa, *Community Dental Health*, 33, 66–68 (2016).
2. A. Banerjee and S. Doméjean, *Primary dental journal*, 2 (3), 30-37(2013).
3. M. Estai, S. Bunt, Y. Kanagasingam, E. Kruger and M. Tennat, *The Journal of Evidence-Based Dental Practice*, 16 (3), 161-172 (2016).
4. J.T. Newton and K. Asimakopoulou, *British Dental Journal*, 223 (3), 147-150 (2017).
5. G. Shaefer, V. Pitchika, F. Litzenburger, R. Hickel and J. Kühnisch, *Clinical Oral Investigations*, 22 (7) 2431-2438 (2018). (DiagnoCam)
6. M. Melo, A. Pascual, I. Camps, A. del Campo and J. Ata-Ali, *Odontology*, 105, 283–290 (2017) (Vistaproof)
7. U. Boye, A. Willasey, T. Walsh, M. Tickle and IA. Pretty, *Community Dentistry and Oral Epidemiology Journal*, 41, 526-533 (2013). (SoproCare)
8. A. Jablonski-Momeni, F. Liebegall, R. Stoll, M. Heinzl-Gutenbrunner and K. Pieper, *Lasers in Medical Science*, 28 (81), 101-109 (2013). (VistaCam)
9. P. Bottenberg, W. Jacquet, C. Behrens, V. Stachniss and A. Jablonski-Momeni, *BMC Oral Health*, 16 (93), <https://doi.org/10.1186/s12903-016-0291-z> (2016).
10. C. Chossengros, L. Guyot, B. Mantout, F. Cheynet, P. Olivi and JL. Blanc, *Revue de stomatologie et de chirurgie maxillo-faciale*, 111, 79-83 (2010).
11. M. Estai, Y. Kanagasingam, H. Boyen, J. Shiikha, E. Kruger, S. Bunt and M. Tennat, *Telemedicine and e-Health*, 23 (5), 435-440 (2017).
12. More information can be found from <http://www.ivoclarvivadent.com/en/p/all/products/clinical-accessories-instruments/application-aids/optragate>

Live Cell imaging with integrated STED-AFM

Elnaz Fazeli^{1*}, Takahiro Deguchi^{2*}, Sami Koho², Juha Peltonen³, Tuomas Näreojä⁴ and Pekka Hänninen¹

¹ *Biophysics Laboratory, University of Turku, Turku, Finland*

² *Istituto Italiano di Tecnologia, Genoa, Italy*

³ *Laboratory of Cell Biology, University of Turku, Turku, Finland*

⁴ *Karolinska Institute, Stockholm, Sweden*

Corresponding author: elnfaz@utu.fi

** equal contribution*

Keywords: Microscopy, osteoclast, super-resolution, AFM, STED

Multi-modal correlative microscopy allows combining the strengths of several imaging modalities while overcoming the shortcoming of each individual technique. Furthermore, combining different techniques will help gain better insight of the specimen. There are various super resolution techniques available to study nano- and sub-cellular organisms in great details. Atomic Force Microscopy (AFM) can provide, with atomic resolution, nanomechanical properties of cells and material and play as a manipulator in order to get specific cellular response [1]. In addition, stimulated emission depletion (STED) super-resolution microscopy technique has been used widely to study structures close to 10-20 nm size [2]. By using STED one can acquire fluorescent images of labelled organisms in live, or fixed cells.

In this study we used a combination of these two techniques in order to study osteoclasts (OCs) adhesion. OCs are bone resorbing cells, which play an important role in the bone remodeling process. They adhere to the substrate using specific actin structures called podosomes and sealing zone, if they are cultured on glass and bone, respectively [3]. If the OCs' activity is disturbed, for example by using inhibitors of actin binding or recycling, or if OCs are taken from diseased individuals with hyperactive osteoclasts, the behavior of cells and actin structures will change dramatically. We use the OCs from healthy donors and donors with neurofibromatosis type 1 (NF1) disease. NF1 is a progressive autosomal dominant disease caused by a genetic mutation in the tumor suppressor Nf1 gene [4]. NF1 hallmark includes neurofibroma tumors, learning deficiencies, skeletal abnormalities and disturbed bone growth starting from childhood [5]. It was presented that NF1 preosteoclasts hyperactively migrate and adhere, leading to osteoclasts, which are bigger and have a higher resorption capacity.

In this study we plan to fulfill two aims. Firstly, we use AFM as a cell manipulator to measure the adhesion forces of healthy and NF1 OCs. We show that the hyperactivity of NF1 OCs is due to stronger attachment to the bone, and therefore, due to differences in actin structures. We also compare attachment strength of OCs to the bone and glass substrates. We do STED imaging of actin structures while manipulating the cells using AFM microscopy to look into the formation of podosomes. Secondly, we use STED imaging to compare the different actin structures; we characterize podosome and sealing zone size and distances to provide further proof to the role of actin organization in overall cellular activity. We are currently analyzing the distance and the structure of podosomes in comparison to sealing zone. Our result would possibly lead to the conclusion that sealing zone is the mature form of podosomes and is formed by joining podosomes in order to provide better attachment to the bone and more efficient resorption.

References

1. Raman, A, S Trigueros, A Cartagena, A P Z Stevenson, M Susilo, E Nauman, and S Antoranz Contera. 2011. "Mapping Nanomechanical Properties of Live Cells Using Multi-Harmonic Atomic Force Microscopy." *Nat. Nanotechnol.* 6 (12): 809–14. M. Mainio, J. Juonio, and T. T. Tutkija, *Optics Journal* **12**, 123-129 (1998).
2. Wildanger, Dominik, Brian R Patton, Heiko Schill, Luca Marseglia, J P Hadden, Sebastian Knauer, Andreas Schönle, et al. 2012. "Solid Immersion Facilitates Fluorescence Microscopy with Nanometer Resolution and Sub-Ångström Emitter Localization." *Adv. Mater.* 24 (44): OP309–OP313.
3. Teitelbaum, S. L. (2011). The osteoclast and its unique cytoskeleton. *Annals of the New York Academy of Sciences*, 1240, 14–17. <https://doi.org/10.1111/j.1749-6632.2011.06283.x>

4. Wallace, M R, D A Marchuk, L B Andersen, R Letcher, H M Odeh, A M Saulino, J W Fountain, A Brereton, J Nicholson, and A L Mitchell. 1990. "Type 1 neurofibromatosis gene: identification of a large transcript disrupted in three NF1 patients." *Science (New York, N.Y.)* 249 (4965): 181–86.
5. Brunetti-Pierri, Nicola, Stephen B Doty, John Hicks, Kelly Phan, Roberto Mendoza-Londono, Maria Blazo, Alyssa Tran, et al. 2008. "Generalized metabolic bone disease in Neurofibromatosis type I." *Molecular Genetics and Metabolism* 94 (1): 105–11. <https://doi.org/10.1016/j.ymgme.2007.12.004>.

Monte Carlo based investigation of spectral reflectance and point spread function in skin tissue model

Kaustav Das, Yuta Kobori, Tomonori Yuasa, Hideki Funamizu, and Yoshihisa Aizu

Muroran Institute of Technology, Muroran, Hokkaido 050-8585, Japan

Corresponding author: aizu@mmm.muroran-it.ac.jp

Keywords: skin tissue, spectral reflectance, point spread function, Monte Carlo simulation

Spectral reflectance is used for estimating absorption and scattering of light in skin tissue, for example, by using multi-variate analysis, and data mining from spectral reflectance database. However, the similar spectral reflectance curves can be obtained from some different combinations of absorption and scattering conditions. In such a case, the estimation of absorption and scattering coefficients suffers from uncertainty. To treat this problem, we expect use of point spread function (PSF) observed in the skin surface under the point-like illumination. In this paper, we investigated properties of both spectral reflectance and PSF on the basis of Monte Carlo simulation (MCS) [1] in the nine-layered skin tissue model [2]. Results potentially indicate that the absorption coefficient in dermal and subcutaneous layers and the scattering coefficient in the upper dermal layer predominantly affect patterns of spectra and PSFs.

A typical structure of human skin tissue can usually be classified into three layers such as epidermis, dermis, and subcutaneous layer in Fig.1(c). In the more detailed and definite way, skin tissue is classified into nine layers as it can be demonstrated in Fig. 1(b). These layers with particular thickness are; layer 1 (L_1): stratum corneum (0.015mm), layer 2 (L_2): stratum granulosum and stratum spinosum (0.060mm), layer 3 (L_3): stratum basale (0.015mm), layer 4 (L_4): papillary dermis (0.045mm), layer 5 (L_5): subpapillary dermis (0.175mm), layer 6 (L_6): upper blood net dermis (0.080mm), layer 7 (L_7): reticular dermis (0.600mm), layer 8 (L_8): deep blood net dermis (0.100mm) and layer 9 (L_9): subcutaneous tissue (6.000mm). In MCS with the help of quite accurate and organized coding, the phenomenon of light propagation in human skin tissue has been mimicked as genuinely as possible.

To carry out MCS, five parameters were required for each layer: scattering coefficient μ_s , absorption coefficient μ_a , anisotropy scattering parameter g , refractive index n and thickness t . The five parameters for each of nine layers result in totally 45 values to be specified for MCS execution. This is quite complicated and impractical for investigation of the spectral reflectance and PSF with respect to changes in values of the five parameters. We propose a moderate approach in which the two main parameters μ_a and μ_s are varied by magnification while values of g , n , and t are fixed. Values of μ_a and μ_s are specified by magnification M_a and M_s with respect to the initially-set values, respectively, as given in Table 1. Here we change the magnification value M_a for the two groups of layers 1-3 and 4-9, and M_s for the three groups of layers 1-3, 4-6, and 7-9.

Figure 2 shows spectra and PSFs in 580 nm and 700 nm with different magnification values of M_a which indicates different conditions of μ_a in dermal and subcutaneous layers ($L_4 - L_9$), keeping all other parameters fixed to be the initial values [2]. With the change in M_a value from the small to large, the spectral reflectance clearly decreases, especially in a wavelength range of 500-600nm. In PSFs, there was no change in the pattern with different values of M_a while difference of broadening is found between the two wavelengths. Figure 3 demonstrates spectra and PSFs in 580 nm and 700 nm with different magnification values of M_s which refers to different condition of μ_s in the upper dermal layer ($L_4 - L_6$), keeping all other parameters fixed to be the initial values [2]. With an increase of M_s -value, the spectral reflectance becomes higher, especially in a wavelength

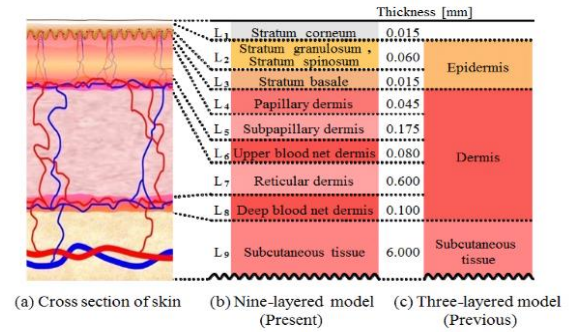


Fig. 1 Skin tissue model of nine-layered and three-layered types.

Table 1 Different magnification of M_a and M_s .

Layers	M_a	M_s
1 ~ 3	$\mu_a L_{1-3}$ 0.6~1.6	$\mu_s L_{1-3}$ 0.6~1.4
4 ~ 6	$\mu_a L_{4-9}$ 0.2~3.6	$\mu_s L_{4-6}$ 0.3~9.3
7 ~ 9		$\mu_s L_{7-9}$ 0.1~1.0

range of 500-600nm. In PSFs, low values of M_s produce spread out of intensity decaying curves and the higher M_s values result in the narrow spread of curves.

Comparison of Fig. 2(a) and Fig. 3(a) indicates that it is difficult to discriminate in the cause of spectral variation between a change of absorption and a change of scattering. In such a case, observation of PSFs gives useful information. When the scattering condition changes, we expect to observe changes in both spectral reflectance curve and PSF, while a change in the absorbing condition may be reflected on spectral reflectance curve only.

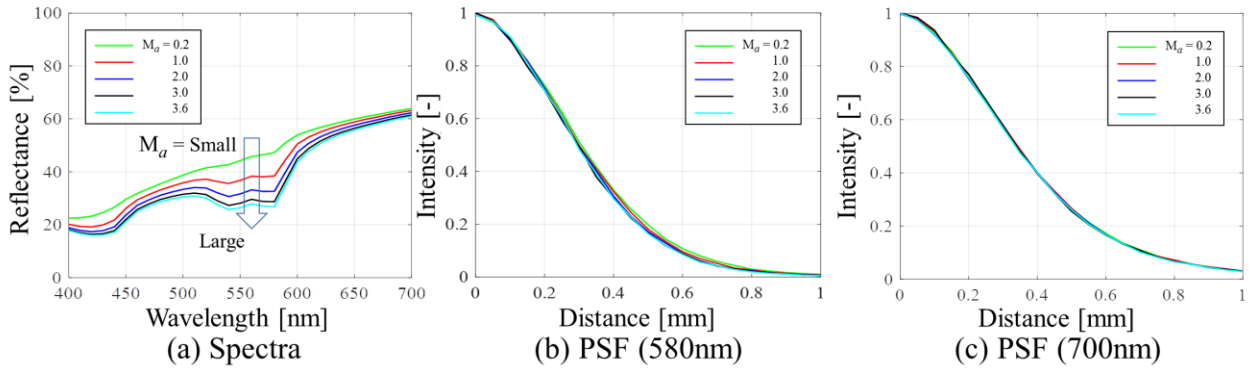


Fig. 2 Typical spectra and PSFs with increasing $M_a L_{4-9}$.

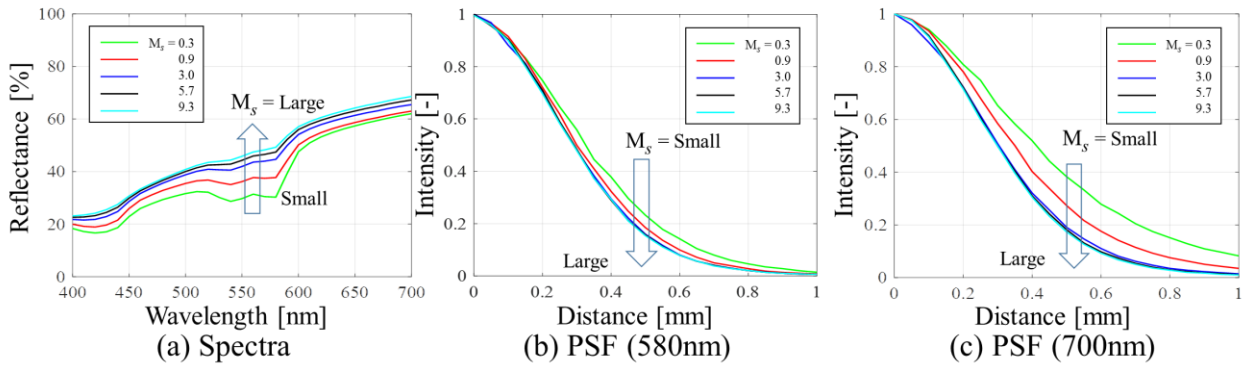


Fig. 3 Typical spectra and PSFs with increasing $M_s L_{4-6}$.

We have investigated spectral reflectance and PSFs for various values of μ_a and μ_s . Change in the absorbing coefficient in the dermal and subcutaneous layers had contribution to change in the pattern of spectral reflectance curves but had no contribution to the pattern of PSFs. Change in the scattering coefficient in the upper dermal layer had contribution to change in the patterns of both spectral reflectance curves and PSFs. In this way, use of both spectral reflectance and PSF is reasonable for estimation of absorbing and scattering conditions in skin tissue. We are developing a Monte Carlo based library of set of spectral reflectance curves and PSF curves for various values of μ_a and μ_s , and further investigate their properties to enrich these library data.

References

1. L. Wang, S.L. Jacques, and L. Zheng, *Comput. Methods Programs Biomed.* **47**, 131-146 (1995).
2. T. Maeda, N. Arakawa, M. Takahashi, and Y. Aizu, *Optical Review* **17**, 223-229 (2010).

On optical sensing of microplastics in water

Benjamin O. Asamoah, James Amoani, Matthieu Roussey, and Kai-E. Peiponen

Department of Physics and Mathematics, University of Eastern Finland, P. O. Box 111, FI-80101 Joensuu, Finland

Corresponding author: benjamin.asamoah@uef.fi

Keywords: microplastics, surface roughness, specular reflection, laser speckle pattern, speckle contrast.

Despite the huge demand for plastics in today's world, they largely contribute to water pollution [1]. Large plastics in water bodies can easily be collected. However, for micro- and nanoplastics, their identification in water bodies become challenging as a result of the varying shape, size, surface and volume properties, transparency and the surrounding ambient conditions. Advanced methods of plastic detection such as Raman spectroscopy, Fourier transform infra-red (FTIR) spectroscopy and the combination of spectroscopy and chemical imaging exist [2]. However, such methods are expensive, not portable, and usually, require sediments from water bodies instead of direct implementation in water bodies. We present a prototype of an optical sensor for the detection of microplastics in water. The sensor detects the specular reflection and the speckle pattern, from which we can estimate the speckle contrast, to discriminate microplastics based on the smoothness, transparency, translucency, surface roughness, and their curvature.

The optical sensor, which is connected to a laptop, is a combination of a portable handheld glossmeter (MGM device, Finland), for measuring the specular reflection, and a charge-coupled device (CCD) camera (DCC1465C-HQ, Thorlabs), for capturing the speckle pattern [3]. The schematics of the sensor is shown in Fig. 1. The handheld sensor consists of a stable red (635 nm) semiconductor laser light focused to 50 μm at 6° angle of incidence. It uniquely obtains the specular component of light reflection by filtering the diffusely reflected light using a diffractive optical element (DOE) [4]. Moreover, to the sensor head, a black cup with a glass (disk) base can be attached to create 800 μl volume compartment for holding liquid. The CCD camera was positioned 11 cm from the glass disk. The commercial plastics studied are transparent polyethylene terephthalate (PET) and translucent low-density polyethylene (LDPE). The plastics were cut into 5×5 mm² to represent the upper bound of microplastic (MP) definition [5]. Additionally, to simulate the case of MPs in water having different roughness on the two surfaces, some PET samples were roughened, before cutting, on both sides with sandpaper having grits of 80, 180, 320, 600 and 1200.

The respective measured average surface roughness was 4.12 μm , 2.52 μm , 1.15 μm , 0.63 μm , and 0.33 μm using Mitutoyo stylus profilometer (SJ-210, Japan). For the roughened MPs, they are accordingly referred to as G80D, G320D, and G600D, as an example, indicating which rough surface of the MP is toward the incident light source. Next, pristine LDPE, PET and PET bottle (B MP), with regular curvature, were also cut to the same size.

The volume compartment was filled with 700 μl of fresh water (FW) and the samples were added. The MPs were studied with a glass disk having one of its surfaces roughened. In this case, with the coherent light source, a speckle pattern, which is grainy structure of bright and dark spots, is formed in the far-field region as a result of the random phase originating from the rough glass surface. The specular reflection and the speckle patterns were simultaneously recorded with the sensor. From the speckle pattern, we calculate the normalized standard deviation to obtain the speckle contrast (C), which has a minimum and maximum value of 0 and 1, respectively, using Eq. (1) [3],

$$C = \frac{[\langle I^2 \rangle - \langle I \rangle^2]^{1/2}}{\langle I \rangle}, \quad (1)$$

where I is the light intensity and $\langle \dots \rangle$ is the ensemble average. Fig. 2 (a) and (b) show the mean specular reflection and the speckle pattern for the pristine MPs with that of water subtracted, respectively. From the specular reflection, which depends on the refractive index (RI) mismatch between the MPs and water (at the

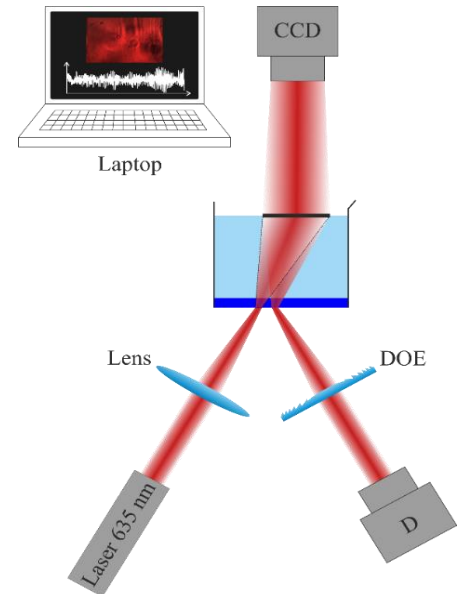


Fig. 1. Schematics of the experimental setup.

probe wavelength), we observe that the PET (RI = 1.5570) gives a higher average reflection signal than FW. On the contrary, LDPE (RI = 1.4920) with volume inhomogeneity, we obtain a lower average reflection signal as it scatters more of the light. Moreover, the B MP with inner curvature (concave) towards the incident (B MP CONC) light shows a higher signal than when the outer curvature (convex) is toward the incident light (B MP CONV). Thus, the B MP CONC tends to act as a converging mirror focusing the reflected light whilst the B MP CONV, on the other hand, diverges the incident light beam. We also observe clear variation from the speckle patterns of the pristine MPs when the speckle pattern from water (and glass) is subtracted. The PET, in comparison, shows an almost dark pattern as expected for a transparent material whereas the LDPE shows a much brighter pattern. Interestingly, for the B MP (CONC and CONV), which is the same MP, we observe clearly how the curvature contributes to the significant modification of the speckle pattern.

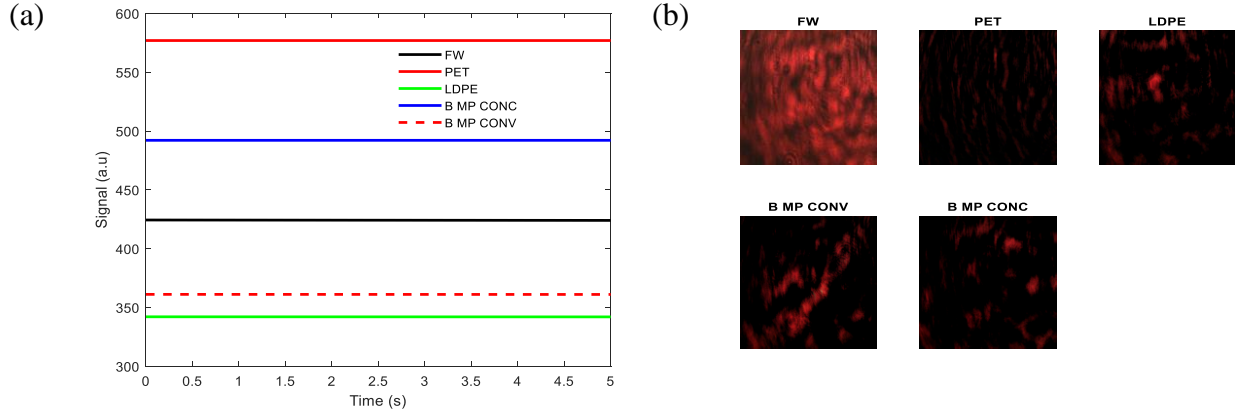


Fig. 2. Average specular reflection (a) and speckle patterns (b) water (FW) and pristine MPs of PET, LDPE and PET bottle (B MPs) with that of water subtracted. (Conv)ex and (Conc)ave.

Tab 1. Speckle contrast of water and pristine MPs.

Sample	Speckle contrast (C)
FW	0.34
PET	0.33
LDPE	0.37
B MP CONV	0.42
B MP CONC	0.49

The speckle contrast, shown in Fig. 3, presents a powerful tool in discriminating between the different pristine MPs and their curvatures as well as the average surface of the MPs. In Tab. 1, the translucent LDPE MPs show a higher speckle contrast than the transparent PET PET MPs as the volume inhomogeneities act as scattering

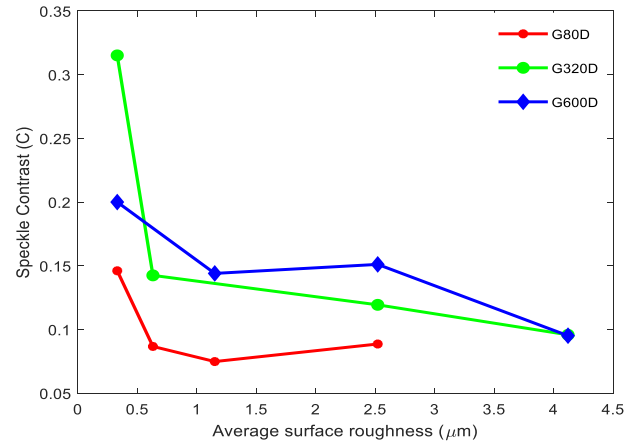


Fig. 3. Speckle contrast of PET MPs with both sides roughened.

sources for the incident light. Thus, the pristine MPs further modify the original speckle pattern of the rough glass. As an example, we show, in Fig. 3, how the upper surface roughness, with reference to the incident light source, influences light and MP interaction for each specific lower surface roughness. We observe that the speckle contrast decreases with increasing upper surface roughness. Moreover, decreasing the average surface roughness of the lower surface correspondingly increases the speckle contrast especially for roughness larger than the probe wavelength of the incident light source.

This study is a step toward the practical implementation of an optical sensor for in-situ detection of MPs in an aquatic environment.

References

1. J. R. Jambeck, *et al.*, *Science*, **347**, 768-771 (2015).
2. M. G. J. Löder and G. Gerdt, *Marine Anthropogenic Litter*, (Springer, Cham, 2015).
3. R. K. Erf, *Speckle Metrology*, (Academic Press Inc, New York, 1978).
4. R. Silvennoinen, K.-E. Peiponen, and K. Myller, *Specular Gloss*, (Elsevier Science, Amsterdam, 2008).
5. More information can be found in: <http://mcc.jrc.ec.europa.eu/documents/201702074014.pdf>, valid 2/2019

Development of self-adjusting photodiode arrangement for accurate laser optical power measurements

A. Pokatilov¹, G. Porrovecchio² and T. Kübarsepp¹

¹AS Metrosert

Central Office for Metrology, Tallinn, Estonia

²CMI

Czech Metrology Institute, Prague, Czech Republic

Corresponding author: tkubarsepp@metrosert.ee

Keywords: optics, semiconductor physics, photodetectors

One of the tasks in the EURAMET/EMPIR project 17FUN06 SIQUEST 'Single-photon sources as new quantum standards' [1] is to develop the measurement devices for the traceable characterisation of single-photon sources. To reduce noise in such a low optical flux detection, a photodetector with improved performance, e.g. zero back-reflection and decreased noise, has been designed.

The zero-back reflection is achieved by aligning six photodiodes in such a way that nonabsorbed light reflected from one photodiode is directed to the next photodiode. In the device six commercial photodiodes having small active area (2.4 mm x 2.4 mm type S1227 33BR from Hamamatsu) are aligned in a polarization-independent configuration (Fig. 1). The careful design provides collinear input and output beams of so-called transmission type detector. The noise is reduced by cooling (down to 12 °C) the photodetector compartment in conjunction with high accuracy readout electronics. The aimed operation range is in the wavelength range from 650 nm to 750 nm.

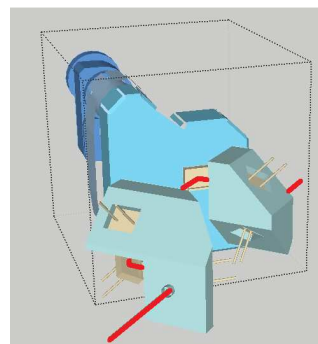


Fig 1. Schematic view of the six photodiodes assembled in the 6-photodiode detector. The red line follows the beam between the photodiodes.

The collinear input and output beams to better than $\pm 0.5^\circ$ are provided by the use of a piezoactuator connected to the feedback sensor at the photodetector optical output. The device with improved performance will be described and presented.

This work has received funding from the European Union Horizon 2020 and the EMPIR Participating States in the context of the projects EMPIR-14IND05 'MIQC2' and EMPIR-17FUN06 "SIQUEST".

References

1. SIQUEST 'Single-photon sources as new quantum standards', <https://www.siqust.eu/>

Polarimeter analysis of the birefringence of thermally modified Scots pine wood

Ilpo Niskanen^{1*}, Hiroshi Hasegawa², Jukka Rätty³, Hariyadi Soetedjo⁴, Kenichi Hibino⁵, Hiroshi Oohashi⁶, Rauno Heikkilä¹, Kiyofumi Matsuda⁷, and Yukitoshi Otani²

¹ Faculty of Technology, Structures and Construction Technology, University of Oulu, Finland

² Department of Optical Engineering / Center for Optical Research and Education, Utsunomiya University, Japan

³ Unit of Measurement Technology (MITY), University of Oulu, Kajaani, Finland

⁴ Center for Integrated Research and Innovation (CIRNOV), University of Ahmad Dahlan, Yogyakarta, Indonesia

⁵ National Institute of Advanced Industrial Science and Technology/National Metrology Institute of Japan, Tsukuba, Japan

⁶ National Institute of Advanced Industrial Science and Technology (AIST), Tsukuba, Japan

⁷ Optical Information Processing and Systems Engineering Division, Hamamatsu, Japan.

*Corresponding author: email ilpo.niskanen@oulu.fi

Keywords: light polarization, wood heat treatment, birefringence, imaging Stokes polarimeter, Mueller matrix

Wood is environmentally friendly material which can use for many purposes. However, some of its properties such as the dimensional stability change along with ambient condition. The characteristics of wood can be modified by different ways. Thermal treatment (at temperatures 185-215 °C) is one of the methods that has been used to improve wood's durability, resistance against mold and decay fungi, dimensional stability, weather resistance, and visual appearance [1-2]. The method is commonly used by wood industry and, for example, applied for c. 194,000 m³ of sawn timber in Finland in 2017 (Thermowood® production statistics 2017) [3]. There is a practical need for easy-to-use, inexpensive and rapid analysis method that could be applied for defining the treatment degree from wood specimens after the thermal modification. This would help monitoring the quality of thermally modified wood in the markets.

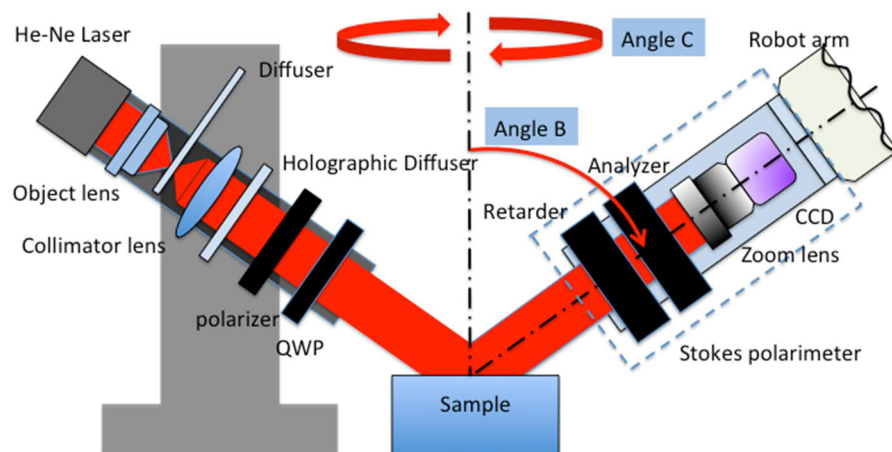


Fig.1 Experimental setup of the Stokes Polarimeter.

Here we assume that the thermal modification alters chemical composition of the wood cells and thus change and decrease the birefringence of molecular structure. This paper describes a light polarization method to determine the loss of birefringence of the thermally modified wood material. The polarized light reflected from the surface of thermally modified Scots pine wood was measured by using an imaging Stokes polarimeter and data analysis utilized the Mueller matrix method. The polarization state of light was characterized by four measurable parameters called the Stokes polarization parameters (S0-S3). [4]. Our detection system consists

of a dual rotating speed of retarder and analyzer at a rotating ratio of 1:3 in Fig.1 [5]. The CCD camera was Prosilicga GS1380 which resolution 1360 x 1024 pixels. The wavelength of the light source (He-Ne laser) was 632.8 nm.

The degree of polarization as a function of temperature for untreated and thermally modified Scots pine samples are presented in Fig. 2. Light and dark stripes in Fig. 2 represent annual growth rings. The density of the earlywood (thinner, lighter stripes) is higher than the density of the latewood (wider, darker stripes). Furthermore, from the figures we can observe that the degree of polarization (DOP) increases (lighten) when the treatment temperature rises. This means that the wood fiber loses birefringence property. The loss of birefringence could be due to crystal to amorphous deformation.

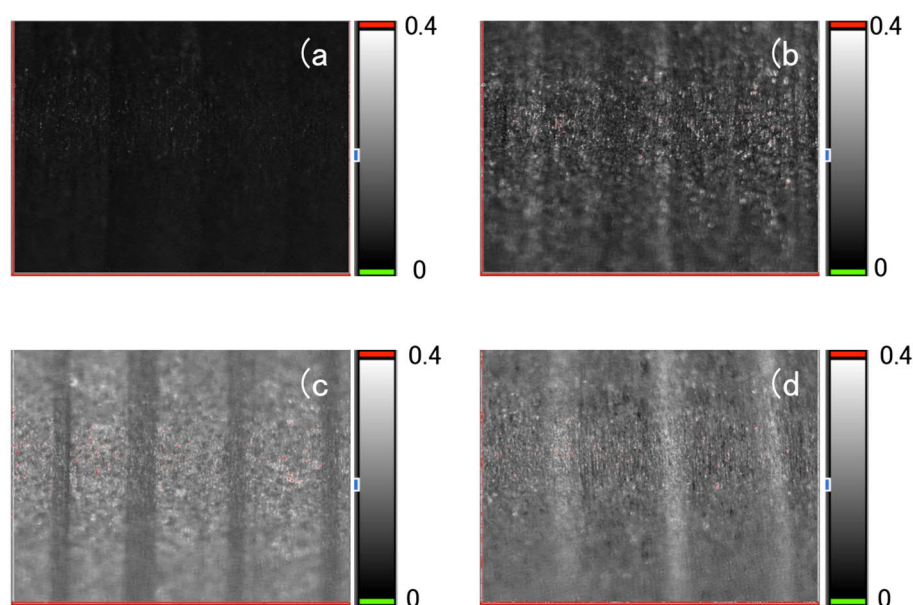


Fig. 2. Stokes image (DOP) of Scots pine wood a) untreated, b) treatment at 160 °C c) treatment at 200 °C, and d) treatment at 220 °C).

The present method could provide useful information that, in principle, can be applied in the optimization of the thermal modification process and inspection of the quality of thermally modified wood products. Major advantages of imaging Stokes polarimeter are that the method is sensitive and nondestructive for measuring the optical properties exhibited by thermal modified wood or untreated wood. We believe that the imaging Stokes parameter method and the polarimeter are useful in the basic studies of optical properties of thermally modified wood. Using the polarization information it is possible to assess changes in the crystalline forms of cellulose of thermally modified wood as a function of temperature and the treatment time.

References

1. M. Romagnoli V. Vinciguerra and A. Silvestri, *J. Wood Chem. Technol.* **38**, 57–70 (2018).
2. B. E. B. Uribe and A. Ayala, *J. Indian Academy of Wood Sci* **12**, 54-62 (2015).
3. Thermowood® production statistics International Thermowood® Association. 2017 <https://asiakas.kotisivu-kone.com/files/en.thermowood.palvelee.fi/uutiset/Productionstatistics2017.pdf>, Accessed 15 February 2019
4. M. Ginya, Y. Mizutani, T. Iwata and Y. Otani, *Sens Actuators A*, **200**, 37–43 (2013).
5. M. Tanaka, M. Chujo and Y. Otani, *Kogaku* **40**, 430-438 (2011).

How to control polarization color and its applications

Kenji Harada, Sho Sakurai, and Yutaro Shibata

Department of Computer Science, Kitami Institute of Technology,

165 Koen-cho, Kitami, Hokkaido 090-8507, Japan

Corresponding author: haraken@cs.kitami-it.ac.jp

Keywords: Birefringence, polarization, polarization color

A birefringent cellophane tape or a polymer sheet exhibits polarization color (interference color) by polarizer. We propose a novel technique for viewing images using polarization [1, 2]. The polarization color is controlled by changing the total retardation of the birefringent materials. Various colors can be displayed without color filters, which can be applied to color imaging device. There are various ways to control the polarization color. In this presentation, we show how to control the polarization color, and its applications for arts and entertainments.

Figure 1(a) shows the conventional optical arrangement. The angle between the transmission axis of a polarizer and the retarder axis of a retarder film is 45° or 135° because the maximum transmittance is obtained at these angles. Figure 1(b) shows the proposed optical arrangement. The angle between the transmission axis of a polarizer and the retarder axis of a retarder film can be varied, and up to four retarder films are stacked. Using this proposed setup, we can display a high chroma image.

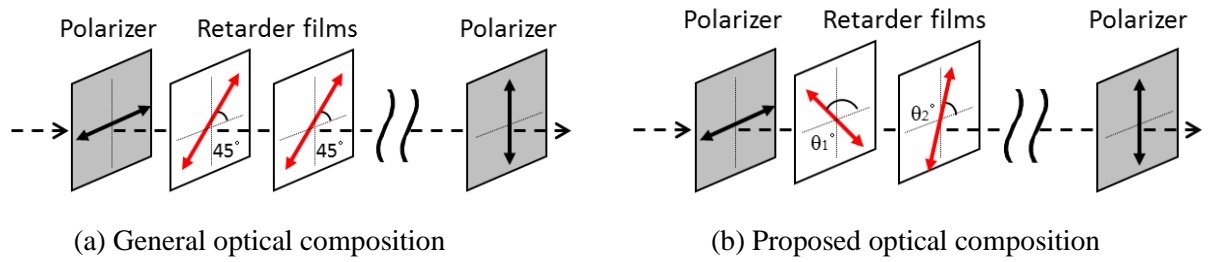


Fig. 1. Optical composition for viewing polarization color image.

Figure 2 shows a color chart of sixty colors using polarization color. The color chart is fabricated by sandwiching up to four retarder films between two polarizing films. We used two types of retarder film with retardations of 140 and 565 nm. Conventional $\lambda/4$ retarder films are used for the 140 nm retarder films, and conventional λ retarder films are used for the 565 nm retarder films. In this way, we can display various high chroma colors. Figure 3 shows a prototype of active polarization color filter. This device consists of four retardation films (two $\lambda/4$ retarder films and two λ retarder films), four stepping motors and a microcomputer to control them.

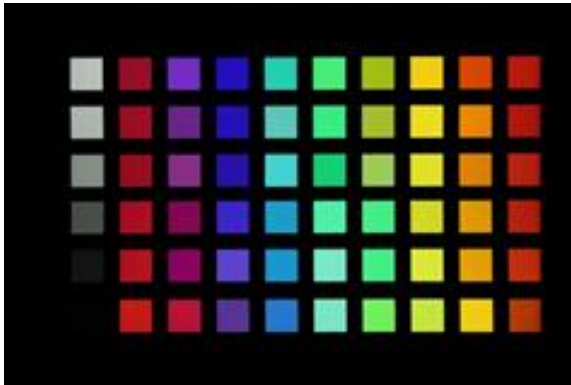


Fig. 2. Color chart using polarization color.

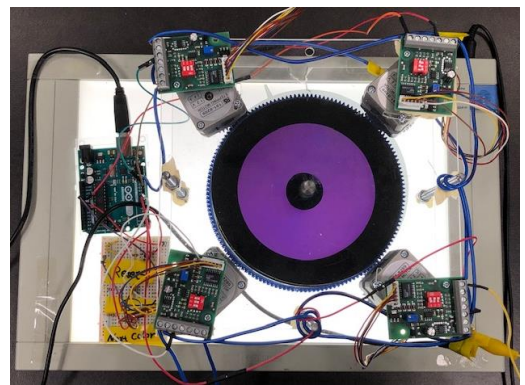


Fig. 3. Prototype of active polarization color filter.

In recent research, we found that we can control not only the color but also the brightness using optical composition shown in Fig.1 (b). Figure 4 shows a calculation result of brightness control of polarization color (red, green and blue). We calculated about arrangement of all combinations of retardation films, and sorted in order of brightness by color. The brightness was calculated using the $L^*a^*b^*$ color system.






















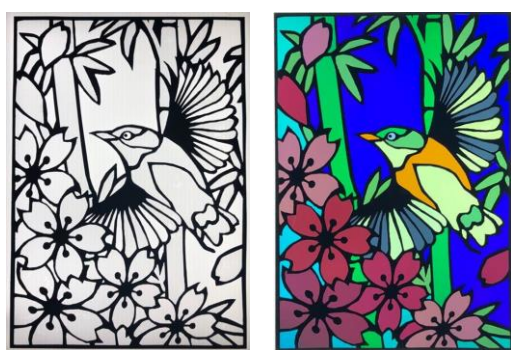
(a)Red							
L^*	18.5	23.3	25.6	27.0	28.8	33.1	37.2
(b)Green							
L^*	25.6	40.9	47.1	53.1	58.1	70.6	75.2
(c)Blue							
L^*	4.5	8.0	15.8	19.7	22.1	23.0	27.8

Fig.4. Brightness control (simulated value).

In this way, we can control the polarization color and brightness. This technique can be also applied for art and entertainment. Figure 5 shows a high chroma polarization art. This is the original design art created with the hint of the Japanese floral playing cards “Hanafuda”. Figure 6 shows another type of polarization art. This device is composed of retarder films, Aluminum rolls and polarizers. Aluminum rolls make interesting geometric patterns. Figure 7 shows a transparent jigsaw puzzle for entertainment. This technique is very simple and can be applied to color filter, educational tools, security, art and entertainment.



(a) Without polarizer (b) With polarizer

Fig.5 Polarization color art 1.



Fig.6 Polarization color art 2.

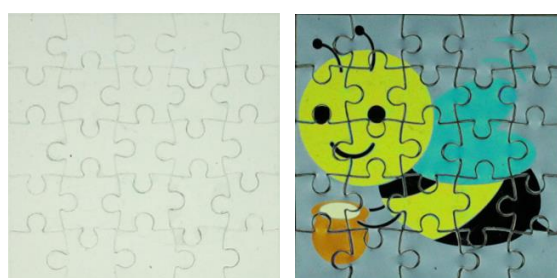


Fig.7 Transparent puzzle using polarization color.

References

1. S. Sugawara, K. Harada, and D. Sakai, “High-Chroma Visual Cryptography Using Interference Color of High-Order Retarder Films”, *Optical Review*, **22** (2015) 544-552.
2. K. Harada, T. Matsuzaki, H. Qin, “Stereoscopic Imaging System Using Interference Color of Retarder Films”, *Optik* **156** (2018) 914–920.

Predicting the refractive index of porous powder samples during compaction using terahertz time-domain spectroscopy

Prince Bawuah¹, Mohammed Al-Sharabi¹, Cathy Ridgway², Anssi-Pekka Karttunen³, Ossi Korhonen³, Patrick Gane⁴, Jarkko Ketolainen³, Kai-Erik Peiponen⁵, J. Axel Zeitler¹, Daniel Markl^{6,7}

¹Department of Chemical Engineering and Biotechnology, University of Cambridge, Cambridge, UK

²Omya International AG, Oftringen, Switzerland

³School of Pharmacy, Promis Centre, University of Eastern Finland, Kuopio, Finland

⁴Chemical Engineering, Bioproducts and Biosystems, Aalto University, Helsinki, Finland

⁵Institute of Photonics, University of Eastern Finland, Joensuu, Finland

⁶University of Strathclyde, Strathclyde Institute of Pharmacy and Biomedical Sciences, Glasgow, UK

⁷EPSRC Future Manufacturing Research Hub for Continuous Manufacturing and Advanced Crystallisation (CMAC),

University of Strathclyde, Glasgow, UK

Corresponding author: pb612@cam.ac.uk

Keywords: terahertz, refractive index, spectroscopy, compaction

Abstract: In this study, a terahertz (THz) based method for accurate prediction of the refractive index during the compaction of porous compacts is introduced. By using training sets of porous particle functionalised calcium carbonate (FCC) based and microcrystalline cellulose (MCC) based compacts, the refractive index of the powder in the compaction die (henceforth referred to as in-die refractive index) was accurately predicted and compared to the measured out-of-die refractive index. Since the refractive index is a fundamental physical property of a material, the ability to track how it evolves during powder compaction will increase our understanding of the overall compaction process and inform the development of compaction models.

Background: Recent studies have shown that terahertz time domain spectroscopy (THz-TDS) coupled with Bruggeman's effective medium theory is a powerful tool for measuring the refractive index of porous materials [1–2]. The ability to accurately measure the refractive index, which is a basic optical property of a material, serves as the basis for model development that can be used for non-destructive and non-invasive process monitoring and material characterisation.

This study uses a THz-TDS method [2] that facilitates the estimation of the in-die refractive index similar to the experimental setup proposed in [3]. This was possible by, firstly, measuring the intrinsic refractive index, n_{solid} , of calibration compacts using the anisotropic Bruggeman effective medium approximation (AB-EMA) followed by the estimation of the in-die effective refractive index.

Materials and Method: Eight batches of porous compacts were compressed from porous particle functionalised calcium carbonate (FCC) and microcrystalline cellulose (MCC) based formulations as shown in Table 1. The compacted samples were flat-faced with a diameter and thickness of 10 mm and 1.6 mm, respectively. The four formulations were compacted to two different porosities. By following the well-established THz porosity measurement approach [2], the intrinsic refractive index of the solid matrix was estimated for both materials. The intrinsic refractive index, n_{solid} , coupled with the known in-die porosity, $f_{\text{in-die}}$, were used to extract the in-die effective refractive index based on the AB-EMA. The in-die porosity, $f_{\text{in-die}}$, was calculated from the known mass, measured volume change and known true density of the solid material.

Table 1: Material composition of the formulation used in the direct compression of all the batches of compacts. The target compact porosities, f , and the intrinsic refractive index, n_{solid} , are given for each formulation.

Formulation	Material	f	n_{solid}
FP	Functionalised calcium carbonate (88 %), croscarmellose sodium (2 %) and paracetamol (10 %)	45%, 60%	2.697
FT	Functionalised calcium carbonate (88 %), croscarmellose sodium (2 %) and theophylline (10 %)	45%, 60%	2.714
MP	Microcrystalline cellulose (88 %), croscarmellose sodium (2 %) and paracetamol (10 %)	10%, 25%	1.869
MT	Microcrystalline cellulose (88 %), croscarmellose sodium (2 %) and theophylline (10 %)	10%, 25%	1.864

Results: The extracted in-die effective refractive index, $n_{\text{eff.in-die}}$, plotted against the compression pressure and the in-die porosity, $f_{\text{in-die}}$, respectively, for both the FCC based and MCC based compacts is shown in Fig. 1. For the sake of comparison, the $n_{\text{eff.in-die}}$ at maximum pressure ($n_{\text{eff.in.max}}$) and the measured out-of-die effective refractive index ($n_{\text{eff.out}}$) are also shown. It is interesting to observe that the out-of-die refractive indices showed an average decrease in magnitude of 0.004 compared to the in-die refractive indices at maximum pressure. The decrease in magnitude of the out-of-die refractive indices can be attributed to after-compaction elastic relaxation of the compacts. Another intriguing observation is the Heckel-like nature of the refractive index curves shown in (a), which buttresses the concept of optical Heckel analyses that was introduced in our previous study [3].

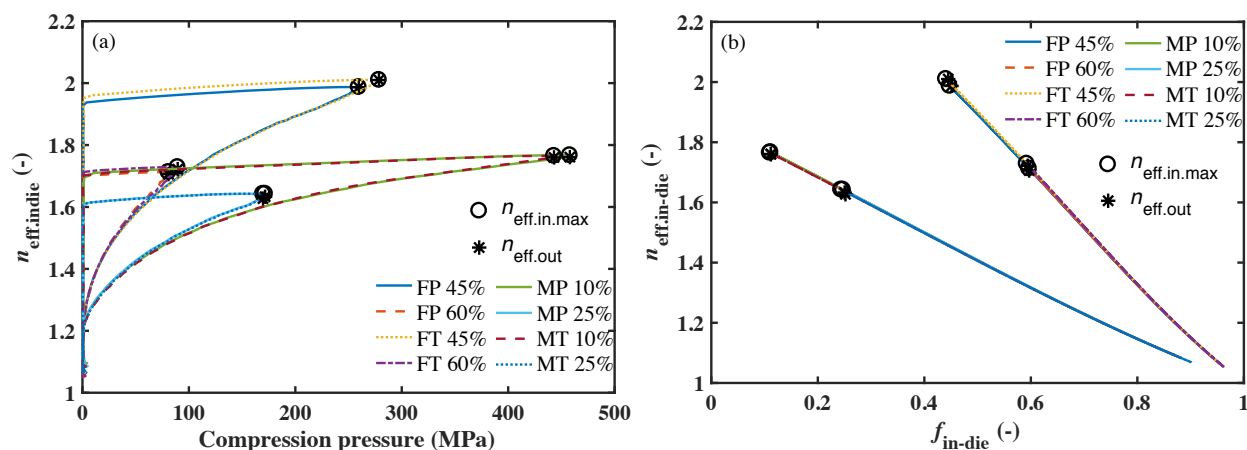


Fig. 1. The evolution of the effective refractive index of porous compacts during compression. FP and MP indicate FCC based and MCC based compacts containing paracetamol as the active ingredient whereas FT and MT represent similar compacts with theophylline as the active ingredient.

Conclusions: This study highlights that it is possible to track how the refractive index evolves during powder compression. By using a prepared training set of powder compacts, the in-die refractive index was extracted and compared to the measured out-of-die refractive index. The relatively low out-of-die refractive index values compared to the in-die counterpart has manifested the effect of elastic relaxation on the optical properties of compacts. The ability to detect the in-die refractive index during powder compaction will increase our understanding of the overall compaction process by tracking the pore shape and orientation in real time based on the well-established shape and structure parameter as described previously [2, 4].

References

1. D. Markl, P. Wang, C. Ridgway, A.-P. Karttunen, P. Bawuah, J. Ketolainen, P. Gane, K.-E. Peiponen, J.A. Zeitler, *Chem. Eng. Res. Des.* **132**, 1082–1090 (2018).
2. D. Markl, P. Wang, C. Ridgway, A.-P. Karttunen, M. Chakraborty, P. Bawuah, P. Pääkkönen, P. Gane, J. Ketolainen, K.-E. Peiponen, J.A. Zeitler, *J. Pharm. Sci.* **106**, 1586–1595 (2017).
3. P. Bawuah, A.-P. Karttunen, D. Markl, C. Ridgway, O. Korhonen, P. Gane, J. A. Zeitler, J. Ketolainen, K.-E. Peiponen, *Int. J. Pharm.* **544**, 278–284 (2018).
4. D. Markl, P. Bawuah, C. Ridgway, S. van den Ban D.J. Goodwin, J. Ketolainen, P. Gane, K.-E. Peiponen, J. A. Zeitler, *Int. J. Pharm.* **537**, 102–110 (2018).

Ambient air spectroscopy and thermometry for accurate distance measurement

Jeremias Seppä and Tuomas Helojärvi

VTT Technical Research Centre of Finland Ltd, Centre for Metrology MIKES, Espoo

Corresponding author: jeremias.seppa@vtt.fi

Keywords: spectroscopy, air, thermometry

Accurate position and distance measurements over tens of metres are needed in e.g. manufacturing and assembly of large components and structures in e.g. aerospace and automobile industry, civil engineering and power generation. Optical measurement systems are usually selected for provision of a versatile and feasible position or distance measurement system - but optical distance measurements suffer from dependency on the effective refractive index of the ambient medium (air) that relates the optical distance to the true, or “mechanical” distance.

When targeting micrometre accuracies over tens of metres distances and longer, usually the most difficult parameter to measure that affects the average air refractive index over the optical measurement path is the average temperature, or effective temperature. For this reason VTT MIKES has already developed methods for spectroscopic measurement of air temperature in relation to optical distance measurements [e.g. 1-2].

The methods are based on measuring the absorption of laser signal, which is finely tuned in optical frequency to match a chosen resonance frequency or frequencies of molecular oxygen. From the absorbance, it is possible to deduce the effective temperature along the absorption path, which can span up to dozens [1] or even hundreds of meters [2]. Optical distance measurements along this path can then be performed with greater precision, with the acquired knowledge of the average refractive index along the measurement path.

In the recently started LaVA project [3-4] we aim to develop faster and more robust measurement than previously, with more compact and cheaper measurement setups that can be integrated with e.g. distance measurement telemeters [5] using retroreflective targets. The integration of the thermometer with a telemeter laser distance measurement head is to be tested during the project, along with development, verification and comparison measurements with other air thermometry systems. Figure 1 shows a system schematic.

The presented thermometry work is performed within the project Large Volume Applications, which is jointly funded by the EMPIR participating countries within EURAMET and the European Union.

And finally, a heads up, we plan to present also something about a new rather phenomenal application of lasers in ambient air that is being developed for commercialization at VTT. The possibilities of the technology have been already discussed in Japan with some potential partners.

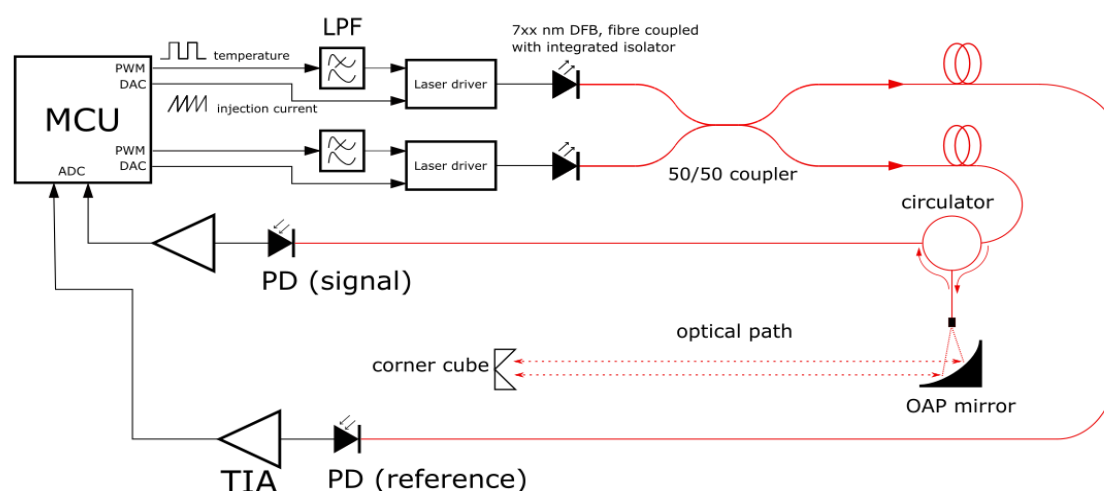


Fig. 1. System schematic for air temperature measurement

References

1. T. Hieta, M. Merimaa, M. Vainio, J. Seppä and A. Lassila, “High-precision diode-laser-based temperature measurement for air refractive index compensation,” *Appl. Opt.* 50, pp. 5990–5998, 2011
2. T. Tomberg, T. Fordell, J. Jokela, M. Merimaa and T. Hieta, “Spectroscopic thermometry for long-distance surveying” *Appl. Opt.* 56, pp. 239–246, 2017
3. Large volume metrology applications (LaVA) project page, available at <https://www.euramet.org/research-innovation/research-empir/empir-calls-and-projects/call-2017-industry-fundamental-normative-research-potential-support-for-impact/>, cited on 2019-02-28
4. Large volume metrology applications (LaVA) project page, available at <https://www.researchgate.net/project/LaVA-Large-Volume-Applications>, cited on 2019-02-28
5. J. Guillory, R. Smid, J. Garcia-Marquez, D. Truong, C. Alexandre and J.-P. Wallerand, “High resolution kilometeric range optical telemetry in air by radio frequency phase measurement” *Rev. Sci. Instrum.* 87, 075105, 2016

Label-free and vibration-free imaging using low-coherent quantitative phase microscope

Natsuki Suzuki^{1,2} and Katsuhiko Ishii¹

¹ *The Graduate School for the creation of new photonics industries, Hamamatsu, Japan*

² *Hamamatsu Photonics K.K., Iwata, Japan*

Corresponding author: natsuki.suzuki@gpi.ac.jp

Keywords: low-coherence interferometry, cell biology, quantitative phase imaging

Cell morphology and its dynamics are widely studied intrinsic properties of biological cells. For example, the motility of cancer cells correlates with their metastatic properties [1], and the membrane fluctuation of red blood cells correlates with their membrane stiffness [2]. In order to study image cell morphology without labeling, imaging techniques exploiting the interference of the optical field were applied to living cells and are called quantitative phase imaging (QPI), quantitative phase microscopy (QPM), or digital holography microscopy (DHM) [3-5].

Regarding the coherence of a light-source, researchers have proven that spectrally and spatially incoherent illumination provides better image quality [6]. A conventional but powerful tool for providing an interference microscope with spectrally and spatially incoherent illumination is a two-beam interference microscope with independent reference and sample arms [7]. However, two-beam interference microscopes used to be a large and heavy.

In this paper, we introduce a compact and standalone QPM setup with independent reference and sample arms. Due to an optical path-length stabilization system implemented in the setup, our setup realized sub-nanometer reproducibility in the optical thickness even without optical tables. In terms of the spatial uniformity, our setup provided 1-2 nanometers of background flatness owing to the spatial incoherency of the illumination.

Figure 1 shows a schematic illustration of quantitative phase microscope system. The observation light from the LED light source is split by the beam splitter, reflected from the sample and reference mirror, and then combined again to form interference fringes on the imaging surface of the camera. The test cells are cultured on the half mirror, and the sample light is specularly reflected from the half mirror immediately below the test cells after passing through the test cells, and interferes with the reference light reflected from the reference mirror. The interference image is taken with phase shift by $\lambda / 4$, and the phase image of the cell can be obtained by calculation of $\phi = \arctan ((I_3 - I_1) / (I_2 - I_4))$. A part of the interference light is guided to a photo detector (PD), and an electrical signal from the PD is input to a control circuit that performs phase shift detection and feedback control to a desired phase. Our control circuit achieves stabilization of the optical path length by controlling the reference mirror with a 5 kHz feedback circuit while detecting the phase shift at a sampling rate of 20 kHz.

Figure 2 shows the imaging results of cultured cell line HeLa cells (derived from human cervical cancer). Figure 2 (a) is a quantitative phase image, and (b) and (c) are emulations of a phase contrast image and a differential interference image created by image processing of the spatial phase of the quantitative phase image and spatial frequency filtering, respectively. The use of LED incoherent lighting provides a precise image without speckle noise. The objective lens used for imaging was a 10X objective lens (NA = 0.45).

We achieved quantitative phase imaging with a two-beam interferometer by using an optical path length stabilization system in an environment without an air table. Our compact system can be applied to the imaging of many biological samples and industrial samples because it can be operated with a reduction in the optical path length even on a normal laboratory desk.

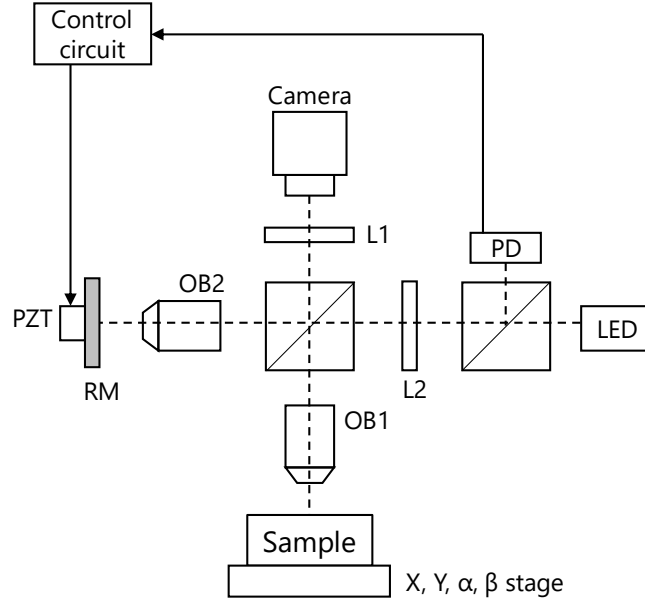


Fig. 1: Schematic illustration of quantitative phase microscope system. PD: photodetector, PZT: piezoelectric transducer, RM: reference mirror, OB: objective lenses, BS: beam splitter, L: lens.

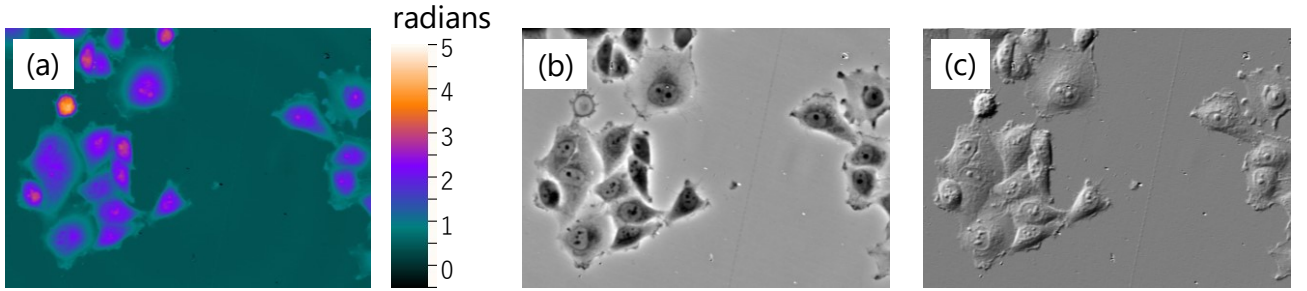


Fig. 2. Full-field images of HeLa cells. (a): Quantitative phase image. (b): Emulated phase contrast image constructed from (a). (c): Emulated differential interference contrast image constructed from (a).

References

- [1] A. W. Partin, J. S. Schoeniger, J. L. Mohler *et al.*, “Fourier analysis of cell motility: correlation of motility with metastatic potential,” *Proc Natl Acad Sci USA*, 86(4), 1254-8 (1989).
- [2] G. Popescu, T. Ikeda, K. Goda *et al.*, “Optical measurement of cell membrane tension,” *Phys Rev Lett*, 97(21), 218101 (2006).
- [3] H. Iwai, C. Fang-Yen, G. Popescu *et al.*, “Quantitative phase imaging using actively stabilized phase-shifting low-coherence interferometry,” *Opt Lett*, 29(20), 2399-401 (2004).
- [4] Z. Wang, L. Millet, M. Mir *et al.*, “Spatial light interference microscopy (SLIM),” *Opt Express*, 19(2), 1016-26 (2011).
- [5] P. Marquet, B. Rappaz, P. J. Magistretti *et al.*, “Digital holographic microscopy: a noninvasive contrast imaging technique allowing quantitative visualization of living cells with subwavelength axial accuracy,” *Opt Lett*, 30(5), 468-70 (2005).
- [6] S. Shin, K. Kim, K. Lee *et al.*, “Effects of spatiotemporal coherence on interferometric microscopy,” *Optics Express*, 25(7), 8085-8097 (2017).
- [7] M. K. Kim, [Digital Holographic Microscopy] Springer, (2011).

Setup for characterising the spectral responsivity of Fabry-Pérot-interferometer-based hyperspectral cameras

Oskari Pekkala¹, Tomi Pulli¹, Alexander Kokka¹ and Erkki Ikonen^{1,2}

¹ Metrology Research Institute, Aalto University, Espoo, Finland

² VTT MIKES, Espoo, Finland

Corresponding author: oskari.pekkala@aalto.fi

Keywords: hyperspectral imaging, spectral responsivity, camera calibration, Fabry-Pérot-interferometer

Hyperspectral cameras collect radiance data of the imaged view via dozens of narrow-bandwidth spectral channels, as opposed to the three color channels of common digital cameras. Knowledge of the spectrum, i.e. spectral power distribution, can be used for example in identification and classification of the materials in the image. Hyperspectral imaging has applications in many fields, for example in agriculture [1] and medicine [2].

A reliable characterisation of the spectral responsivity of the channels is essential for processing hyperspectral data and when assessing its reliability. Different camera architectures set different requirements for studied camera features and characterisation measurements. The camera under study was a Fabry-Pérot-interferometer-based camera, which required the characterisation of its channels both spectrally and spatially.

This study presents the measurement setup (figure 1) and analysis for characterising the spectral responsivity of hyperspectral cameras. The main part of the setup was a tuneable, monochromatic radiance source. The camera under study was mounted on a motorised turntable, imaging an illuminated diffuser at different wavelengths and from different viewing angles. The spectral responsivities of the camera channels were extracted from the pixel values of the images, yielding results both as a function of wavelength and as a function of image plane coordinates. The results were validated by imaging an incandescent lamp-based radiance source with a known spectrum.

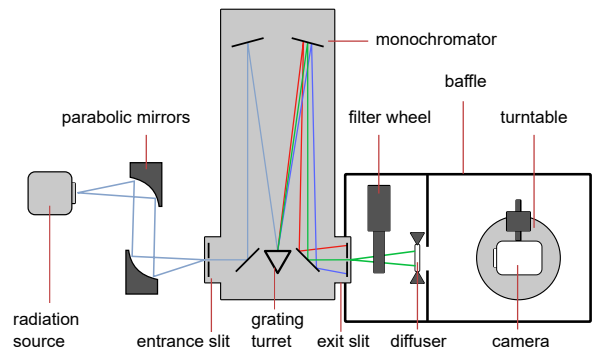


Figure 1: Measurement setup.

The setup was used in characterising the spectral responsivity of a Fabry-Pérot-interferometer-based hyperspectral camera. The results show that the bandwidth and the centroid wavelengths of the channels change across the image plane, and that some of the channels have regions of sensitivity outside the main channel. Channel centroid wavelengths shift up to 1.5 nm when moving from the image centre to edges of the image, as shown in figure 2. The bandwidth of the channels changes by up to 10% in the image area and with different patterns for each channel. The validation of the results yielded a root mean square error of 3.6% between the reference and the measured spectral power distributions. The expanded uncertainties ($k = 2$) for the measured camera channel characteristics, namely bandwidths, sensitivities and wavelengths, were 7.9%, 9.5% and 0.64 nm, respectively. The measured spectral responsivities of the channels are shown in figure 3.

The results confirm the viability of the measurement setup for hyperspectral camera calibrations. A more advanced calibration facility will be implemented at the Metrology Research Institute based on the described setup.

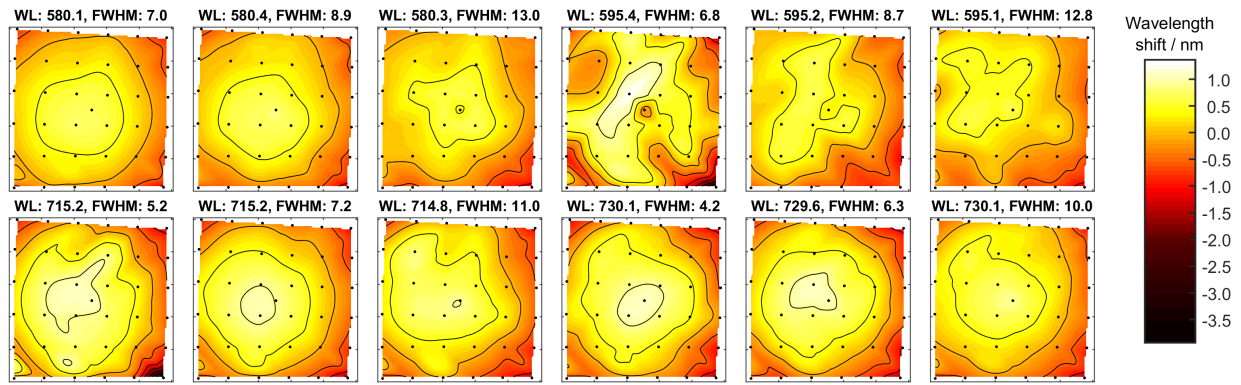


Figure 2: Wavelength shift in the image plane.

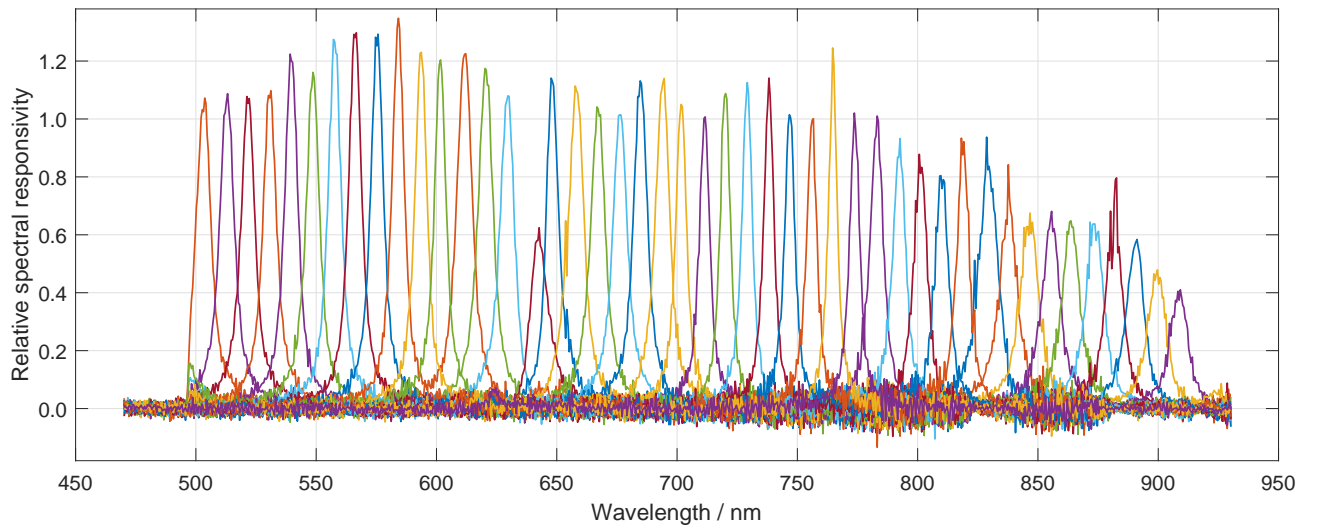


Figure 3: Relative spectral responsivities of the measured camera channels.

References

- [1] M. Teke, H. S. Deveci, O. Haliloğlu, S. Z. Gürbüz, and U. Sakarya. A short survey of hyperspectral remote sensing applications in agriculture. In *2013 6th International Conference on Recent Advances in Space Technologies (RAST)*, pages 171–176, June 2013.
- [2] Guolan Lu and Baowei Fei. Medical hyperspectral imaging: a review. *Journal of Biomedical Optics*, 19(1):010901, 2014.

Comparison of experimental and the Mie scattering coefficients of bulk suspensions of ideal and deformed cylindrical particles

Harri J. Juttula¹, Matti Törmänen² and Anssi J. Mäkynen³

¹ Unit of Measurement Technology, University of Oulu, Kajaani

² Valmet Automation Inc., Oulu

³ Optoelectronics and Measurement Techniques Unit, University of Oulu, Oulu

Corresponding author: harri.juttula@oulu.fi

Keywords: cellulose, scattering

Paper and paperboard are made of paper machine furnish which consists of water suspended mixture of paper pulp and various additives. Paper pulp consists of cellulose fibers extracted from trees and additives may include dyes or inorganic fillers like kaolin, calcium carbonate, talc or titanium dioxide, for example. One of the most important control parameters of paper making is the total mass fraction, or total consistency, of the furnish which is defined as a mass percentage of all solid material of the furnish. Today, there are a number of commercial online instruments which measure the mass fraction. Measurement principles may include, for example, attenuation and scattering of optical signals, the attenuation of microwaves or mechanical shear force detectors [1]. Besides the total mass fraction, modern paper making needs online information about mass fractions of fibers and fillers separately. Some experimental optical methods are capable of providing separate mass fractions but may not be practical for industrial use [2, 3]. Alternatively, the existing optical online instruments can be tuned to provide separate fiber and filler mass fractions. However, the wide variation in fiber and filler materials make this kind of tuning very complex and difficult to conduct reliably. For example depending on fiber physical dimensions, fibrillation and the amount of fiber fines may lead to widely different results with optical methods. One possible solution would be to utilize quality information about the fibers and then resolve their effect on optical mass fraction sensors by using precise optical modelling based on the material properties. In this work, we have studied the necessary preconditions for this kind of approach by comparing experimental scattering properties of ideal and natural (deformed) fibers and theoretical values based on their size distribution as a function of the mass fraction.

Cylindrical fibers with their diameter in the micrometer size scale interact with light via elastic scattering and absorption which can be modelled with the Mie scattering theory [4]. Mie scattering provides solutions for the scattering and absorption properties of spherical or infinite cylindrical particles as a function of the wavelength, particle radius and complex refractive index. Cellulose fibers used in paper making, however, are far from ideal cylinders and they suffer from deformations such as bending, flattening, axial twisting or kinks when compared with ideal cylinders. Simple cylindrical scattering models cannot explain the scattering properties of single fibers. Furthermore, the orientation angle of the fiber axis with the incidence light affects the scattering efficiency and cross section of the fiber. We assume that the effects of structural deformations and orientation on the bulk scattering properties of pulp can be taken into account if we treat the diameter and orientation as probability density functions and integrate Mie solutions over them. With this approach, we can predict the bulk scattering properties of fiber suspensions as a function of the mass fraction.

In order to test our assumption we chose cellulose fibers (bleached Nordic pine) used in paper mill and artificial rayon fibers to represent deformed and ideal cylindrical particles as shown in Figure 1. We determined their cross sectional

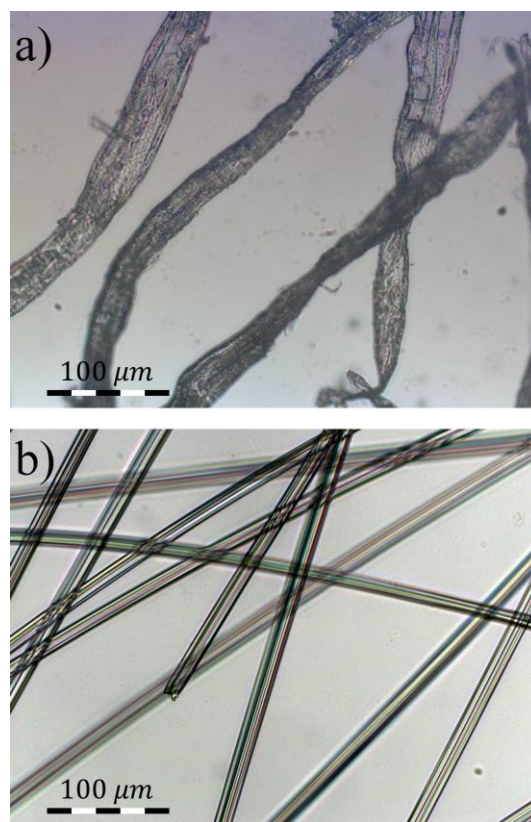


Figure 1. a) Natural cellulose fibers resembling flattened deformed cylinders and b) near ideal cylindrical artificial rayon fibers.

diameter distribution from microscope images and used a log-normal distribution to fit and represent the fibers in Mie calculations. We used the log-normal diameter distributions with an additional assumption of isotropical orientation of the fibers together with the Mie theory in order to solve the scattering properties of bulk fiber suspension as a function of the total mass fraction.

We compared the Mie results based on fiber statistical morphology with the experimental results of two independent measurements of fiber suspensions with a varying mass fraction simulating the real life process environments. Closed loop circulation measurement setup was used to examine the sample fibers in aqueous solutions between 0.1% and 1% mass fractions. The setup is shown in Figure 2. Two measurement devices were attached to the circulation system to provide independent results. First device used double integrating spheres and narrow flow through cuvette in conjunction with a well known IAD program [5] to determine the scattering coefficient of the sample suspension from the measured reflectance and transmittance. Second device measured the scattering coefficient by analyzing the backscattering of a laser with 45 degree angle of incidence [6] with the sample suspension in a cuvette with large turbulent volume. Both devices operated at 660 nm wavelength. Two devices were used in order to eliminate the possible orientation effect on the scattering coefficient in the narrow cuvette between integrating spheres. Measurement results shown in Table 1. were in agreement with each other and were close to the values determined from the fiber cross sectional diameter distribution with the Mie theory. Both fiber suspensions showed a linear response of the scattering coefficient to the total mass fraction.

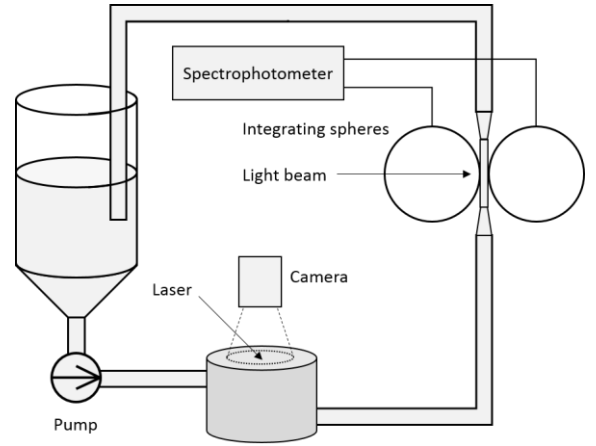


Figure 2. Measurement setup.

Table 1. Measured reduced scattering coefficient per mass concentration for fibers in aqueous suspension.

	$\mu'_s/w_{\%} [\text{mm}^{-1}] \pm 2\sigma$		
	Mie	IAD	Laser backscattering
NP	$0.043 \pm 11\%$	$0.044 \pm 13\%$	$0.050 \pm 27\%$
Rayon	$0.090 \pm 3\%$	$0.076 \pm 15\%$	$0.072 \pm 18\%$

Our experiments show that simple cylindrical scattering model holds true for the ensemble of fibers if their diameter is represented with a probability distribution and that the scattering coefficient has a linear response to the total mass fraction. This is important as many industrial measurements based on the scattering of light are non-linear by nature and can behave in unpredictable manner due to changes in fiber morphology. While our experiments were limited to pure fibers with no fillers or fines and no fibrillation these can be taken into account as separate scatterers which obey their own size distribution and number density. Results also indicate that, if available, qualitative morphological data could be used to improve the analysis of optical quantitative measurements.

References

1. B. G. Liptak, "Instrument Engineers' Handbook, Volume One: Process Measurement and Analysis," 4th ed., CRC Press, 2003.
2. M. Törmänen, J. Niemi, T. Löfqvist, R. Myllylä, "Pulp consistency determined by a combination of optical and acoustical measurement techniques," Meas. Sci. Technol., Vol. 17, 2006.
3. Z. Zhao, M. Törmänen, R. Myllylä, "Backward-mode photoacoustic transducer for sensing optical scattering and ultrasonic attenuation: determining fraction consistencies in pulp suspensions," Meas. Sci. Technol., Vol. 21, 2010.
4. C. F. Bohren, D. R. Huffman, "Absorption and scattering of light by small particles," Wiley, New York, 1983.
5. S. A. Prahl, M. J. C. van Gemert, A. J. Welch, "Determining the optical properties of turbid media by using the adding doubling method," Appl. Opt. Vol. 32, pp. 559–568, 1993.
6. H. J. Juttula, T. P. Kananen, A. J. Mäkynen, "Instrument for measurement of optical parameters of turbid media by using diffuse reflectance of laser with oblique incidence angle", IEEE Trans. Instrum. Meas., vol. 63, no. 5, pp. 1301–1309, May 2014.

Development of metrological atomic force microscope

Virpi Korpelainen, Johan Nysten, Jeremias Seppä and Antti Lassila

VTT MIKES, Espoo, Finland

Corresponding author: Virpi.korpelainen@vtt.fi

(Optional small paragraph describing the additional information concerning the authors may be added here, extending to several lines if needed)

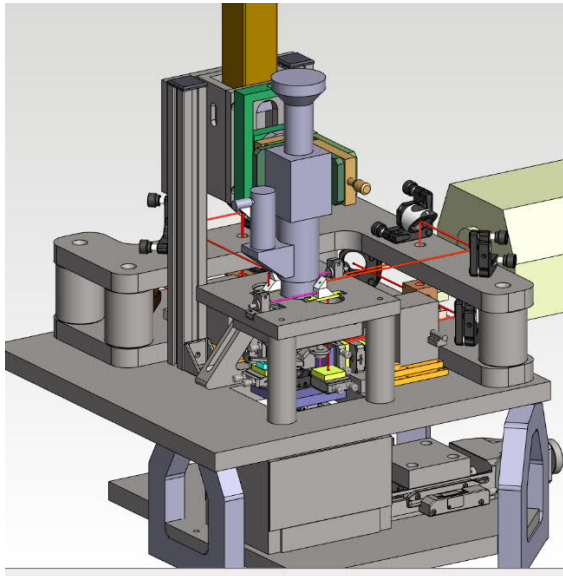
Keywords: metrology, AFM, measurements of nanostructures, uncertainty estimates

Traceability to the SI metre is the basis for dimensional measurements in the nanoscale. Atomic Force Microscopes (AFM) are used to measure surface features with subnanometre resolution. Unidirectional measurements, e.g. of grating pitch and step height, are partly self-compensating and can also reach sub-nanometre uncertainty [1]. However, fully 3D measurements in nanoscale introduce a number of uncertainty sources, most notably probe geometry effects, probe-sample interaction and probe positioning control [2]. Thus, the existing level of 5 nm uncertainty falls short of the requirements of industry and research.

A metrological atomic force microscope (MAFM) has been developed at MIKES [3], featuring direct traceability to the SI metre via laser interferometry. The new setup has large measurement range ($950\text{ }\mu\text{m} \times 950\text{ }\mu\text{m} \times 100\text{ }\mu\text{m}$). The development done under the EMPIR initiative's 3DNano project [4] also brings us closer to truly 3D measurements of vertical and lateral surface features. To achieve this goal, measurement uncertainty will be reduced to below 1 nm.

Uncertainty components of the MAFM are characterized experimentally, and the total uncertainty budget is evaluated by Monte Carlo sampling on a virtual AFM (VAFM, a numerical model of the system). The VAFM is a numerical model of the physical system, implementing the key physics affecting the measurement, e.g. parasitic rotations in linear movement.

Monte Carlo uncertainty estimation can be extended to include any number of uncertainty components without added complexity. Initial results validate the method by comparing existing results against model evaluation on existing data. A conceptual model of the VAFM is produced, to serve as documentation and design aid.



The new setup allows measurements of large areas, which makes it more suitable for measurements of e.g. optical components and surface roughness. That will improve measurement uncertainty and fill the gap between MAFM measurement and other traceable surface characterization methods (e.g. white light inference microscopy, stylus instrument).

This project has received funding from the EMPIR programme co-financed by the Participating States and the European Union's Horizon 2020 research and innovation programme. The work is part of the Academy of Finland Flagship Programme, Photonics Research and Innovation (PREIN), decision 320168.

Fig. 1: CAD model of the updated MIKES MAFM

References

1. V. Korpelainen, J. Seppä and A. Lassila, "Measurement strategies and uncertainty estimations for pitch and step height calibrations by metrological atomic force microscope." *J. Micro/Nanolith. M., and M.*, **11**, 2012.
2. R. Dixon, N. Orji, I. Misumi and G. Dai, "Spatial dimensions in atomic force microscopy: Instruments, effects, and measurements". *Ultramicroscopy*, **194**, pp. 199-214, 2018
3. V. Korpelainen, J. Seppä and A. Lassila, "Design and characterization of MIKES metrological atomic force microscope." *Precision Engineering* **34**, pp. 735-744, 2010
4. Traceable Three-Dimensional Nanometrology, www.ptb.de/emrp/15sib09-project.html, valid 4/2019

3D printed lens project for bachelor's education

Eero O. Molkoselkä¹, Gleb A. Bulygin¹, Justus F. Kleine¹ and Anssi J. Mäkynen¹

¹ Unit of Measurement Technology, University of Oulu, Oulu, Finland

Corresponding author: eero.molkoselka@oulu.fi

Keywords: optical design, digital fabrication, 3D printing, lens polishing, teaching

3D printing technology has made steady progress for a while now and is becoming more and more accessible. While the printing quality and materials of the commercial models might not be good enough to fabricate precise optical systems, they can still be used for applications where the accuracy isn't as important. One of these is teaching.

We present a lens design project for educational purposes that is aimed for bachelor's level students. In the project students are given a task of designing, 3D printing and polishing their own biconvex or plano-convex lenses. The process teaches students the basics of lens design in a practical way and allows them to familiarize with some of the common software used in the industry. The project has been developed and tested as a part of a technical optics course with two small groups of students. The students joined the course voluntarily using university's common registration methods and had varying experience in digital fabrication and the field of optics.

All the students were given a loose lens specification (refractive index, focal length limits and diameter) which they then used to design their own lenses first by hand using the lens-maker's equation [1] and then with OpticStudio by Zemax [2]. OpticStudio was chosen because it provides built-in functionality for exporting lens designs to 3D printable CAD files. However, for the future courses a Python library and web based user interface for generating basic spherical lens objects were developed [3]. This way the design process itself can also be done with other common programs such as OSLO [4].

Stereolithography based 3D printer Formlabs Form 2 was used for the printing process [5]. The transparent printing material of Form 2 is light-activated resin with a measured refractive index of 1.54. Hardened resin is an easy material to polish and work with which makes it good for beginners. Three different polishing methods were tested:

1. Polishing with sandpaper, sanding pads and liquids,
2. Polishing by grinding the lens against 3D printed counterpart and
3. Dipping the lens in liquid resin and post-curing with UV light.

Generally, the sanding and grinding methods produced decent lenses but required more time and effort to polish. Using pads and liquids also generates extra material costs. The dipping method can be a better choice if there is a large number of students or multiple lenses for each participant. The quality was also more consistent because the variance caused by different polishing times and techniques decreased. Some examples of final lenses can be seen in Fig. 1.

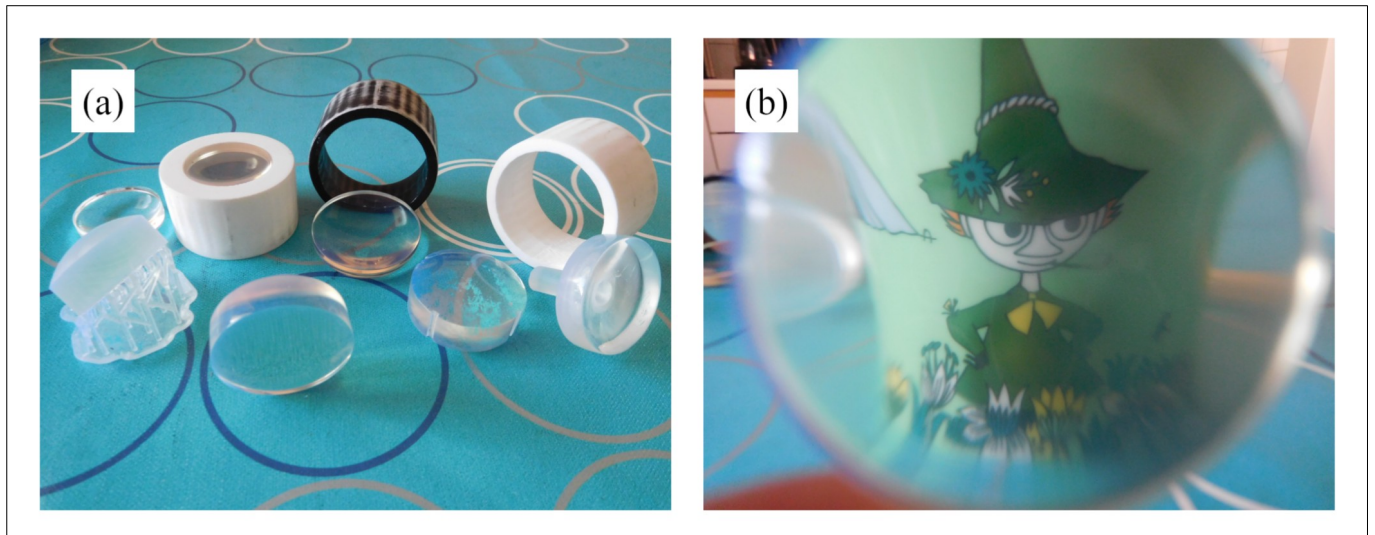


Fig. 1. 3D printed lenses, holders and counterparts (a). An object viewed through a 3D printed lens (b).

Lenses were tested by using a modified digital projector. The original optical system of the projector was removed and replaced with 3D printed holder that could fit the lenses. Performance of the lenses was then compared to industry made glass lens. The chromatic and spherical aberration of the printed lenses could be easily seen in the projection which helped teaching the theory to the students. Various optical properties such as MTF (modulation transfer function) could also be approximated from the projection. In the future, the goal is to run the project with a larger group of students and see whether the whole process can still be executed successfully.

References

1. E. Hecht, *Optics*, (Addison-Wesley, 1987).
2. Zemax OpticStudio: <https://www.zemax.com/products/opticstudio>, valid 4/2019
3. Our Python lens library: <https://github.com/molkoback/lensmesh>, valid 4/2019
4. OSLO: <https://www.lambdares.com/oslo/>, valid 4/2019
5. Formlabs Form 2: <https://formlabs.com/3d-printers/form-2/>, valid 4/2019

Three-dimensional flow measurements around micro-pillars in water by micro-digital holographic particle tracking velocimetry

Yasuhiro Matsuda¹ · Hiroshi Kigami¹ · Noriyuki Unno² · Jun Taniguchi¹ · Shin-ichi Satake¹

¹ Department of Applied Electronics, Tokyo University of Science, 6-3-1 Nijuku, Katsushika-ku, Tokyo 125-8585 Japan

² Tokyo University of Science, Yamaguchi, 1-1-1 Daigakudo-ri, Sanyo-onoda, Yamaguchi, 756-0884 Japan

Corresponding author: satake@te.noda.tus.ac.jp

Keywords: Digital holography, Index matching method, micro-pillars

A refractive index matching method in water to measure the velocity field around micro-pillars was investigated. The micro-pillars were fabricated from an optical material (MY-133-V2000) whose refractive index was 1.333, which is the same as that of water. The fabrication method used was UV imprint lithography (UV-NIL) with photolithography with a replica mold. The moving tracer particles on the pillars were measured by micro-digital holographic particle tracking velocimetry (micro-DHPTV). Because the refractive indices of the pillars and water were the same, the hologram images could be obtained clearly without diffraction around the micro-pillars. As a result, tracking of particles and measurement of velocity fields using reconstructed particles could be achieved without optical distortion. The moving particles could be captured around the micro-pillars.

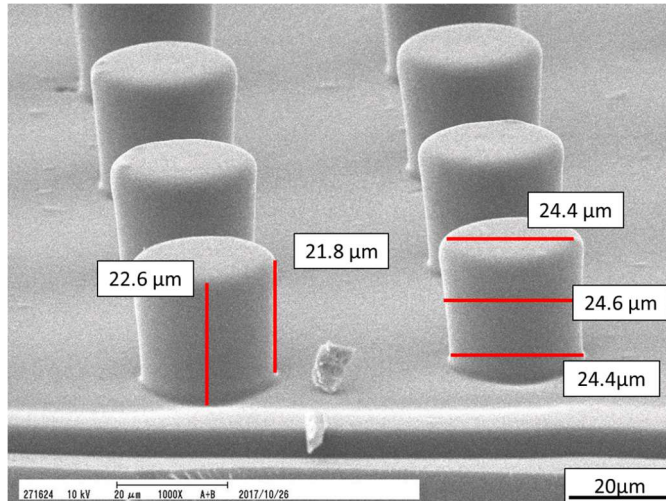


Fig. 1 SEM image of the microstructures fabricated from MY-133-V2000 by the vacuum UV imprinting technique

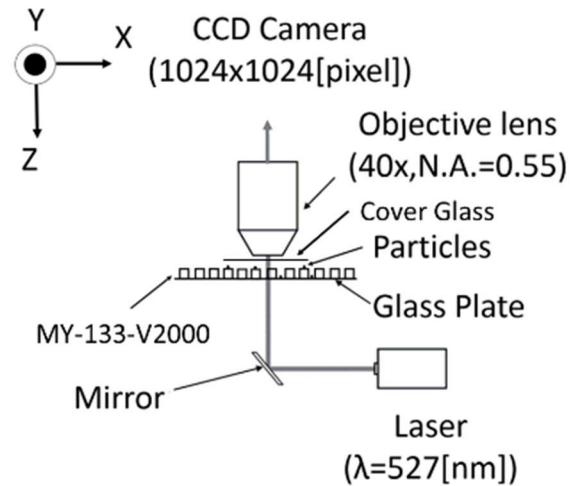


Fig. 2 Experimental setup for a micro-digital holographic PTV system.

Techniques for three-dimensional velocity measurements are required to detect flow fields in the microfluidic devices used in bioresearch. In a previous study, an investigation into the mechanism of actin network accumulation was carried out by measuring flow fields in a micro-device with a pattern of PDMS micro-pillars [1]. The flow field was obtained by digital inline holographic microscopy (DIHM). However, particle tracking was difficult because of the optical distortion resulting from the difference between the refractive indices of water and PDMS. Given that water is generally used as the working fluid in biofluidics, the refractive index of MY-133-V2000 must match that of water, so that obstacles caused by optical distortion, such as those observed with PDMS, can be avoided. In past research, fluid measurements for macroflow [2] and nanoflow [3] were successfully achieved via a refractive index matching method [4] using MEXFLON, an optical material whose refractive index matches that of water. In addition, MY-134 ($n = 1.34$) a ultraviolet (UV)-curable resin [5], is a potential refractive index matching material. In a previous study, a cell on the micro-pillar fabricated by the material in the cell culture liquid ($n = 1.338$) was observed. Additionally, the calibration plate was fabricated for multilayer nanoparticle image velocimetry using UV nanoimprint lithography (UV-NIL) with MY-133-V2000 [6]. The fabrication process involved the use of photolithography and UV-NIL with a replica mold. In the present study, we measured three-dimensional flow fields around a micro-pillar prepared by the abovementioned technique. Figure 1 shows a micro-pillar pattern imaged by

scanning electron microscopy (SEM). Figure 2 shows the experimental setup. The equipment was the same as that used in our previous study [7]. The plate was covered by glass and had micro-pillars made of MY-133-V2000, whose refractive index is 1.333. A high-resolution digital charge-coupled device (CCD) camera (Redlake, MotionProX-3; resolution 1024×1024 pixel, image $12 \mu\text{m} \times 12 \mu\text{m}$) with an objective lens (Nikon, $40\times$, $\text{NA} = 0.55$) was used to record fringe images of the particles. A neodymium-doped yttrium lithium fluoride (Nd:YLF) laser (Photonics Industries DS20-527, $\lambda = 527 \text{ nm}$) was used as the light source, which produced a pair of laser pulses at a repetition rate of 1 kHz with a pulse length of 58 ns and a pulse delay of 100 μs . The polystyrene spherical particles (Thermo Fisher Scientific 4010A Polystyrene) had a diameter of 1 μm and specific gravity of 1.05. NaCl (10 mM) was added to the particle suspensions to enable solid contact between the particles and the micro-pillar pattern. The refractive index of the 10 mM NaCl solution is the same as that of water. Particle suspensions or 10 mM NaCl particle suspensions were dropped on the micro-pillar pattern, and the plate was covered by a cover glass. Hologram images were recorded at a repetition rate of 1 kHz. The particles were tracked by DHPTV [7]. Hologram images of the micro-pillar pattern is showed in Figure 3. Figures 3(a) and 3(b) show the micro-pillar patterns of MY-133-V2000 and PAK-01, respectively. Figure 3(c) shows the micro-pillar pattern of MY-133-V2000 in the 10 mM NaCl particle suspension, while Fig. 3(d) shows the micro-pillar pattern of PAK-01 in the particle suspension. On the one hand, the edge of the micro-pillar pattern of MY-133-V2000 became invisible as a result of refractive index matching when the pattern was immersed in the 10 mM NaCl particle suspension. On the other hand, the edge of the micro-pillar pattern of PAK-01 was visible even when the pattern was immersed in the particle suspension. It is clear, therefore, that the micro-pillar pattern of MY-133-V2000 can be used for refractive index matching with water. In this study, the micro-pillar pattern of MY-133-V2000 was fabricated, and refractive index matching was performed using MY-133-V2000 and water. The particle on the micro-pillar was reconstructed and tracked using micro-DHPTV [7]. Refractive index matching with water will help in enhancing our understanding of the 3D flow around microstructures in water. We believe that our method will provide a deeper insight into the 3D flow around complex microstructures and allow for the detection of flow fields in the bioresearch and chemical fields.

References

1. Sebastian, Weiße., Matthias, Heydt., Timo, Maier., Simon, Schulz., Joachim, P. Spatz., Michael, Grunze., Tamás, Haraszti., and Axel, Rosenhahn., *Phys. Chem. Chem. Phys.*, **2011**, **13**, 13395-13402 (2011)
2. Masataka, Kuniyasu., Yusuke, Aoyagi., Noriyuki, Unno., Shin-ichi, Satake., Kazuhisa, Yuki., Yohji, Seki., *Optical Review*, Volume **23**, Issue **3**, 529-534 (2016)
3. Noriyuki, Unno., Shuichiro, Nakata., Shin-ichi, Satake., Jun, Taniguchi., *Experiments in Fluids* **57**: 120. (2016)
4. R. Budwig., *Experiments in Fluids* **17**: **350.**, 350-355 (1994)
5. Andrea, Ravasio., Sree, Vaishnavi., Benoit, Ladoux., Virgile, Viasnoff., *Acta Biomaterialia*, Volume **14**, 1 March 2015, 5360 (2015)
6. Noriyuki, Unno., Hiroshi, Kigami., Taku, Fujinami., Shuichiro, Nakata., Shin-ichi, Satake., Jun, Taniguchi., *Microelectronic Engineering* **180**, 86-92 (2017)
7. Shin-ichi, Satake., Tomoaki, Kunugi., Kazuho, Sato., Tomoyoshi, Ito., Hiroyuki, Kanamori., and Jun, Taniguchi., *Measurement Science and Technology*, **17**, **7**, 1647-1651, (2006)

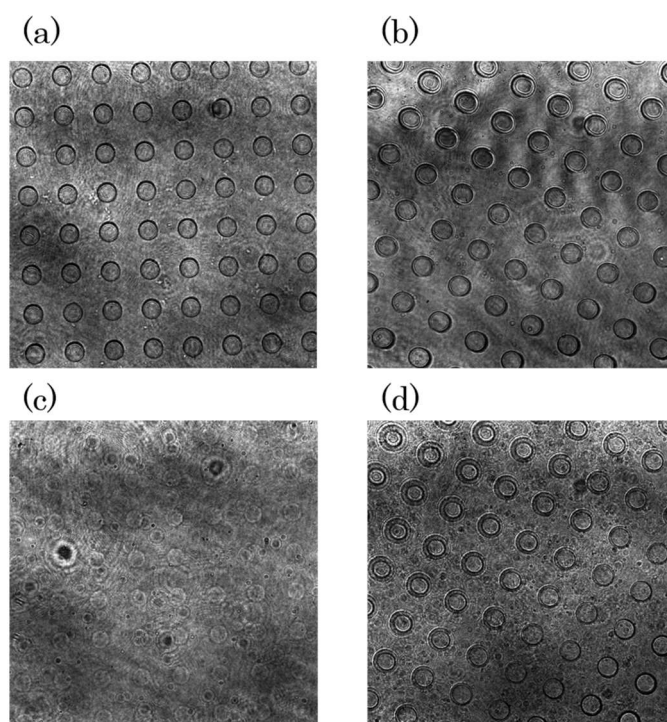


Fig. 3 Hologram images of microstructures (a) fabricated from MY-133-V2000 (dry), (b) fabricated from PAK-01 (dry), (c) fabricated from MY-133-V2000 (underwater), and (d) fabricated from PAK-01 (underwater).

Evaluation of yield stress from velocity fluctuations of microfibrillated cellulose suspension flow by optical coherence tomography

Janne Lauri¹, Antti Koponen², Sanna Haavisto³⁻⁴ and Tapio Fabritius¹

¹ Optoelectronics and Measurement Techniques Unit, University of Oulu, Oulu

² VTT Technical Research Centre of Finland Ltd., Jyväskylä

³ Department of Physics, University of Jyväskylä, Jyväskylä

⁴ Spinnova Ltd., Jyväskylä

Corresponding author: janne.lauri@oulu.fi

Keywords: shear viscosity, velocity profile, yield stress, optical coherence tomography

Micro- and nanofibrillated cellulose (MFC) have raised great interest as a sustainable and biodegradable material. It is used in various applications, for instance, in composites, barrier materials, viscosity modifiers and antimicrobial films [1]. Many applications of MFC, such as 3D printing and self-assembly of nanocellulose-based filaments, require prior knowledge of flow dynamics. Despite of extensive research, complex flow properties of MFC are still not comprehensively understood and novel experimental data and analysis methods are needed. An optical method, called optical coherence tomography (OCT), has recently been demonstrated to be an excellent tool to monitor fiber suspension flow and flocculation in a rotational rheometer [2]. OCT has a superior resolution compared to other modalities such as ultrasound velocimetry and magnetic resonance velocimetry. The high resolution enables accurate measurements for wall layer dynamics. Rheological and flocculation analysis in a pipe rheometer equipped with the OCT device, a more realistic geometry for practical applications, has been recently presented [3-5]. In this study, a novel method to estimate yield stress from optical coherence tomography (OCT) velocity data is presented for 0.5 % microfibrillated cellulose (MFC) suspension in a tube flow.

The microfibrillated cellulose sample was prepared from never-dried bleached kraft birch pulp via grinding three times in a supermasscolloider (Masuko Sangyo Co. Ltd., Kawaguchi, Saitama-pref., Japan). The configuration of the experimental system is shown in Fig 1. Measurements were performed in a glass tube with an inner diameter of 8.6 mm. The OCT device was in-house built. More details of the measurement setup and the device can be found in Refs. [4-5].

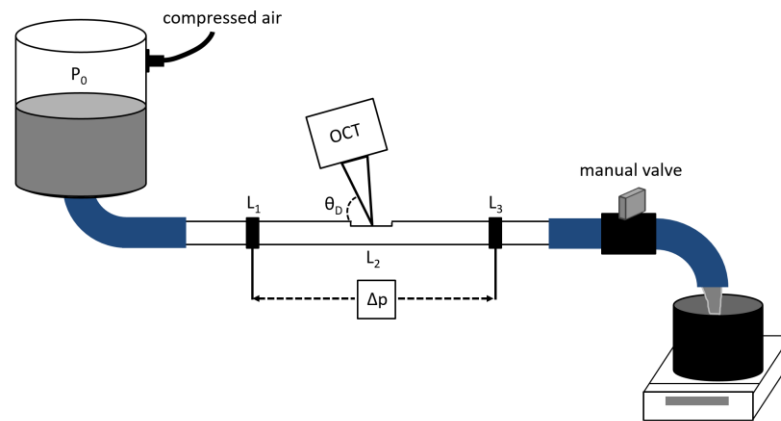


Fig. 1. The measurement setup. L1 and L2 are locations of the pressure sensors, θ_D is Doppler angle and P_0 is overpressure.

Measurements were performed at the A-scan rates of 31 kHz and 123 kHz. The phase variance was calculated from the bulk region of the suspension (distance from the pipe wall more than 20 μm) to eliminate the effect of reduced MFC concentration due to wall depletion. The data was fitted with two lines (Fig. 2.) The obtained yield stress, defined as the intersection point of the two fitted lines, was 3.4 Pa which correlates excellently with the values defined directly with a bob and cup rheometer [2] and with the viscosity data variations of the

pipe rheometer [3]. Furthermore, the relative floc sizes, calculated from the structural data [4], started to decrease at the same point, which indicated breakage of the fibrous networks structure due to shear stress exceeding the yield stress.

The velocity variance data from OCT can obviously be used to determine the yield stress of complex suspensions. In future, more solid concentrations and different grades of MFC will be measured to validate this novel method for determining the yield stress.

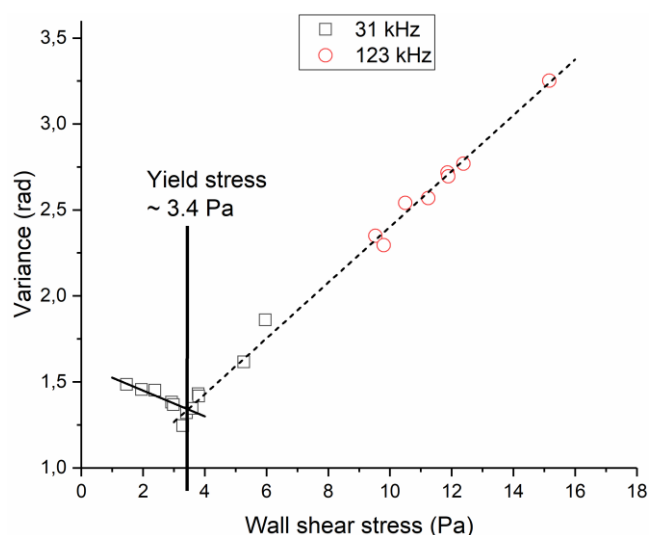


Fig. 2. Measured variances of the OCT velocity signal with two fitted lines. The intersection of the lines depicts the yield stress point. Rectangular and round points have been measured at the 31 kHz and 123 kHz scan rates, respectively.

References

1. R.J. Moon, G.T. Schueneman, and J. Simonsen, *JOM* **68**, 2383–2394 (2016).
2. T. Saarinen, S. Haavisto, A. Sorvari, J. Salmela, and J. Seppälä, *Cellulose* **21**, 1261–1275 (2014).
3. S. Haavisto, J. Salmela, A. Jäsberg, T. Saarinen, A. Karppinen, and A. Koponen, *TAPPI J.* **14**, 291–302 (2015).
4. J. Lauri, A. Koponen, S. Haavisto, J. Czajkowski, and T. Fabritius, *Cellulose* **24**, 4715–4728 (2017).
5. A.I. Koponen, J. Lauri, S. Haavisto, and T. Fabritius, *Applied Sciences* **8**, 755 (2018).

Measurement setup for differential spectral responsivity of solar cells

Petri Kärhä, Hans Baumgartner, Kasper Kylmänen, Benjamin Oksanen and Erkki Ikonen

Metrology Research Institute, Aalto University, Espoo

Corresponding author: petri.karha@aalto.fi

Keywords: radiometry, solar cell, spectral responsivity, efficacy, electricity

The spectral responsivity of a photovoltaic device is needed for solar cell development and cell analysis. It can also be used in testing of solar cells, to correct for the spectral mismatch between the light source used in the measurement from the standardized reference spectral irradiance data. Measurement setups of spectral responsivity have been standardized in [1]. Solar cells can be nonlinear which poses a challenge in measurements. Differential spectral intensity in biased conditions needs to be measured. Such measurement setups have been presented in [2 – 5]. The cells measured are biased with incandescent or Xe light sources. Monochromatic measurement beam is chopped and measured with a lock-in amplifier from the cell output. Combining the bias light with the measurement beam can be made in an integrating sphere, or the beams can be imposed on the cell surface.

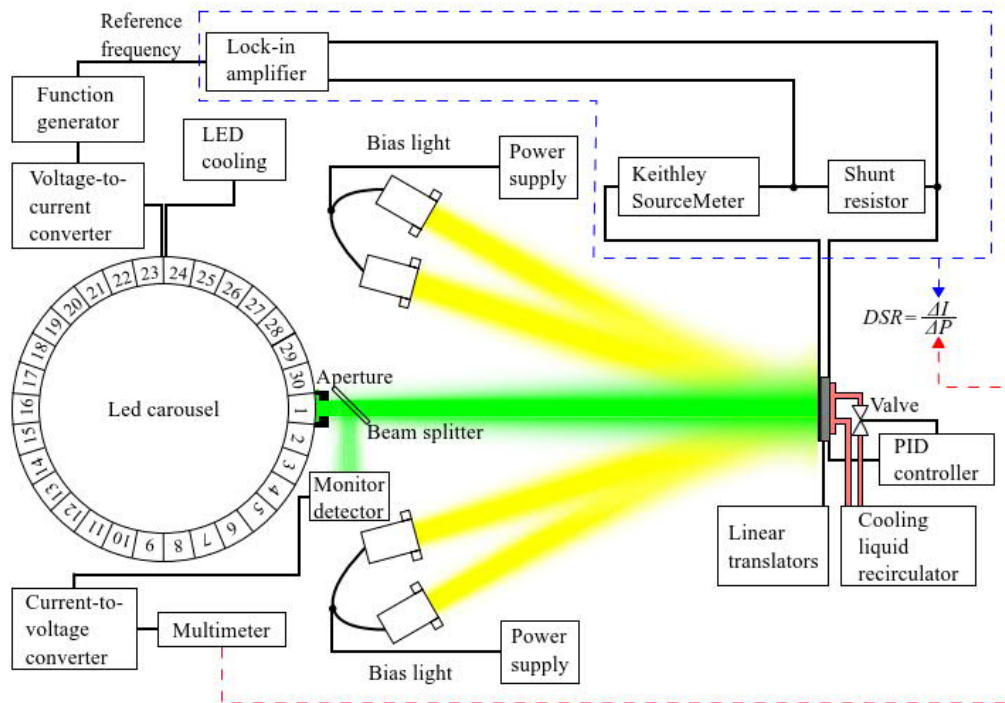


Fig. 1. Schematic presentation of the differential spectral responsivity setup.

We have developed a measurement setup for differential spectral responsivity of solar cells using towers of halogen lights ($4 \times 7 \times 50$ W) for bias light, and 30 narrow-band LEDs for measurement (Fig. 1). The bias lights are used to set radiation conditions close to AM 1.5 (1000 W/m^2) as specified in [6]. The measurement LEDs are mounted in a carousel, guiding one LED at a time to light the cell. The carousel has been earlier used in measurement of cameras [7]. The LEDs are temperature controlled (Fig. 2) and operated with a modulated operating current. A lock-in amplifier is used to detect the weak signal from the induced photocurrent of the solar cell. The cell to be measured is temperature stabilized to 25°C with liquid cooling. The photocurrent is measured with a shunt resistor (2Ω) and a source meter keeping the voltage across the cell negligible.

The setup has been fully characterized and tested for measurements. Figure 3 shows the spectra of the measurement LEDs assembled, and a test measurement of a solar cell. As a reference, a trap detector and a precision aperture is used to measure irradiances of the individual LEDs with the bias lights switched off.

The uncertainty of the obtained differential spectral responsivities over the visible region is 2.5 % ($k = 2$). This is mainly dominated by the standard uncertainties of the spatial uniformity of the measurement beam (0.6 %), gain of the lock-in amplifier (0.6 %), short term stability of the LED source (0.5 %), and the repeatability of

the measurements (0.5 %). The standard deviation of the spatial uniformity of the bias lighting is 1.7 % over a solar cell area of 15×10 cm. The corresponding uniformity for the measurement beam is of the order of 0.6 % depending on the LED used. In the UV and IR regions, the non-uniformities are higher.

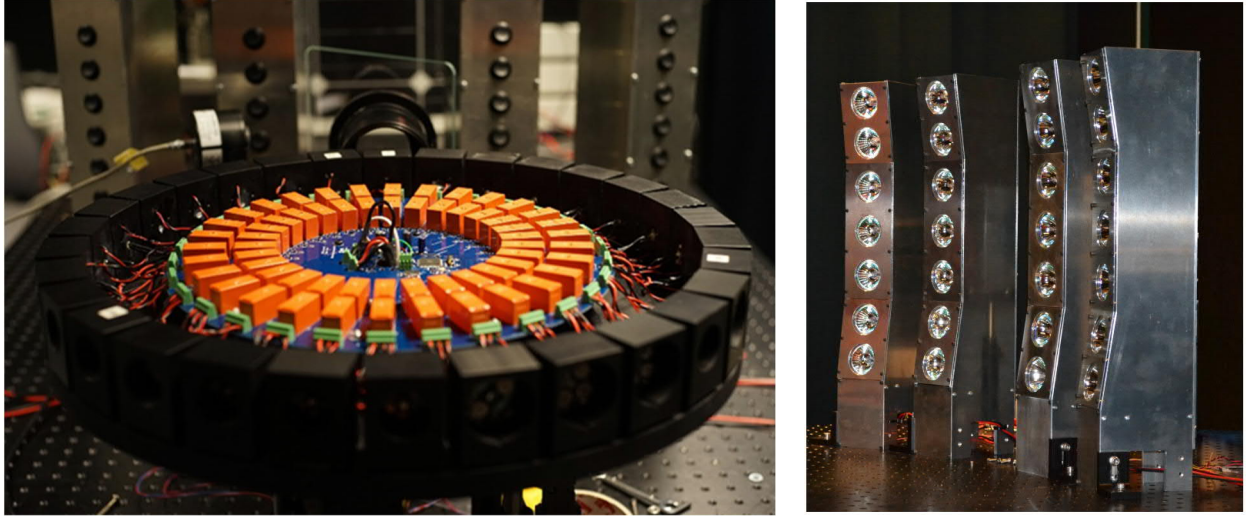


Fig. 2. Details of the setup. Left: A carousel containing LEDs. The round circuit board in the middle contains relays used for connecting the electronics to one LED at a time. Right: Four towers containing the bias lights.

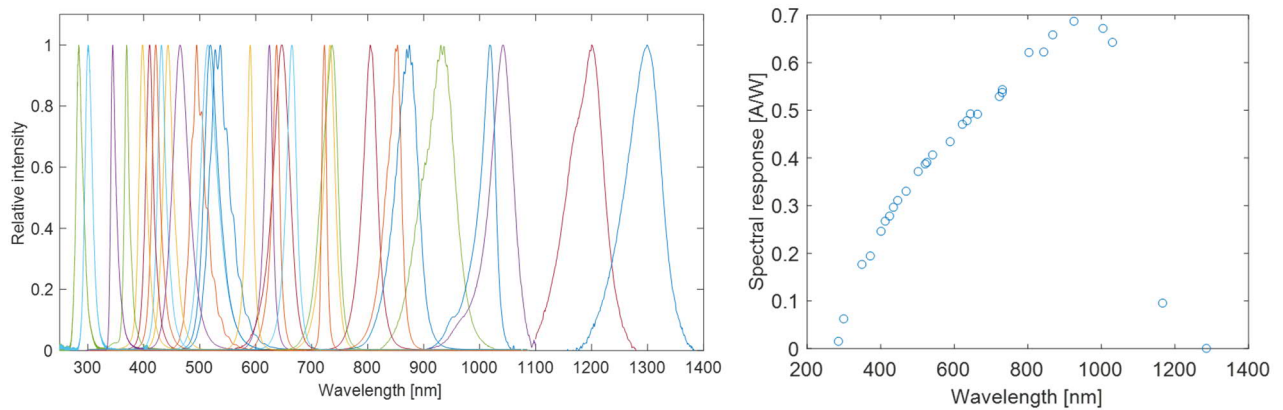


Fig. 3. Left: relative spectra of the measurement LEDs. Right: Test measurement of a solar cell.

References

1. IEC 60904-8:2014, *Photovoltaic devices - Part 8: Measurement of spectral response of a photovoltaic (PV) device* (The International Electrotechnical Commission IEC, Geneva, 2014).
2. Jürgen Metzdorf, "Calibration of solar cells 1: The differential spectral responsivity method," *Appl. Opt.* **26**, 1701-1708 (1987).
3. Ghuftron Zaid, Seung-Nam Park, Seongchong Park, and Dong-Hoon Lee, "Differential spectral responsivity measurement of photovoltaic detectors with a light-emitting-diode-based integrating sphere source," *Appl. Opt.* **49**, 6772-6783 (2010).
4. Behrang H. Hamadani, John Roller, Brian Dougherty, Fiona Persaud, and Howard W. Yoon, "Absolute spectral responsivity measurements of solar cells by a hybrid optical technique," *Appl. Opt.* **52**, 5184-5193 (2013).
5. Behrang H. Hamadani, John Roller, Andrew M. Shore, Brian Dougherty, and Howard W. Yoon, "Large-area irradiance-mode spectral response measurements of solar cells by a light-emitting, diode-based integrating sphere source," *Appl. Opt.* **53**, 3565-3573 (2014).
6. IEC 60904-3:2014, *Photovoltaic devices - Part 3: Measurement principles for terrestrial photovoltaic (PV) solar devices with reference spectral irradiance data* (The International Electrotechnical Commission IEC, Geneva, 2014).
7. Juha-Matti Hirvonen, Tuomas Poikonen, Anna Vaskuri, Petri Kärhää, and Erkki Ikonen, "Spectrally adjustable quasi-monochromatic radiance source based on LEDs and its application for measuring spectral responsivity of a luminance meter," *Meas. Sci. Technol.* **24**, 115201 (8 pp), (2013).

VTT's versatile 3 μm silicon photonics platform

Päivi Heimala, Mikko Harjanne, Ari Hokkanen, Matteo Cherchi, Tapani Vehmas,
Srivathsa Bhat, Timo Aalto

VTT, Espoo

Corresponding author: paivi.heimala@vtt.fi

Keywords: silicon photonics, optical waveguides, integrated optics, multiplexers, photodetectors

Silicon photonics (SiPh) represents a scalable path to the deployment of photonic integrated circuits (PICs) [1]. The fundamental idea is to integrate a large number of photonic functions in a small footprint on the surface of a silicon chip. SiPh applies the proven success of silicon microelectronics into photonics.

VTT's PIC platform uses 3 μm thick silicon-on-insulator (SOI) waveguides [2] as illustrated in Fig. 1 and Fig. 2. This platform, known also as “Thick-SOI” is offered by VTT as open access via multi-project wafer (MPW) runs, dedicated process runs, prototyping and small-to-medium volume production services. The main benefits of the Thick-SOI platform are low losses (0.1 dB/cm), dense integration (bending radii down to $<2 \mu\text{m}$), polarization independent operation, wide wavelength range (1.2–4 μm), ability to tolerate high optical powers ($>1 \text{ W}$) and smooth transition from R&D and prototyping to volume production. Here we show latest results of some key devices realized on our Thick-SOI platform. We also present device examples to demonstrate its suitability for sensing and datacom/telecom applications.

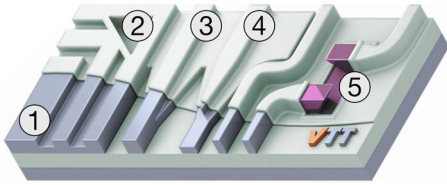


Fig. 1. Basic building blocks on Thick-SOI PIC platform: 1) SM rib waveguide, 2) horizontal mirror, 3) rib-strip converter, 4) spot-size converter, and 5) up-reflecting mirror.

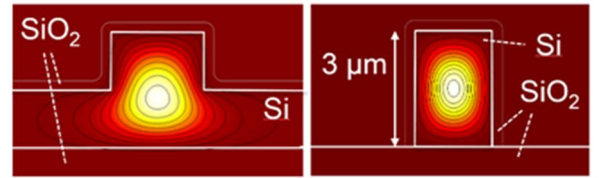


Fig. 2. Simulated intensity distributions of the fundamental mode fields in a SM rib waveguide (left) and a strip waveguide (right).

Wavelength (de)multiplexers are versatile components that are crucial for increasing link data-rates in telecommunication applications by increasing the channel counts but can also be used for optical spectrum sampling in spectroscopic sensors. The usual way to do the multiplexing is either with an arrayed waveguide grating (AWG) or with an echelle grating (EG). While AWG has the advantage in terms of easy scaling up of the channel count for low channel spacing values, EG is potentially more compact and better suited for larger channel spacing with a comparatively lower channel count. Fig. 3 A and B show a schematic of a 1 x 11 channel AWG design with 400 GHz channel spacing in the 1550 nm wavelength area (C-band), fabricated in thick-SOI. Measured transmission characteristics confirm low loss (1.2-2.0 dB) and high extinction ratio (35 dB) for the measured TE polarization. Similarly, the fabricated EG design (Fig. 3 C and D) centered around 1550 nm show extinction of over 25 dB and low losses in the 1.3-2.5 dB (TE) and 0.9-1.8 dB (TM) range.

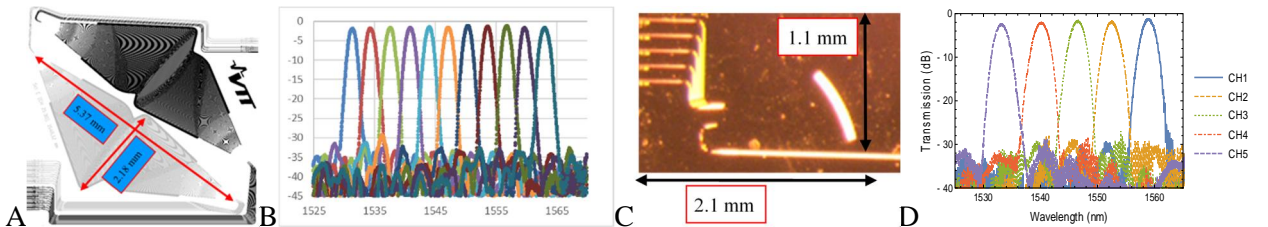


Fig. 3. Schematic of an 11-channel AWG design (A) with 400 GHz channel spacing and the measured transmission (B) showing low insertion loss and high extinction ratio in TE polarization. Microscope image (C) of the fabricated 5x1 EG with 800 GHz channel spacing and the measured transmission characteristic (D) in TE polarization.

For light input and output coupling purposes we have developed up-reflecting total internal reflection (TIR) mirrors integrated at the end of the Si waveguides (Fig. 4). The 45° degree vertical coupling mirror surface has been realized with wet etching. The mirror to fiber coupling loss has been measured to be below 0.5 dB over the entire C-band, and for both polarizations. These mirrors are ideal for integration of vertical-cavity surface

emitting lasers (VCSELs) and detectors on the SOI chips, and also for characterizing device performance with a wafer-level testing (WLT) setup.

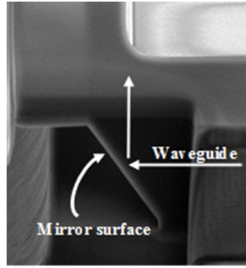


Fig. 4. SEM image of a cross-section of a 45° TIR vertical coupling mirror.

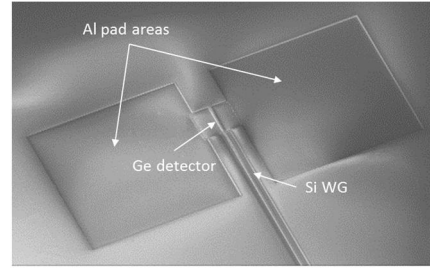


Fig. 5. SEM image of the fabricated horizontal Ge PDs integrated with 3 μm SOI waveguide

For light detection, we have also developed Ge-based, monolithically integrated PIN photodetectors (PD) on our Thick-SOI platform (Fig. 5) using the horizontal PD configuration as reported in [3]. Wafer level measurements have shown PD responsivity of about 0.9 A/W with dark current of about 1 μA , measured at -1V bias. The PDs also show excellent 3dB bandwidth response (>35 GHz).

In the EU project MIREGAS, the platform was used for creating a switchable and tunable light source in the 2.7 to 3.5 μm wavelength range, with a spectral resolution below 1 nm. The mid-IR light source consisting of an SLED (provided by TAU/ORC) flip-chipped on 3 μm SOI chip is shown in Fig. 6. The 3 μm integrated optical circuit on SOI contains arrays of optical switches and a wavelength multiplexer.

We have also realized in the Thick-SOI a LIDAR operating at 1.55 μm , the design is shown in Fig. 7. The beam can be steered horizontally by changing wavelength. The LIDAR is edge emitting and only requires a cylindrical lens to reduce vertical beam divergence.

In the EU project PASSION, the platform is used for creating a 40 channel transmitter module capable of up to 2 Tb/s transmission rates. The chip incorporates four AWG multiplexers, coupled to arrays of VCSELs via the up-reflecting mirrors. A picture of the fabricated chip is shown in Fig. 8.

We have demonstrated that the Thick-SOI platform can be used in a wide variety of applications, ranging from telecom and datacom to mid-IR gas sensing. For low-cost, low-barrier access the platform is offered as an MPW service, with full support for scaling up to volume production.



Fig. 6. Mid-IR tunable light source consisting of an SLED integrated on Thick-SOI. Chip size 5 \times 10 mm.

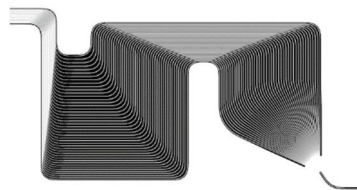


Fig. 7. Wavelength tunable LIDAR design. Component size is 1 mm \times 2mm.

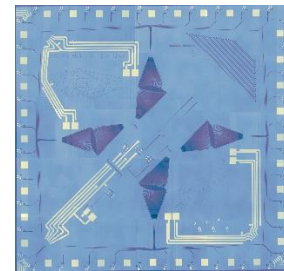


Fig. 8. 40 channel transmitter chip for 2 Tb/s. Chip size 20 \times 20 mm.

Acknowledgements

The work is part of the Academy of Finland Flagship Programme, Photonics Research and Innovation (PREIN), decision 320168.

References

1. D. Thomson et al., *Journal of Optics* **18**, 073003 (2016).
2. T. Aalto et. al., *J. Sel. Top. Quantum Electron.* (2019), DOI 10.1109/JSTQE.2019.2908551.
3. D. Feng et al., *Appl. Phys. Lett.* **95**, 261105 (2009).

Effect of nanometrically thin nickel catalyst on the properties of CVD synthesized graphitic films

M. Baah¹, T. Kaplas^{1,2} and Y. Svirko¹

¹*Institute of Photonics, University of Eastern Finland, P.O. Box 111, FI-80101, Joensuu Finland.*

²*Department of Optoelectronics, Centre for Physical Sciences and Technology, Sauletekio av. 3, LT-10257 Vilnius, Lithuania*

Corresponding author: marian.baah@uef.fi

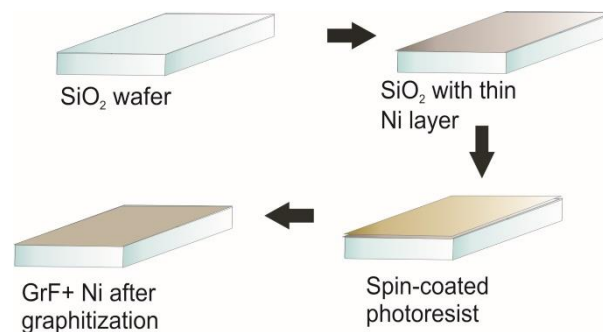
Keywords: Graphitic thin films, chemical vapor deposition (CVD), direct synthesis, nickel catalysis

Abstract – The use of graphitic thin films in optoelectronic and photonic applications is increasing due to their unique optical and electrical properties. The recently fine-tuned, metal-catalysis, CVD synthesis of these films also increases their applicability. Even though such films are being used now, not much light has been thrown on the properties of these films that makes them appealing. Here we present our findings on the spectroscopic and microscopic investigations, highlighting the effect of the nanometrically thin Ni catalyst used in the synthesis.

Introduction – Graphitic films have now made a huge impact on the opto-electronic and nanofabrication industry as they are now used in such applications [1]. One drawback of these thin films, when it comes to photonics application, is the ability to synthesize them on transparent dielectric substrates. Over the past few years scientists have come up with different techniques to overcome this backset and one of these is the use of thin films of metal catalysts such as nickel (Ni) and copper (Cu) [2,3]. The most frequently used metal catalyst is the Ni catalyst. This technique of synthesis mainly involves the receding of the metal catalyst, the pyrolysis of the carbon precursor, growth of carbon film on the air-metal interface as well as the metal substrate interface.

Results – Our work focuses on the synthesis technique that allows the use of direct growth of graphitic films on transparent dielectric substrates, by making use of nanometrically thin nickel catalysis. Using a process temperature of 800 °C, we grow graphitic thin films using the technique of CVD on transparent dielectric substrate. We now compare films synthesized with and without the Ni nanocatalyst by looking at their physical properties. Using spectroscopic measurements, we study the optical and electrical properties of these films establishing the effect of the Ni nanolayer.

Fig. 1. An illustration of the process flow for the growth of graphitic thin films on transparent dielectric substrate fused silica (SiO₂) using CVD synthesis process.



From our study, we observed that removal of the Ni nanolayer from the film does not affect the lattice structure of the film (from Raman) and increases transmittance in the VIS-IR regions of the electromagnetic spectrum [4]. Such graphitic thin films have exhibited good potential in applications such as nonlinear optics and surface-enhanced Raman spectroscopy [5, 6].

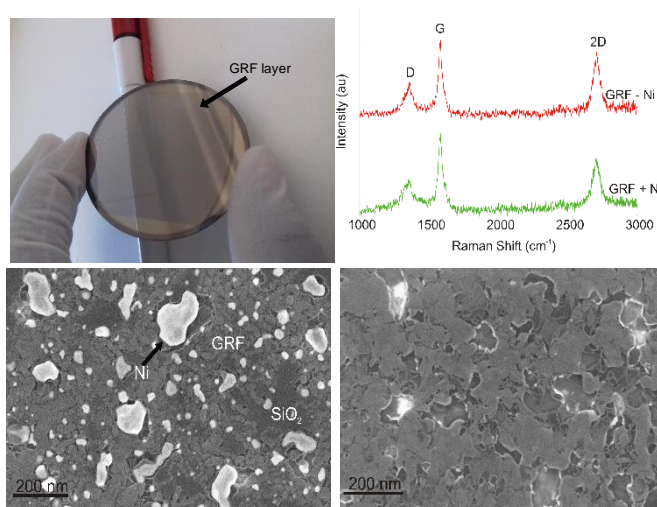


Fig. 2. Top left corner: image of synthesized graphitic film, top right corner: Raman spectra of graphitic film with Ni (GRF + Ni) and with Ni removed (GRF - Ni), by etching. Lower left corner: SEM image of GRF + Ni and lower right corner: SEM image of GRF - Ni.

Summary – To conclude we present our findings of the effect of the inclusion of a thin film of nickel metal catalyst in our CVD synthesis of graphitic films, we discuss this effect on the optical and physical properties of these thin films.

References

1. F. Bonaccorso, T.H.Z. Sun, T. Hassan, and A.C. Ferrari, *Nature Photonics*, **4**(9), 611-622 (2010).
2. R.S. Edwards and K.S. Coleman, *Accounts of Chemical Research*, **46**(1), 23-30 (2013).
3. T. Kaplas, D. Sharma, and Y. Svirko, *Carbon*, **50**(4), 1503-1509 (2012)
4. M. Baah, P. Obraztsov, A. Paddubskaya, A. Biciunas, S. Suvanto, G. Niaura, and T. Kaplas. (*To be submitted 2019*).
5. T. Kaplas, L. Karvonen, J. Rönn, M.R. Saleem, S. Kujala, S. Honkanen, and Y. Svirko *Optical Materials Express*, **2**(12), 1822-1827, (2012).
6. O. Fesenko, G. Dovbeshko, A. Dementjev, R. Karpicz, T. Kaplas, and Y. Svirko, *Nanoscale research letters*, **10**(1), 163, (2015).

Qualitative analysis for presence of Sudan IV in edible palm oil

Sampson S. Andoh^{1*}, Kenneth Nyave¹, Boniphace Kanyathare^{1,2}, Benjamin Asamoah¹, Tarmo Nuutinen^{1,3}, Cheetham Mingle⁴, Kai-E. Peiponen¹ and Matthieu Roussey¹

¹*University of Eastern Finland, Institute of Photonics, Joensuu, Finland*

²*Dar es Salaam Institute of Technology, Department of Electronics and Telecommunications Engineering, Dar es Salaam, Tanzania*

³*University of Eastern Finland, Department of Environmental and Biological Sciences, Joensuu, Finland*

⁴*Food and Drugs Authority, Food Physio-Chemical Laboratories, Accra, Ghana*

*Corresponding author: sampson.andoh@uef.fi

Keywords: palm oil, Raman spectroscopy, SERS, adulteration, authentication, PCA

Palm oil, a highly nutritious dietary oil and currently the most used edible oil in the world, is found to contain Sudan IV dye as hue enhancer. Sudan IV dye is an industrial dye that is used fraudulently in enhancing the color of palm oil due to its wide availability, low cost, and intense hue. Due to their proven carcinogenicity and mutagenicity, it is banned as food additives [1]. Yet this problem is still prevalent in developing countries, The Ghana Food and Drugs Authority (FDA) through a communique in October 2015, cautioned the public of the distribution and sale of Sudan IV dye adulterated palm oil adulterated in the open market. This was after 98 % of the samples collected from sellers in different markets in Accra region in Ghana for testing, showed positive results to Sudan dyes. The method used in identifying these adulterations are usually laboratory based and requires high level of expertise in operation and interpretation of results. We propose a method based on the principle of surface-enhanced Raman spectroscopy in authenticating and detecting Sudan IV dye adulteration of edible palm oil from Ghana. We then apply principal component analyses on classical transmission spectra to confirm the results. This method provides a quick, less expensive, ready and easy-to-use platform in its operation.

A substrate functionalized with silver nanoparticles (AgNPs) is used in this work. Its fabrication is detailed in [2]. In this method, a silicon wafer is periodically and systematically dipped in two 5 mM precursor solutions of silver nitrate (AgNO_3) (Sigma-Aldrich, 99 % purity) and sodium chloride (NaCl) (Sigma-Aldrich, 99.8 % purity), see Fig. 1. (a), to produce silver chloride particles. This is an intermediary step to prevent tarnishing of the AgNPs. The growth rate and size of the AgCl particles depends on the dipping cycles, concentrations of the precursor solutions and the duration of each dip. For this work, we used 1.5 s per dip and submersion cycle of 50. The AgCl particles produced are not SERS active they are made as such by exposing section of the AgCl to about 5 mW of laser power for about 2 min (see Fig. 1(b)), to reveal fresh AgNPs for measurements. The FDA provided the samples used in the study.

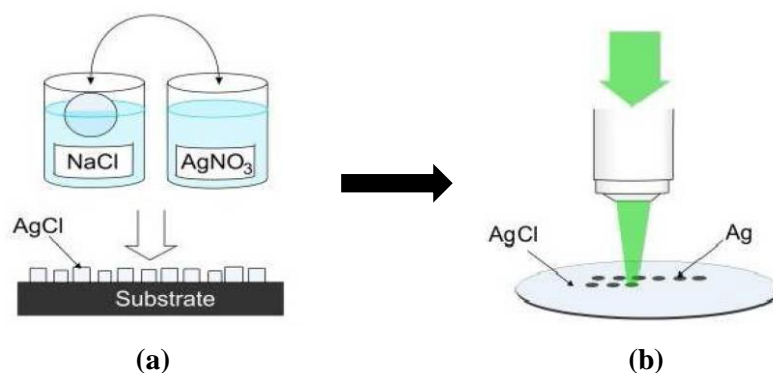


Fig. 1. Schematic flow chart of the substrate production: (a) AgCl fabrication process and (b) photo reduction process to reveal fresh AgNPs for measurement. Adopted from [2].

The SERS profile of analytical grade palm oil (STDPO), Sudan IV dye, and four of the Ghanaian samples (labelled as FDA1-4) is measured with a 514 nm laser, power of 50 μW and acquisition time of 10 s. Fig. 2 shows the spectra of Sudan dye and Ghanaian samples. The Raman spectral peak at 1389 cm^{-1} was the main identifier peak used in the authentication to predict adulteration in the Ghanaian samples. We were able to detect traces of Sudan IV dye adulteration in all the palm oil samples from Ghana as indicated by the FDA. This method provides a quick, ready-to-use, on demand, and less expensive platform in determining adulteration, saving time and money.

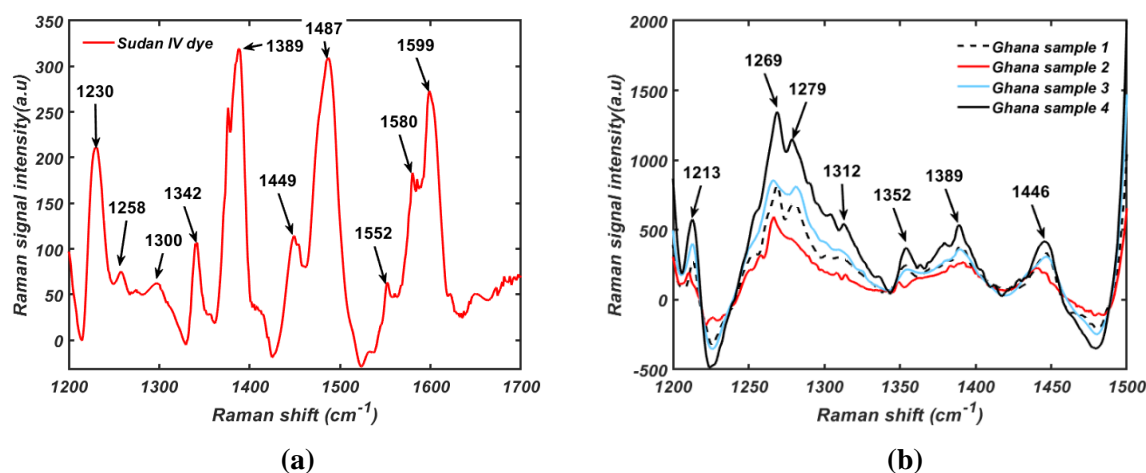


Fig. 2. SERS spectra of: (a) Analytical Sudan IV dye and (b) Ghanaian samples, taken with 514 nm laser of power 50 μ W and acquisition of 10 s.

In addition to SERS characterization of the samples, we performed spectrophotometric measurement with a Perkin-Elmer Lambda 9 UV/VIS/NIR spectrophotometer. We measured both samples collected on the open markets of several Ghanaian regions and prepared adulterated samples with different concentration of the Sudan IV dye. We compared the results using principal component analysis, which confirmed our results.

This method can be implemented on the field using handheld devices for rapid and cost efficient screening by local authorities of the market samples. Suspicious samples would however have to be analyzed carefully by robust methods in laboratory. Finally, the technique can be applied to many other food or cosmetic product to fight against counterfeiting.

References

1. R. Rebane, I. Leito, S. Yurchenko, and K. Herodes, A review of analytical techniques for determination of Sudan I–IV dyes in food matrixes, *J. Chromatogr. A* **1217**, 2747–2757, (2010).
2. A. Matikainen, T. Nuutinen, P. Vahimaa and S. Honkanen, A solution to the fabrication and tarnishing problems of surface-enhanced Raman spectroscopy (SERS) fiber probes, *Sci. Rep.* **5**, 8320, (2015).

OPTical Imager for Comets (OPIC) for ESA's F-class mission *Comet Interceptor* Optics in Engineering OIE19

Andris Slavinskis^{1,3}, Antti Näsilä², Mihkel Pajusalu³, Jaan Praks¹, Anu Reinart³, Iaroslav Iakubivskyi^{1,3},
Tomas Kohout⁴, Colin Snodgrass⁵, Geraint Jones⁶

¹ School of Electrical Engineering, Aalto University, Espoo

² VTT Technical Research Centre of Finland, Espoo

³ Tartu Observatory, University of Tartu, Tartu

⁴ Department of Geosciences and Geography, University of Helsinki, Helsinki

⁵ School of Physics and Astronomy, University of Edinburgh, Edinburgh

⁶ Mullard Space Science Laboratory, University College London, London

Corresponding author: andris.slavinskis@ut.ee

Keywords: comet, Öpik–Oort cloud, visual and near-infrared imaging, tunable Fabry–Pérot interferometer

Comet Interceptor is a recently-selected F-class mission to a dynamically-new Solar System object. Enabled by recent advances in observational surveys which will cover the sky more deeply, coherently and rapidly, the spacecraft will be parked at the Sun–Earth Lagrange Point L2 waiting for a suitable target to be discovered. It will be a multi-element spacecraft comprising a primary platform which also acts as the communications hub, and sub-spacecraft, allowing multi-point observations around the target during a flyby. The B1 sub-spacecraft is proposed by University of Tokyo and JAXA. The B2 sub-spacecraft will carry Optical Imager for Comets (OPIC) whose goal is mapping of the nucleus and its dust jets at visible and infrared wavelengths. Here we present the preliminary design and considerations. The instrument is named after an Estonian astronomer Ernst Öpik who proposed a reservoir of comets which is now called the Öpik–Oort cloud, from where the *Comet Interceptor* target would originate.

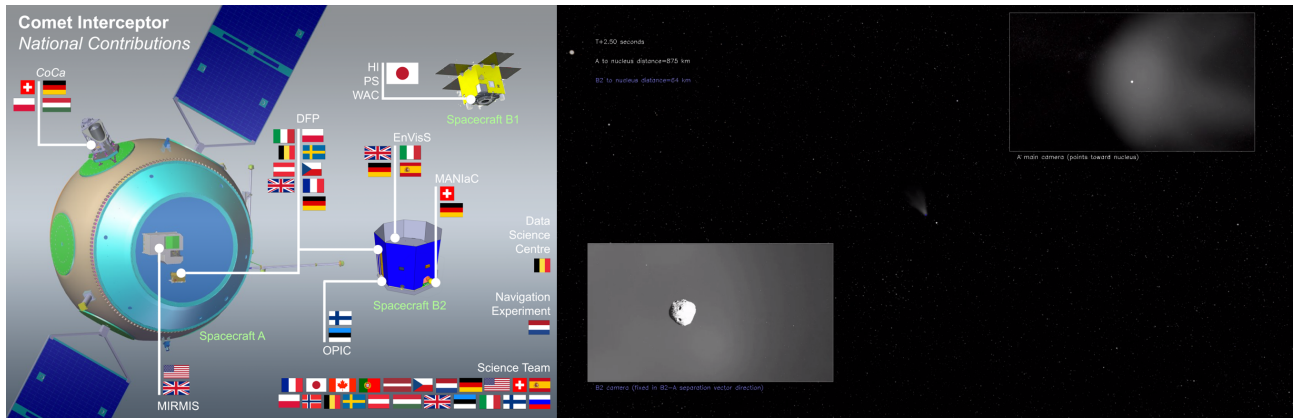


Fig. 1. Left: *Comet Interceptor* overview. Right: A simulated view from the OPIC on-board the B2 spacecraft travelling at 65 km/s with respect to the comet. Full animation: <https://vimeo.com/321107967/bca114809a>

The visible (VIS) camera will be a monochrome imager with a wavelength range of 400–800 nm, while the near-infrared (NIR) camera will be a spectral imager capable of imaging the comet at 5–20 different wavelength bands in the 1000–1600 nm region with the spectral resolution of 20 nm. The spectral imaging is realized with a tunable passband filter. The effective aperture for both cameras is in the range of 1.5–3 cm. The OPIC instrument will provide images continuously as the B2 spacecraft approaches the comet.

As it is considered too risky to point the cameras directly at the direction of travel, OPIC will be pointed to the side of the spacecraft (i.e., perpendicular to the flight direction) and a folding mirror is used to point the instrument towards the flight direction (similar to a periscope). During the closest flyby, the mirror is moved aside and, if the flyby geometry allows, the instrument will point sideways to the comet as the B2 flies past the closest approach.

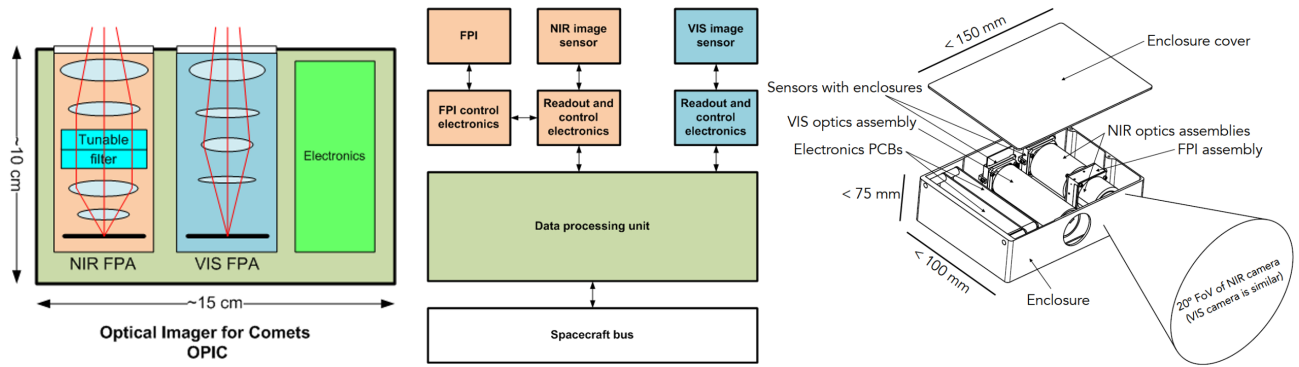


Fig. 2. OPIC concept.

The instrument also includes a Data Processing Unit (DPU) to prioritize the images for transfer to the main spacecraft during the flyby. The DPU will be capable of storing the collected raw data, which can then be transferred onwards if the spacecraft survives the flyby.

The NIR spectral imager is based on VTTs tunable Fabry–Pérot Interferometer (FPI) technology, which is combined with an InGaAs image sensor (640×512 pixels) to create the spectral imager. The NIR spectral imager concept has been successfully demonstrated in Low Earth Orbit (LEO) onboard the Reaktor Hello World CubeSat. The same design is considered as the baseline for Comet Interceptor, but the FPI technology is compatible with any image sensor, so it is possible to modify the design if necessary. The spectral imager will include an internal calibration source for wavelength calibration, so it will be possible to re-calibrate the instrument during the commissioning.

The design of the visual spectrum camera is based on a space-qualified 3D-Plus' FPA 4Mpx CMOS 3DCM73x. It features the CMV4000 sensor (2048×2048 pixels) from AMS (formerly CMOSIS). The same sensor has been used in the VTTs visual range hyperspectral camera on the Aalto-1 nanosatellite with good results. University of Tartu is also developing a high-sensitivity Earth observation imager using Gpixels GSENSE series scientific CMOS sensor. If the sensor and readout electronics will be approved within ESAs Industry Incentive Scheme, it can be considered for OPIC.

In order to maximize the science return of OPIC, a DPU is used to automatically prioritize the images for transfer during the flyby (e.g., to transfer images with the most useful signal and the least smear). This is needed because the high probability of dust impacts that could harm the instrument and the spacecraft during the approach and flyby. Image compression will also be used for the high priority data in order to maximise the link throughput. The DPU also controls imaging parameters in case all images are too dark, saturated or smeared. The DPU can be based on the space-qualified Q7 system-on-chip by Xiphos Technologies which integrates dual ARM Cortex™-A9 MPCore processor together with an FPGA. This board has been tested in space on-board Reaktor Hello World nanosatellite together with VTT's hyperspectral imager, and it is also being implemented and tested for ESA's PICASSO and APEX cubesats.

Direct 3D-printing of optical components at the University of Eastern Finland

Markku Pekkarinen, Petri Karvinen and Jyrki Saarinen

Institute of Photonics, University of Eastern Finland, P.O. Box 111, FI-80100 Joensuu, Finland

Corresponding author: markku.pekkarinen@uef.fi

Keywords: 3D-printing, additive manufacturing, optics

A need for rapid prototyping and customized small-series production of polymer optics is increasing. While the production cycle times for new products are decreasing, the component geometries and functions are getting more and more complex. Additive manufacturing (AM), or 3D printing, offers one way to speed up product development and decrease costs.

Using AM process, an object is created in a layer-by-layer manner. Most commonly known methods to create 3D printed optics are two-photon lithography [1,2] and micro-stereolithography [3], which are offering promising results for small objects in micro- and millimeter-scale. At the University of Eastern Finland we are utilizing Printoptical Technology [4], proprietary of Luxexcel. This is an inkjet-based method for fabrication of centimeter-scale components with smooth surfaces. The process yields consistently prints with surface roughness in single nanometer scale without any post-processing, which is enough to directly print optical quality components.

In our recent work [5] we have applied 3D printing to realize freeform optics for industrial based tailored illumination, where the goal was to design and fabricate a freeform lens array for light-emitting diodes (LEDs). We demonstrated an iterative fabrication scheme [6], which improves shape accuracy of the 3D printed optics even up to imaging quality. Utilizing this scheme, we demonstrate an imaging lens with centimeter-scale diameter featuring optical performance comparable to that of a commercial glass lens. In this presentation we will discuss the features, limitations and most notably potential and realized applications of the 3D printed optics.

Future research will concentrate on multi-material printing for support materials and materials which are offering, e.g., different refractive indices. Support materials, which can be dissolved after the printing process, would allow, e.g., printing of hollow structures. Printing two materials with different refractive indices would give possibility to research gradient-index (GRIN) optics. These developments will allow 3D printing of optical components that cannot be manufactured with traditional subtractive methods.

References

1. S. Thiele, K. Arzenbacher, T. Gissibl, H. Giessen, and A. M. Herkommer, “3d-printed eagle eye: compound micro-lenssystem for foveated imaging,” *Sci. Adv.* 3, e1602655 (2017).
2. C. Liberale, G. Cojoc, P. Candeloro, G. Das, F. Gentile, F. D. Angelis, and E. D. Fabrizio, “Micro-optics fabrication on top of optical fibers using two-photon lithography,” *IEEE Photon. Technol. Lett.* 22, 474–476 (2010).
3. X. Chen, W. Liu, B. Dong, J. Lee, H. O. T. Ware, H. F. Zhang, and C. Sun, “High-speed 3d printing of millimeter-size customized aspheric imaging lenses with sub 7 nm surface roughness,” *Adv. Mater.* 30, 1705683 (2018).
4. K. Blessing and R. van de Vrie, “Print head, upgrade kit for a conventional inkjet printer, printer and method for printing optical structures,” U.S. Pat. Appl. No.13/924 (March 14, 2012).
5. B. G. Assefa, T. Saastamoinen, M. Pekkarinen, J. Biskop, V. Nissinen, M. Kuittinen, J. Turunen, and J. Saarinen, “Realizing freeform optics using 3D-printer for industrial based tailored irradiance distribution,” *OSA Continuum* 2, 690–702 (2019).
6. B. G. Assefa, M. Pekkarinen, H. Partanen, J. Biskop, J. Turunen, and J. Saarinen, “Imaging-quality 3D-printed centimeter-scale lens,” *Optics Express* 27, 12630–12637 (2019).

Super-resolution imaging by scanning subdiffraction-limit optical pattern

Yusuke Ogura¹, Daiki Shinkawa¹, Takahiro Nishimura², Yosuke Tamada³, and Jun Tanida¹

¹ Graduate School of Information Science and Technology, Osaka University, Suita

² Graduate School of Engineering, Osaka University, Suita

³ Division of Evolutionary Biology, National Institute for Basic Biology, Okazaki

Corresponding author: ogura@ist.osaka-u.ac.jp

Keywords: super-resolution, subdiffraction limit, imaging, computer generated hologram,

Fluorescence microscopy is a promising tool to visualize the structure and/or dynamics of biological samples including cells and micro-organelles by labeling specific biomolecules with fluorophores. However, the resolution of the image obtained by wide-field illumination is restricted based on the diffraction limit, and many types of super-resolution techniques have been proposed[1]. Laser scanning microscopy (LSM) is an option for fluorescence imaging which is based on scan of a focused laser spot for excitation and reconstruction from a set of point-detected fluorescence signals. Although this microscopy can provide high contrast images thanks to limited-volume excitation, the resolution and speed are still restricted owing to single diffraction-limit-spot scanning. This paper presents a method of super-resolution imaging where a subdiffraction-limit optical pattern is used as illumination. Subdiffraction-limit optical patterns are generated flexibly using computer generated holograms (CGHs), and our method is expected to improve the performance of the LSM. In this study, we investigated capability of the method in bio-imaging.

In LSM, the point spread function (PSF) of a reconstructed image is expressed as the multiplication of the function of the illumination-intensity distribution and the PSF of the imaging optics. This equation indicates that use of a smaller focused spot is effective to improve the resolution. Thus a subdiffraction-limit optical pattern that is finer than the diffraction-limit spot is employed. We have already demonstrated that well-designed CGHs can generate an array of subdiffraction-limit spots[2]. It is also possible to generate subdiffraction-limit spots with multiple wavelengths on multiple planes[3]. Note that the subdiffraction-limit optical patterns are provided by propagating light, and therefore they are straightforwardly utilized as illumination in microscopy.

In our super-resolution method, a subdiffraction-limit optical pattern is generated and scanned on the sample plane. During scanning, a sequence of fluorescence images is captured; then a high-resolution image is reconstructed through digital processing. When multiple spots are utilized as illumination, the individual spots can cover different field of views (FOVs), and thus time for image acquisition can be shortened.

Figure 1 shows the experimental setup. A light wave from a laser source (wavelength: 488 nm) hits a spatial light modulator (SLM; HOLOEYE Photonics AG, LC2012) that works as a CGH, then a subdiffraction-limit

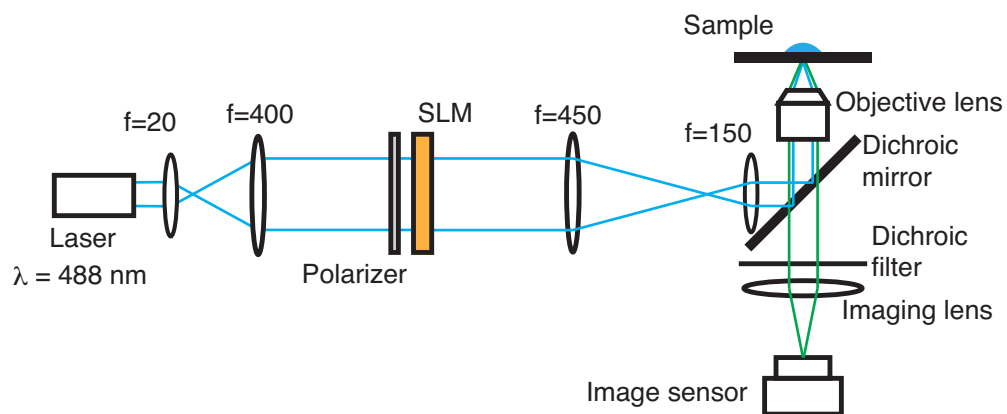


Figure 1: Experimental setup.

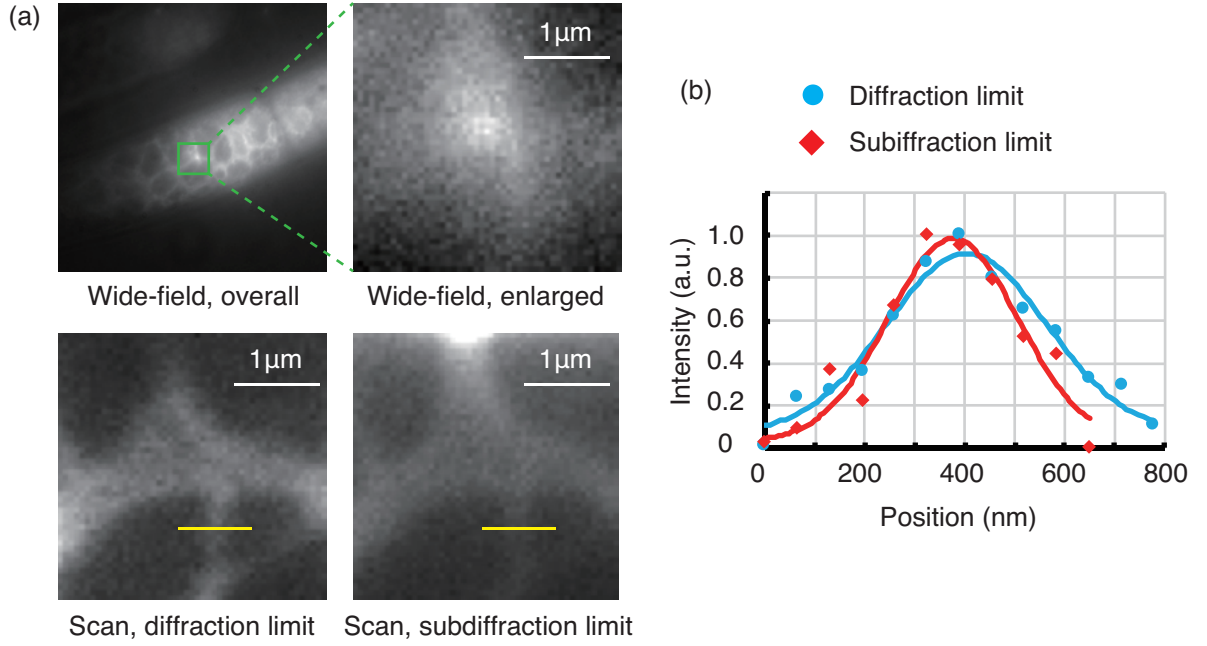


Figure 2: (a) Images of GFP-labeled tubulin. (b) Intensity profiles along yellow lines shown in (a).

optical pattern is generated on the sample plane through optics including an objective lens (100 \times , oil immersion, numerical aperture (NA): 1.40). The fluorescence images are captured by an image sensor (Hamamatsu Photonics K.K., C14440-20UP).

To investigate the ability for resolution improvement in bio-imaging, we observed green fluorescence protein (GFP)-labeled tubulin, which is a configuration factor of cytoskeleton. We designed a CGH that generated an array of 3×3 subdiffraction-limit spots, using the Gerchberg-Saxton algorithm with our own constraints[2]. The spot size, defined as the full width at half maximum, of the center spot was reduced from 257 nm (diffraction limit) to 187 nm (subdiffraction limit). In the image reconstruction, the center spot alone among 3×3 spots was used because the size of the center spot was reduced most effectively. Figure 2 shows an imaging result, where the scan pitch is 65 nm and the number of scan steps is 49×49 . Although a detailed structure is not observed by wide-field imaging, some tube-like structures are observable when scanning with a diffraction-limit spot and with the central subdiffraction-limit spot. A comparison of the intensity profiles (Fig. 2(b)) indicates that the width of the structure is reduced from 342 nm to 294 nm. The result demonstrates that the use of a subdiffraction-limit optical pattern is effective to improve the resolution in LSM. We performed an additional experiment where 5×5 subdiffraction-limit spots among 7×7 spots were used for illumination, to shorten the time for capturing images. Different FOVs were assigned to the individual spots in the reconstruction, and a final large FOV image was synthesized by connecting the reconstructed images. The result confirmed that a large-FOV super-resolution image was obtained by the method.

In this study, super-resolution imaging by laser scanning microscopy with a subdiffraction-limit optical pattern is presented. The experimental results indicate the capability for resolution improvement. We will further investigate the performance to characterize the method in bio-imaging.

This research was supported by the grant of Joint Research by the National Institutes of Natural Sciences (NINS program No. 01111702).

References

1. L. Schermelleh, R. Heintzmann, H. Leonhardt, *J. Cell Biol.* **190**, 165–175 (2010).
2. Y. Ogura, M. Aino, and J. Tanida, *Opt. Express* **22**, 25196–25207 (2014).
3. Y. Ogura, M. Aino, and J. Tanida, *Appl. Opt.* **55**, 6371–6380 (2016).

The beneficial effects of the sauna exposures measured by PPG

Matti Huotari¹, Kari Määttä² and Juha Rönning¹

¹ Biomimetics and Intelligent Systems Group (BISG), University of Oulu, Finland

² Circuits and Systems (CAS), University of Oulu, Finland

Corresponding author: matti.huotari@oulu.fi

Keywords: Photoplethysmography, pulse waveform, decomposition, sauna exposure, arterial elasticity

This study concerns sauna and environment heat exposures regarding bathing methods for health enhancement, e.g., sauna bathing is very popular in Finland, and hot water bath is popular in Japan. A systematic review has shown that a regular hot exposure has the potential to provide beneficial health effects on healthy people, but also for those with cardiovascular-related and many other diseases, such as rheumatological diseases, and also very good for sport people [1].

Photoplethysmographic (PPG) signals measurement system consists of ir (infra red) and red LEDs which illuminate the responses recorded by the photodiodes in the PPG probes. In PPG technology, the main difficulty is its quantitative analysis, calibration can be challenging, and comparison of PPG wave easily obtained from different body locations, several persons, and with their skin color. In our measurements the light intensities and wavelengths (red 640 nm & infrared 920 nm) are fixed. In practice, the results are the arterial pulse PPG waveforms which are based on the propagating pulse wave during each heart cycle the pulse coming from the heart's left ventricle. The pulse waveforms travel through the arterial circulatory system and arrive the peripheral, parallel capillary arteries to the finger and toe tips under the nails to be measured optically. The elasticity index was calculated as the relation of the peak time of primary percussion wave to the peak time sum of the four other primary waves [2].

Young female and male volunteers with good heart health status were included from the University departments in the dry sauna test group of 14 subjects. Finnish saunas involve short exposures (20-30 minutes) at temperature of 80°C with dry air. Before the sauna and the recovery from the sauna exposure were measured with the subjects in the supine position. The study was approved by the ethical review board of the Oulu University.

The primary wave components can be used for, e.g., elasticity calculations. However, full optical understanding of PPG waveforms and their physiology are still lacking. After investigation the intrinsic connection between infrared and red PPGs from finger and toe tips, and derived an elasticity index to describe the relationship between biophysical parameters, needs fewer assumptions than other methods. PPG recording before (left) (300 s), in sauna (middle) (1200 s), and after (right) (1300 s) sauna exposure is shown and 5 sec insert.

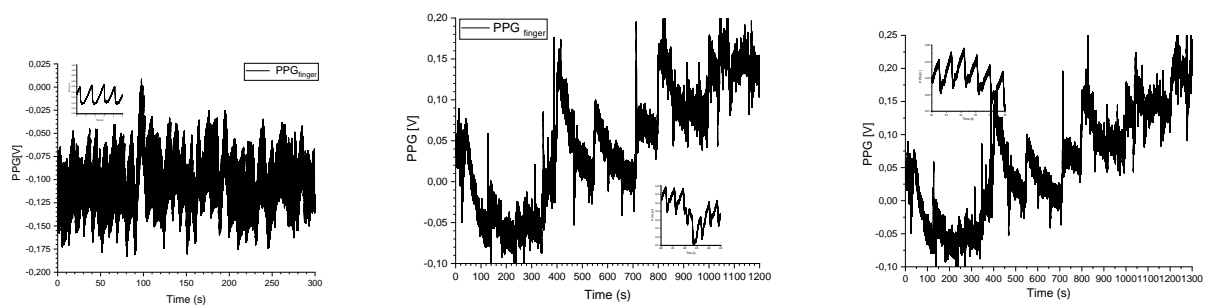


Fig1. PPG recordings from a 32 y male subject before (left), in sauna (middle), and after sauna (right)

PPG measurement gives bid data without proper analysis procedures, like decomposition of pulse waveforms. However, further PPG research from sauna settings relating to the physiological mechanisms of sauna exposure that promote both arterial and cardiac health is needed.

References

1. Kamioka H, et al. (2019) Relationship of daily hot water bathing at home and hot water spa bathing with underlying diseases in middle-aged and elderly ambulatory patients: A Japanese multicenter cross-sectional study, *Complementary Therapies in Medicine*, Volume 43, Pages 232-239.
2. Peltokangas, M, et al. (2017). Combining finger and toe photoplethysmograms for the detection of atherosclerosis, *Physiological Measurement*, 38, (2).

Creation and observation of a longitudinally-polarized optical needle

Léo Turquet¹, Xiaorun Zang¹, Joonas-Pekko Kakko², Harri Lipsanen², Godofredo Bautista¹, and Martti Kauranen¹

¹ Photonics Laboratory, Physics Unit, Tampere University, P. O. Box 692, FI-33014 Tampere, Finland

² Department of Electronics and Nanoengineering, Aalto University, P. O. Box 13500, FI-00076 Aalto, Finland

Corresponding author: leo.turquet@tuni.fi; godofredo.bautista@tuni.fi

Keywords: nonlinear microscopy, nanostructures, optical needle, longitudinal electric field

The term longitudinally-polarized optical needle is used to represent longitudinal electric fields that show spot-like intensity distribution in the transverse (xy) plane with sub-wavelength confinement over a distance of several λ along the longitudinal axis (z), where λ is the excitation wavelength. Such optical fields are expected to be valuable in providing alternative illumination conditions in optical microscopes, for multi-plane imaging or micromanipulation of nanoparticles. Various methods, based on radially-polarized (RP) beams, have theoretically predicted the generation of optical needles [1]. To date, however, experimental verifications of the generation a longitudinally-polarized optical needle in three dimensions have been scarce and incomplete.

In this work, we experimentally demonstrate the creation and observation of a longitudinally-polarized optical needle that is produced by a radially-polarized Bessel-Gauss beam (RPG) generated at the focus of a microscope objective [2]. This choice was motivated by the well-known large depth of field of vector BG beams [3], and the longitudinal fields that arise from tight focusing of RP beams [4]. The RPG beam was created by focusing a RP thin ring through a high numerical aperture (NA) objective. The ring itself was generated by a RP doughnut beam and an axicon.

We managed to probe the longitudinally-polarized optical needle in three-dimensions using spatial mapping of the second-harmonic generation (SHG) from a single vertically-aligned GaAs nanowire, which were shown to be sensitive to longitudinal fields excitation only [5–7].

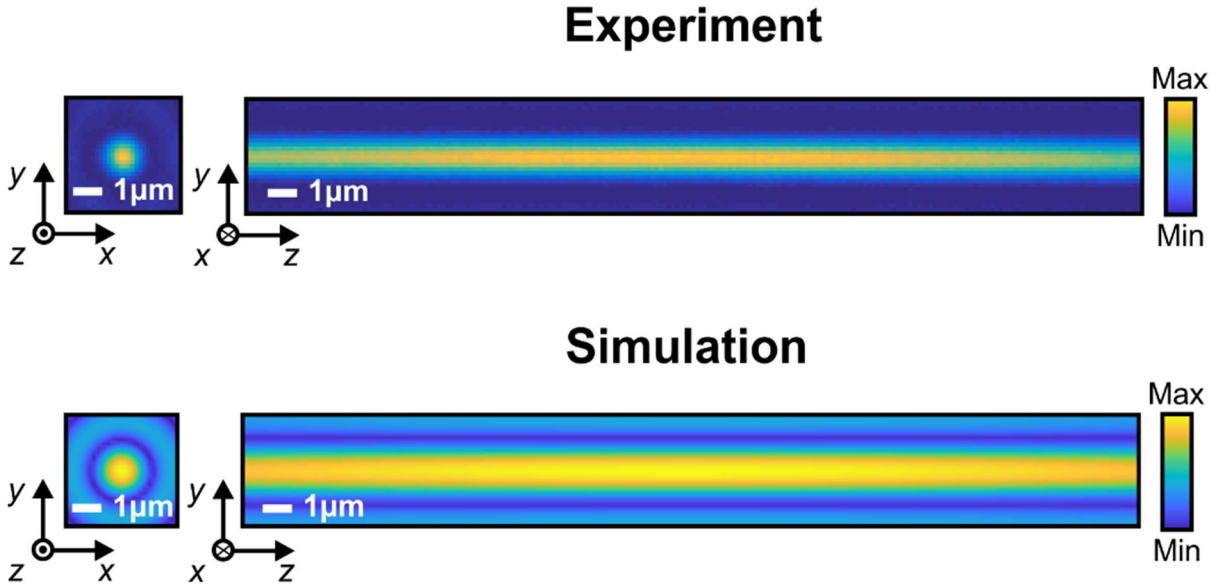


Fig. 1. Comparison of experimental focal intensity distribution (top) and theoretical focal electric field distribution (bottom) of the optical needle, under identical focusing conditions, in the xy - and yz -planes.

In conclusion, we have experimentally generated and probed a longitudinally-polarized optical needle in the focal region of a high NA objective. It was formed by a RPG beam and characterized using SHG from vertically-aligned nanowires, sensitive to longitudinal electric fields. Our optical needle shows a depth of field of over 30λ and subwavelength transverse confinement (0.41λ). It also shows great spatial homogeneity and almost perfect agreement with numerical simulations. This demonstration confirms the new opportunities opened by optical needles for microscopy, light shaping and optical micromanipulation.

References

1. H. Wang, L. Shi, B. Lukyanchuk, C. Sheppard, and C. T. Chong, *Nat. Photonics* **2**, 501–505 (2008).
2. L. Turquet, X. Zang, J.-P. Kakko, H. Lipsanen, G. Bautista, and M. Kauranen, *Opt. Express* **26**, 27572–27584 (2018).
3. Z. Bouchal and M. Olivík, *J. Mod. Opt.* **42**, 1555–1566 (1995).
4. B. Richards and E. Wolf, *Proc. R. Soc. London Ser. A* **253**, 358–379 (1959).
5. G. Bautista, J. Mäkitalo, Y. Chen, V. Dhaka, M. Grasso, L. Karvonen, H. Jiang, M. J. Huttunen, T. Huhtio, H. Lipsanen, and M. Kauranen, *Nano Lett.* **15**, 1564–1569 (2015).
6. L. Turquet, J.-P. Kakko, X. Zang, L. Naskali, L. Karvonen, H. Jiang, T. Huhtio, E. Kauppinen, H. Lipsanen, M. Kauranen, and G. Bautista, *Laser Photon. Rev.* **11**, 1600175 (2017).
7. L. Turquet, J.-P. Kakko, L. Karvonen, H. Jiang, E. Kauppinen, H. Lipsanen, M. Kauranen, and G. Bautista, *J. Opt.* **19**, 084011 (2017).

Opto-fluidic biosensors by roll-to-roll fabrication

Jussi Hiltunen, Sanna Uusitalo, Sanna Aikio, Marianne Hiltunen, Olli-Heikki Huttunen, Johanna Hiitola-Keinänen, Christina Liedert and Pentti Karioja

VTT-Technical Research Centre of Finland, Kaitoväylä 1, 90570 Oulu, Finland

Corresponding author: Jussi.hiltunen@vtt.fi

Keywords: biosensors, microfluidics, SERS, nanoimprinting

Opto-fluidics is defined as a synergistic integration of photonics and microfluidics [1]. The research and development is driven by the potential for enhanced sensing performance and simplification of microsystems. However, only few concepts have been transferred successfully into upscaled fabrication of integrated microsystems because of the lack of processing and integration methods. The question is not only about direct commercialization of designs and concepts, but also academic researchers benefit from the high-volume sensor fabrication when the number of samples is not limiting the assessment of the designs and associated test protocols. Our work deals with the production upscale to manufacture optical sensor elements and microfluidic sample handling platforms at high volumes.

Nano-scaled structures have been widely studied with several application areas as they exhibit interesting physical and chemical properties which differ from the properties of the bulk material made of the same composition. The development of different planar plasmonic substrates tries to reduce the repeatability issues of the colloids through periodicity of the nanostructures on top of the substrates. Fig. 1a) shows roll-to-roll (R2R) imprinted periodic nanostructures. After coating the surface with a thin layer of gold, they are suitable for surface-enhanced-Raman-spectroscopy (SERS) applications. Scanning-electron-microscope from the surface is shown in Fig. 1b). We demonstrated the feasibility of such polymer-based low-cost SERS substrate in analyzing the microbes with characteristic Raman spectrum [2]. Microfluidic channels enable flowing sample solution on chip in a controlled way and the sample molecules can be also accumulated onto the sensor surface by analyte capture. Fig. 1c) presents an opto-fluidic sensor configuration where optical sensor surface is integrated with polymeric microfluidic and lid layers.

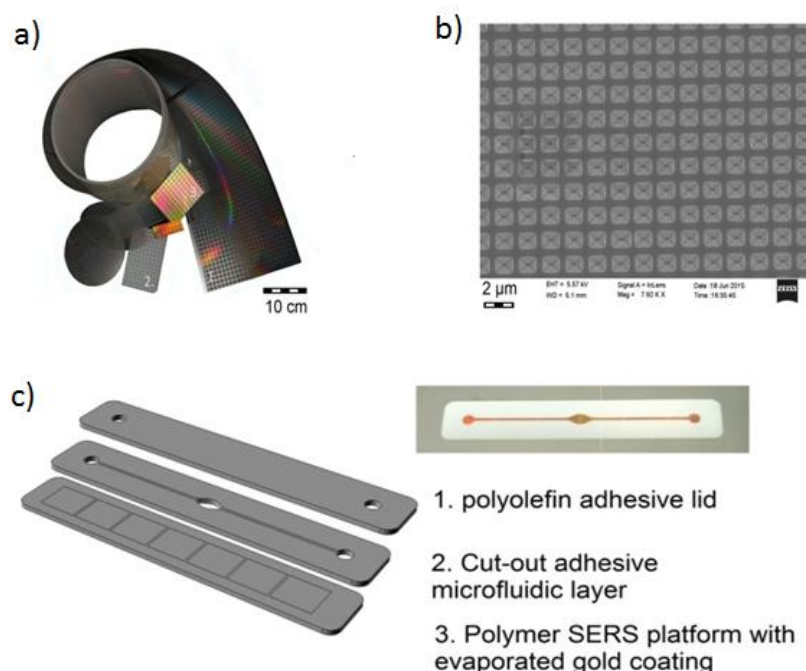


Fig.1. a) Roll-to-roll nanoimprinted optical surface on plastics, b) SEM-image from the surface, c) opto-fluidic sensor configuration with integrated microfluidics and a sensors surface.

Elastomer poly(dimethylsiloxane) (PDMS) has become, and remained, one of the most used material in realization of microfluidic devices in academic environment. The wide usage of PDMS material is originated from number of factors with most importantly the relatively cheap and easy prototyping of small numbers of devices

using master moulds for structure replication. PDMS surface properties can be also tuned and to bond PDMS with glass and PDMS itself. These factors have enabled made the realization of prototype devices that test new ideas in a shorter time and with lower cost than that which is reachable using silicon technology. Probably the biggest factor in limiting the usage PDMS outside laboratory relates to the lack of high-volume fabrication methods to produce microfluidics. In our recent work [3], it was demonstrated that also PDMS-based microfluidics can be roll-to-roll produced. Fig. 2a) shows a photograph from the R2R replication process, where PDMS material is casted on Al-coated paper and microfluidic features are replicated by thermal curing. A test device cut from a roll is shown in Fig. 2b). For the illustrative purposes, the fluidic channels were filled with colored water. In order to validate the replicated molecular diagnostic platforms, on-chip amplification of viral ribonucleic acid (RNA) with loop-mediated isothermal amplification (LAMP) was demonstrated. Amplification of negative control (no RNA) and positive control (RNA) were monitored optically in real-time by taking fluorescence images with interval of 1 min. Test arrangement with positive and negative samples is shown in Fig. 2c) and corresponding fluorescence signal as a function of time in Fig. 2d). LAMP amplification was triggered by increasing the chip temperature from room temperature (RT) to 70° C within a time period of about 3 mins. The onset of amplification occurred at a time period of about 13 – 16 min.

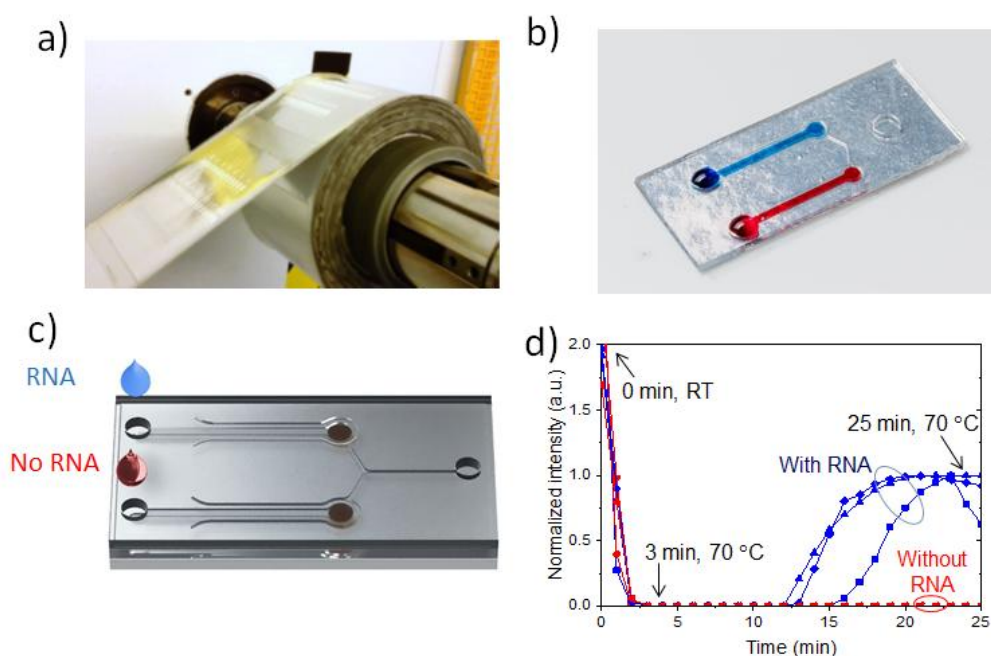


Fig.2. a) Roll-to-roll fabrication of PDMS-microfluidics on paper, b) sensor device where fluidic channels are filled with colored water, c) test configuration for nucleic acid amplification and d) fluorescence signal from reaction chambers with and without RNA template molecules.

References

1. X. Fan and I. M. White, *Nature Photonics*, **5**, 591–597 (2011)
2. S. Uusitalo, M. Kögler, A.-L. Välimaa, A. Popov, Y. Ryabchikov, V. Kontturi, S. Siitonen, J. Petäjä, T. Virtanen, R. Laitinen, M. Kinnunen, I. Meglinski, A. Kabashin, A. Bunker, T. Viitala, J. Hiltunen, *RSC Advances*, **6**, 62981 - 62989 (2016)
3. J. Hiltunen, C. Liedert, M. Hiltunen, O.-H. Huttunen, J. Hiitola-Keinänen, S. Aikio, M. Harjanne, M. Kurkinen, L. Hakalahti, L. P. Lee, *Lab on a Chip* **18**, 1552-1559 (2018)

Quantitative CARS spectral imaging in studying protein droplets

Yelena Kan^{1,2}, Sapun Parekh^{2,3}, Erik M. Vartiainen¹ and Lasse Lensu¹

¹ LUT School of Engineering Science, LUT University, Lappeenranta

² Dept. Bonn: Molecular Spectroscopy, Max Planck Institute for Polymer Research, Mainz

³ Dept. of Biomedical Engineering, Univ. of Texas at Austin, Austin

Corresponding author: erik.vartiainen@lut.fi

Keywords: coherent anti-Stokes Raman scattering (CARS), microspectroscopy, hyperspectral imaging, intrinsically disordered proteins, protein droplets

Protein-protein interactions underlie nearly all biological functions. Many proteins that mediate DNA transcription in so-called RNA granules appear to have unique characteristics that lead to protein aggregation under certain conditions. Many of these proteins are ‘intrinsically disordered’ and undergo a liquid-liquid phase separation (forming droplets) within cells [1] and *in vitro* [2]. The presence of plaques containing these proteins is linked with many neurodegenerative disorders, including Parkinson’s, Alzheimer’s and Huntington’s disease [3]. The physical-chemical structure of the protein droplets is a subject of much debate as they are speculated to be precursors to proteinaceous plaques and possibly amyloid fibrils. To that end, we applied the broadband coherent anti-Stokes Raman scattering (CARS) spectral imaging to study protein droplets for obtaining quantitative and chemically specific information. The protein structure was examined in different states of the RNA-binding protein fused in sarcoma low complexity domain (FUS LC) *in vitro*.

For CARS measurements, the samples were "sandwiched" between two glass slides and secured on the translation stage in a broadband CARS/bright-field microscope. The broadband CARS microscope (Fig. 1) included a pump laser (Spectra Physics Tsunami, 800 nm, 1 ps, 80 MHz), a photonic crystal fiber (PCF), a microscope with a cooled microscope stage, a monochromator and a cooled CCD camera. Light from the laser was split into two paths, one for generating a broadband (~ 3430 cm⁻¹) Stokes pulse, and the other to provide narrowband pump/probe pulses. Pulses were focused through the sample to produce a broadband (~ 500 – 3500 cm⁻¹) CARS signal. Typically, a 30x30-pixel area was scanned with a focused laser beam and from each pixel, a CARS spectrum was recorded. For each pixel, a typical integration time of the measurement was from 30 to 60 ms.

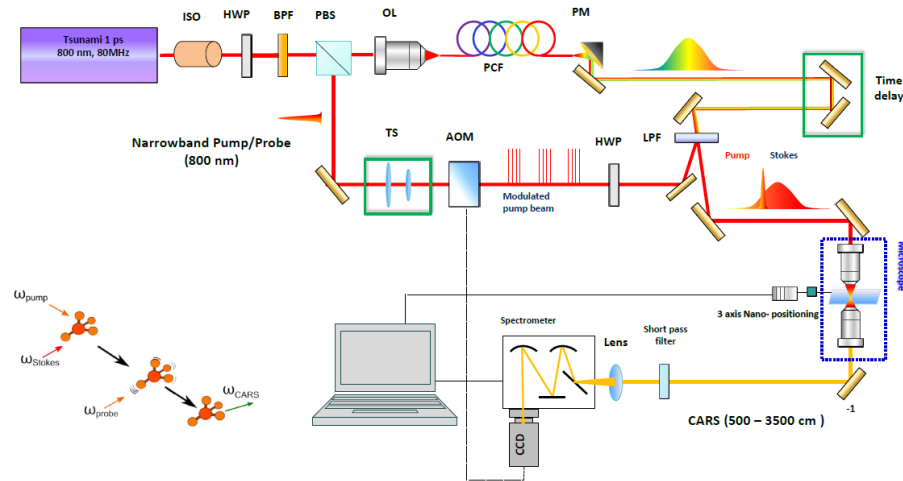


Fig. 1. Broadband CARS setup.

The raw CARS spectra as such do not provide useful quantitative information. Such information is obtained by retrieving the Raman spectra from CARS data [4]. Typically, this includes wavelet analysis to remove the (non-additive) experimental artifacts from CARS spectra [5], and then the MEM analysis to automatically extract the Raman line-shape spectra from the CARS line-shapes [4]. The CARS line-shapes, where the experimental artifacts are removed, are also used to make integrated microscopic images as shown in Fig. 2(a). The Raman line-shapes (Fig. 2(c)) provide the basis for the protein analysis, i.e., chemical mapping inside a protein droplet and to recognize the possible changes in protein structure within phase transitions from a monomeric solution to liquid droplets and from liquid droplets to solid aggregates. Moreover, statistical

multivariate methods, such as the Multivariate Curve Resolution–Alternating Least Squares (MCR-ALS) [6], implemented to the extracted Raman data, enables the separation of spectral and spatial distributions of chemical constituents of a sample (Fig. 3).

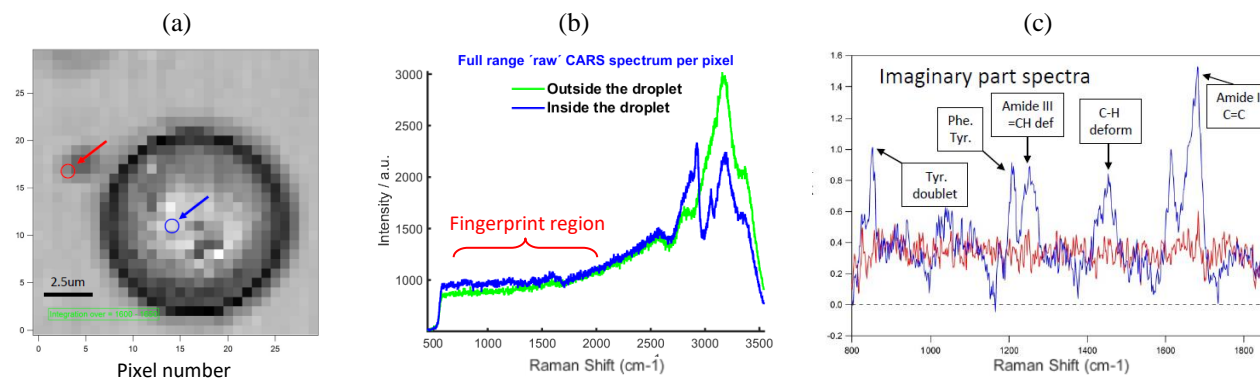


Fig. 2. Broadband CARS imaging of a protein droplet: (a) hyperspectral (integrated) CARS image, (b) broadband CARS spectra, (c) the retrieved Raman line-shapes at fingerprint region, inside (blue lines) and outside the protein droplet.

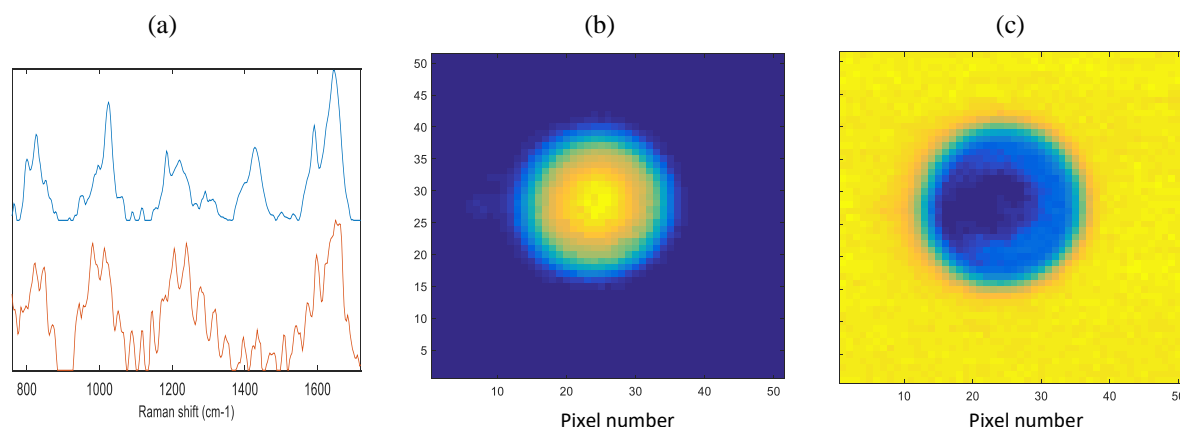


Fig 3. Statistical multivariate analysis (MCR-ALS) on extracted Raman spectra: Pure component spectral profiles (blue line: comp. 1) and corresponding distribution maps of liquid-liquid phase separated FUS LC.

References

1. A. A. Hyman, C. A. Weber, and F. Jülicher, *Annual Rev. Cell Dev. Biol.* **30**, 39-58 (2014).
2. K. A. Burke, A. M. Janke, C. L. Rhine, and N. L. Fawzi, *Mol. Cell* **60**, 231-241 (2015).
3. E. H. Koo, P. T. Lansbury and J. W. Kelly, *Proc. Natl. Acad. Sci.* **96**, 9989-9990 (1999).
4. E. M. Vartiainen, H. A. Rinia, M. Bonn, and M. Müller, *Optics Express* **14**, 3622–3630.
5. Y. Kan, L. Lensu, G. Hehl, A. Volkmer, E. M. Vartiainen, *Optics Express* **24**, 11905–11916 (2016).
6. J. Felten, H. Hall, J. Jaumot, R. Tauler, de Juan A, and A. Gorzsás, *Nature Protocols* **10**, 217–240 (2015).

Synthetic aperture phase-shifting measurement for high numerical-aperture spherical surfaces

Kenichi Hibino¹, Toshiki Kumagai² and Yasunari Nagaïke²

¹ Geological Survey of Japan, AIST, Tsukuba, Ibaraki 305-8567, Japan

² Olympus Corporation, Tatsuno, Kamiina, Nagano 399-0495, Japan

Corresponding author: k.hibino@aist.go.jp

Keywords: phase measurement, interferometry, Fizeau interferometer, phase shift, spherical test

High numerical-aperture (NA) spherical lens are now common and required for wide-angle view and high-magnification in optical products such as endoscopes, microscopes, and compact camera. The measurement repeatability of the spherical lens testing has reached a ~ 0.1 nm by a phase-shifting Fizeau interferometer, which improves the quality control of the optical products.

In a high NA lens testing, however, spatial nonuniformity of the phase modulation becomes critical in the Fizeau interferometers with mechanical phase shifting. Fig. 1 illustrates the illuminating geometry of a spherical (convex) testing through the transmission reference sphere with a monochromatic light of $\lambda = 633$ nm wavelength, as an example. When the reference sphere is translated along the optical axis by distance δ , the phase φ of the interference fringes is shifted by $4\pi\delta/\lambda$ radians on the optical axis. In contrast, the amount of phase shift in the marginal region of the aperture decreases by $4\pi\delta\cos\theta/\lambda$ where the cosine factor is a geometrical effect. This nonuniformity can couple with the multiple-reflection light between the reference and test surfaces and result in the phase measurement errors. There have been designed many error-compensating phase-shifting algorithms that can compensate for these phase increment errors. However, it is pointed out [1] that these algorithms no longer show enough reduction of the errors when the NA becomes larger than 0.7, or nonuniformity exceeds -30% ($\sin\theta = NA > 0.7$). In industry, we like to test spherical lens whose numerical aperture is up to 0.9, in which the nonuniformity is typically -50%.

We have proposed a synthesis of phase-shifting algorithms in which the observing aperture is divided into seven annular regions and the object phase for each region is estimated by a different algorithm [2]. Fig. 2 illustrates the division of the aperture. In each region, the actual phase increment for each shift is approximately equal and is thus represented by $2\pi/N$ radians ($N = 6, 7, 8, \dots, 12$). The phase-shift algorithm for each region is designed with $2\pi/N$ radians step. The divisor N should be integer for the sake of the orthogonality among the harmonic components of the signals. By selecting these different phase steps, the spatial nonuniformity decreased from -49% to -7.7%. Numerical simulations show that the averaged phase measurement errors by the present technique decreases to less than 1 nm, while those are 4 ~ 6 nm for conventionally covering whole observing aperture by a single algorithm.

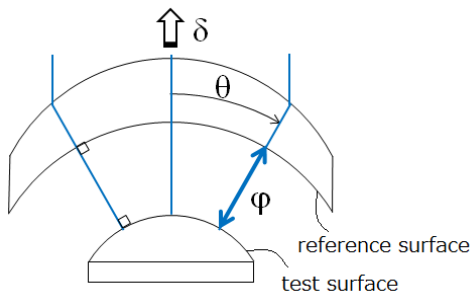


Fig. 1. Illumination geometry of a spherical convex test in a Fizeau interferometer.

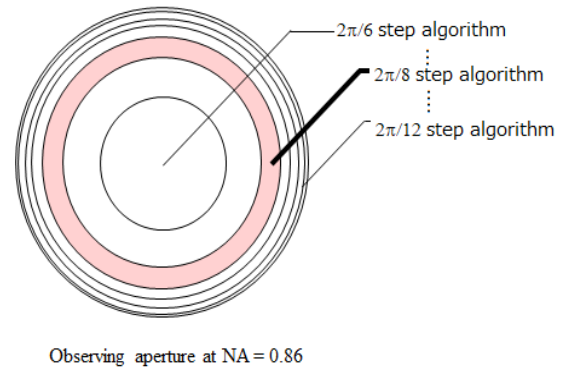


Fig. 2. Observing aperture division into seven annular regions.

In the experiment, a glass spherical concave surface of 0.86 NA and 10 mm diameter was compared to a reference transmission concave surface of the same numerical aperture and 22 mm diameter. To reduce the internally scattered light noise, the source beam from a 633 nm wavelength He-Ne laser is transmitted through a rotating ground glass diffuser and a multi-mode fiber of 200 μm diameter to reduce the lateral coherence [3] (coherence within the normal plane to the beam). The reference surface was translated along the optical axis by a PZT and 13 interference images were recorded with equal time intervals by a CMOS detector of 1024 x 1024 pixels. The relative phase step between the frames was designed to be 60° at the center of the aperture. The seven different algorithms were generated by the convolutions of the two rectangle sampling windows. Fig. 3 shows the phase distribution of the test surface calculated by the present method. In order to estimate the magnitude of systematic errors, we intentionally introduced a slightly tilt in the reference surface relative to the test surface, as was not the case of ordinary industrial measurements. The raw interference image is shown in the small window of Fig. 3 which has several carrier fringes. Since we cannot observe the similar straight lines in the resultant phase map, we can see that the phase shift error was very well reduced.

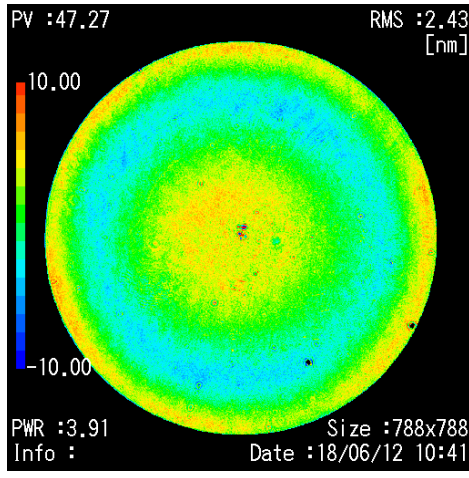


Fig. 3. Phase distribution of the 0.86 NA spherical concave surface and its raw interference image.

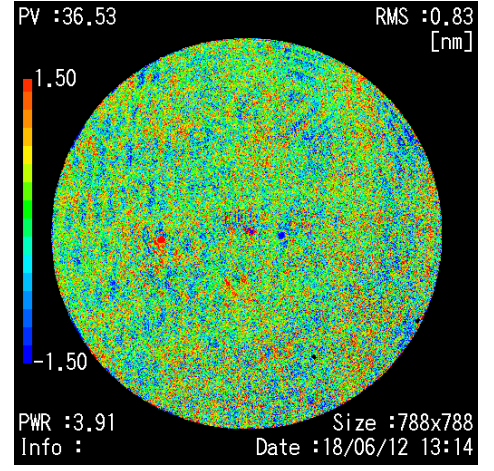


Fig. 4. Phase difference between null and tilt alignments after removing the Zernike 36 components.

Fig. 4 shows the residual phase difference between the null (not shown) and tilt alignment (Fig. 3) phase maps after we removed the Zernike 36 components from the phase. We can observe the fine structure of the random and systematic errors. In the figure, we can observe concentric discontinuous errors of ~ 0.2 nm magnitudes. The positions of these concentric errors coincide with the borders between the two neighboring regions. The sensitivity of the algorithm to the phase-shift error is generally different from algorithm to algorithm. If we denote the error coefficient of the phase shift by ε_i , we can denote the linear term of the phase measurement error as

$$\Delta\varphi = J\varepsilon_1 \sin 2\varphi + K_0\varepsilon_2 + K_1\varepsilon_2 \cos 2\varphi + F_1 R \varepsilon_1 \sin \varphi + F_2 R \varepsilon_1 \sin 3\varphi. \quad (1)$$

where R is the reflection index of the surfaces and φ is the object phase. The error coefficients J , K_i and F_i distribute from 0.0 to 0.5 depending on the algorithms. We think that these error discontinuities in Fig. 4 are caused by the different sensitivity of the algorithms to the errors. Our next goal is how to reduce these discontinuous errors caused from the different sensitivities of the algorithms in the divided regions.

References

1. de Groot, P.J., "Correlated errors in phase-shifting laser Fizeau interferometry," *Appl. Opt.* **53**, 4334-4342 (2014).
2. T. Kumagai, Y. Nagaike, K. Hibino, "Dual phase-shift schemes for internal-reflection noise reduction in a spherical Fizeau interferometer," *Interferometry XIX: Techniques and Analysis* (San Diego), SPIE **10749**, 1074915-1-8 (2018).
3. Kumagai, T., Hibino, K., and Nagaike, Y., "Dual-phase-shift spherical Fizeau interferometer for reducing the internally scattered light noise," *Opt. Eng.* **56** (3), 034102 (2017).

3D measurements of freeform samples using multi sensor optical profilometer

Ville Heikkinen¹, Johan Nysten¹, Ville Byman¹, Björn Hemming¹ and Antti Lassila¹

¹ VTT Technical Research Centre of Finland Ltd, Centre for Metrology MIKES, P.O. Box 1000, 02044 VTT Tekniikantie 1, 02150 Espoo, Finland

Corresponding author: ville.heikkinen@vtt.fi

Keywords: Traceability, stitching, scanning white light interferometer, chromatic confocal sensor, interferometry

Scanning white light interferometer (SWLI) allow fast measurements of relatively large areas with nm class vertical precision. Compared to coherent interferometers it has the advantage of measuring across vertical steps. However, measurement of small details and high slopes requires large magnification, while measurement of larger samples requires smaller magnification and larger pixel size. Thus measurement of sloping surfaces or small features is often impossible using the same magnification that would allow measurement of the whole sample. This limitation can be solved by stitching several images together into a large high-resolution image. Traditionally stitching would require adjusting the tilt around three axes and 3-D shifts of the adjacent sub-images due to accuracy of the sample/sensor translation. This makes the method computationally difficult and decreases the accuracy of the combined 3-D profile.

For more accurate and computationally easier approach, a SWLI was combined with precise sample movement on air bearings and heterodyne laser interferometers tracking sample movement and rotation. The precisely controlled and tracked sample movement allows accurate stitching of sub-images by only adjusting height between images. The setup also used a chromatic confocal height sensor that is added to the setup for quick coarse scans of large areas.

Samples up to 10 x 10 cm wide can be measured with 50 nm nanometer level vertical accuracy and nanometer level resolution. For fine details, hundreds of SWLI sub images can be combined into datasets of over 100 million pixels. For fast results, the sample can be quickly scanned using the confocal sensor. Slope limit for smooth samples for the confocal sensor is 15 degrees and for the SWLI the slope limit varies from 3 to 18 degrees using the currently used magnifications. Rough samples can be measured with higher slopes.

To test the profilometer samples up to 10 cm using were measured using the confocal sensor and samples up to 5 cm in were measured using the SWLI and stitching. Sample movement straightness was below μm in all axes and confocal noise below 50 nm. Stitching accuracy in 10 nm range could be achieved for >100 SWLI images as shown in Fig. 1.

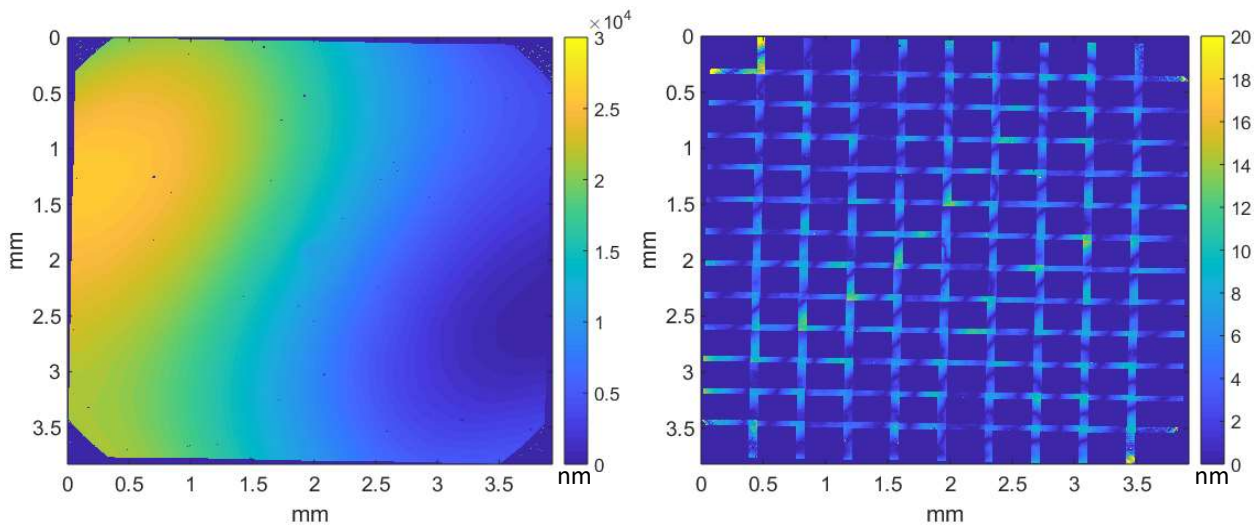


Fig. 1. Height map created by stitching 130 sub-images stitched together (left) and standard deviation of overlapping pixels (right) illustrating stitching accuracy.

Thickness distribution measurement with a full-field pulsed SD-OCT

Takamasa Suzuki¹, Bin Liu², Samuel Choi¹, and Osami Sasaki¹

¹ Faculty of Engineering, Niigata University, Niigata

² Graduate School of Science and Technology, Niigata University, Niigata

Corresponding author: takamasa@eng.niigata-u.ac.jp

Keywords: optical coherence tomography, phase analysis, wavelet transform, pulse irradiation

Optical coherence tomography (OCT) has been used in medical applications such as ophthalmoscopy [1], skin examination [2], and circulatory system examination [3] because it allows for noncontact and noninvasive measurements with high resolution and sensitivity. A spectral domain OCT (SD-OCT) uses a low coherence light source and consists of a Michelson interferometer, a diffraction grating, and image sensor for spectroscopy. The sensor captures the spectrum of the interference signal. However, the phase of the interference signal varies nonlinearly because the phase is inversely proportional to the wavelength that spreads linearly in space by the diffraction grating. Thus, the interference signal becomes a nonstationary signal (e.g., chirp signal) in space in an SD-OCT.

We propose a signal analytical technique that uses continuous wavelet transform (CWT) [4], where a conventional Fourier transform (FT) is not suitable for processing nonstationary signals. Moreover, we propose a pulse irradiation technique for capturing fringe. It allows us to capture clear fringes even when an object, such as a transparent glass plate, may have a low reflection rate. Several experiments indicate that the pulse irradiation technique is effective at improving measurement accuracy.

The relationship between phase and wavelength is given by:

$$\alpha_i = 2\pi L / \lambda_i = \theta + \Delta\alpha_i, \quad (1)$$

where L , θ , and $\Delta\alpha_i$ are the optical path difference (OPD), phase offset, and phase distribution, respectively. The equation indicates that the phase varies nonlinearly according to the linear change of the wavelength. From (1), L is expressed as:

$$L = (\theta + \Delta\alpha_i) \lambda_i / (2\pi). \quad (2)$$

The phase α_i that corresponds to λ_i can be calculated by CWT, which detects the phase and instantaneous frequency simultaneously. The phase offset θ is given by:

$$\theta = \Delta h / \Delta \lambda = (\Delta\alpha_2 \lambda_2 - \Delta\alpha_1 \lambda_1) / (\lambda_1 - \lambda_2). \quad (3)$$

Figure 1 shows the procedure for the data analysis. Specifically, the figure schematically explains the signal processing in our technique. The parameters of OPD, wavelength range, and data number used in the simulation were $L = 40 \mu\text{m}$, $\lambda_i = 730\text{--}930 \text{ nm}$, and 1000, respectively. The calculated one-dimensional (1D) fringe is shown in Fig. 1(a). Here, we can see that it becomes a chirp signal. Modulus and phase maps were obtained as shown in Fig. 1(b) and 1(c), respectively, after CWT for the fringe was calculated.

A schematic of the experimental setup is shown in Fig. 2. We used a super-luminescent diode with a spectral bandwidth of 60 nm at a center wavelength of 845 nm. The beam is split into two beams using a beam splitter (BS). One beam passes through a cylindrical lens 1 and a galvanometer and was focused onto the surface of the object. The other beam passes through to the reference mirror. These beams are recombined at the BS and interfere with each other. The interference signals are focused linearly on a charge-coupled device camera using a cylindrical lens 2.

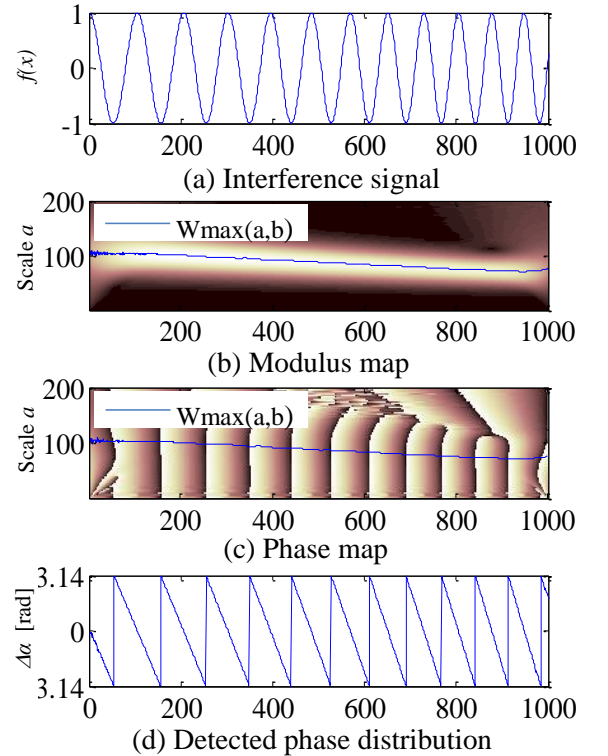
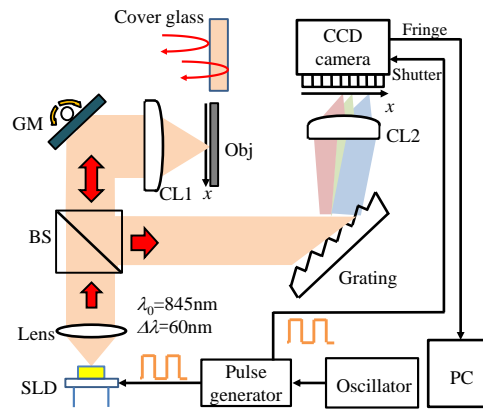


Fig. 1 Signal processing based on CWT.



The 2D thickness distribution of the cover glass was measured. Figure 3 shows the results obtained with continuous irradiation. The contrast of the captured fringe as illustrated in Fig. 3(a) appears not to be high with continuous irradiation. The obtained 2D thickness distribution is shown in Fig. 3(b). After several measurements at the same position, we confirmed the repeated measurement error of 0.16 μm at root mean square. The same measurement was conducted with a pulse irradiation. We found that a fringe is captured with high contrast, as shown in Fig. 4(a). The 2D thickness distribution is shown in Fig. 4(b). The repeated measurement error was 0.09 nm. We confirmed that the repeatability was improved with the pulse irradiation.

In this study, a full-field SD OCT driven by a pulse irradiation was proposed and demonstrated. The nonstationary signal was successfully processed by using continuous wavelet transform. A pulse irradiation was effective at obtaining a clear fringe and reducing the measurement error.

Fig. 3 2-D thickness distribution
with continuous irradiation.

Fig. 4 2-D thickness distribution
with pulse irradiation. w

Fig. 5 3-D thickness distributions
a) CW and (b) pulse irradiation.

1. A.G. Podoleanu, J.A. Rogers, D.A. Jackson, S. Dunne, Opt. Express 7 (9), 292–298 (2000) .
2. E. Dalimier, D. Salomon, Determatology 224 (1), 84–92 (2012) .
3. W. Luo, D.L. Marks, T.S. Ralston, S.A. Boppart, J. Biomed. Opt. 11 (2) (2006) 021014.
4. M. Sifuzzaman, M.R. Islam, M.Z. Ali, J. Phys. Sci. 13, 121–134 (2009) .

Low-coherence interferometer with 10MHz repetition rate

Katsuhiro Ishii¹, Masaharu Hoshikawa^{1,2}, Takeshi Makino³, Takahiro Hashimoto³,
Hideaki Furukawa³ and Naoya Wada³

¹ The Graduate School for the Creation of New Photonics Industries, Hamamatsu

² Electron Tube Division, Hamamatsu Photonics K. K., Hamamatsu

³ National Institute of Information and Communications Technology, Koganei

Corresponding author: ishii@gpi.ac.jp

Keywords: Highly repetitive low-coherence interferometer, time stretch dispersive Fourier transform technique

We constructed a low-coherence interferometer with 10MHz repetition rate and confirmed its basic characteristics. The low-coherence interferometry consists of a mode-locked laser diode and a fiber-optic interferometer. Based on the time stretch dispersive Fourier transform technique, highly repetitive measurement is achieved. We demonstrate the 10MHz measurement of interference signals and path-length deference.

1. Introduction

Low coherence interferometry (LCI) and optical coherence tomography (OCT) have attracted attention for in-situ measurement of laser processing [1-3]. In the spectral domain OCT(SD-OCT) and swept source OCT(SS-OCT), the repetition rate of measurement is limited to several hundred kHz at present. Since laser processing is a rapid phenomenon with a time scale faster than several hundred ns, a measurement method with higher repetition rate is required to observe such a fast phenomenon.

One of high repetition measurement is a time-stretch technique [4-6]. The time-stretch technique is highly-repetitive spectroscopy, and its repetition rate is several MHz or more. By combining time-stretch technique and low-coherence interferometry, we can construct highly-repetitive low-coherence interferometer with a repetition rate of several MHz or more [7].

In this paper, we construct a measurement system of low coherence interferometry with 10MHz repetition rate using ultra-short pulse and time-stretch technique and confirm its basic characteristics.

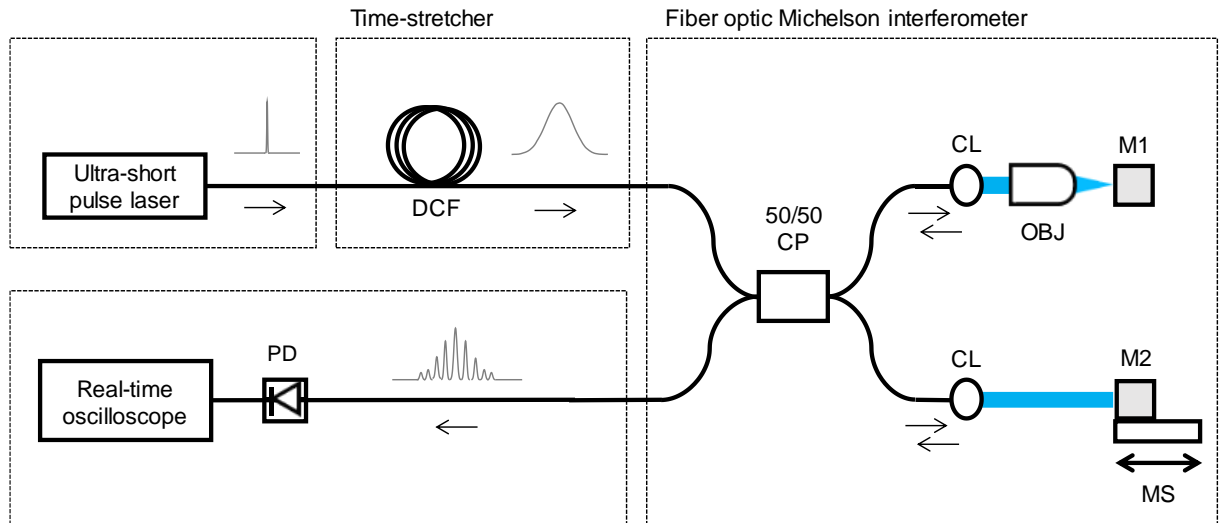


Fig. 1. A Schematic diagram of measurement system of highly-repetitive low-coherence interferometer. DCF: dispersion compensation fiber, CP: fiber coupler, CL: collimating lens, M1 and M2: reflective mirror, OBJ: objective lens, MS: manual stage, PD: photo diode.

2. Measurement system

A schematic diagram of the measurement system is shown in Fig.1. It was composed of an ultra-short pulse laser with pulse width less than 1ps, time-stretcher using dispersion compensating fiber (DCF), optical interferometer, photodiode (PD) and real-time oscilloscope. The ultra-short pulse from MLLD was passed through a dispersion flat fiber to generate supercontinuum light with 23.5nm wavelength bandwidth. Repetition frequency of the laser pulse is down-converted to be 10MHz by the LiNbO₃ modulator. Then it feeds to a time-stretcher composed of a dispersion compensation fiber (DCF) with a wavelength dispersion of 8959ps². The pulse width after passing through the time-stretcher is 28.2ns. The fiber-optic Michelson interferometer consists of a 50:50 optical fiber coupler, two collimating lenses, an objective lens and two reflective mirrors. Interference signals are detected by photodiode (32GHz) and recorded by a real-time oscilloscope (16GHz, 20GS/s).

3. Results and discussion

Figure 2(a) shows an obtained signal recorded by the real-time oscilloscope. The optical path length difference between the signal and reference paths is set to $\Delta L = 2$ mm. A pulse train is observed every 100ns. Enlarged view of one pulse is shown in Fig. 2(b). An interference signal is also observed in each pulse. It is confirmed that interference signal measurement of the low-coherence interferometer can be performed at a high repetition rate of 10MHz. We also confirmed that optical path length difference can be estimated accurately from the obtained interference signals.

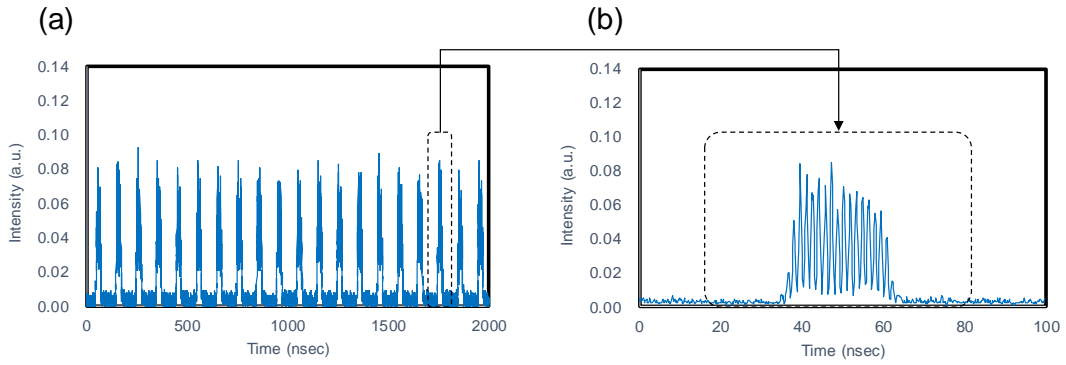


Fig. 2. (a) Pulse train recorded by the real-time oscilloscope and (b) its enlarged view of one pulse.

4. Summary

We constructed a measurement system of highly repetitive low-coherence interferometry using time-stretch technique. It was confirmed that interference signals can be measured at high repetition rate of 10MHz. The estimated optical path length and the measured values showed good agreement.

References

1. P. J. L. Webster *et. al.*, *Optics Letters* **21**, 6217-6220 (2014).
2. T. Bautze *et. al.*, *Lasers in Manufacturing Conference 2015*, 73 (2015).
3. N. Authier *et.al*, *Proc. ICALEO2016*, 904 (2016).
4. D. R. Solli, J. Chou, and B. Jalali, *Nature Photonics* **2**, 45-51 (2008).
5. G. Herink, B. Jalali, C. Ropers and D. R. Solii, *Nature Photonics* **10**, 321-51 (2016).
6. H. Furukawa, *et. al.*, *Proc. SPIE* **10089**, 10089A1-H6 (2017).
7. K. Ishii and M. Hoshikawa, *Proc. OIE2017*, S9 (2017).

Analyzing and applying light with randomness; from speckles to fractals and to spectra

Jun Uozumi

Faculty of Engineering, Hokkai-Gakuen University, Sapporo, Japan
uozumi@eli.hokkai-s-u.ac.jp

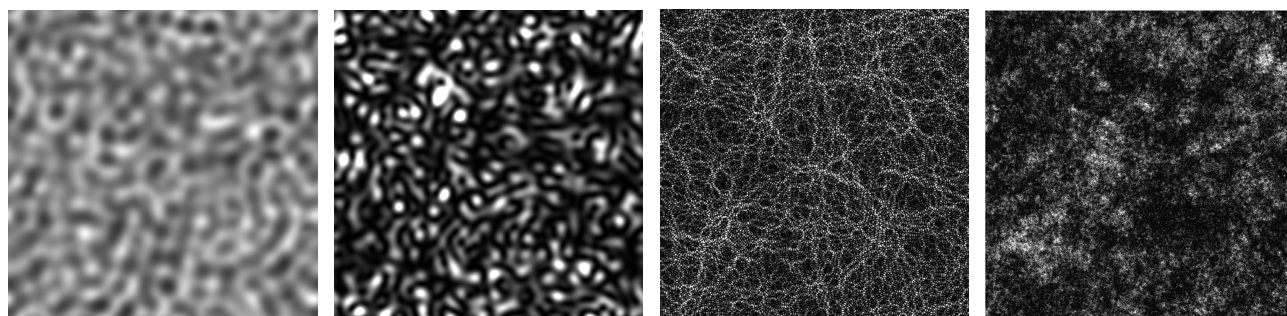
Keywords: laser speckle, fractal optics, near infrared spectroscopy, fractional derivative

The optical engineering abounds with randomness. Most of objects have random features such as their shapes, surface conditions and inside structures, and intervening optical systems may also contain randomness arising from irregularities, dusts or refractive index fluctuations of optical elements, atmosphere and so on. The development of optical technology is, therefore, always a battle against such randomness. My researches have been mostly related with analyzing, applying and sometimes controlling light affected by the randomness. In this report, I would like to look back to my researches in this respect.

Most common random phenomenon in optics may be scattering. Light is scattered on encounter with any object. When the object is random, the scattering becomes also a random phenomenon. As a study on an interesting random scattering, I started my research life with a computer simulation study of image speckle patterns in relation to surface roughness profile [1]. During this study, I was captivated by speckles, and analysis and application of speckle statistics continue to be one of my main research subjects since. Throughout my undergraduate and graduate study, I concentrated on analysis of partially developed Gaussian and non-Gaussian speckles. Partially developed speckle as shown in Fig. 1(a) is generated from a weak diffuser, and its contrast defined by the ratio of the standard deviation of the speckle intensity to its mean varies between zero and unity, depending on the surface roughness. Meanwhile, speckle is referred to as Gaussian or non-Gaussian when its complex amplitude obeys complex Gaussian statistics or not, respectively.

Among different types of randomness of objects, fractals came to attract me because of their exotic and nevertheless ubiquitous features. Since many natural and artificial objects have fractal properties as Mandelbrot showed [2], I thought it would be interesting and important to reveal optical phenomena related to fractals. Therefore, we started to work for *fractal optics* as my second main research subject, and examined diffraction and scattering from fractal objects, different kinds of optical procedures to measure fractal properties such as fractal dimension, and methods for generating fractal wavefield [3]. Noncontact feature of optical techniques is particularly favorable for fractal objects, which are mostly fragile.

A random fractal object gives rise to speckles in its diffraction field. In the study of speckles produced by a randomized Koch curves, we found two strange phenomena; high contrast and clustered speckles. Most researchers involved in statistical optics may think that the maximum contrast for Gaussian speckle is unity, corresponding to zero-mean circular complex Gaussian statistics, and such speckle is said to be fully developed (Fig. 1(b)). However, it was revealed that contrast can be higher than unity even for Gaussian speckles with the true maximum contrast of $\sqrt{2}$ [4]. Such a high contrast Gaussian speckle appears when the scatterer has a central symmetry or binary randomness and, therefore, can be an indication of the existence of such special



(a) Partially developed speckle (b) Fully developed speckle (c) Nondiffracting speckle (d) Fractal speckle

Figure 1: Various types of speckle patterns produced by computer simulations.

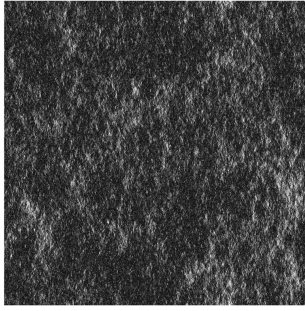


Figure 2: Anisotropic fractal speckle.

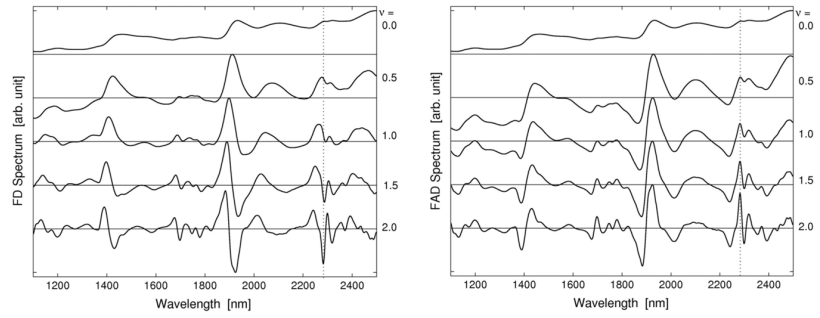


Figure 3: Fractional (left) and fractional absolute (right) derivatives of NIR spectra of rice flour.

random features in the scattering object. The clustering feature observed in the above situation has led to the study of nondiffracting speckle, which is a random version of nondiffracting beam. Namely, illuminating a diffuser with a ring-slit aperture gives rise to approximately nondiffracting speckles in the space behind a lens placed a focal length away from the diffuser [5]. They have a clustered and snake-like appearance as shown in Fig. 1(c) with smaller speckle size than the case with a circular aperture for illumination. This feature was recently employed in the enhancement of spatial resolution in digital holographic microscopy [6].

In fractal optics, we also interested in generating speckle field with fractal property, namely fractal speckles [7, 8]. Since a fractal structure has a long extending correlation tail, fractal speckle is expected to extend the measurement range in the speckle metrology using spatial correlation. Fractal speckles as shown in Fig. 1(d) can be produced as speckled speckle using two scatterers of random fractal object and an ordinary phase screen. Fractal speckles are also observed in bio-speckles produced in some situations, and their fractal dimension was found to convey important information about the biological tissue [9]. It was also shown that, in the diffraction geometry, the fractal speckle has different dimensions between in the lateral plane and longitudinal direction [10]. I am currently investigating such anisotropic fractal speckles by computer simulations as shown in Fig. 2.

After I finished my doctoral course, I joined National Food Research Institute (NFRI), Japan, for five years, where I was engaged in the near infrared spectroscopy (NIRS) for nondestructive food analysis. This was a drastic change of my research object from speckles to spectra. However, the research on NIRS was another battle against randomness involved in measured spectra; random shape of object, scattering due to internal and surface irregularities, and random distribution of constituent concentrations, and became another member of my main research subjects. This multifold randomness in spectra is processed with various statistical treatments including elaborated regression analyses. With these statistical analyses, derivative spectra are sometimes employed to resolve complex spectral features. I paid particular attention to the derivative, trying to provide additional flexibilities by extending the derivative order from integers to fractional values and by controlling positions of derivative peaks (Fig. 3) [11]. Application of these treatments is still on the way, and I believe that it will contribute to improving the measurement accuracy in NIRS.

Random light is annoying but sometimes conveys interesting information, proving useful if properly processed.

References

- [1] H. Fujii, J. Uozumi and T. Asakura, *J. Opt. Soc. Am.*, **66**(11) (1976) 1222–1236.
- [2] B. B. Mandelbrot, *The Fractal Geometry of Nature*, (Freeman, San Francisco, 1982).
- [3] J. Uozumi and T. Asakura, *Current Trends in Optics*, ed. J. C. Dainty (Academic, London, 1994) 83–93.
- [4] J. Uozumi, K. Uno and T. Asakura, *Opt. Rev.*, **2**(3) (1995) 174–180.
- [5] M. Ibrahim, J. Uozumi and T. Asakura, *Opt. Rev.*, **5**(3) (1998) 129–137.
- [6] H. Funamizu, J. Uozumi and Y. Aizu, *OSA Continuum*, **2**(6) (2019) 1822–1837.
- [7] K. Uno, J. Uozumi and T. Asakura, *Opt. Commun.*, **124**(1,2) (1996) 16–22.
- [8] J. Uozumi, M. Ibrahim and T. Asakura, *Opt. Commun.*, **156**(4–6) (1998) 350–358.
- [9] N. Yokoi, Y. Aizu and J. Uozumi, *J. Biomed. Opt.*, **24**(3) (2018) 031018–(1–7).
- [10] K. Tsujino and J. Uozumi, *Asian J. Phys.*, **27**(9–12) (2018) 515–528.
- [11] J. Uozumi, *Asian J. Phys.*, **27**(9–12) (2018) 573–585.

Wavelength-tunable common-path interferometer with a diode source

Yukihiro Ishii^{1,2}, Shunpei Yukita¹, Kosuke Kiyohara³, Jun Chen⁴, and Eiji Tokunaga¹

¹Department of Applied Physics, Tokyo University of Science, Tokyo 125-8585, Japan

²Photonics Control Technology Team, RIKEN Center for Advanced Photonics, Wako 351-0198, Japan

³Kiyohara Optics Inc., Tokyo 174-0041, Japan

⁴Tokyo Polytechnic University, Atsugi 243-0297, Japan

e-mail; y.ishii@rs.kagu.tus.ac.jp, yukihiro.ishii@riken.jp

Keywords: wavelength-tunable heterodyne interferometer, common-path layout, birefringent beam splitter

The temporal carrier beat frequencies in an optical heterodyne interferometer can be generated by ramping the wavelength in a laser diode (LD) based on the frequency-modulated continuous-wave (FMCW) techniques [1,2]. The beat frequency is proportional to the optical path difference (OPD) of each pair of interfering beams in an interferometer [3]. It enables us to construct an optical heterodyne interferometer on an unbalanced OPD without auxiliary frequency modulators [4,5]. We demonstrate a new type of optical heterodyne common-path interferometer with a birefringent beam splitter with a wavelength-tunable external-cavity laser-diode (ECLD) source. A two-dimensional (2-D) phase map of a phase object in transmission can be derived from the numerical Fourier transformation of measured heterodyne interference fringes. Successful measurements are precisely made during tuning because the common-path interferometer [6] is quite insensitive to external disturbances.

A common-path interferometer is shown in Fig. 1 with a plane-parallel plate with a thickness d giving an unbalanced OPD. A light source is a wavelength-tunable ECLD (v-focus, v-6300) those widely tuned wavelength diversity in the experiment is $\Delta\lambda = \sim 2$ nm at a central wavelength of $\lambda = 680$ nm. A collimated beam from an ECLD has an upper object beam with a phase object in transmission adding with an unbalanced OPD $2\pi nd/\lambda$ where n is an index of an optical-polished plane-parallel plate glass. An ITO (indium tin oxide) thin film to be measured is evaporated on a slide glass of an index n_i , and is put on an object beam as a phase object of the thickness variation $\epsilon(x,y)$ of an index n_i . A lower beam is a reference wave. Both object and reference waves are magnified with a microscope objective plus a convex lens and imaged onto a CMOS camera with a $7\times$ lateral magnification. Both beams are incident on a Wollaston prism through a half-wave plate of a 45° -azimuth polarization that splits into O and E rays travelling in different direction. Both waves are laterally sheared upward (red circle) and downward (blue circle), and are interfered with each other after passing through a polarizer.

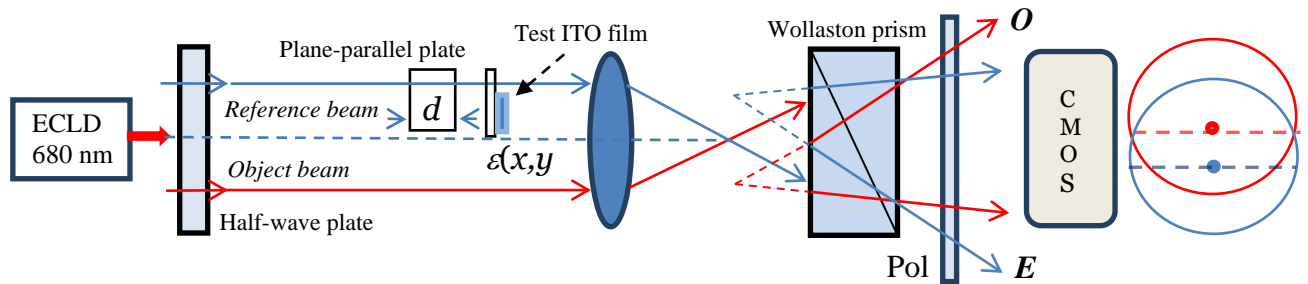


Fig. 1. Setup of a heterodyne common-path interferometer.

On the measurement, the square wave from an electronic function generator is applied to an ECLD diode source and triggered to a high-speed CMOS camera for capturing the heterodyne interference signals [7]. Camera data are sent to a computer that calculates the Fourier transform of the interference signals. By extracting the Fourier spectra of the interference signals at a beat frequency $f_s = 33$ Hz, a phase data of a test ITO evaporated film can be measured as shown in Fig. 2. Phase gradient of ITO film can be measured with subtracting an additional phase measurement those experiment is made when the ITO thin film does not put on

an object arm to remove the unnecessary phase errors. Figs. 2 (a) and (c) show the wrapped phase map (a) and the unwrapped phase map (c) in grey demonstration exhibiting the phase $2\pi(n-1)d/\lambda$. Figs. 2 (b) and (d) show the wrapped phase map (b) and the unwrapped phase map (d) in grey demonstration in which the ITO thin film is inserted into an object arm exhibiting the phase $2\pi\{(n_i-1)\varepsilon+(n-1)(d+s)\}/\lambda$. The subtraction of the phase in Fig. 2 (c) from the phase in Fig. 2 (d) gives the phase $2\pi\{(n_i-1)\varepsilon+(n-1)s\}/\lambda$ of an ITO thin film shown in Figs. 2 (e) in grey demonstration and (f) in 3-D phase map. The phase demonstrates a stepped part at an edge of the ITO film evaporated on a slide glass. The small phase step of ~ 2.2 rad ($=\sim\lambda/3$) in Fig. 2 (f) can be measured.

A heterodyne common-path interferometer with a Wollaston birefringent beam splitter acts to eliminate the external disturbances, assuring that precise phase measurement is performed. The optical heterodyne signals can be generated by a wavelength-tunable laser-diode source. The phase distribution can be measured from the Fourier transform of 2-D heterodyne interference signals.

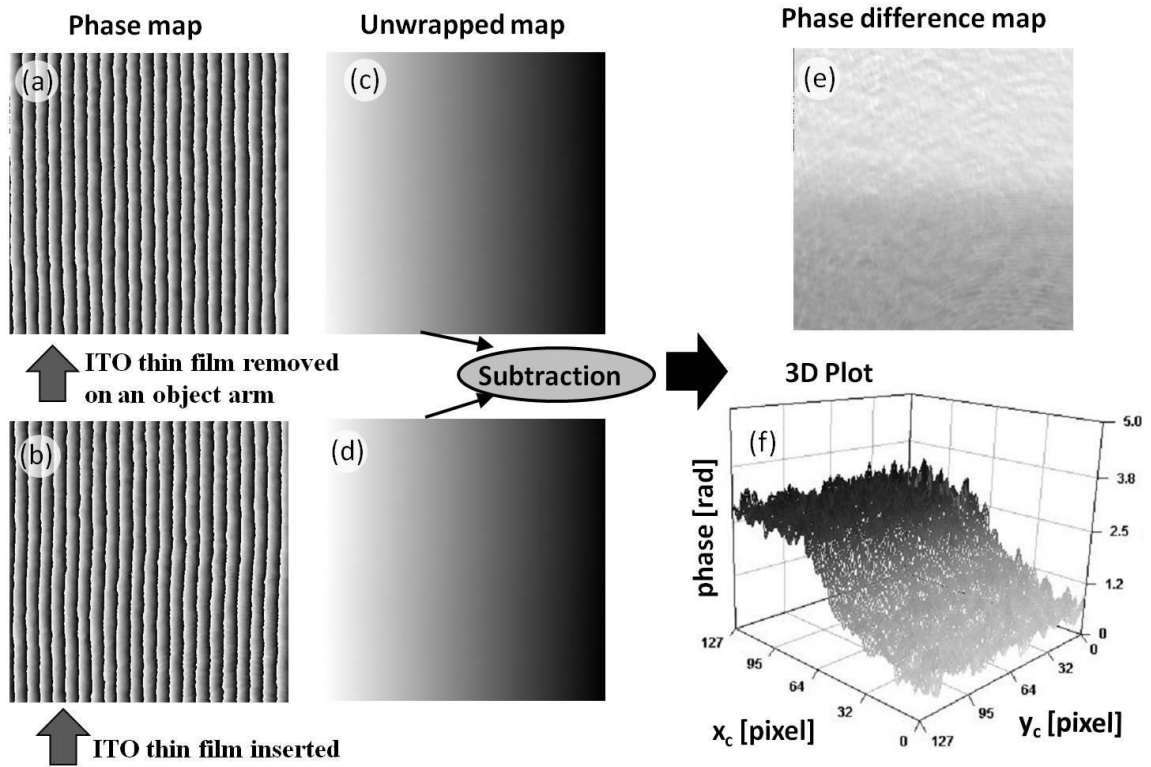


Fig. 2. Subtraction of unwrapped phase (c) of the object film removed from unwrapped phase (d) of the object inserted gives the measured phase difference of ITO film in (e) and (f).

References

1. I. P. Giles, D. Uttam, B. Culshaw, and D. E. N. Davies, *Electronics Letters* **19**, 395-396 (1983).
2. J. Zheng, *Optical frequency-modulated continuous-wave (FMCW) interferometry*, (Springer, New York, 2005).
3. Y. Ishii, *Laser-diode interferometry, Progress in Optics*, E. Wolf, Ed., **46**, 243-309 (Elsevier, Amsterdam, 2004).
4. M. Suematsu and M. Takeda, *Applied Optics* **30**, 4046-4055 (1991).
5. F. Lexer, C. K. Hitzenberger, A. F. Fercher, and M. Kulhavy, *Applied Optics* **36**, 6548-6553 (1997).
6. J. Endo, J. Chen, D. Kobayashi, Y. Wada, and H. Fujita, *Applied Optics* **41**, 1308-1314 (2002).
7. R. Onodera and Y. Ishii, *Applied Optics* **35**, 4355-4360 (1996).

Speckle Shearing Interferometric Vibrometer for Heartbeat Monitoring

Ryohei Hanayama and Katsuhiro Ishii

The Graduate School for the Creation of New Photonics Industries, Hamamatsu

Corresponding author: hanayama@gpi.ac.jp

Keywords: speckle interferometry, vibration measurement, human skin, high-speed camera

We developed a speckle shearing interferometer for measuring micro vibration of human skin such as skin vibration caused by heartbeat. We focused on the volume pulse, or plethysmogram, that is used to diagnose diseases of blood vessel. It can be observed as the motion of skin surface. As with this case, it can be thought that the vibration of skin surface shows the condition of human body. Moreover, we are planning to apply this method for monitoring emotion of a car driver. We adopted monolithic prism type shearing interferometer. Because it is very robust to disturbances, such as external vibration or shock. An anti-shock type high-speed camera is also adopted for this interferometer.

The photo and schematic diagrams of developed interferometer are shown in figs.1 and 2. It consists of two parts. One is the illumination part, which irradiate laser beam for the target. Another is interferometer part. The optical system of the interferometer is based on the twyman-green interferometer. The mirror of one arm of the interferometer is slightly tilted from the optical axis, to realize the shearing interferometer. Then, the two reflected beams are slightly sheared each other on the imaging plane of the camera. This lateral shearing interferometer measures the spatial differences. In other words, the inclination of the target can be measured. When the laser beam illuminates the target surface, which is rough surface made of general materials, the speckle can be observed. The speckle image has the information of the target surface, nevertheless it looks random pattern. This interferometer brings the information, especially the inclination, into sight. We acquire the speckle pattern using high-speed camera. The maximum frame rate of this camera is 30kfps when the spatial resolution is 256×256 pixels.

We investigate the sensitivity of developed instrument. In the developed interferometer, there is 0.2deg. of angle difference between the two of beams, because there is 0.1deg. of inclination in one face of the prism (show Fig.2). The angle difference leads the image shearing. The shear amount depends on the distance from the interferometer to the object plane. When the working distance is 0.5m, the shear amount is 1.8mm. The height difference between two of corresponding point on the object surface causes the interferometric signal. When $\lambda/4$ of height difference exists, the inclination change is:

$$\frac{\lambda/4}{s} = \frac{213.75nm}{1.8mm} = 1.2 \times 10^{-4} rad. \quad (1)$$

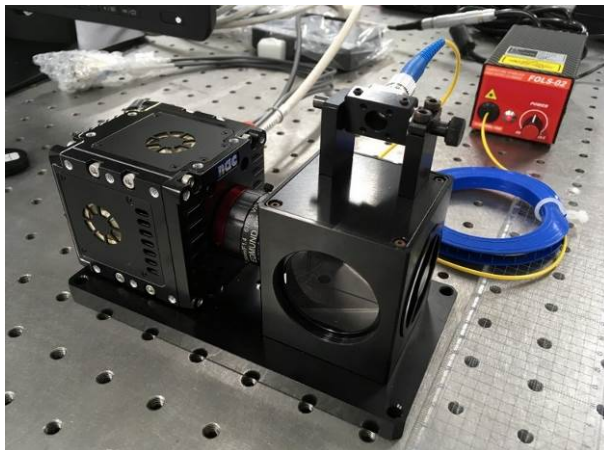


Fig.1 Developed vibration measuring speckle shearing interferometer

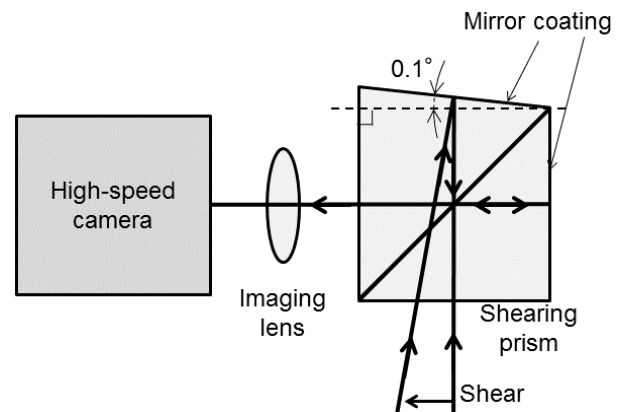


Fig.2 Schematic diagram of speckle shearing interferometer

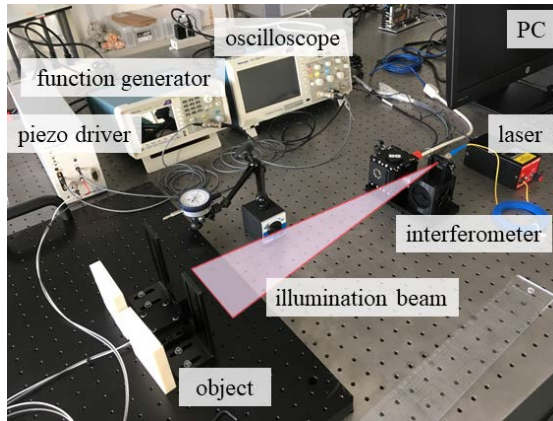


Fig.3 experimental setup

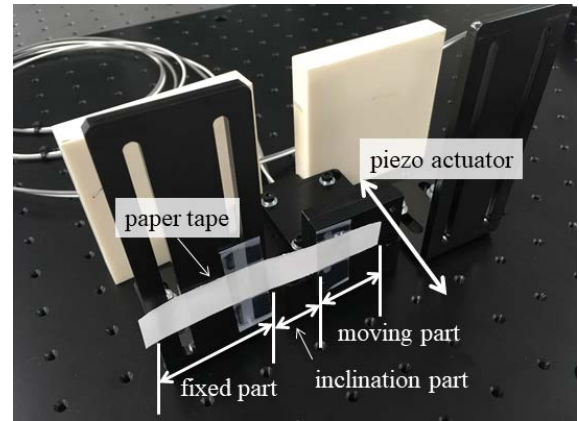


Fig.4 inclinational deformation simulator with piezo actuator

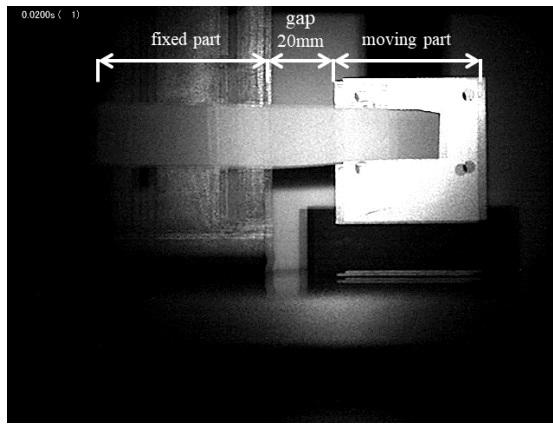


Fig.5 acquired raw image

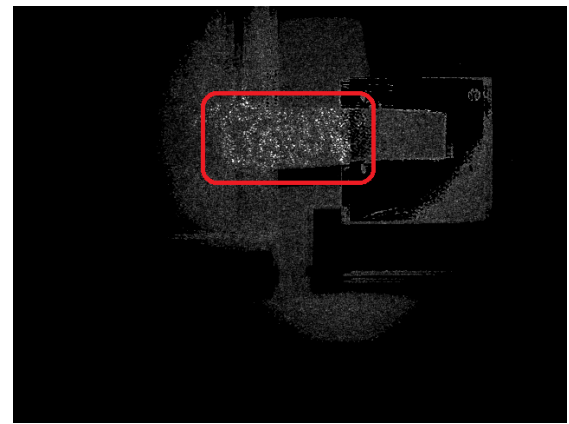


Fig.6 ESPI image. The red square shows the inclined area

In this case, wavelength λ is 855nm. s is shear amount. Diameter of blood vessel changes by modulation of blood pressure. It is said that the diameter change is about 1% of the diameter. When diameter of a blood vessel is 1mm, the amplitude of diameter modulation is about $10\mu\text{m}$. If the baseline of inclination is several mm, the inclination caused by the diameter change is the order of 10^{-3}rad . Therefore it can be thought that $1.2 \times 10^{-4}\text{rad}$. of inclination sensitivity is enough for heartbeat monitoring. The experimental results show that the developed interferometer can detect $3 \times 10^{-4}\text{mrad}$. of inclination. The experiment setup and the inclination simulator are shown in figs 3,4 and 5. In the inclination simulator, micro inclination vibration can be created on a paper tape using piezo actuator. Fig 6 shows the acquired ESPI image. As we can see the inclined area was highlighted and can be detected, successfully.

As far as it concerns to heartbeat motion, the main and largest spike in electrocardiogram is known as QRS complex. The usual width of QRS complex is from 60 to 100msec. The largest slope change occurs in from 30 msec. to 50 msec. Then it can be thought that the slope change of human skin caused by heartbeat can be acquired using high-speed camera whose maximum frame rate is more than 50 fps. Therefore, it can be thought that the skin vibration can be measured by the developed interferometer and high-speed camera. In the future work, we will apply this technique to human emotion monitoring during driving a car.

This work was supported by the Center of Innovation Program from Japan Science and Technology Agency, JST.

References

1. Hirohide Iwata and Masafumi Hirai, *J Jpn Coll Angiol* **45**, 329-332 (2005). (in Japanese)
2. German Da Costa, *Opt. Comm.* **117**, 395-398 (1995).
3. Sergey Y. Kusmin, *Proc. SPIE* **3053**, 9-17 (1997).

Multimode interferometers on strip-loaded waveguide for sensing

M. Roussey¹, R. Rao¹, and S. Pélisset¹

¹ University of Eastern Finland, Institute of Photonics, Joensuu, FI-80101, Finland

Corresponding author: matthieu.roussey@uef.fi

Keywords: Integrated optics, waveguides, sensing, micro- and nano-structures

A channel waveguide can be either single mode or multimode. In the second case, the intermodal interference will result in self-imaging effect of input field at periodic intervals [1]. This effect constitutes the basic operation of multimode interference (MMI) devices. An MMI structure consists of one (or several) single-mode waveguide, i.e., the input field, a free propagation region, i.e., a section with a wide width, where the intermodal interferences occur, and several output single-mode waveguides. MMI structures possess unique properties such as tolerance to a wide wavelength range, low loss, ease of the fabrication, and small footprint. These properties make them attractive for applications in coupling and splitting technologies in different configurations such as Mach-Zehnder interferometers, modulators, switches, and wavelength division (de)multiplexers. Different MMI configurations as 1xN and NxM power couplers and splitters can be efficiently produced over a very small area of a few hundred microns. In recent years, MMI structures are greatly used in developing chemical- and bio-sensors also. The idea behind using MMI structure as sensors is due to their high sensitivity to refractive index changes and polarization states. For instance, the MMI section can act as the sensing zone if this one is covered or replaced by an analyte. The optical parameters change of the cover material corresponds to the change in the propagation conditions of the modes within the structure. By observing the field intensity at the output of structure, we can track the chemical parameters of the analyte. The concept can be easily adapted to various sensing applications by appropriate selection of the sensor material constituting the MMI itself. The sensitivity can also be increased by varying the geometrical parameters of the MMI section.

We propose here the concept of MMI on strip-loaded platform to perform sensing. A strip-loaded waveguide consists of a high refractive index thin film to confine vertically light. A polymer strip is deposited on top of the thin film in order to induce a local effective index change of the slab waveguide mode. This leads to a lateral confinement of the field in the thin film [2]. One condition on the correct operation of this type of waveguide is that the refractive index of the loading strip must be lower than the effective index of the guided mode. Otherwise, light will be preferentially guided in the loading strip.

By realizing an MMI device on such a platform one can easily split the field between several outputs. We recently proposed a demonstration on a strip-loaded slot waveguide platform, for which the thin film is a horizontal slot waveguide [3-5]. Figure 1 (a) is a micrograph of the top view of the fabricated device on a TiO₂/SiO₂/TiO₂ slot waveguide using an electron beam resist (AZ nLof) as a loading strip material. One can see the realized 1x2 MMI coupler. The free propagation region is 226 μm long.

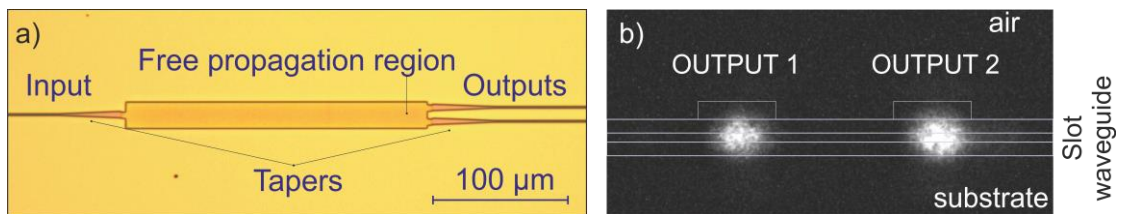


Fig. 1. Demonstration of a 1x2 MMI device on horizontal slot waveguide. (a) Microscope picture of the top view of the device. (b) Photograph of the output modes at $\lambda = 1550$ nm. The white lines represent the contour of the device.

Fig. 1(b) is a photograph obtain with a near infrared camera of the output modes, which roves the well operation of the device at $\lambda = 1550$ nm.

The design of such a device is extremely important. This is an interferometric system, which means that all the parameters may affect the response of the device. However, the fact of using a loading structure, instead

of a direct pattern etched on the surface of the waveguide, yields weakly guided modes. This means that the effect of the MMI may be less strong than if it was fabricated in a high refractive contrast platform such as silicon, for example.

The polarization for instance is a crucial parameter. The effective index of the mode depends on the polarization and the fluctuation on strip-loaded slot waveguide are important between TE (electric field parallel to the slot plane) and TM (electric field perpendicular to the slot plane). One can thus think that the length of the MMI will be a sufficient parameter to discriminate between TE and TM modes. Fig. 2 shows the results obtained by simulation of the output power for both TE and TM modes while varying the length of the MMI (free propagation region). One can clearly see that if TM (fundamental slot mode) present a net peak and obvious optimized length at 240 μm , this is not the case for TE. For this polarization the field is more confined in the two rails that are affected differently by the loading strip leading to not so clear maximum. To fit the curve, we have considered a Lorentz model, as a first approximation.

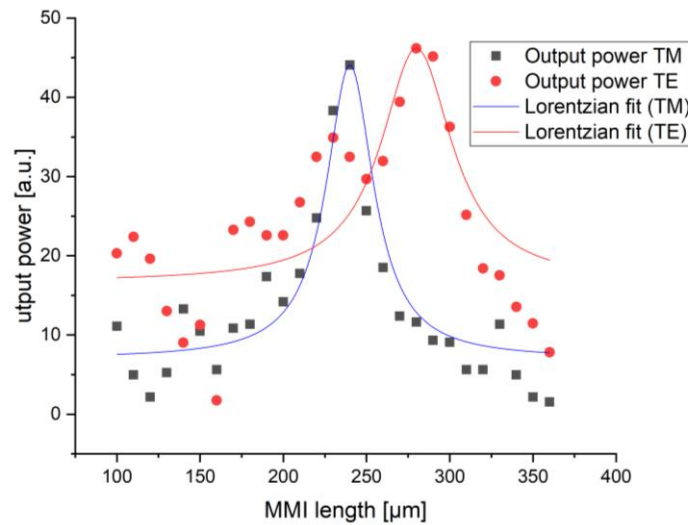


Fig. 2. Output power in one of the branches of the MMI as a function of the length of the free propagation region and the polarization (quasi-TM mode in blue and quasi-TE mode in red). Squares and dots are simulation data and the solid lines are Lorentzian fits.

In addition to its dependence to the geometrical and polarization parameters, an MMI depends also on the refractive index of the cover medium. In the case of a strip-loaded waveguide the mode is buried far from the surface and is thus not much affected by the surrounding material variation. But if the loading strip is open into a sensing window, the analyte is in direct contact with the thin film and thus changes the effective index of the guided mode. This will then affect the image position inside the MMI. By carefully designing the shape of the free propagation region, one can attribute to each output of the MMI a particular effective index and thus a refractive index of the cladding layer: the analyte material to be sensed.

References

- [1] Y. Zhang, Z. Li, and B. Li, "Multimode interference effect and self-imaging principle in two-dimensional silicon photonic crystal waveguides for terahertz waves," *Opt. Express* **14**, 2679-2689 (2006).
- [2] H. Furuta, H. Noda, A. Ihaya, "Novel optical waveguide for integrated optics," *Appl. Opt.* **13**, 322-326 (1974).
- [3] V.R. Almeida, Q. Xu, C.A. Barrios, M. Lipson, "Guiding and confining light in void nanostructure," *Opt. Lett.* **29**, 1209-1211 (2004).
- [4] M. Roussey, L. Ahmadi, S. Pélisset, M. Häyrynen, A. Bera, V. Kontturi, J. Laukkanen, I. Vartiainen, S. Honkanen, M. Kuittinen, "Strip-loaded horizontal slot waveguide," *Opt. Lett.* **42**, 211-214 (2017).
- [5] S. Pélisset, J. Laukkanen, M. Kuittinen, S. Honkanen, M. Roussey, "Modal properties of a strip-loaded horizontal slot waveguide," *J. Eur. Opt. Soc. – Rapid Publ.* **13**:37 (2017).

Finnish Flagship Program on Photonics Research and Innovation

Juha Toivonen

Photonics Laboratory, Tampere University, Tampere, Finland

Corresponding author: juha.toivonen@tuni.fi

Keywords: photonics, education, research and innovation cluster

The Flagship on Photonics Research and Innovation (PREIN) is one of the six Finnish Flagships [1], a northern fleet of excellent science, successful collaboration and solutions for tomorrow. The Flagship programme managed by the Academy of Finland provides a new and unique way for R&D&I in Finland. It supports future knowledge and sustainable solutions to societal challenges and seeks to advance economic growth by developing new business opportunities. PREIN is a light-based technologies competence cluster formed by four partners: Tampere University, Aalto University, University of Eastern Finland, and VTT Research Center [2]. Combining the extensive resources and infrastructures of all the partners, PREIN covers the value chain from fundamental research to applied research, product development and commercialization.

The overall rationale of PREIN is to merge leading-edge Finnish activities in photonics through the whole innovation value chain. Its four partners share the vision that future breakthroughs in photonics depend on deep understanding of light-matter interactions, new materials and nanostructures with enhanced optical responses, advanced laser sources with unique output characteristics, and photonic integration. Through rapid transfer of such advances into potential applications, PREIN will produce disruptive innovations to a variety of application areas and markets. Based on its current high-quality research and commercialization experience, the Consortium will leverage the full potential of joint work between its partners to significantly increase the impact of Finnish Photonics and support the economic growth.

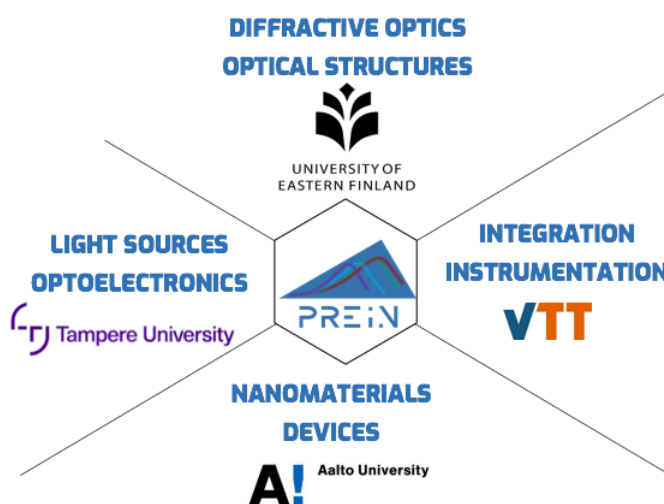


Fig. 1. Photonics Flagship is a cluster of three universities and a research center with diverse profiles and complementary infrastructure.

PREIN organizes outreach events for industry together with Photonics Finland to disseminate information about photonics product and technology opportunities. The events are organized all around Finland, under themes “Photonics in X”, where X stands for an industrial sector, such as Food, Forestry, and Healthcare. We envision organizing 1-2 such events annually.

Academic research provides a crucial platform for educating skilled workforce. Both highly educated workforce with technical skills associated with new technologies and experienced people who understand how problems in the innovation chain can be circumvented by creative solutions. The M.Sc.’s and Ph.D.’s trained by PREIN are highly employable, and to increase this further, the programme organizes recruitment events of early stage researchers for companies and partners, and expand the volume of summer jobs/Master/PhD theses

supported by companies. The full educational path from the second degree to polytechnics and universities needs to be addressed in order to meet the shortage of skilled workforce for various industrial tasks. Pilot projects on this are starting in the Joensuu and Tampere regions, making Finland one of the few countries offering photonics education in polytechnics and vocational schools. Via outreach activities in schools, the programme informs schoolchildren about photonics and its applications, encouraging them to opt for scientific disciplines and consider such disciplines as a career option.

References

1. <https://www.aka.fi/en/research-and-science-policy/flagship-programme/>
2. <https://prein.fi>

Designing random structures for random laser media

Takashi Okamoto¹ and Keigo Imamura¹

¹ Faculty of Computer Science and Systems Engineering, Kyushu Institute of Technology, 680-4 Kawazu, Iizuka, Fukuoka 820-8502, Japan

Corresponding author: okamoto@ces.kyutech.ac.jp

Keywords: random laser, scattering, nanostructures, optical design and fabrication

1. Introduction

Random lasers have been studied for more than two decades from both physical and technical points of view [1–3]. From a physical point of view, random lasing is an interesting subject in that both optical nonlinearity, stemming from absorption and amplification, and multiple light scattering coexist in a random laser medium. From a technical point of view, random lasers are a promising light source because they have high spectral radiance owing to stimulated emission, while they are also speckle-free light sources owing to their low spatial coherence [4].

It is, however, difficult to control the spectrum and the direction of random laser emissions owing to the intrinsically random nature of their emission mechanisms. Some investigations have focused on tuning the emission spectrum and direction by designing a two-dimensional (2D) pattern of pump intensity distributions [5–7]. Although a single sharp spectral peak or a directional control of laser emission can be realized with this method, the pump pattern should be optimized for each random laser medium, making it unsuitable for mass production.

In this study, we investigate the possibility of designing the structure of a random laser medium itself. To simplify the complicated random structures of conventional random lasers, we employ a 2D random medium having a checkerboard pattern structure. This type of device structure has already been utilized in designing a polarization beam splitter as small as $2.4 \times 2.4 \mu\text{m}^2$ with 20×20 pixels [8]. We apply this new design approach to random gain media. Simulations of light scattering and emission are performed using the 2D finite-difference time-domain (FDTD) method. The FDTD method is a time-consuming method; however, limiting the number of scatterer positions in the lattice structure helps to search for an optimal random structure in an affordable time.

2. Simulations

We performed electromagnetic simulations of light scattering for the transverse electric (TE) waves (p-polarization). The model and parameter values used for the simulations are shown in Fig. 1 and Table 1, respectively. The 2D random medium had optical gain (orange) in an area of $4 \times 4 \mu\text{m}^2$ and a refractive index of 1.5. Scattering particles of $0.2 \times 0.2 \mu\text{m}^2$ (white) with a refractive index of 1.0 (without gain) were distributed randomly in the gain region. To eliminate the effect of reflection from the boundary of the medium, the refractive index of the surrounding medium without gain was set at 1.5. The assumed gain medium was Rhodamine 6G, and it was pumped by a continuous light source with a wavelength of 532 nm.

The observation points were set outside the gain medium, and the time variations of the electric field at each point were recorded. The spectrum of emitted light was calculated by Fourier transform of the time variations. We prepared ten samples for each configuration of the random gain media for averaging.

3. Results

A typical emission spectrum observed in this model is the one shown in Fig. 2(e). Several spikes appear in the spectrum. We first examined which conditions are suitable for random lasing by changing the filling fraction of scatterers from 5% to 50%.

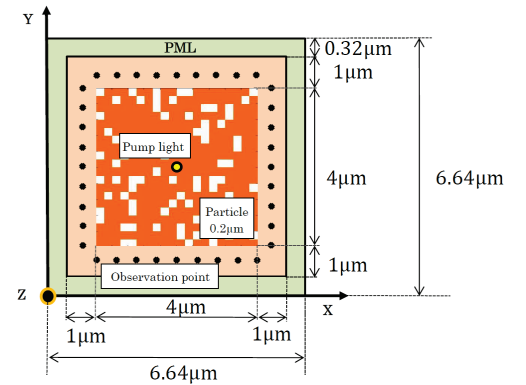


Fig. 1. Schematic of the simulation model. (PML: perfectly matched layer)

Table 1. Parameter values for the simulation.

Refractive index of amplifying medium	1.5
Refractive index of scatterers	1.0
Refractive index of outside medium	1.5
Filling fraction of scatterers (%)	5,10,...,50
Scatterer size (μm)	0.2
Dimension of medium (μm)	4.0×4.0
Number of PML layers	16
Cell size (nm)	20
Wavelength of pump light (nm)	532
Wavelength of gain center (nm)	580

The peak spectral intensity is maximal at a filling fraction of 20%, while the average intensity in the wavelength range of 570–590 nm decreases with an increase of the filling fraction due to a decrease in the area of the gain region. We chose 10%, which showed large values for both the peak and the average intensities.

Next, we optimized the random structure for producing an emission spectrum with a single sharp peak. As a single-peak index, we defined the peak ratio R as the ratio of the highest peak spectral intensity to the second highest peak intensity. We employed a simplified version of the direct binary search (DBS) method [8] to limit the computational time. The algorithm is as follows: (1) prepare five different media; (2) calculate spectra observed from each of the four sides (20 spectra in total); (3) choose the one that shows the largest R value (initial state); (4) choose a scatterer and move it by one pixel (0.2 μm) in a randomly selected direction; (5) if the value R is larger than the previous one, fix the scatterer at the new position, and if it is smaller than the previous one, move it back to its original position; and (6) perform steps 4 and 5 for all scatterers (final state).

A successful example is shown in Fig. 2. As the number of trials increases, the difference between the intensities of the largest peak and the other lower peaks in the emission spectrum gradually increases, and eventually only a single peak survives. However, a small change is observed in the peak wavelength from one trial

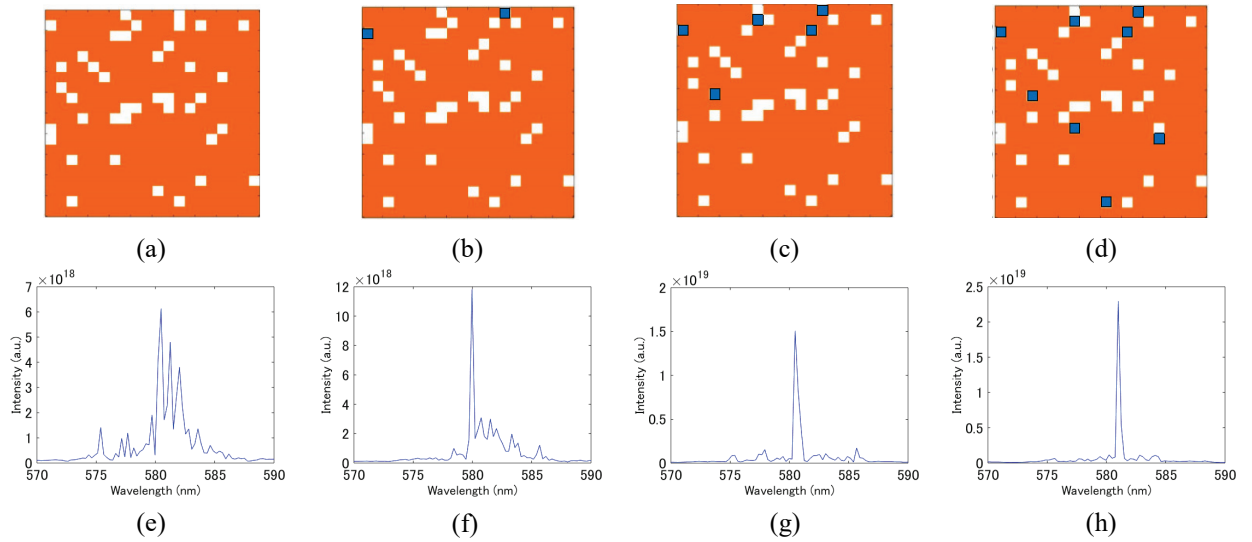


Fig. 2. Optimization of scatterer positions to generate a single spectral peak. The configuration of scatterers and the corresponding spectra for the initial state (a, e), the third scatterer (b, f), the 19th scatterer (c, g), and the final state (d, h). The pixels in blue in (a) – (d) represent moved scatterers.

to the next, which indicates the unstable nature of this nonlinear system. Figure 3 illustrates this unstable behavior, showing how the peak ratio can change dramatically by shifting even a single scatterer.

4. Conclusions

We investigated the possibility of designing the scatterer configuration of random laser media for generating a single peak spectral emission. We found that control of the emission spectrum could be realized with the DBS method to some extent. However, further work is needed to produce a specific spectrum in a precise manner.

References

1. D. S. Wiersma, *Nat. Phys.* **4**, 359–367 (2008).
2. H. Cao, *J. Phys. A: Math. Gen.* **38**, 10497–10535 (2005).
3. M. A. Noginov, *Solid-State Random Lasers*, (Springer, New York, 2005).
4. B. Redding, M. A. Choma, and H. Cao, *Nat. Photonics* **6**, 355–359 (2012).
5. M. Leonetti and C. López, *Appl. Phys. Lett.* **102**, 071105 (2013).
6. N. Bachelard, S. Gigan, X. Noblin, and P. Sebbah, *Nat. Phys.* **10**, 426–431 (2014).
7. T. Hirsch, M. Lierzer, D. Pogany, F. Mintert, and S. Rotter, *Phys. Rev. Lett.* **111**, 023902 (2013).
8. B. Shen, P. Wang, R. Polson, and R. Menon, *Nat. Photonics* **9**, 378–382 (2015).

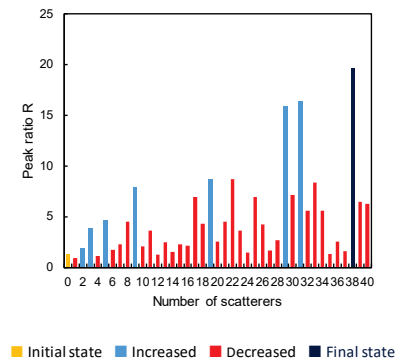


Fig. 3. Peak ratio R as a function of the number of trials (one trial for each scatterer).

Broadband Electromagnetic Radiation Detector Based on Photoacoustic Effect

Jussi Rossi¹, Juho Uotila³, Toni Laurila², Erkki Ikonen² and Markku Vainio^{1,4}

¹ Photonics Laboratory, Physics Unit, Tampere University, Tampere, Finland

² Metrology Research Institute, Aalto University, Espoo, Finland

³ Gasera Ltd, Turku, Finland

⁴ Department of Chemistry, University of Helsinki, Helsinki, Finland

Corresponding author: jussi.rossi@tuni.fi

Keywords: photoacoustic, power detector, silicon cantilever microphone

Power detector is a central component in nearly all measurement and imaging technologies that use electromagnetic radiation for either scientific or industrial purposes. Currently a large selection of different detectors is needed to cover all the required wavelengths, power levels and sensitivities, especially in research laboratories. The goal of the present research is to develop a highly sensitive general purpose room-temperature photoacoustic power detector that can be used for traceable detection of electromagnetic radiation covering broad spectral range from the UV to the far-IR and THz (30 μm – 300 μm) range and wide power range between nW and W levels. In the far-IR and THz regions, the availability of power detectors that do not require cryogenic operating conditions is rather poor [1].

The basic idea of a photoacoustic power detector is the following: incident electromagnetic radiation is chopped and absorbed by a black absorber, which is placed in a closed volume filled with acoustic carrier gas converting the small increase in the heat of the absorber into a pressure signal. This pressure signal, which is directly proportional to the energy of absorbed radiation, is detected with a microphone. The photoacoustic effect is highly linear and the measurement devices using novel silicon cantilever microphone solutions are highly sensitive [2] and compact. Such properties combined with cost-effectiveness and wavelength independence make the photoacoustic principle an ideal candidate for power detection applications. In this contribution, we demonstrate a very good linear dynamic range, high detection sensitivity and broad wavelength coverage using a photoacoustic optical power detector based on a low-noise silicon cantilever microphone.

We constructed a power detector prototype, which was tested with different types of absorber materials such as carbon nanotubes and metal foils blackened by painting or sooting. The power detector prototype was characterized at several wavelengths between the visible (633 nm) and mid-infrared (10 μm) spectral regions. Fig. 1 shows an example demonstrating the large linear dynamic range of the detector. As shown in Fig. 1b, the linear power range can be shifted by changing the radiation chopping frequency. According to the first measurements at 1532 nm, the limit of detection is in the single nW range.

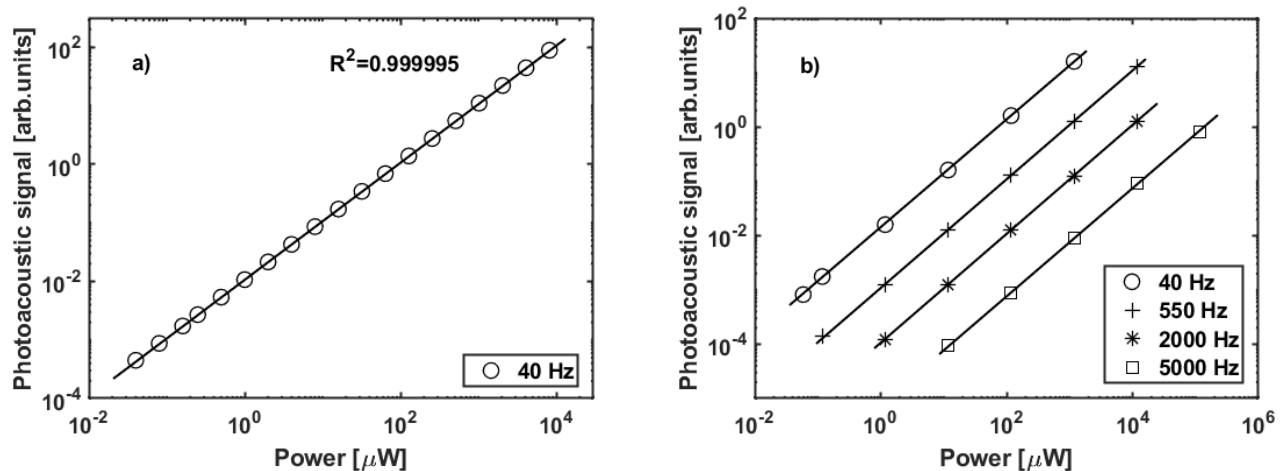


Fig. 1: a) A linearity measurement made with a 633 nm He-Ne laser. The power range is 40 nW – 8 mW. b) The linear range was extended to 60 nW – 120 mW by increasing the modulation frequency and using a 1064 nm high-power fiber laser. Reference power levels were measured with NIST calibrated Thorlabs S120C and S305 detectors.

The very good linearity is visible in the graphs. Typical R-squared values for a linear fit are of the order 0.99999 – 0.999999. The demonstrated power detector concept has good market potential. Table 1 contains specifications for six different types of commercial power detectors on market. The values are collected from the datasheets of the manufacturers. The last row represents the target specifications for our detector.

Table. 1: Comparison of commercially available power detectors covering wavelengths from visible to microwave range.

Detector	Detector type	Wavelength range	Dynamic range
Thorlabs S120C	Si photodiode	400 – 1100 nm	50 nW – 50 mW
Ophir RM-9 Pyro	Pyroelectric	0.15 - 12 μm	100 nW- 100 mW
Ophir RM-9 THZ	Thermal	10 - 3000 μm	100 nW- 100 mW
TYDEX GC-1P	Golay cell	15 - 8000 μm	0.15 nW – 10 μW
IRLabs General 4.2 K	Bolometer	15 - 2000 μm	0.12 pW -
TK instruments	Photoacoustic	100 - 10000 μm	5 μW - 500 mW
Our detector	Photoacoustic	0.4 – 400 μm	1 nW – 1 W

We have measured the limit of detection and the maximum detected power with our current detector prototype to be c.a. 10 nW and 1 W, respectively, which corresponds to a dynamic range of eight orders of magnitude. The longest calibration wavelength we have used so far is 10 μm but, according to the theory and prior experimental research on hyperblack blackbody absorbers [3], the detector responsivity should remain flat all the way to the THz range.

In the future, the sensitivity of the power detector will be further improved by more detailed modeling of the properties of the photoacoustic measurement chamber, light absorber and the silicon cantilever microphone. Measurements and calibrations with far-IR and THz radiation sources will also be carried out.

References

1. Antoni Rogalski, "Infrared detectors: status and trends", *Progress in Quantum Electronics* **27** (2), pp. 59-210, 2003.
2. Teemu Tomberg, Markku Vainio, Tuomas Hieta, and Lauri Halonen, "Sub-part-pertrillion level detection of hydrogen fluoride by cantilever-enhanced photo-acoustic spectroscopy", *arXiv:1707.01312*, 2017.
3. John Lehman et al., "Planar hyperblack absolute radiometer", *Optics Express*, Vol. **24**, No. 23, 14 Nov 2016.

Measurement facility for high accuracy multiphoton absorption spectra

Meelis-Mait Sildoja¹, Charles W. Stark¹, Jüri Pahapill¹, Matt Rammo¹, Katrin Petritsenko¹ and Aleksander Rebane^{1,2}

¹National Institute of Chemical Physics and Biophysics (NICPB), Tallinn

²Montana State University, Bozeman, Montana

Corresponding author: meelis.sildoja@kbfi.ee

Keywords: nonlinear optics, multiphoton absorption, 2PA, MPA

Multiphoton absorption (MPA) is a nonlinear-optical process, where two or more photons induce a vertical electronic transition from a lower-energy state to a higher-energy state, such that the energy difference between the states equals the combined energy of the absorbed photons. Such transitions have very low probability under ambient illumination. However, their efficiency increases rapidly as a power function under increasing photon flux.

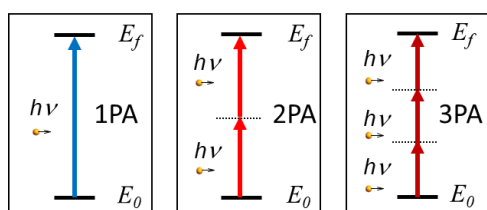


Fig. 1. Absorption processes. 1PA, 2PA and 3PA indicate how many photons participate in the absorption process.

Quantitative nonlinear multiphoton detection is driven by the needs of non-invasive medical diagnostics [1], material science [2] and secure optical communications [3, 4]. We have established a world-class facility for the measurement of nonlinear multiphoton spectra. The femtosecond laser system allows broad wavelength tunability throughout VIS and NIR range to determine absolute 2-photon and 3-photon absorption cross-section spectra of emissive compounds or materials. Detailed description of the system is shown in Figure 2. Emission from the laser is directed through beam shaping optics and a variable neutral density filter to adjust the pulse power. The polariser and waveplate before the sample allow studying the effects of varied polarisations on the absorption. Emission from sample is collected via focusing optics and spectrometer equipped with a photomultiplier tube. Pulse power is monitored with pyroelectric detector. Signals are recorded with fast 10-bit digital oscilloscope synced with the laser pulses. The facility is automated and controlled via LabView.

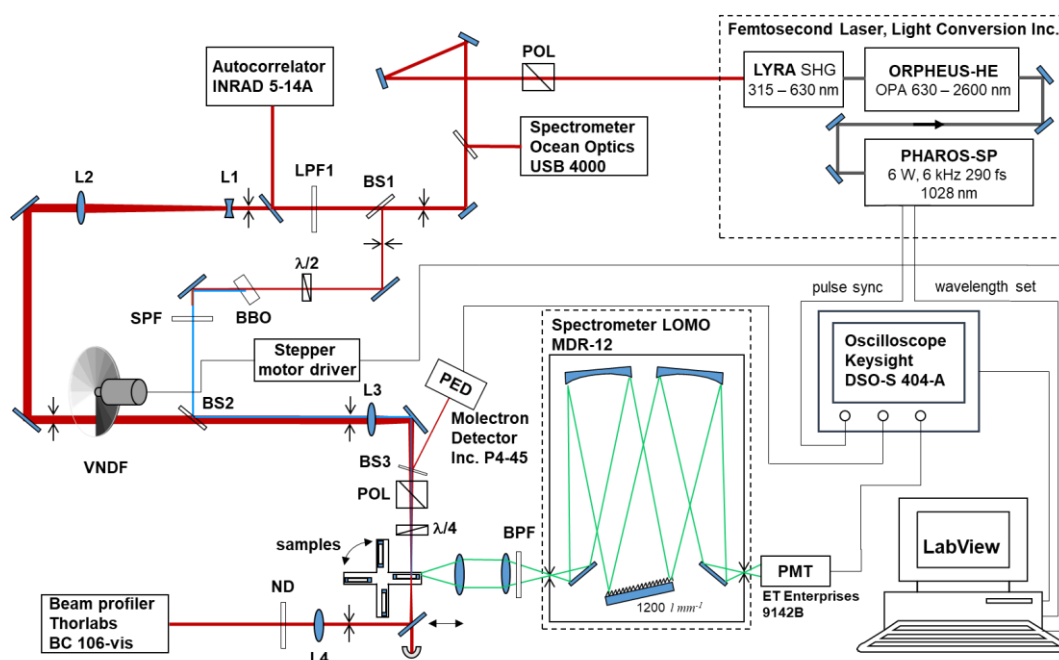


Fig. 2. Schematic of the automated femtosecond 2PA/3PA spectrometer. POL - polarizer; BS - beam splitter; LPF - long-pass filter; SPF - short-pass filter; BPF - band-pass filter; L1, L2, L3, L4 - focusing lenses; $\lambda/2$ - half-wave plate; BBO - barium borate crystal; VNDF - variable neutral density filter; ND - neutral density filter; PED - pyroelectric detector; $\lambda/4$ - quarter wave plate; PMT - photomultiplier tube.

The unique properties of the facility include the wide tunability of the wavelengths from 315 nm to 2600 nm, wavelength adjustment resolution of 1-2 nm, consecutive measurements of up to four samples, four order magnitude range of signal detection, beam profiling as well as pulse shape measurement capabilities. In Figure 3. the black-dotted line shows our latest high-resolution absorption cross-section spectrum of Ru(1,10-phenanthroline)₃(PF₆)₂ complex. As a comparison, measurements from other research groups (green-diamond and red-triangle lines) and our previous facility (blue-square line) are given. The green and red lines are extracted from references [5, 6].

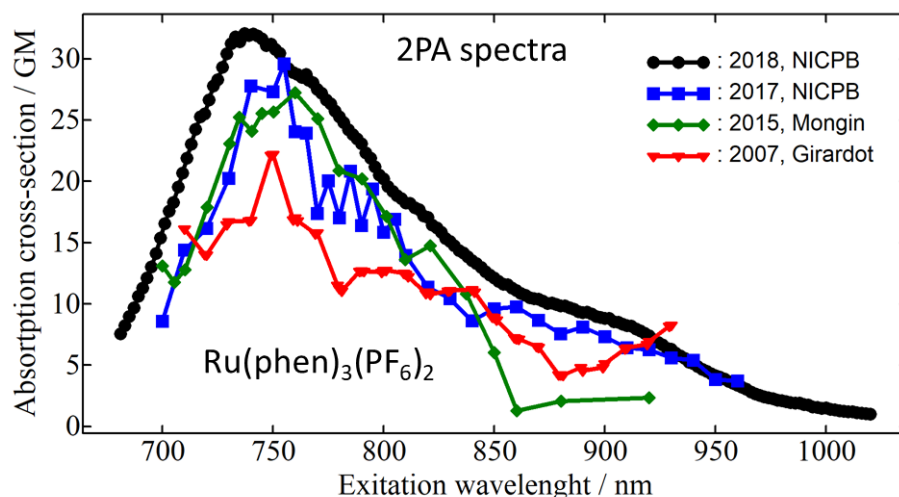


Fig. 3. Absorption cross-section spectra, in Goeppert-Mayer (GM) ($10^{-50} \text{ cm}^4 \cdot \text{s} \cdot \text{photon}^{-1}$), of Ru(phen)₃(PF₆)₂ reference complex in acetonitrile measured by different workgroups. Black line indicates vastly improved result with respect of range and resolution achieved with the new setup shown in Fig. 2.

Currently the absolute uncertainty of the measured absorption cross-section is in the order of 10-15%. After the full characterisation of the setup we aim to perform traceable 2PA cross-section measurements with less than 5% of absolute and relative uncertainty. One factor that helps to achieve the low uncertainty is to measure exactly the time resolved power of the incident high energy pulses ($>10^{30} \text{ photon cm}^{-2} \text{ s}^{-1}$) as current indirect estimation is prone to errors. Namely, we plan to exploit the inherent two-photon absorption properties of GaP sensors as the generated photocurrent is directly proportional to the nonlinear photon flux [7].

Our broader goal is to develop a world-class metrological facility for nonlinear multiphoton light absorption- and calibration measurements and provide service for other research labs as well as for industry (medical imaging, fundamental research, quantum information applications). We have already established a database of our 2PA (in future also 3PA) measurements which can be found in www.kbfi.ee/mpa.

References

1. A. Mikhaylov, S. de Reguardati, J. Pahapill, P. R. Callis, B. Kohler and A. Rebane, *Biomed. Opt. Expr.* **9**(2), 447 – 452 (2018).
2. R. S. Price, G. Dubinina, G. Wicks, M. Drobizhev, A. Rebane and K. S. Schanze, *ACS Appl. Mater. Interfaces* **7**, 10795-10805 (2015).
3. F. Schlawin, *J. Phys. B: At. Mol. Opt. Phys.* **50**, 203001 (2017).
4. O. Varnavski, B. Pinsky and T. Goodson III, *J. Phys. Chem. Lett.* **8**, 388–393 (2017).
5. O. Mongin, M. Four, S. Chevreux, M. Blanchard-Desce, G. Lemerrier, *CHIMIA International Journal for Chemistry*, **69**(11), 666-669 (2015).
6. C. Girardot, G. Lemerrier, J.- C. Mulatier, J. Chauvin, P. L. Baldeck and C. Andraud, *Dalton Transactions* **0**(31) (2007).
7. E. Z. Chong, T. F. Watson, and F. Festy, *Appl. Phys. Lett.* **105**, 062111 (2014).

Printed electronics in pilot scale processing and production of organic photovoltaics, CIGS solar cells and OLEDs

Marja Vilkmán¹, Kaisa-Leena Väisänen², Marja Välimäki², Mari Ylikunnari², Thomas Kraft²

¹ VTT Technical Research Centre of Finland, Tietotie 3, P.O. Box 1000, FI-02150 Espoo, Finland

² VTT Technical Research Centre of Finland, Kaitoväylä 1, P.O. Box 1100, FI-90571 Oulu, Finland

Corresponding author: marja.vilkmán@vtt.fi

Keywords: Printed electronics, organic solar cell, lifetime, production

Printed Electronics offers tools for large-area processing of novel products, enabling e.g. flexibility and freedom of design. This presentation introduces printed electronics as a processing method and shows how it can be used in production of optoelectronic components. Specifically, I will focus on showing how to guarantee optimal lifetime, quality and performance in pilot scale processing of organic solar cells (see image from Fig. 1). In addition, I will give you an outlook on production of organic and CIGS solar cells and OLEDs – a Factory of the Future.

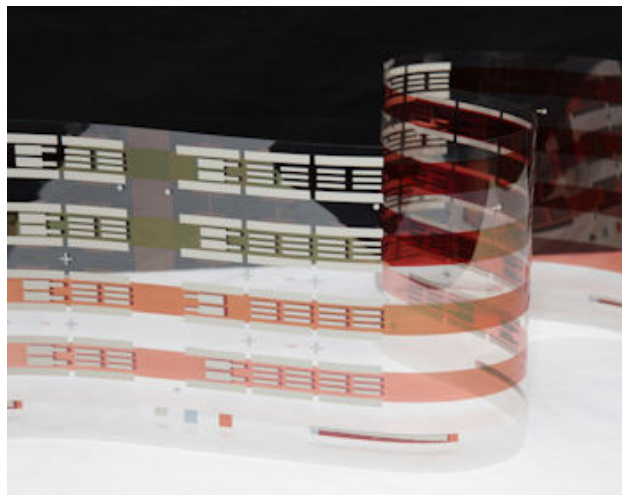


Fig. 1. A picture of a flexible organic solar cell roll.

Understanding the phenomena, which have an effect on performance and lifetime of flexible solar cells, is essential when transferring the process to pilot scale. Often the promising results in laboratory do not directly convert into good performance with large-area roll-to-roll (R2R) processed and encapsulated solar modules. We have faced this challenge while testing new materials for organic solar cells.

For example, replacing PCBM with ICBA as an acceptor should result in increased performance due to higher V_{oc} . In sheet-to-sheet (S2S) scale this is true, but R2R processing gave different results. ICBA-containing modules required also long light soaking to recover from an S-shaped IV curve, which appeared after encapsulation. In addition, we use plasma treatment for improving the adhesion of a ZnO nanoparticle layer and this process works in R2R scale. However, we have observed that the plasma-treated modules also require more light soaking after encapsulation to work well. Motivated by these challenges, we wanted to study the S-shape related phenomena closer. Naturally, the focus was in energy level alignment. I will show that energy level matching is crucial especially for R2R processed, encapsulated solar cell modules. In addition, I will also show that the improved adhesion leads to significantly improved lifetime – even without mechanical stressing. Both of the observations give guidelines for producing stable solar modules in R2R environment.

Finally, even with carefully selected materials and processes, the R2R processing itself can create challenges. It is not anymore easy to follow the quality and avoid waste when the processing speed is high and the production volumes are large. There are several characterization methods available but they are not necessarily suitable for large-area production. To overcome this challenge and to be able to follow and control the quality of large-scale production of organic and CIGS solar cells and OLEDs, we have launched an EU project, OLEDSOLAR. Together with 16 partners – VTT, Fraunhofer, TNO, IRIS, Opvius, TWI, CSEM, Solibro, Meyer Burger, Brunel University London, Leitat, Coatema, DuPont Teijin Films, CTR, Advent and Inuru –

we aim to find the best quality control methods and implement those in the pilot and production lines to allow high yield and process speed. This presentation will summarize the objectives of the OLEDsOLAR project and give an outlook for future production of flexible electronics.

References

1. M. Vilkmann, K.-L. Väisänen, P. Apilo, R. Po, M. Välimäki, M. Ylikunnari, A. Bernardi, T. Pernu, G. Corso, J. Seitsonen, S. Heinilehto, J. Ruokolainen, J. Hast, *ACS Applied Energy Materials*, 1, 5977-5985 (2018).
2. OLEDsOLAR project: <https://oledsolarproject.eu/>

Predictable Quantum Efficient Detector (PQED) based on n-type silicon induced junction photodiodes

Timo Dönsberg¹, Santeri Porrasmaa², Farshid Manoocheri² and Erkki Ikonen^{1,2}

¹ National Metrology Institute VTT MIKES, VTT Technical Research Centre of Finland Ltd, Espoo, Finland

² Metrology Research Institute, Aalto University, Espoo, Finland

Corresponding author: timo.donsberg@vtt.fi

Keywords: radiometry, optical power, induced junction photodiode, simulation

The Predictable Quantum Efficient Detector (PQED) [1-2] is a semiconductor based primary standard of optical power that can be operated at room temperature [3-4]. It consists of two induced-junction photodiodes, which are mounted in a wedged trap configuration for the control of specular reflectance losses. Using one-dimensional modelling, the near-zero internal quantum deficiency (IQD) of the custom photodiodes has been predicted with an estimated standard uncertainty of 70 ppm in the visible wavelength range [5]. The modelled results have been experimentally confirmed with measurements against cryogenic radiometers [2]. There is an ongoing work to improve the prediction using three-dimensional modelling [6].

Until recently, all PQEDs were based on induced junction photodiodes, where a SiO₂ layer is thermally grown on top of very lightly doped p-type silicon substrate. This structure inherently contains trapped positive surface charge close to the Si-SiO₂ boundary, which generates an n-type inversion layer in the p-type silicon and produces a depletion region required for photocurrent generation [1]. This approach, however, has two downsides. First, the availability of suitable substrate material is problematic. Second, the thermal growing process operating at around 1000 K is time-consuming, expensive and increases the risk of contamination.

Recently, a new type of PQED photodiodes were introduced [7] that utilize induced junction, which is manufactured using n-type silicon substrate. The underlying structure of the new photodiode, shown in Fig. 1.a. is similar to the previous design, but the n-type substrate requires negative charge to be trapped in the passivation layer in order to form the depletion region. This was achieved by fabricating an Al₂O₃ layer on top of the substrate. Due to the higher fixed charge density, the Al₂O₃ layer can be a factor of 10 thinner than the SiO₂ layers used with p-type PQED photodiodes.

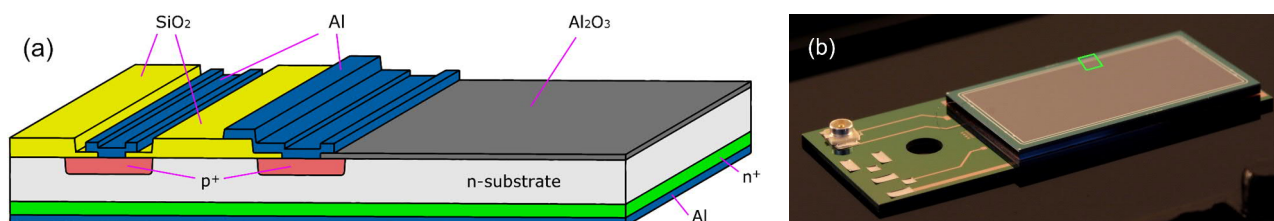


Fig. 1. (a) Cross section of the structure of the set B photodiode (not to scale). (b) A PQED photodiode of size 11 mm x 22 mm attached to the photodiode carrier. The added green square indicates the area of (a).

Two sets of photodiodes, denoted as set A and B, were manufactured using substrates with doping concentrations of $2.5 \cdot 10^{11} \text{ cm}^{-3}$ and $4.4 \cdot 10^{11} \text{ cm}^{-3}$, respectively [7]. The Al₂O₃ layers were grown using atomic layer deposition (ALD) [8], which provides a controlled method to produce uniform oxide layers to an atomically specified thickness. Oxide thicknesses ranging from 25 nm to 30 nm were produced. The responsivity was modelled for both sets, and detectors from both sets were characterized for temperature dependence of dark current, spatial uniformity of responsivity, reflectance and absolute responsivity.

In addition to smaller doping concentration, the set A photodiodes also had 16 guard rings in the photodiode layout as opposed to the one of set B (the outermost p⁺ implantation of Fig. 1.a.). These factors lead to the decrease of dark current at room temperature by a factor of five, down to around 1 nA level when biased with a 10 V voltage. When the photodiode is cooled in a cryostat [9], the dark current decreases exponentially; approximately a decade for every decrease of 15 °C in temperature. Improved dark current properties become significant at low flux applications of the PQED, such as photometric measurements [10-11], or single or few photon applications [12]. Preliminary measurements indicate that the absolute power of a laser in the picowatt scale can be measured with a standard uncertainty of 0.3% within 5-minute measurement period.

Due to different oxide thicknesses of the photodiodes, reflectances measured at the wavelength of 488 nm varied between 110 ppm and 170 ppm. The reflectance is higher than that of p-type PQEDs of around 27 ppm.

Nevertheless, the responsivity of the n-type PQED is similarly uniform as that of the p-type PQED; the responsivity in the central active area is flat within 30 ppm peak-to-peak deviation.

A 3D simulation model of the photodiode structure was built into the semiconductor simulation software Cogenda Genius v. 1.8.0. With the exception of surface recombination velocity (SRV) for electrons and holes and Al_2O_3 layer fixed charge (FC), the modelling parameters were obtained from the wafer manufacturer or they can be directly measured. We developed a method to extract the values for the SRV and FC, where simulated bias voltage dependence of photocurrent is fitted to experimental data (see Fig. 2.a.). SRV values of $3 \cdot 10^4$ cm/s and $5 \cdot 10^5$ cm/s, and FC values of $3.9 \cdot 10^{12}$ cm $^{-2}$ and $4.5 \cdot 10^{12}$ cm $^{-2}$ were obtained for set A and B, respectively.

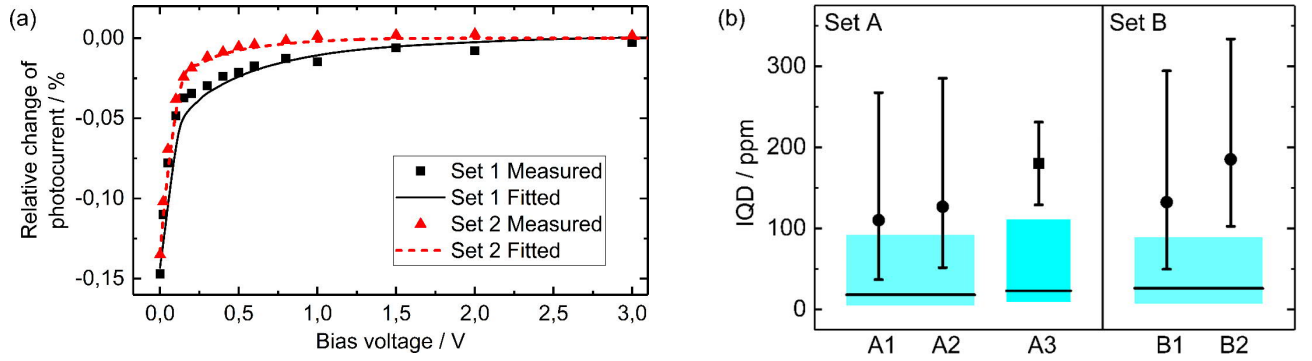


Fig. 2. (a) Relative change of photocurrent as a function of bias voltage at 488 nm. The simulated curves are fitted to experimental values in order to obtain SRV and FC values. (b) Absolute IQD measured at 488 nm (dots) and 532 nm (square). Horizontal lines show the predicted IQD and cyan boxes indicate the estimated uncertainty of the model at 95% confidence level.

The predicted IQD values for set A and B were 18 – 23 ppm and 26 ppm, respectively. Tentative analysis indicates estimated standard uncertainty of around 40 ppm for the predicted IQD at room temperature. The responsivities of the n-type detectors were also measured against a p-type PQED, similar to those characterized in [2] and [3]. The IQD values obtained from responsivity and reflectance measurements, together with the predicted values, are shown in Fig. 2.b.

A new type of PQED was developed – first ever to utilize n-type silicon and ALD. Two sets of detectors were manufactured, modelled and characterized. The agreement between experimental and modelled results indicates that the n-type structure is a very promising alternative to the existing p-type PQEDs, and exhibits better dark current properties. Consequently, it proves that the manufacturing of PQEDs is no longer dependent on the availability of a particular silicon process. Finally, this work gives additional credibility to the concept of a modelled quantum detector serving as a primary standard.

References

1. M. Sildoja, F. Manoocheri, M. Merimaa, E. Ikonen, I. Müller, L. Werner, J. Gran, T. Kübarsepp, M. Smîd and M. L. Rastello, *Metrologia* **50**, 385–394 (2013).
2. I. Müller, U. Johannsen, U. Linke, L. Socaciu-Siebert, M. Smîd, G. Porrovecchio, M. Sildoja, F. Manoocheri, E. Ikonen, J. Gran, T. Kübarsepp, G. Brida and L. Werner, *Metrologia* **50**, 395–401 (2013).
3. T. Dönsberg, M. Sildoja, F. Manoocheri, M. Merimaa, L. Petroff and E. Ikonen, *Metrologia* **51**, 197–202 (2014).
4. J. Zwinkels, A. Sperling, T. Goodman, T. J. C. Acosta, Y. Ohno, M. L. Rastello, M. Stock and E. Woolliams, *Metrologia* **53**, G1 (2016).
5. J. Gran, T. Kübarsepp, M. Sildoja, F. Manoocheri, E. Ikonen and I. Müller, *Metrologia* **49**, S130–S134 (2012).
6. M. U. Nordsveen, C. K. Tang and J. Gran, *Opt. Express* **25**, 8459–8469 (2017).
7. T. Dönsberg, F. Manoocheri, M. Sildoja, M. Juntunen, H. Savin, E. Tuovinen, H. Ronkainen, M. Prunnila, M. Merimaa, C. K. Tang, J. Gran, I. Müller, L. Werner, B. Rougié, A. Pons, M. Smîd, P. Gál, L. Lolli, G. Brida, M. L. Rastello and E. Ikonen, *Metrologia* **54**, 821–836 (2017).
8. M. Leskelä and M. Ritala, *Thin Solid Films* **409**, 138–146 (2002).
9. F. Manoocheri, T. Dönsberg, M. Sildoja, M. Smîd, G. Porrovecchio and E. Ikonen, *J. Phys. Conf. Ser.* **972**, 012021 (2018).
10. T. Dönsberg, T. Pulli, T. Poikonen, H. Baumgartner, A. Vaskuri, M. Sildoja, F. Manoocheri, P. Kärhä and E. Ikonen, *Metrologia* **51**, S276–S281 (2014).
11. T. Pulli, T. Dönsberg, T. Poikonen, F. Manoocheri, P. Kärhä and E. Ikonen, *Light Sci. Appl.* **4**, e332 (2015).
12. A. Vaigu, G. Porrovecchio, X.-L. Chu, S. Lindner, M. Smid, A. Manninen, C. Becher, V. Sandoghdar, S. Götzinger, and E. Ikonen, *Metrologia* **54**, 218 (2017).

TAPERED FIBER AMPLIFIER FOR COHERENT LIDAR

Kim Patokoski¹, Joonas Rissanen², Teppo Noronen², Regina Gumenyuk^{1,2}, Yuri Chamrovskii³, Valery Filipov², Juha Toivonen¹

¹Photonics Laboratory, Tampere University, Tampere, Finland

²Ampliconyx Ltd, Tampere, Finland

³Kotel'nikov Institute of Radio Engineering and Electronics, Moscow, Russian Federation,

Corresponding author: kim.patokoski@tuni.fi

Keywords: optics, lithography, nanostructures

Coherent lidars in atmospheric sensing rely on narrow linewidth fiber amplifier based light sources. The achievable peak power with typical single mode fibers is limited to tens of watts [1], still enabling the heterodyne detection of wind speed from particle backscatter [2]. Kilowatt-level peak power could enable detection of spectrally broader molecular backscatter, yielding access to simultaneous visibility and particle type profiling alongside the wind speed measurement. Even temperature profiling, considered as a holy grail of weather forecasting, has been demonstrated with high spectral resolution analysis of molecular backscatter [3].

Stimulated Brillouin scattering (SBS) in the optical fibers is the main effect limiting the peak power. The strong electric field density induces lattice vibrations (phonons) creating a temporary reflection grating inside the fiber. The backwards travelling wave is especially harmful inside the amplifier as it experiences high gain causing instability and possible damage to the amplifier. In this work, we present successful light source development results for coherent lidar using tapered ytterbium doped fiber amplifier at 1.053 μm . By combining several SBS mitigation techniques simultaneously we are able to reach more than two order of magnitude enhancement in output peak power compared to single mode fiber.

The light source design follows a typical seed laser - pre-amplifier - power amplifier scheme and is shown in detail in Fig.1.

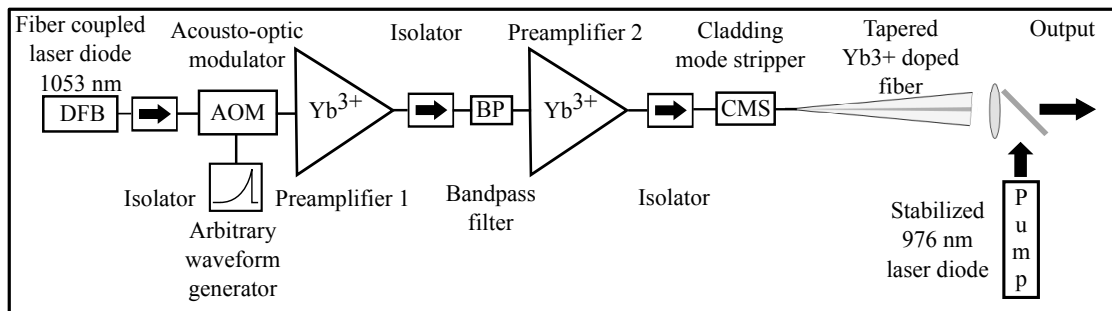


Fig. 1. Schematic picture of the fiber amplifier system.

Light from distributed feedback laser diode is chopped to pulses by an acousto-optic modulator and coupled through a dual stage pre-amplifier. The single mode ytterbium doped gain fibers are core pumped counter to signal propagation and the amplified spontaneous emission is filtered between stages.

The pulses are finally coupled to a power amplifier containing an ytterbium doped cladding pumped fiber, which has a tapered longitudinal profile. A cladding mode stripper is used to remove unabsorbed counter propagating pump. The core radius grows slowly from 16 μm to 50 μm along the 1.2-m-long fiber and the profile can be seen in Fig. 2. All fiber components, including the tapered fiber, are polarization maintaining.

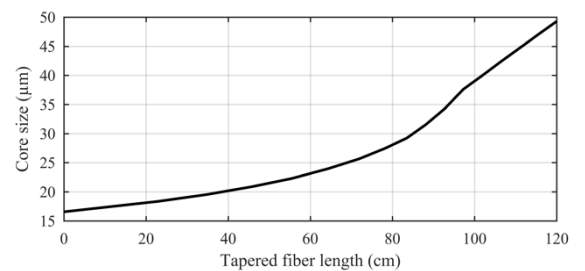


Fig. 2. Measured core size along the tapered double clad fiber

The main advantage compared to other coherent lidar light sources becomes from the power amplifier design. The seed laser and pre-amplifier are similar to typical coherent lidar sources and the output peak power

after pre-amplifier is SBS limited to 10 W. However, with the unique tapered power amplifier we achieved record high peak power of 2.2 kW with linear polarization and single mode output. The polarization extinction ratio is 20 dB and the measured $M^2=1.05/1.08$ indicates excellent beam quality, unreachable by other competing technologies such as large mode area fibers.

Coherent lidar signal-to-noise ratio is highly dependent on good beam quality and linear polarization [4]. Combined with high peak power, we expect unparalleled performance with coherent lidar. We continue to assemble a prototype system to demonstrate lidar performance in simultaneous wind speed, visibility and particle profiling. The tapered fiber amplifier is definitely a key technology enabler for coherent lidar reaching record high multi kilowatt peak power, while maintaining excellent beam quality and linear polarization state.

References

1. Canat, C., Jaouën, Y., Mollier, J.C, C. R. Physique, **7**, 177-186 (2006).
2. Hirsikko, A. et al, Atmos. Meas. Tech., **7**, 1351–1375 (2014)
3. Witschas et al., Optics letters, **39**, 1972-1975 (2014)
4. J.-P. Cariou et al., C. R. Physique **7**, 213-223 (2006)

Fourier Transform Photoacoustic Spectroscopy with Supercontinuum Light Source

Tommi Mikkonen¹, Caroline Amiot^{1,2}, Antti Aalto¹, Kim Patokoski¹, Goëry Genty¹, Juha Toivonen¹

¹ Photonics Laboratory, Physics Unit, Tampere University, PO Box 692, FI-33014 Tampere, Finland

² Institut FEMTO-ST, UMR 6174 CNRS - Université Bourgogne Franche-Comté, 15B av. des Montboucons, F-25030 Besançon, France

Corresponding author: juha.toivonen@tuni.fi

Keywords: broadband photoacoustic sensing, supercontinuum light source, Fourier transform spectroscopy

In contrast to conventional absorption spectroscopy methods, photoacoustic spectroscopy (PAS) measures the absorbed light power directly, which makes the technique highly sensitive and also enables small sample volumes [1]. These properties are important in multicomponent trace-gas analysis, which is possible in PAS using a broadband light source together with a Fourier transform spectrometer (FTS) as a light modulator. Scanning FTS creates a distinct modulation frequency for each wavelength of the source, which leads to the formation of several pressure waves in the photoacoustic cell due to periodic gas absorption and thermal relaxation. Pressure variations are then detected using a cantilever microphone with optical readout. Cantilever-enhanced photoacoustic spectroscopy (CEPAS) is a non-resonant photoacoustic technique enabling sensitive detection over a wide range of frequencies [2]. The CEPAS technique together with FTS has so far been used only with conventional infrared radiators, which suffer from poor spectral power density [3].

In this work, we demonstrate broadband Fourier transform photoacoustic spectroscopy using two supercontinuum light sources at 1–3.5 μm wavelength range [4]. The supercontinua were generated using the same optical fibers and a pump laser, whose repetition rate was varied between 70 kHz and 400 kHz. The experimental setup is illustrated in Figure 1. Compared to conventional infrared radiators, the supercontinua provide larger spectral power density and therefore larger photoacoustic signal. We measured rovibrational photoacoustic spectra of water vapor in air and methane (400 ppm) in nitrogen at atmospheric pressure using an infrared radiator and the supercontinua as light sources. The sample volume was smaller than 8 mL. The measured spectra shown in Figure 2 were recorded in 50 s (10 scans) with 120 GHz resolution and they are in good agreement with a model based on HITRAN database.

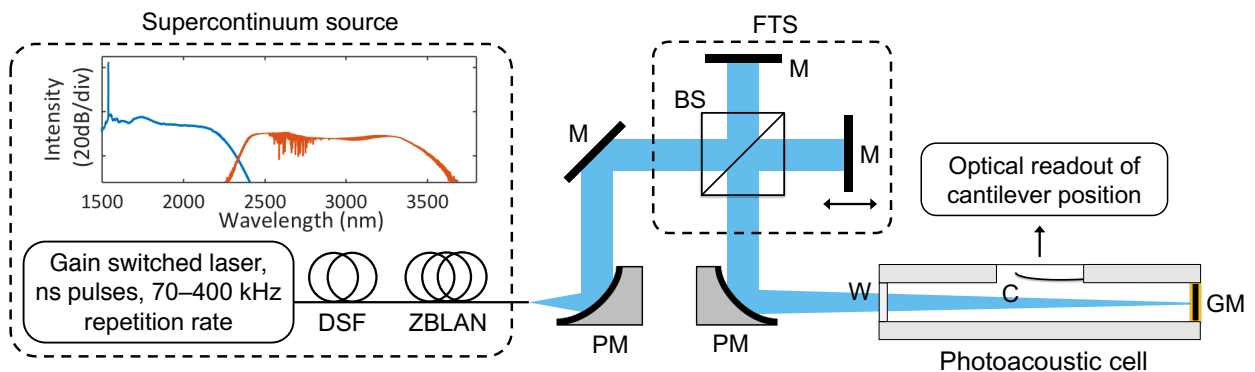


Fig. 1. Experimental setup. PM, off-axis parabolic mirror; M, mirror; BS, beam splitter; W, window; GM, gold mirror; C, cantilever. Note that the supercontinuum generated using lower repetition rate (red spectrum) was long-pass filtered at 2.3 μm .

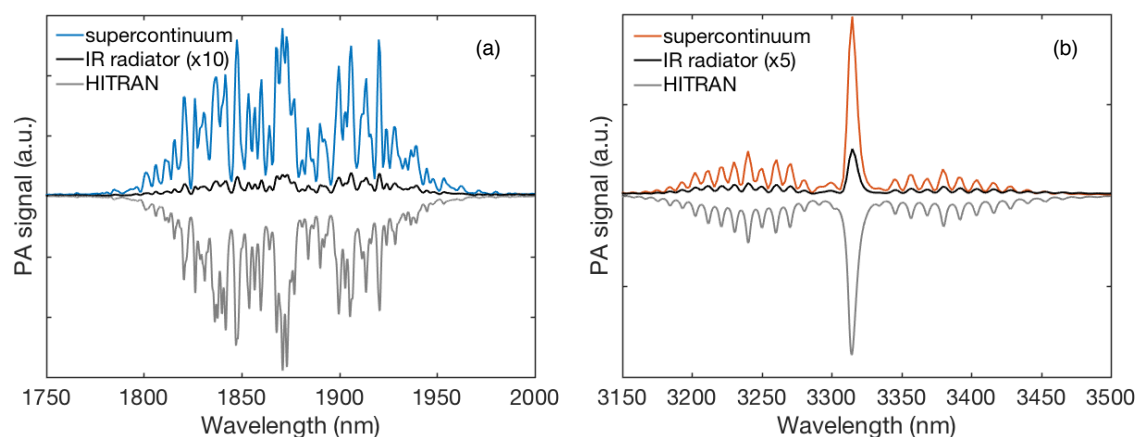


Fig. 2. Photoacoustic spectra of (a) water vapor and (b) methane measured using two supercontinua (blue and red) and a broadband infrared source (black, magnified). Reference spectra from HITRAN database are also shown (grey, inverted).

We achieved a 20- and 70-fold increase in photoacoustic signal with the supercontinua compared to the infrared radiator, demonstrating the advantage of larger spectral power density of the supercontinuum sources. In addition to the improvement in sensitivity, the spatially coherent and collimated supercontinuum beam enables miniaturization of the FTS and better resolution as compared to the infrared radiator. Thus, the combination of supercontinuum light source, FTS and CEPAS detection enables broadband multi-gas analysis using small sample volumes.

References

1. J. Li, W. Chen, B. Yu, *Recent Progress on Infrared Photoacoustic Spectroscopy Techniques*, Appl. Spectrosc. Rev. **46**, 440-471 (2011).
2. T. Kuusela, J. Kauppinen, *Photoacoustic gas analysis using interferometric cantilever microphone*, Appl. Spectrosc. Rev. **42**, 443-474 (2007).
3. C. B. Hirschmann, J. Uotila, S. Ojala, J. Tenhunen, R. L. Keiski, *Fourier transform infrared photoacoustic multicomponent gas spectroscopy with optical cantilever detection*, Appl. Spectrosc. **64**, 293-297 (2010).
4. T. Mikkonen, C. Amiot, A. Aalto, K. Patokoski, G. Genty, J. Toivonen, *Broadband cantilever-enhanced photoacoustic spectroscopy in the mid-IR using a supercontinuum*, Opt. Lett. **43**, 5094-5097 (2018).

Novel hyperspectral imager based on angle-tuned multi pass band filter, Leds and RGB image sensor

Heikki Saari¹, Harri Ojanen¹, and Ingmar Stuns¹

¹ VTT Microspectrometers, VTT Technical Research Centre of Finland Ltd., Espoo, Finland

Corresponding author: heikki.saari@vtt.fi

Keywords: optics, tunable filter, hyperspectral imaging

The multi-passband interference filters can be manufactured using the known thin film technologies based on multi-cavity technology as explained in references 1 (Denton et.al.) and 2 (Abdullah et.al.). The transmission spectrum of the interference filter can be tuned by changing the angle of the filter and this kind of filters are commercially available from Semrock (3). We have created a hyperspectral imager concept (4, 5) which is based on an angle-tuned multi-passband interference filter, multi wavelength Led illumination and RGB color image sensor. This construction can be used to form hyperspectral image of the target at narrow wavelength bands each related to the dedicated pass bands of multiple pass band filter, rotation angle of the filter and illumination of multi wavelength Leds. For example with 12 - 15 different Leds, an angle-tuned TiO₂-SiO₂ thin film stack based filter and RGB image sensor it is possible to perform hyperspectral imaging in the wavelength range 450 – 850 nm. In case of ambient light illumination or broadband lamp illumination the number spectral bands is limited by the number spectrally different pixels in the image sensor.

The design of TiO₂-SiO₂ angle-tuned multi-passband filter was made based implementing the short wavelength range (450 - 625 nm) on the front surface of fused silica substrate and the long wavelength range (625 - 850 nm) on the back surface. The depositions of the thin film stacks on ShinEtsu Synthetic Quartz wafer (d= 675 μ m, diameter = 150 mm) were made Oplatek Oy with the process detailed design made by Aki Syväluoto from Oplatek. The short wavelength range filter was based on seven layer Bragg mirrors optimized for 550 nm and operating at FPI order 10 @ 550 nm. The long wavelength range filter has seven layer Bragg mirrors optimized for 780 nm and it has optical depth between Bragg mirrors corresponding the FPI order 8 @ 780 nm. Measured transmission spectra of the filter are shown in Fig. 1 for the rotation angles 0°, 20°, 30°, 35° and 40°.

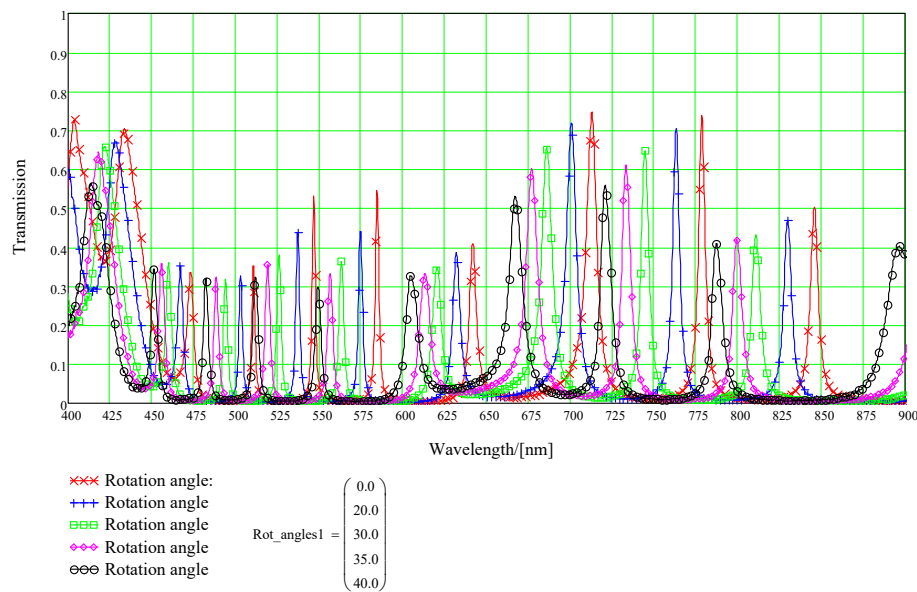


Fig. 1. Measured spectral transmissions of the TiO₂-SiO₂ angle-tuned multi-passband filter for the rotation angles 0°, 20°, 30°, 35° and 40°.

We have built a laboratory prototype of the hyperspectral imager based on the TiO₂-SiO₂ angle-tuned multi-passband filter designed for 450 - 850 nm, on 12 different Leds with wavelengths 450, 470, 525, 540, 595, 625, 660, 690, 729, 780, 810 and 850 nm (three of each Led type) and on Sony IMX174 CMOS image sensor based machine vision camera. The camera is the Point Grey USB3 GS3-U3-23S6C-C which has 1200 x 1900 pixels and 5.86 μm x 5.86 μm pixel size.

The results of the hyperspectral imager characterization and specifications are presented in Table 1

Table 1 Specifications and characterization results of the hyperspectral imager laboratory prototype based on angle-tuned multi pass band filter, Leds and RGB image sensor.

Parameter	Typical/measured value
System focal length	100 mm
F-number	4.0
Spectral range	450 - 850 nm
Spectral resolution @ FWHM	2.5...12.5 nm (pending on the wavelength)
Maximum image/object sizes	1920 x 1200 pixels 7.02 mm/14.0 mm 11.23 mm/22.5 mm 13.3 mm/26.6 mm
Dimensions	80 mm x 80 mm x 300 mm



Fig 2. Hyperspectral imager laboratory prototype based on angle-tuned multi pass band filter, Leds and RGB image sensor.

We have shown that it is possible to build a hyperspectral imager using low cost parts for the wavelength range 450 - 850 nm. The concept can be used in a wide wavelength range from 250 to 5000 nm by designing the multi pass band filter high (HfO₂, ZrO₂, Poly-Silicon, TiO₂ etc.) and low (SiO₂, MgF₂ etc.) refractive index materials accordingly.

References

1. D. Morton, Society of Vacuum Coating Technology, conf. proc, (2003), pp. 1-6.
2. H. A., Gaillan, R. M. Bushra, A. Nahla and Al. Jabar, Design Thin Film Narrow Band-pass Filters For Dense Wavelength Division Multiplexing, International Journal of Advances in Applied Sciences (IJAAS), Vol. 1, No. 2, June 2012, pp. 65-70.
3. Semrock angle-tuned filter information can be found in: https://www.semrock.com/Data/Sites/1/semrockpdfs/opticalengineering_anderson.pdf
4. US9835847 B2, 5.12.2017, Hyperspectral imaging arrangement.
5. FLIR (Point Grey) camera information can be found in: <https://www.flir.eu/products/grasshopper3-usb3?model=GS3-U3-23S6C-C>

Miniaturized spectral imaging technologies at VTT

Antti Näsilä, Heikki Saari, Kai Viherkanto, Christer Holmlund, Rami Mannila, Roberts Trops, Endija Briede, Akseli Miranto, Altti Akujärvi, Harri Ojanen, Ismo Näkki, Ingmar Stuns, Hans Toivanen, Tahvo Havia, Martti Blomberg, Sari Elomaa and Tapani Antila

VTT Technical Research Centre of Finland Ltd, Espoo, Finland

Corresponding author: antti.nasila@vtt.fi

Keywords: optics, hyperspectral imaging, fabry-perot interferometer

In the recent years, VTT Technical Research Centre of Finland Ltd has developed several miniaturized spectral imaging instruments, that are suitable for applications ranging from nanosatellites to skin cancer detection and cell phone integrated gas sensors. The common topic in all these applications is that they require small and robust instrumentation. VTT's spectral imagers are based on a tunable spectral filter, a Fabry-Perot Interferometer. This filter allows the acquisition of images at a single, freely selectable, wavelength, i.e. it is possible to record a complete 2D image at any single wavelength with a single snapshot. In the past similar functionality has been usually achieved by filter wheels, which are not very suitable for small instruments to their bulky construction. Also the tuning speed of VTT's spectral filters is very fast, which enables the recording of the complete spectrum in a short time. The filter structure is very simple, compact and robust, and thus makes this technology usable in small airborne platforms or handheld devices, which has not been possible in the past.

After a decade of research and development, spectral filter solutions have been realized for almost any wavelength from ultraviolet to thermal infrared. This means the technology can be tailored for almost all applications which utilize optical spectroscopy in some form. This has already been demonstrated in several cases, where the same basic instrument principle has been used for skin-cancer detection, ship emission monitoring, gas sensing and precision agriculture, only to list a few.

In addition to ground based applications, VTT has pioneered spectral imaging in space with nanosatellite platforms. The first space demonstration of the technology was on-board the Aalto-1 nanosatellite, which was launched in June 2017. The Aalto-1 Spectral Imager operates in the visible and near-infrared wavelengths between 500 and 900 nm. Aalto-1 Spectral Imager was also the first nanosatellite compatible camera capable of hyperspectral imaging ever to be flown in space. The second demonstration mission was for the shortwave infrared wavelengths (900 - 1400 nm) on-board the Reaktor Hello World nanosatellite, which was successfully launched in November 2018. The Hello World Spectral Imager was the first demonstration of shortwave infrared spectral imager on a nanosatellite. Both of these missions have been successful, and all the technical objectives have been completed. Future space applications include planetary exploration and missions focused on atmospheric science.

To summarize, VTT's spectral imaging technology has already been successfully demonstrated in many different applications. This has been made possible by advances in the development of the tunable Fabry-Perot Interferometers, and now VTT can provide solutions to almost any wavelength range, from UV to thermal infrared. We believe that the development will continue, as further miniaturization of the instruments will create more applications in the future.

Author Index

Lastname	Firstname	Article page numbers	
Aalto	Timo	52	
Aalto	Antti	99	
Aikio	Sanna	66	
Aizu	Yoshihisa	24	
Akujärvi	Altti	103	
Al-Sharabi	Mohammed	33	
Amiot	Caroline	99	
Amoani	James	26	
Andoh	Sampson S.	56	
Antila	Tapani	103	
Anttonen	Vuokko	20	
Aoi	Toshi	3	
Aoki	Yoshinobu	7	
Asamoah	Benjamin O.	26	56
Baah	M.	54	
Baumgartner	Hans	50	
Bautista	Godofredo	64	
Bawuah	Prince	33	
Bhat	Srivathsa	52	
Blomberg	Martti	103	
Briede	Endija	103	
Bulygin	Gleb	20	44
Byman	Ville	72	
Chamrovskii	Yuri	97	
Chen	Jun	79	
Cherchi	Matteo	52	
Choi	Samuel	73	
Costache	Mariana	18	
Das	Kaustav	24	
Deguchi	Takahiro	22	
Dumitru	Adrian	18	
Dönsberg	Timo	95	
Elomaa	Sari	103	
Fabritius	Tapio	48	
Fazeli	Elnaz	22	
Filippov	Valery	97	
Funamizu	Hideki	24	
Furukawa	Hidekai	75	
Gane	Patrick	33	
Genty	Goëry	99	
Gumenyuk	Regina	97	
Haavisto	Sanna	48	

Hagen	Nathan	11	17		
Hanayama	Ryohei	81			
Harada	Kenji	31			
Hariyadi	Soetedho	29			
Harjanne	Mikko	52			
Hasegawa	Shuma	3			
Hasegawa	Hiroshi	29			
Hashimoto	Takahiro	75			
Havia	Tahvo	103			
Hayasaki	Yoshio	9			
Heikkilä	Rauno	29			
Heikkinen	Ville	72			
Heimala	Päivi	52			
Helojärvi	Tuomas	35			
Hemming	Björn	72			
Hibino	Kenichi	29	70		
Hiitola-Keinänen	Johanna	66			
Hiltunen	Jussi	66			
Hiltunen	Marianne	66			
Hiroshi	Oohashi	29			
Hokkanen	Ari	52			
Holmlund	Christer	103			
Hoshikawa	Masaharu	75			
Hristu	Radu	18			
Huotari	Matti	63			
Huttunen	Mikko J.	18			
Huttunen	Olli-Heikki	66			
Hänninen	Pekka	22			
Iakubivskyi	Iaroslav	58			
Ikonen	Erkki	39	50	89	95
Imamura	Keigo	87			
Ishii	Katsuhiro	37	75	81	
Ishii	Yukihiro	79			
Ishikawa	Tatsuya	7			
Ito	Yujiro	9			
Jones	Geraint	58			
Juttula	Harri J.	41			
Kaikkonen	Ville A.	1	20		
Kaikkonen	Ville	20			
Kakko	Joona-Pekko	64			
Kan	Yelena	68			
Kanyathare	Boniphace	56			
Kaplas	T.	54			
Karioja	Pentti	66			
Karttunen	Anssi-Pekka	33			

Karvinen	Petri	60			
Kaseda	Kento	3			
Kauranen	Martti	64			
Ketolainen	Jarkko	33			
Kigami	Hiroshi	46			
Kiyohara	Kosuke	79			
Kleine	Justus F.	44			
Kobori	Yuta	24			
Koho	Sami	22			
Kohout	Tomas	58			
Kokka	Alexander	39			
Koponen	Antti	48			
Korhonen	Ossi	33			
Korpelainen	Virpi	43			
Kraft	Thomas	93			
Kukkola	Katri	20			
Kumagai	Toshiki	70			
Kübarsepp	T.	28			
Kylmänen	Kasper	50			
Kämppi	Antti	20			
Kärhä	Petri	50			
Lassila	Antti	43	72		
Lauri	Janne	48			
Laurila	Toni	89			
Lensu	Lasse	68			
Liedert	Christina	66			
Lipsanen	Harri	64			
Liu	Bin	73			
Makino	Takeshi	75			
Mannila	Rami	103			
Manoocheri	Farshid	95			
Markl	Daniel	33			
Matsuda	Kiyofumi	29			
Matsuda	Yasuhiro	46			
Mikkonen	Tommi	99			
Mingle	Cheetham	56			
Miranto	Akseli	103			
Miyata	Yuki	13			
Molkoselkä	Eero O.	1	20	44	
Mäkynen	Anssi J.	1	20	41	44
Määttä	Kari	63			
Nagaike	Yasunari	70			
Nielikäinen	Nanni	20			
Nishimura	Takahiro	13	61		
Niskanen	Ilpo	29			

Noronen	Teppo	97		
Nuutinen	Tarmo	56		
Nyave	Kenneth	56		
Nysten	Johan	43	72	
Näkki	Ismo	103		
Näreoja	Tuomas	22		
Näsilä	Antti	58	103	
Odoi	Keisuke	3		
Ogura	Yusuke	13	61	
Ojanen	Harri	101	103	
Okamoto	Takashi	87		
Oksanen	Benjamin	50		
Oshima	Juro	3		
Otani	Yukitoshi	17	29	
Pahapill	Jüri	91		
Pajusalo	Mihkel	58		
Parekh	Sapun	68		
Patokoski	Kim	97	99	
Peiponen	Kai-Erik	26	33	56
Pekkala	Oskari	39		
Pekkarinen	Markku	60		
Pélisset	S.	83		
Peltonen	Juha	22		
Petritsenko	Katrin	91		
Pikkarinen	Niklas	20		
Pokatilov	A.	28		
Porrasmaa	Santeri	95		
Porrovecchio	G.	28		
Praks	Jaan	58		
Pulli	Tomi	39		
Rammo	Matt	91		
Rantanen	Aleksi	20		
Rao	R.	83		
Rebane	Aleksander	91		
Reinart	Anu	58		
Ridgway	Cathy	33		
Rissanen	Joona	97		
Rossi	Jussi	89		
Roussey	Matthieu	26	56	83
Räty	Jukka	29		
Röning	Juha	63		
Saari	Heikki	101	103	
Saarinen	Jarkko J.	5		
Saarinen	Jyrki	60		
Sakurai	Sho	31		

Sasaki	Osami	73		
Satake	Shin-ichi	46		
Sato	Ryo	9		
Seppä	Jeremias	35	43	
Shibata	Shuhei	17		
Shibata	Yutaro	31		
Shimomura	Suguru	13		
Shinkawa	Daiki	61		
Sildoja	Meelis-Mait	91		
Slavinskis	Andris	58		
Snodgrass	Colin	58		
Stanciu	Stefan C.	18		
Stark	Charles W.	91		
Stuns	Ingmar	101	103	
Suzuki	Masayuki	17		
Suzuki	Natsuki	37		
Suzuki	Takamasa	73		
Svirko	Y.	54		
Tamada	Yosuke	61		
Tanida	Jun	13	61	
Taniguchi	Jun	46		
Tanner	Tarja	20		
Tate	Naoya	13		
Taue	Shuji	15		
Temerov	Filipp	5		
Toivanen	Hans	103		
Toivonen	Juha	85	97	99
Tokunaga	Eiji	79		
Tomita	Yasuo	3		
Trops	Roberts	103		
Turquet	Léo	64		
Törmänen	Matti	41		
Unno	Noriyuki	46		
Uotila	Juho	89		
Uozumi	Jun	77		
Uusitalo	Sanna	66		
Wada	Naoya	75		
Vainio	Markku	89		
Vartiainen	Erik M.	68		
Vehmas	Tapani	52		
Viherkanto	Kai	103		
Vilkman	Marja	93		
Väisänen	Kaisa-Leena	93		
Välimäki	Marja	93		
Ylikunnari	Mari	93		

Yokota	Masayuki	7
Yuasa	Tomonori	24
Yukita	Shunpei	79
Zang	Xiaorun	64
Zeitler	J. Axel	33